

NORTHWESTERN UNIVERSITY

Symmetry, Synchronization, and Switching Chimeras

A DISSERTATION

SUBMITTED TO THE GRADUATE SCHOOL
IN PARTIAL FULFILLMENT OF THE REQUIREMENTS

for the degree

DOCTOR OF PHILOSOPHY

Field of Physics

By

Yuanzhao Zhang

EVANSTON, ILLINOIS

September 2020

© Copyright by Yuanzhao Zhang 2020

All Rights Reserved

ABSTRACT

Symmetry, Synchronization, and Switching Chimeras

Yuanzhao Zhang

There is a rich history on the study of the interplay between symmetry and synchronization in networks. At the most fundamental level, many synchronization patterns are induced by underlying network symmetries. However, when stability is taken into account, the relation between symmetry and synchronization is far from monotonic. In this dissertation, we first demonstrate that introducing asymmetry in a network can often improve its synchronizability. Such asymmetry can reside in either the network structure or the node properties. In both cases, we characterize the unexpected positive effect of asymmetry on synchronization through theory, simulations, and experiments. On the other hand, even networks with the highest degree of symmetry can support very complex synchronization patterns. One prominent example is the so-called chimera states—patterns of synchrony representing coexistence of coherence and incoherence among identically coupled identical oscillators. Here, we give a detailed characterization of switching chimeras, which are chimera states that are robust and sensitive to noise at the same time. We also establish incoherence-stabilized coherence as a model-free mechanism that gives rise

to chimeras in a wide range of systems. The phenomena above provide valuable insights into the intricate relation between symmetry and synchronization, and they call for a general framework to analyze network synchronization that is not encumbered by symmetry considerations. Utilizing the theory of matrix-* algebra, we develop such a symmetry-independent framework, which leads to fast and versatile algorithms that can characterize the stability of arbitrary synchronization patterns on networks. This framework is then further extended to treat dynamical processes in complex systems with generalized interactions, including hypergraphs, simplicial complexes, multilayer networks, and temporal networks.

Acknowledgements

It's a strange time to be completing a thesis, with the outside world descending into chaos, crippled by deadly virus, mass unemployment, racial injustice, and xenophobia.

This crisis makes me appreciate even more the unconditional support I have received from my parents, Liqun and Tanyun, and the peaceful and prosperous world I enjoyed for the past 28 years.

Thanks to my advisor Adilson, for the freedom he entrusted in me over the past five years and his unwavering support on my career.

Thanks to my committee members, Michelle, Danny, and Erik for their encouragement and insight during the writing of this thesis.

Thanks to all the wonderful people I met and had the privilege to work with during my PhD, without whom my journey would have been a much duller and unremarkable experience.

Thanks to my girlfriend Claire, for keeping me company in this lonely world.

I am grateful to [TGS](#), [ARPA-E](#), [ARO](#), [MURI](#), and [CR-PSOC](#) for supporting my research at Northwestern.

I am also grateful to the Santa Fe Institute and the Schmidt Science Fellows team for offering me a job during this difficult time, without which I would have been enduring plenty more anxiety as I wrap up my PhD.

Let's all wish for world peace and the speedy development of an effective vaccine.

Table of Contents

ABSTRACT	3
Acknowledgements	5
Table of Contents	6
List of Tables	12
List of Figures	13
Chapter 1. Introduction	18
Chapter 2. Topological Control of Synchronization Patterns	22
2.1. Background	22
2.2. Isolating clusters for stability analysis	24
2.3. Asymmetric clusters are more synchronizable	28
2.4. Experimental validation	30
2.5. Generalizing topological control to intertwined clusters	32
2.6. Concluding remarks	35
Chapter 3. Asymmetry-Induced Synchronization in Multiscale Networks	36
3.1. Background	36
3.2. Definition of AISync	38

3.3. Multilayer systems considered	40
3.4. Establishing AISync	42
3.5. Examples of AISync	43
3.6. Propensity for AISync	50
3.7. Concluding remarks	54
Chapter 4. Identical Synchronization of Nonidentical Oscillators	56
4.1. Background	57
4.2. Generalized master stability analysis for nonidentical oscillators	62
4.3. Finding the finest simultaneous block diagonalization	74
4.4. AISync in delay-coupled oscillator networks	78
4.5. Concluding remarks	92
Chapter 5. Outperforming Design with Random Heterogeneity in Network Synchronization	95
5.1. Background	96
5.2. Modeling the dynamics of heterogeneous oscillators	97
5.3. Synchronization states and stability conditions	100
5.4. Disorder consistently promotes synchronization	103
5.5. Disorder is better than design	105
5.6. Insight from a minimal system	107
5.7. Electrochemical experiments	109
5.8. Concluding remarks	113
Chapter 6. Synchronizing Chaos with Imperfections	116

6.1. Background	116
6.2. Experimental setup	118
6.3. Synchronization emerges from random oscillator heterogeneity	121
6.4. Concluding remarks	128
Chapter 7. Critical Switching in Globally Attractive Chimeras	130
7.1. Background	130
7.2. Computational observation of switching chimeras	133
7.3. Power-law switching	137
7.4. Experimental observation of switching chimeras	153
7.5. Connections with biological and other physical systems	157
7.6. Concluding remarks	159
Chapter 8. Mechanism for Strong Chimeras	161
8.1. Background	161
8.2. Incoherence-stabilized coherence	164
8.3. Relation with noise-induced synchronization	169
8.4. Insight into previously-studied chimera systems	171
8.5. Concluding remarks	173
Chapter 9. Symmetry-Independent Stability Analysis of Synchronization Patterns	175
9.1. Background	176
9.2. Finest simultaneous block diagonalization	179
9.3. Cluster synchronization from a symmetry-independent perspective	184
9.4. Extension to nonidentical oscillators and coupling functions	200

9.5. Concluding remarks	205
Chapter 10. Unified Treatment of Dynamical Processes on Higher-Order and Temporal Networks	207
10.1. Background	208
10.2. Simplifying master stability functions for hypergraphs	210
10.3. Chimera states arising from higher-order interactions	214
10.4. The case of temporal networks	217
10.5. Concluding remarks	219
Chapter 11. Outlook	220
References	222
Appendix A. Supplemental Information on Topological Control of Synchronization Patterns	248
A.1. Stability analysis of nondiagonalizable clusters	248
A.2. Improving synchronizability through minimal link rewiring	251
A.3. Application of the minimal-rewiring algorithm to global synchronization	252
A.4. Experimental implementation of the coupled optoelectronic oscillators	254
A.5. Robustness of structural AISync	255
A.6. Optimizing intertwined clusters	256
A.7. Prevalence of structural AISync	259
Appendix B. Supplemental Information on Asymmetry-Induced Synchronization in Multiscale Networks	262

B.1.	Definition of Cayley graphs	262
B.2.	Details on multilayer models	262
B.3.	Details on MSF analysis	264
B.4.	Verifying the AISync conditions	265
B.5.	Details on the example in Fig. 3.3	266
B.6.	Sampling protocol used in Fig. 3.5	268
B.7.	Approximate symmetry in Fig. 3.5	269
Appendix C. Supplemental Information on Outperforming Design with Random Heterogeneity in Network Synchronization		271
C.1.	Random heterogeneity in all parameters	271
C.2.	Effect of network size	271
C.3.	Random heterogeneity in random networks	272
C.4.	Experimental protocols	272
Appendix D. Supplemental Information on Critical Switching in Globally Attractive Chimeras		275
D.1.	Switching chimeras in systems with continuous-time dynamics	275
D.2.	Linear stability analysis of chimera states	276
D.3.	Dominant switching route	278
D.4.	Transversal section of intermingled basins	280
D.5.	Robustness against oscillator heterogeneity	281
D.6.	Animated dynamics of a switching chimera	282
D.7.	Predicted intermingled basins in experimental system	282

D.8. Effect of system size

List of Tables

2.1	Connected symmetry clusters of 6 nodes and optimal clusters embedded within them	29
3.1	Number of isomorphically distinct AISync-favoring networks	51
3.2	Diagrams of symmetric networks with $N = 6, 7,$ and 8 nodes	52
4.1	Necessary and sufficient conditions for the existence of a complete synchronization state $\mathbf{s}(t)$	60

List of Figures

2.1	Experimental demonstration of structural AISync in a nonintertwined cluster	32
2.2	Demonstration of structural AISync in intertwined clusters	34
3.1	Multilayer construction of AISync networks	39
3.2	Example of consensus system showing AISync	45
3.3	Example of coupled Lorenz systems showing AISync	47
3.4	Example of coupled electro-optic systems showing AISync	48
3.5	Statistics on the prevalence of AISync-favoring networks	53
4.1	Demonstration of the SBD transformation	67
4.2	Master stability function for different h	82
4.3	Dependence of the MTLE on heterogeneity	84
4.4	Trajectories of homogeneous and heterogeneous systems	86
4.5	State diagram for the 6-node directed ring network	87
4.6	AISync in a symmetric non-circulant network	88
4.7	Synchronization induced by oscillator heterogeneity in a non-symmetric network	90

5.1	Impact of oscillator heterogeneity on the synchronization dynamics of Stuart-Landau oscillators	99
5.2	Distribution of the phase lags δ_j and the normalized amplitudes r_j/r_0 for $\sigma = 0.06$	101
5.3	Statistics on the synchronizing effect of disorder	103
5.4	Comparing systems with random and designed heterogeneity	106
5.5	Synchronization among three nonidentical Stuart-Landau oscillators coupled through a directed ring network	108
5.6	Electrochemical oscillator experiments showing that random heterogeneity promotes synchronization	111
5.7	Comparison between the dynamics of homogeneous and heterogeneous systems in the electrochemical oscillator experiment	113
6.1	Circuit diagram of coupled Chua's oscillators in our experiment	120
6.2	Experimental time series of the voltage $v_x^{(i)}$ in two different networks	122
6.3	Experimental and numerical results for a directed ring network of three oscillators	124
6.4	Synchronization stability as a function of heterogeneity β	126
6.5	Synchronizing effect of heterogeneity in γ_i	127
7.1	Globally attractive chimera state whose coherent and incoherent clusters switch under extremely small noise	135
7.2	Average switching period \bar{T} as a function of the noise intensity ξ	138

		15
7.3	Modeling transitions in switching chimeras	140
7.4	Dominant transition pathway between the two symmetric subchimeras	144
7.5	Projections of invariant sets and transition paths	146
7.6	Action profile for transition paths	149
7.7	Two-dimensional section of the state space showing intermingled basins of the two subchimeras	151
7.8	Experimental realization of globally attractive switching chimeras	154
7.9	Statistics and dynamics of a switching chimera in the experiments	156
8.1	Example scenario considered in this chapter	163
8.2	Strong chimeras in a network of diffusively coupled oscillators	167
8.3	Impact of the incoherent cluster on the stability of the coherent one	168
8.4	Incoherence-stabilized coherence for the influence of the incoherent cluster modeled as a noise effective input	171
8.5	Strong chimeras in a network of non-diffusively coupled oscillators	172
9.1	Input clusters not induced by network symmetry	195
9.2	Comparing the efficiency of the SBD algorithm and the IRR algorithm	197
9.3	Symmetry-breaking bifurcations of cluster synchronization patterns in a dense random network	198
9.4	Chimera states in a multilayer network	202
9.5	Trajectories in a multilayer network converging to a chimera state	203

10.1	Applying SBD transformations to simplicial complexes	213
10.2	SBD transformations applied to a directed simplicial complex constructed from the macaque brain connectome	214
10.3	chimera state arising from higher-order interactions	216
10.4	Equivalent of Fig. 10.1 for temporal network	217
A.1	Improvement of synchronizability by breaking the cluster symmetry through link rewiring	251
A.2	Experimental demonstration of structural AISync in global synchronization	253
A.3	Schematic illustration of the apparatus used in the optoelectronic experiments	254
A.4	Robustness of structural AISync against noise and oscillator heterogeneity	255
A.5	Cluster synchronization stabilized by breaking the structural symmetry of the cluster	260
B.1	Stability function $\psi(\lambda)$ for the AISync system in Fig. 3.3.	267
C.1	Effect of random heterogeneity in all parameters	271
C.2	Effect of random heterogeneity across network sizes	272
C.3	Effect of random oscillator heterogeneity in random networks	273
D.1	Switching chimera in a multilayer network of Lorenz oscillators	277

D.2	Average switching period \bar{T} as a function of noise intensity ξ with the short-wavelength component filtered out	279
D.3	Transversal section of the intermingled basins that directly connects the two symmetric subchimeras	280
D.4	Effect of oscillator heterogeneity on the switching behavior	281
D.5	Animation of a switching chimera from the optoelectronic experiment	282
D.6	Counterpart of Fig. 7.7 for the optoelectronic system	283
D.7	Impact of system size on switching propensity	283

CHAPTER 1

Introduction

The relational data describing the interactions between different components of a complex system are often represented as networks, and their field of study is referred to as network science [23, 183]. Given the prevalence of different forms of interactions, the study of dynamical processes on networks has become a rapidly developing topic for the past two decades [275]. Unsurprisingly, researchers realized early on that the underlying structure of a network can profoundly influence the collective dynamics it supports. Examples include epidemic spreading in human contact networks [213], cascading failure in power grids [53], and navigation in the Internet [127]. Given the societal and economic significance of these collective processes, a deeper insight into their organizing principles will be imperative for harnessing the potential of our increasingly interconnected world.

In this dissertation, we focus on network synchronization as one of the central manifestations of collective dynamics that occurs widely in both natural and man-made systems [13]. At the core of this quest is to understand when and how can coordinated behavior emerge from decentralized interactions among otherwise independent components. In particular, one fundamental objective is to disentangle the intricate play between network structure and the dynamics taking place on top of it.

The structure of a network can be characterized from many different angles, using measures such as degree distribution, modularity, centrality, and reciprocity [183]. However, perhaps none of them has a more profound impact on the observable dynamics on a

network than symmetry, which describes the ways nodes can be permuted without affecting the underlying network property [149]. It is easy to see that symmetry has a direct influence on the existence of synchronization solutions. If there is a symmetry operation that maps one node to another, then the two nodes are guaranteed to receive the same input from the rest of the network and thus admit a synchronization solution [219]. The relation between symmetry and stability, however, is much more subtle.

In Chapter 2, we show that the stability of a cluster synchronization state can almost always be enhanced precisely by breaking the structural symmetry of the network. As a consequence, less symmetry in a network can give rise to more synchronized dynamics. These results lead to new possibilities for the topological control of synchronization patterns, which we substantiate by presenting an algorithm that optimizes the network structure under various constraints and is further validated by experiments performed by collaborators.

The symmetry of a network can also be broken by making the nodes nonidentical. In Chapter 3, we show that synchronization in multiscale systems can often be improved by introducing internal differences on the node level. The only requirement is that each node can be decomposed into two or more interacting subnodes. This discovery calls for a general formalism to study the identical synchronization of nonidentical oscillators, even when the multiscale structure is absent. In Chapter 4, we develop such a formalism and demonstrate its utility using heterogeneous Stuart-Landau oscillators. These theoretical results naturally raise the question of whether similar phenomena can be observed in experiments. In Chapter 5, we establish that random heterogeneity among delay-coupled Stuart-Landau oscillators can often stabilize synchronization states that

are otherwise unstable, which we verify experimentally using electrochemical oscillators. In Chapter 6, we present experimental evidence that for chaotic Chua's oscillators implemented as electronic circuits, random mismatches in their capacitances consistently lead to better synchronization performance.

On the other hand, a fully symmetric network may also exhibit dynamics less uniform than global synchrony. One such example is chimera states, which represent symmetry-breaking phenomena in networks. Most of the early examples of chimeras are somewhat fragile and require specific initial conditions to be observed. In Chapter 7, we report on a new type of chimera state that attracts almost all initial conditions. Despite their global attractiveness, these chimeras are extremely sensitive to noise: the coherent and incoherent part of the system switch roles in the presence of arbitrarily small noise (but not in the absence of noise). The average switching rate scales as a power law with the noise intensity, which is in stark contrast with the exponential scaling observed in typical stochastic transitions (think of protein folding, chemical reactions, and spin systems). We explain the origin of this power-law switching behavior using tools from random walk, quasi-potential theory, and intermingled basins. Finally, we demonstrate that these intricate dynamics can be reproduced in optoelectronic experiments. In Chapter 8, we further explore whether there is a common mechanism that gives rise to chimeras in networks with very different local dynamics. We show that a broad class of chimeras are stabilized by an analog of noise-induced synchronization, in which coherence emerges because of (not despite) the co-occurrence of incoherence. This finding provides a system-independent explanation for the coexistence of coherence and incoherence in network systems.

The results in the chapters above demonstrate that symmetry has its limitations when it comes to predicting observable synchronization patterns, and a symmetry-independent framework is needed to fully capture the rich dynamics that can appear in networks. In Chapter 9, we establish a framework that does not rely on information about network symmetry, which makes it versatile enough to characterize the stability of any cluster synchronization pattern, even when the oscillators and/or their interactions are nonidentical. The new framework is based on finding the finest simultaneous block diagonalization of matrices in the variational equation and leads to an algorithm that is error-tolerant and orders of magnitudes faster than existing symmetry-based algorithms. It is worth noting that this method can even be applied beyond the realm of traditional networks, which assume connections to be static and only describe pairwise interactions. Thus, in Chapter 10, we present an extension of the framework to include networks with non-pairwise interactions and networks whose connections vary over time. This extension allows the discovery of interesting dynamics that are not possible in traditional networks.

Each of the chapters in this dissertation is self-contained. Notations are consistent across chapters but are also independently introduced in each chapter. Thus, chapters do not have to be read in an sequential order. A brief outlook for future research is given in Chapter 11.

CHAPTER 2

Topological Control of Synchronization Patterns

Symmetries are ubiquitous in network systems and have profound impacts on the observable dynamics. At the most fundamental level, many synchronization patterns are induced by underlying network symmetry, and a high degree of symmetry is believed to enhance the stability of identical synchronization. Yet, here we show that the synchronizability of almost any symmetry cluster in a network of identical nodes can be enhanced precisely by breaking its structural symmetry. This counterintuitive effect holds for generic node dynamics and arbitrary network structure and is, moreover, robust against noise and imperfections typical of real systems, which we demonstrate by implementing a state-of-the-art optoelectronic experiment. These results lead to new possibilities for the topological control of synchronization patterns, which we substantiate by presenting an algorithm that optimizes the structure of individual clusters under various constraints.

This chapter is based on the joint work with Joseph D. Hart, Rajarshi Roy, and Adilson E. Motter. The presentation closely follows Ref. [109].

2.1. Background

Symmetry and synchronization are interrelated concepts in network systems. Synchronization, being a symmetric state among oscillators, has its existence and stability influenced by the symmetry of the network [272, 187, 6]. For example, recent research

has shown that network symmetry can be systematically explored to identify stable synchronization patterns in complex networks [219]. Different work has shown that structural homogeneity (and hence a higher degree of network symmetry) usually enhances synchronization stability [72, 68, 194]. Any given network of identical oscillators can always be partitioned into so-called symmetry clusters [149], characterized as clusters of oscillators that are identically coupled, both within the cluster and to the rest of the network, making them natural candidates for cluster synchronization [219, 265]. Cluster synchronization has been investigated in numerous experimental systems, including networks of optoelectronic oscillators [219, 265, 302], semiconductor lasers [195, 14], Boolean systems [238], neurons [291], slime molds [278], and chemical oscillators [288]. Many of these experiments explicitly investigated the beneficial impact of network symmetries on cluster formation [288, 278, 219, 265, 106]. Taken together, previous results support the expectation that oscillators that are indistinguishable on structural grounds are also more likely to exhibit indistinguishable (synchronous) dynamics.

In this chapter, we investigate the relation between symmetry and synchronization in the general context of cluster synchronization (including global synchronization). We show that, in order to induce stable synchronization, one often has to break the underlying structural symmetry. This counterintuitive result holds for the general class of networks of diffusively coupled identical oscillators with a bounded and connected stability region, and it follows rigorously from our demonstration that almost all clusters exhibiting optimal synchronizability are necessarily asymmetric. In particular, the synchronizability of almost any symmetry cluster can be enhanced precisely by breaking the internal structural symmetry of the cluster. These findings add an important new dimension to the recent

discovery of *parametric* asymmetry-induced synchronization [192, 317, 313], a scenario in which the synchronization of identically coupled identical oscillators is enhanced by assigning nonidentical parameters to the oscillators. Here, we show that synchronization of identically coupled identical oscillators is enhanced by changing the connection patterns of the oscillators to be nonidentical. We refer to this effect as *structural* asymmetry-induced synchronization (AISync). We confirm that this behavior is robust against noise and can be found in real systems by providing the first experimental demonstration of structural AISync using networks of coupled optoelectronic oscillators. In excellent agreement with theory, the experiments show unequivocally that both intertwined and nonintertwined clusters can be optimized by reducing structural symmetry.

2.2. Isolating clusters for stability analysis

We consider a network of n diffusively coupled identical oscillators,

$$(2.1) \quad \dot{\mathbf{x}}_i = \mathbf{f}(\mathbf{x}_i) - \sigma \sum_{j=1}^n L_{ij} \mathbf{h}(\mathbf{x}_j),$$

where \mathbf{x}_i is the state of the i th oscillator, \mathbf{f} is the vector field governing the uncoupled dynamics of each oscillator, $\mathbf{L} = \{L_{ij}\}$ is the Laplacian matrix describing the structure of an arbitrary unweighed network, \mathbf{h} is the interaction function, and $\sigma > 0$ is the coupling strength. We are interested in the dynamics inside a symmetry cluster. To facilitate presentation, we first assume that the cluster is nonintertwined [219, 59]; that is, it can synchronize independent of whether other clusters synchronize or not. The general case of intertwined clusters—in which desynchronization in one cluster can lead to loss of

synchrony in another cluster—requires considering the intertwined clusters concurrently, and this important case is addressed after our analysis of nonintertwined clusters.

Numbering the oscillators in that cluster from 1 to m , we obtain the dynamical equation for the cluster:

$$\begin{aligned}
 \dot{\mathbf{x}}_i &= \mathbf{f}(\mathbf{x}_i) - \sigma \sum_{j=1}^m L_{ij} \mathbf{h}(\mathbf{x}_j) + \sigma \sum_{j=m+1}^n A_{ij} \mathbf{h}(\mathbf{x}_j) \\
 (2.2) \quad &= \mathbf{f}(\mathbf{x}_i) - \sigma \sum_{j=1}^m L_{ij} \mathbf{h}(\mathbf{x}_j) + \sigma \mathbf{I}(\{\mathbf{x}_j\}_{j>m}),
 \end{aligned}$$

where $L_{ij} = \delta_{ij}\mu_i - A_{ij}$, $\mathbf{A} = \{A_{ij}\}$ is the adjacency matrix of the network, μ_i is the indegree of node i , and the equation holds for $1 \leq i \leq m$. Here, we denote the input term from the rest of the network $\sum_{j=m+1}^n A_{ij} \mathbf{h}(\mathbf{x}_j)$ by $\mathbf{I}(\{\mathbf{x}_j\}_{j>m})$ to emphasize that this term is independent of i and hence equal for all oscillators $1, \dots, m$. This term is zero only when the cluster receives no connection from the rest of the network, such as the important case in which the entire network consists of a single symmetry cluster (i.e., $m = n$).

For $m < n$, if we regard the cluster subnetwork consisting of oscillators $1, \dots, m$ as a separate network (by ignoring its connections with other clusters), then its $m \times m$ Laplacian matrix $\tilde{\mathbf{L}}$ is closely related to the corresponding block of the $n \times n$ Laplacian matrix \mathbf{L} of the full network:

$$(2.3) \quad L_{ij} = \begin{cases} \tilde{L}_{ij}, & 1 \leq i \neq j \leq m, \\ \tilde{L}_{ij} + \tilde{\mu}, & 1 \leq i = j \leq m, \end{cases}$$

where $\tilde{\mu} \geq 0$ is the number of connections each oscillator in the cluster receives from the rest of the network. It is then clear that there are two differences in the dynamical equation when the cluster subnetwork is part of a larger network [i.e., as a symmetry cluster, described by Eq. (2.2)] rather than as an isolated network. First, the Laplacian matrix $\tilde{\mathbf{L}}$ in the dynamical equation is replaced by $\hat{\mathbf{L}} = \{L_{ij}\}_{1 \leq i, j \leq m} = \tilde{\mathbf{L}} + \tilde{\mu} \mathbf{1}_m$; that is, the diagonal entries are uniformly increased by $\tilde{\mu}$. Second, each oscillator now receives a common input $\sigma \mathbf{I}(\{x_j\}_{j>m})$ produced by its coupling with other clusters, which generally alters the synchronization trajectory $\mathbf{s}_I \equiv \mathbf{x}_1 = \cdots = \mathbf{x}_m$, causing it to be typically different from the ones generated by the uncoupled dynamics $\dot{\mathbf{s}} = \mathbf{f}(\mathbf{s})$. This has to be accounted for when calculating the maximum Lyapunov exponent transverse to the cluster synchronization manifold to determine the stability of the cluster synchronous state.

Despite these differences, a diagonalization procedure similar to the one used in the master stability function approach [217] can still be applied to the variational equation in order to assess the cluster's synchronization stability. The variational equation describing the evolution of the deviation away from \mathbf{s}_I inside the cluster can be written as

$$(2.4) \quad \delta \dot{\mathbf{X}} = [\mathbf{1}_m \otimes J\mathbf{f}(\mathbf{s}_I) - \sigma \hat{\mathbf{L}} \otimes J\mathbf{h}(\mathbf{s}_I)] \delta \mathbf{X},$$

where $\delta \mathbf{X} = (\delta \mathbf{x}_1^\top, \dots, \delta \mathbf{x}_m^\top)^\top = (\mathbf{x}_1^\top - \mathbf{s}_I^\top, \dots, \mathbf{x}_m^\top - \mathbf{s}_I^\top)^\top$ and \otimes denotes the Kronecker product. The rest of the network does not enter the equation explicitly, other than through its influence on the coupling matrix $\hat{\mathbf{L}}$ and the synchronization trajectory \mathbf{s}_I . If $\hat{\mathbf{L}}$ is diagonalizable (as for any undirected network), the decoupling of Eq. (2.4) results in

m independent d -dimensional equations corresponding to individual perturbation modes:

$$(2.5) \quad \dot{\boldsymbol{\eta}}_i = \left[J\mathbf{f}(\mathbf{s}_I) - \sigma\hat{v}_i J\mathbf{h}(\mathbf{s}_I) \right] \boldsymbol{\eta}_i,$$

where d is the dimension of node dynamics, J is the Jacobian operator, $\boldsymbol{\eta} = (\boldsymbol{\eta}_1^\top, \dots, \boldsymbol{\eta}_m^\top)^\top$ is $\delta\mathbf{X}$ expressed in the new coordinates that diagonalize $\hat{\mathbf{L}}$, and $\hat{v}_i = \tilde{v}_i + \tilde{\mu}$ are the eigenvalues of $\hat{\mathbf{L}}$ in ascending order of their real parts [with $\{\tilde{v}_i\} = \text{eig}(\tilde{\mathbf{L}})$]. If $\hat{\mathbf{L}}$ is not diagonalizable [189], the analysis can be carried out by using the Jordan canonical form of this matrix to replace diagonalization by block diagonalization, as explicitly shown in Appendix A.1. In both cases the cluster synchronous state is stable if $\Lambda(\sigma\hat{v}_i) < 0$ for $i = 2, \dots, m$, where Λ is the largest Lyapunov exponent of Eq. (2.5) and $\hat{v}_2, \dots, \hat{v}_m$ represent the transverse modes; the maximum transverse Lyapunov exponent (MTLE) determining the stability of the synchronous state is $\max_{2 \leq i \leq m} \Lambda(\sigma\hat{v}_i)$. Moreover, for the large class of oscillator networks for which the stability region is bounded and connected [24, 145, 80, 115], as assumed here and verified for all models we consider¹, the synchronizability of a cluster can be quantified in terms of the eigenratio $R = \text{Re}(\tilde{v}_m)/\text{Re}(\tilde{v}_2)$: the smaller this ratio, in general, the larger the range of σ over which the cluster synchronous state can be stable. The cluster subnetwork is most synchronizable when $\tilde{v}_2 = \dots = \tilde{v}_m$, which also implies that all eigenvalues are real and in fact integers if the network is unweighted [191], as considered here. It is important to notice that the optimality of the cluster subnetwork is conserved in the sense that if $\tilde{v}_2 = \dots = \tilde{v}_m$ for the isolated cluster, then $\hat{v}_2 = \dots = \hat{v}_m$ will hold for the cluster as part of a larger network. Since the analysis

¹For nonlinear oscillators, this can be done numerically by calculating the master stability function for a sufficiently large region in the complex plane that encompasses all eigenvalues of the coupling matrix scaled by the permissible coupling strength.

above does not invoke the continuity of the equations anywhere, it holds for discrete-time systems as well. In this case one can simply replace $\delta\dot{\mathbf{X}}$ and $\delta\mathbf{X}$ in Eq. (2.4) by $\delta\mathbf{X}(t+1)$ and $\delta\mathbf{X}(t)$, respectively.

2.3. Asymmetric clusters are more synchronizable

Now we can compare symmetry clusters with optimal clusters and show rigorously that almost all optimally synchronizable clusters are asymmetric. Without loss of generality, we consider an unweighted cluster in isolation and assume it has m nodes and ℓ directed links internal to the cluster. In a symmetry cluster, because the nodes are structurally identical, the in- and outdegrees of all nodes must be equal. Thus, ℓ must be divisible by m if the cluster is symmetric. In an optimal cluster, because $\tilde{v}_2 = \dots = \tilde{v}_m \equiv \tilde{v}$ and thus $\text{tr}(\tilde{\mathbf{L}}) = (m-1)\tilde{v}$, it follows that $\tilde{v} = \ell/(m-1)$. The fact that \tilde{v} is an integer implies that ℓ must be divisible by $m-1$ if the cluster is optimal. Since $\ell \leq m(m-1)$, the two divisibility conditions can be satisfied simultaneously if and only if $\ell = m(m-1)$ (i.e., when the isolated cluster is a complete graph). But there are numerous optimal clusters for $\ell < m(m-1)$ [189, 191]. Therefore, for any given number m of nodes, all optimal clusters other than the complete graph are necessarily asymmetric, meaning that (with the exception of the complete graph) the synchronization stability of any symmetry cluster can be improved by breaking its structural symmetry.² This general conclusion forms the basis of structural AISync and holds, in particular, when an entire network consists of a single symmetry cluster.

²Note that although structural symmetry is broken in this process, the oscillators can still synchronize identically as a Laplacian cluster because of the diffusive coupling.

Symmetry clusters					
Eigenratio	4	2.5	2	1.5	1
Optimal clusters					
Eigenratio	1	1	1	1	1

Table 2.1. Connected symmetry clusters of 6 nodes and optimal clusters embedded within them. Some symmetry clusters have more than one embedded optimal network, in which case we show one that can be obtained through a minimal number of link deletions.

When viewed as isolated subnetworks, symmetry clusters are equivalent to the vertex-transitive digraphs in algebraic graph theory, defined as directed graphs in which every pair of nodes is equivalent under some node permutation [40, 168]. Thus, in order to improve the synchronizability of any nonintertwined symmetry cluster from an arbitrary network, we only need to optimize the corresponding vertex-transitive digraph by manipulating its (internal) links. In particular, this can always be done by removing links inside the symmetry cluster [190, 191], despite the fact that sparser networks are usually harder to synchronize. For concreteness, we focus on clusters that are initially undirected and consider the selective removal of individual directional links. As an example, we show in Table 2.1 all connected undirected symmetry clusters of 6 nodes and their embedded optimal networks. Apart from the complete graph, which is already optimal to begin with, the synchronizability of the other symmetry clusters as measured by the eigenratio R is significantly improved in all cases.

Because in practice it can be costly or unnecessary to fully optimize a symmetry cluster, it is natural to ask whether its synchronizability can be significantly improved

by just modifying a few links. We developed an efficient algorithm for this purpose and summarize the statistical results based on all connected undirected symmetry clusters of sizes between $m = 8$ and 17 in Appendix A.2. On average, only about 14% of the links need to be rewired to reduce $R - 1$ by half and thus significantly improve synchronizability of symmetry clusters. This illustrates the potential of structural AISync as a mechanism for the topological control of synchronization stability. Our simulated annealing code to improve cluster synchronizability is available online at https://github.com/y-z-zhang/optimize_sym_cluster/. This algorithm can also be used to demonstrate structural AISync in global synchronization, as shown in Appendix A.3.

2.4. Experimental validation

Having established a theoretical foundation for our main finding, we now turn to our experimental results. The experiments are performed using networks of identical optoelectronic oscillators whose nonlinear component is a Mach-Zehnder intensity modulator. The system can be modeled as

$$(2.6) \quad x_i(t+1) = \beta I[x_i(t)] - \sigma \sum_{j=1}^n L_{ij} I[x_j(t)] \text{ mod } 2\pi,$$

where t is now a discrete time, β is the feedback strength, $I(x_i) = \sin^2(x_i + \delta)$ is the normalized intensity output of the modulator, x_i is the normalized voltage applied to the modulator, and δ is the operating point (set to $\pi/4$ in our experiments). Each oscillator consists of a clocked optoelectronic feedback loop. Light from a 780 nm continuous-wave laser passes through the modulator, which provides the nonlinearity. The light

intensity is converted into an electrical signal by a photoreceiver and measured by a field-programmable gate array (FPGA) via an analog-to-digital converter (ADC). The FPGA is clocked at 10 kHz, resulting in the discrete-time map dynamics of the oscillators. The FPGA controls a digital-to-analog converter (DAC) that drives the modulator with a voltage $x_i(t+1) = \beta I[x_i(t)]$, closing the feedback loop. The oscillators are coupled together electronically on the FPGA according to the desired Laplacian matrix. Specifically, the experimental system uses time multiplexing and time delays to realize a network of coupled oscillators from a single time-delayed feedback loop, as described in detail in Ref. [108]. A schematic illustration of the experimental setup can be found in Appendix A.4.

We first consider the network configuration shown in Fig. 2.1(a), which is a complex network with five symmetry clusters. The symmetry cluster highlighted in magenta is nonintertwined, and can be optimized by removing the red dashed links. The MTLE calculation in Fig. 2.1(b) predicts AISync to be common in the parameter space. Fixing $\beta = 6$, we performed 8 runs of the experiment starting from different random initial conditions, and measured the normalized voltages x_i for 8196 iterations at each fixed coupling strength before increasing σ by 0.015. The synchronization error is defined as $\Delta = \sqrt{\sum_{1 \leq i \leq m} \|x_i - \bar{x}\|^2 / m}$, where \bar{x} is the mean inside the cluster. The data points in Fig. 2.1(c) correspond to the average synchronization error $\langle \Delta \rangle$, defined as Δ averaged over the last 5000 iterations for each σ and then further averaged over the 8 experimental runs. The error bars corresponding to the standard deviation across different runs are smaller than the size of the symbols. One can observe AISync over a wide range of the coupling strength σ , matching the theoretical prediction. Structural AISync is also

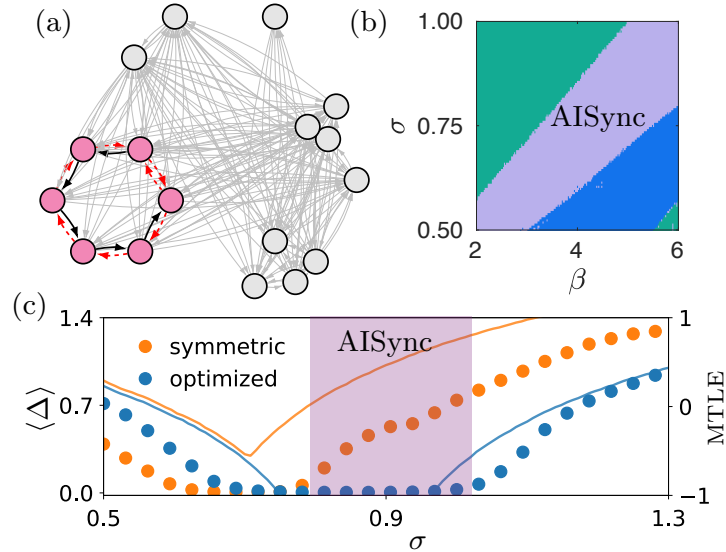


Figure 2.1. Experimental demonstration of structural AISync in a nonintertwined cluster. (a) Example network in which a symmetry cluster (magenta) is optimized for synchronization by removing the red links. (b) Predictions based on the theoretical computation of the MTLE, showing that in the $\sigma \times \beta$ parameter space there is an AISync region (purple); the other colors indicate the regions where both clusters synchronize (blue) and where neither cluster can synchronize (green). (c) Experimentally measured average synchronization error $\langle \Delta \rangle$ in the original (orange) and optimized (blue) clusters for $\beta = 6$. The experimental results are in good agreement with the MTLE calculations (color-coded curves).

common for different oscillator types and network structures and is robust against noise and parameter mismatches, as demonstrated systematically in Appendix A.5.

2.5. Generalizing topological control to intertwined clusters

We now turn to the case of intertwined clusters. Consider two intertwined clusters X and Y subject to transverse perturbations $\delta\mathbf{X}$ and $\delta\mathbf{Y}$, respectively. The variational equation for $\delta\mathbf{X}$ has the same form as Eq. (2.4) except for an additional cross-coupling term $\sigma\mathbf{C} \otimes J\mathbf{h}(\mathbf{s}_{I_Y})\delta\mathbf{Y}$ added to the right, where \mathbf{C} is the adjacency matrix describing the intercluster coupling from cluster Y to cluster X . The variational equation for $\delta\mathbf{Y}$ is

defined similarly. Now, if $\delta\mathbf{X}$ ($\delta\mathbf{Y}$) does not converge to zero according to Eq. (2.4), then the cross-coupling term must not vanish and $\|\delta\mathbf{Y}\|$ ($\|\delta\mathbf{X}\|$) must stay away from zero in order for $\|\delta\mathbf{X}\| \rightarrow 0$ ($\|\delta\mathbf{Y}\| \rightarrow 0$) in the full variational equation. Thus, in order to stabilize synchronization in intertwined clusters, the following condition must be satisfied for each cluster:

$$(2.7) \quad \|\boldsymbol{\eta}_i\| \rightarrow 0 \text{ in Eq. (2.5) for all transverse modes.}$$

In other words, $\|\delta\mathbf{X}\|$ and $\|\delta\mathbf{Y}\|$ converging to zero in Eq. (2.4) is a necessary condition for stable synchronization in X and Y . Because optimizing the clusters independently (as if they were nonintertwined) is guaranteed to expand the region satisfying the condition in Eq. (2.7), such independent optimization is an effective strategy for improving synchronization in intertwined clusters. For more details on this analysis, see Appendix A.6.

We demonstrate the strength of our approach on a random network containing two intertwined clusters, which are highlighted in Fig. 2.2(a). Each cluster is optimized by removing the red dashed links, which breaks the structural symmetry but reduces the eigenratio of the cluster to 1. The orange shade in Fig. 2.2(b) indicates the region where the condition in Eq. (2.7) is satisfied by the original clusters. The region satisfying this condition is expanded to include the purple region when the clusters are optimized. Direct simulations allow us to identify a large parameter region exhibiting AISync, which is highlighted in dark shades in Fig. 2.2(b) and is included mainly in the expanded (purple) region. A small portion of the AISync region also extends into the orange region, which follows from the condition in Eq. (2.7) being necessary but not sufficient for synchronization in the original clusters. To validate the theory and the numerics, we perform

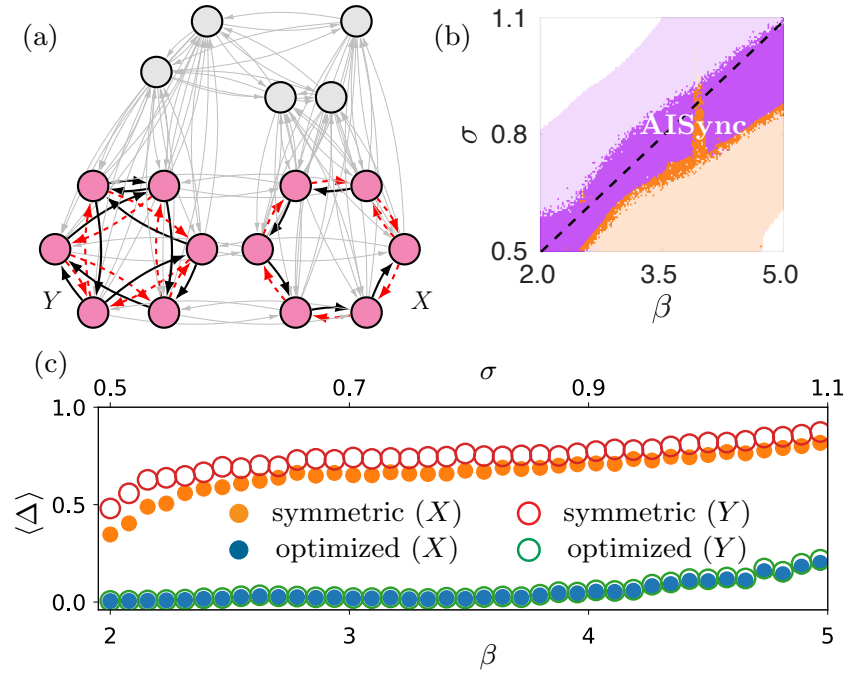


Figure 2.2. Demonstration of structural AISync in intertwined clusters. (a) Network in which two intertwined clusters (magenta) are optimized to induce synchronization by removing the red links. (b) Region in the $\sigma \times \beta$ parameter space satisfying the condition in Eq. (2.7), which is expanded from the orange shaded area to include the purple shaded area when the clusters are optimized. The dark shades (orange and purple) highlight the AISync region determined through direct simulations. (c) Experimentally measured average synchronization error $\langle \Delta \rangle$ in the original and optimized clusters when moving through the parameter space quasistatically along the dashed line in (b).

experiments with parameters varied quasistatically along the dashed line in Fig. 2.2(b). As shown in Fig. 2.2(c), the symmetry clusters are both incoherent for the entire range of parameters studied. The two optimized clusters exhibit perfectly synchronized dynamics except at the very edge of the AISync region, where the noise in the ADC has a marked impact on the dynamics (nevertheless, they are still much more synchronized than the

symmetry clusters). It is interesting to mention that although both optimized clusters are in synchrony themselves, they are not synchronized with each other.

2.6. Concluding remarks

In summary, we established the role of structural asymmetry (or structural heterogeneity) in promoting spontaneous synchronization through both theory and experiments. Our theory confirmed the generality of the phenomenon, while our experiments demonstrated its robustness. Because symmetry clusters arise naturally in complex networks, our findings are applicable to a wide range of coupled dynamical systems. In particular, since identical synchronization in a symmetry cluster is the basic building block of more complex synchronization patterns, our results can be used for the *targeted* topological control of cluster synchronization in complex networks, which echoes the positive effect of structural asymmetry on input control [298].

CHAPTER 3

Asymmetry-Induced Synchronization in Multiscale Networks

A scenario has recently been reported in which in order to stabilize complete synchronization of an oscillator network—a symmetric state—the symmetry of the system itself has to be broken by making the oscillators nonidentical. But how often does such behavior—which we term asymmetry-induced synchronization (AISync)—occur in oscillator networks? Here we present the first general scheme for constructing AISync systems and demonstrate that this behavior is the norm rather than the exception in a wide class of physical systems that can be seen as multilayer networks. Since a symmetric network in complete synchrony is the basic building block of cluster synchronization in more general networks, AISync should be common also in facilitating cluster synchronization by breaking the symmetry of the cluster subnetworks.

This chapter is based on the joint work with Takashi Nishikawa and Adilson E. Motter. The presentation closely follows Ref. [317].

3.1. Background

A common assumption in the field of network dynamics is that homogeneity in the local dynamics [233, 276] and interaction network [194, 68, 72]—or in the combination of both [176, 320]—can facilitate complete synchronization. It has been recently shown, however, that structural heterogeneity in networks of identical oscillators [191]

or oscillator heterogeneity in structurally symmetric networks [192] can stabilize otherwise unstable synchronous states, thus effectively breaking the symmetry of a system to stabilize a symmetric state. These scenarios, which we refer to as *asymmetry-induced synchronization* (AISync), can be interpreted as the converse of symmetry breaking, and hence as a converse of chimera states [133, 3]. Perhaps the most striking and the strongest form of AISync is the one in which oscillators coupled in a symmetric network (i.e., each oscillator plays exactly the same structural role) can converge to identical dynamics only when they themselves are nonidentical; this has been demonstrated, however, exclusively for rotationally symmetric networks and one type of periodic oscillators [192]. Whether such AISync behavior can be shown to be common among systems with other symmetric network structures and oscillator dynamics, including experimentally testable ones, has been an open question.

In this chapter, we introduce and analyze a broad class of AISync systems that can have general symmetric network structure with multiple link types and general oscillator dynamics (which can be chaotic, periodic, continuous-time, discrete-time, etc.). This in particular includes physical systems previously used in network synchronization experiments, thus providing a recipe for future empirical studies. For this class, we demonstrate that AISync is indeed common and provide a full characterization of those networks that support AISync behavior, showing that the fraction of such networks is significant over a range of network sizes and link densities.

3.2. Definition of AISync

To formulate a precise definition of AISync, we consider networks of N (not necessarily identical) oscillators coupled through K different types of interactions. The network dynamics is described by

$$(3.1) \quad \dot{\mathbf{X}}_i = \mathbf{F}_i(\mathbf{X}_i) + \sum_{\alpha=1}^K \sum_{\substack{i'=1 \\ i' \neq i}}^N A_{ii'}^{(\alpha)} \mathbf{H}^{(\alpha)}(\mathbf{X}_i, \mathbf{X}_{i'}),$$

where $\mathbf{X}_i = \mathbf{X}_i(t)$ is the M -dimensional state vector of node i , the function \mathbf{F}_i governs the intrinsic dynamics of node i , the adjacency matrix $A^{(\alpha)} = (A_{ii'}^{(\alpha)})$ represents the topology of interactions through links of type α , and $\mathbf{H}^{(\alpha)}$ is the coupling function associated with the link type α . A completely synchronous state of the network is defined by $\mathbf{X}_1(t) = \mathbf{X}_2(t) = \dots = \mathbf{X}_N(t)$.

To isolate the effect of breaking the homogeneity of oscillators, we consider adjacency matrices $A^{(\alpha)}$ that together represent a *symmetric network*, defined as a network in which every node can be mapped to any other node by some permutation of nodes without changing any $A^{(\alpha)}$. Thus, the set of links of any given type must couple every node identically (see Fig. 3.1(a) for an example). The rationale for using symmetric network structures here is to ensure that any stabilization of complete synchronization by oscillator heterogeneity is due to the reduced system symmetry (as required for AISync) and not due to having network heterogeneity and oscillator heterogeneity compensating each other, which may not break the system symmetry.

When restricted to undirected networks with a single link type, our definition of symmetric networks yields the class of vertex-transitive graphs from graph theory [40]. This

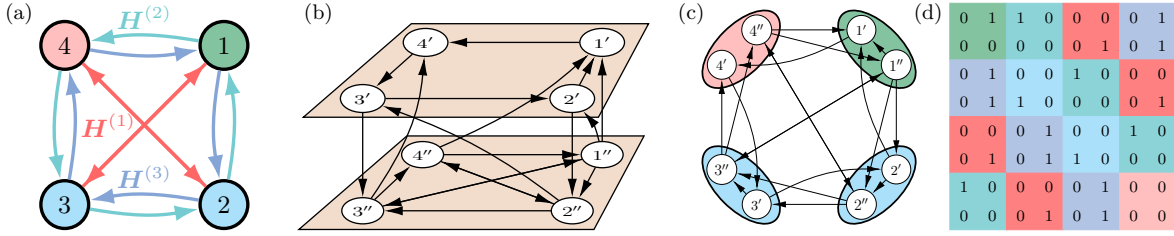


Figure 3.1. Multilayer construction of AISync networks. (a) Example of a symmetric network of $N = 4$ heterogeneous oscillators and $K = 3$ types of (directed) links with associated coupling functions $\mathbf{H}^{(1)}$, $\mathbf{H}^{(2)}$ and $\mathbf{H}^{(3)}$. (b) One of many possible multilayer networks corresponding to the network in (a), with $L = 2$ layers and $n = LN = 8$ identical subnodes. Subnodes are labeled with node indices, with prime and double prime indicating layer 1 and 2, respectively. (c) Flattened, monolayer representation of the multilayer network in (b). (d) Block structure of the adjacency matrix \tilde{A} for the monolayer network in (c). Colors indicate different types of nodes ($F^{(i)}$, diagonal blocks) and links ($\tilde{A}^{(iil)}$, off-diagonal blocks).

rich class encompasses Cayley graphs (defined as a network of relations between elements of a finite group; Appendix B.1) and circulant graphs (defined as a network whose nodes can be arranged in a ring so that the network is invariant under rotations), which have previously been used to study chimera states [210]. Enumerating *all* vertex-transitive graphs of a given size N becomes challenging as N grows and has so far been completed only for $N < 32$.³ The symmetric networks we consider here generalizes vertex-transitive graphs to the even richer class of networks that can be directed and include multiple link types.

Given a symmetric network structure, the system in Eq. (3.1) exhibits AISync if it satisfies the following two conditions: (C1) there are no asymptotically stable synchronous states for any *homogeneous system* (i.e., with $\mathbf{F}_1 = \dots = \mathbf{F}_N$), and (C2) there is an

³See Sequence A006799 in the On-Line Encyclopedia of Integer Sequences, published electronically at <https://oeis.org>.

asymptotically *heterogeneous system* (i.e., with $\mathbf{F}_i \neq \mathbf{F}_{i'}$, for some $i \neq i'$) for which a stable synchronous state exists. A challenge in establishing AISync is that the form of Eq. (3.1) does not guarantee the existence of a completely synchronous state. Another challenge concerns the stability analysis of such a state, since Eq. (3.1) is beyond the framework normally used in the master stability function (MSF) approach and its generalizations currently available [276, 62, 219, 67]: oscillators can be nonidentical (different \mathbf{F}_i), and the network can host $K > 1$ types of directed interactions.

3.3. Multilayer systems considered

To overcome these challenges, below we propose a *multilayer construction* that defines a large, general subclass of systems within the class given by Eq. (3.1). We show that any system in this subclass is guaranteed to have a synchronous state, and the stability of that state can be analyzed by applying the MSF framework to the flattened representation of the system. The MSF approach decouples the oscillator dynamics from the network structure, which enables us to draw conclusions about AISync for general oscillator dynamics.

In our multilayer system, each node is composed of L identical *subnodes*, belonging to L different layers and connected by a set of *internal sublinks*. The pattern of these internal sublinks is thus part of the node's properties and determines the heterogeneity across nodes. For a pair of connected nodes, the type of the connecting link is determined by the pattern of *external sublinks* between the subnodes of these two nodes. This construction yields a multilayer network [88, 98, 66, 42, 65] of subnodes and sublinks with L layers; see Fig. 3.1(b) for an $L = 2$ example. Note that in general there is more than one possible

multilayer network for a given symmetric network. Networks with such layered structure have been used extensively as realistic models of various natural and man-made systems. The class of systems just defined is broader than most classes of systems used in previous studies of synchronization on multilayer networks [312, 85], since the links between two different layers are not constrained to be one-to-one. The underlying hierarchical organization, in which each node decomposes into interacting subnodes, is shared by many physical systems, such as the multi-processor nodes in modern supercomputers.

Coupling the dynamics of subnodes diffusively in this network, the multilayer system can be described at the subnode level as

$$(3.2) \quad \dot{\mathbf{x}}_\ell^{(i)} = \mathbf{f}(\mathbf{x}_\ell^{(i)}) + \sum_{i'=1}^N \sum_{\ell'=1}^L \tilde{A}_{\ell\ell'}^{(ii')} [\mathbf{h}(\mathbf{x}_{\ell'}^{(i')}) - \mathbf{h}(\mathbf{x}_\ell^{(i)})],$$

where $\mathbf{x}_\ell^{(i)} = \mathbf{x}_\ell^{(i)}(t)$ is the m -dimensional state vector for subnode ℓ (i.e., in layer ℓ) of node i , the function \mathbf{f} determines the dynamics of every isolated subnode, and \mathbf{h} is the coupling function common to all sublinks. Here, for all links of a given type between different nodes, the corresponding coupling matrix $\tilde{A}^{(ii')} := (\tilde{A}_{\ell\ell'}^{(ii')})$, $i \neq i'$, is the same and encodes the subnode connection pattern for that link type. In contrast, the subnode connection pattern within each node i is encoded in the matrix $F^{(i)} := (\tilde{A}_{\ell\ell'}^{(ii)})$. Since the subnode-to-subnode interactions are diffusive, the synchronous state given by $\mathbf{x}_\ell^{(i)}(t) = \mathbf{s}(t)$, $\forall i, \ell$ with $\dot{\mathbf{s}} = \mathbf{f}(\mathbf{s})$ is guaranteed to exist. Note that the diffusive coupling among subnodes do not necessarily imply that the node-to-node interactions are diffusive, as intralayer synchronization of the form $\mathbf{x}_\ell^{(i)} = \mathbf{s}_\ell$ among subnodes is also valid as a state of complete synchronization among all nodes. The interactions among nodes do not vanish in this case due to the existence of external sublink connections among different layers. To summarize,

Eq. (3.2) describes a general class of multilayer models of symmetric networks that admit a state corresponding to complete synchronization, $\mathbf{X}_i(t) = \mathbf{S}(t)$, $\forall i$, when written in the form of Eq. (3.1) (see Appendix B.2 for details).

3.4. Establishing AISync

To facilitate the stability analysis required to establish AISync, we flatten the multilayer network representation into a single layer (see Fig. 3.1(c) for an example). We use $\tilde{A} = (\tilde{A}_{jj'})$ to denote the adjacency matrix that encodes the structure of the resulting monolayer network (see Fig. 3.1(d) for an example). This matrix has a block structure in which the matrices $F^{(i)}$ appearing on the diagonal blocks characterize node properties, while $\tilde{A}^{(ii')}$ appearing on the off-diagonal blocks reflect the link types. Since subnodes and sublinks are identical, we can directly apply the MSF analysis [217] to the monolayer network and obtain the stability function $\psi(\lambda)$ (see Appendix B.3 for details). The maximum transverse Lyapunov exponent (MTLE) of the synchronous state is then computed as $\Psi := \max_{2 \leq j \leq n} \psi(\lambda_j)$, where $\lambda_1, \dots, \lambda_n$ are the eigenvalues of the corresponding Laplacian matrix $\tilde{L} := (\tilde{L}_{jj'})$, defined as $\tilde{L}_{jj'} := \delta_{jj'} \sum_{k=1}^n \tilde{A}_{jk} - \tilde{A}_{jj'}$, where $\delta_{jj'}$ is the Kronecker delta function. Here, λ_1 is the identically zero eigenvalue, which is excluded in the definition of Ψ for corresponding to a mode of perturbation that does not affect synchronization. Thus, the synchronous state is asymptotically stable if $\Psi < 0$ and unstable if $\Psi > 0$.

To establish AISync for our multilayer system, we first verify that all homogeneous systems have $\Psi > 0$ (i.e., synchronous state $\mathbf{x}_\ell^{(i)} = \mathbf{s}$, $\forall i, \ell$, is unstable), and check numerically that all other synchronous states $\mathbf{x}_\ell^{(i)} = \mathbf{s}_\ell$, $\forall i, \ell$, are also unstable. This

establishes condition (C1). We then find a heterogeneous system with $\Psi < 0$, which establishes condition (C2). This procedure is detailed in Appendix B.4.

In the case of linear \mathbf{f} and \mathbf{h} , which is widely used to study consensus dynamics and encompasses a variety of nontrivial stability regions [145], the problem of verifying AISync is fully solvable. To see this, we first note that in this case the stability function $\psi(\lambda)$ determines the (common) stability of *all* completely synchronous states of the form $\mathbf{x}_\ell^{(i)} = \mathbf{s}_\ell$, $\forall i, \ell$, where the subnode states \mathbf{s}_ℓ can in general be different for different ℓ . Next, for a given (homogeneous or heterogeneous) system, we sort its Laplacian eigenvalues into two groups: $\lambda_1, \dots, \lambda_{j^*}$, corresponding only to those perturbations parallel to the synchronization manifold, and $\lambda_{j^*+1}, \dots, \lambda_n$, corresponding to perturbations that are transverse to the manifold and thus destroy synchronization. The stability (of all completely synchronous states) is then determined by $\Psi' := \max_{j^* < j \leq n} \psi(\lambda_j)$, noting that both j^* and λ_j generally depend on the network structure. This leads to the following solution for the AISync conditions: $\Psi' \geq 0$ for all homogeneous systems and $\Psi' < 0$ for some heterogeneous system (where we include $\Psi' = 0$ in the first condition because $\Psi' = 0$ for linear system would exclude asymptotically stable synchronization).

3.5. Examples of AISync

3.5.1. Consensus dynamics

Here we establish AISync for the system with the symmetric network structure shown in Fig. 3.2, in which the subnodes follow the consensus dynamics used in Ref. [145]:

$$(3.3) \quad \dot{\mathbf{x}}_i = D\mathbf{f}\mathbf{x}_i - \sum_j \tilde{L}_{ij} D\mathbf{h}\mathbf{x}_j,$$

where

$$(3.4) \quad D\mathbf{f} = \begin{pmatrix} -2 & 2 & -1 & 2 \\ -1 & 1 & 0 & 0 \\ 0 & 0 & -3 & 4 \\ 0 & 0 & -1 & 1 \end{pmatrix} \quad D\mathbf{h} = \begin{pmatrix} 0 & 0 & 0 & 0 \\ 0 & 0 & 0 & 0 \\ 0 & 1 & 0 & -1 \\ -1 & 0 & 1 & 0 \end{pmatrix}.$$

This leads to the stability region $\psi(\lambda) < 0$ shown in Fig. 3.2(c), defined by

$$(3.5) \quad x(x+3) - y^2 - (2x+3)^2 y^2 > 0,$$

where x and y denote the real and imaginary parts of λ , respectively.

For $L = 2$ there are only two possible homogeneous systems, associated with the two possible directions of the internal sublink in each node. The homogeneous system in Fig. 3.2(a) has Laplacian eigenvalues $\lambda_1 = 0$, $\lambda_2 = 2$, $\lambda_{3,4} \approx 0.5 \pm 0.866i$, and $\lambda_{5,6} \approx 1.5 \pm 0.866i$, where λ_1 and λ_2 correspond to the perturbations parallel to the synchronization manifold and $\lambda_3, \dots, \lambda_6$ correspond to those in the transverse directions (i.e., $j^* = 2$). Since $\psi(\lambda_j) > 0$ for $j = 3, 4, 5, 6$ [i.e., all these λ_j 's fall outside the stability region defined by Eq. (3.5), as indicated by the red squares in Fig. 3.2(c)], we have $\Psi' = \max_{2 < j \leq 6} \psi(\lambda_j) > 0$. The other homogeneous system is not synchronizable since all the single-prime subnodes have no incoming sublink. In contrast, for the heterogeneous system in Fig. 3.2(b), the Laplacian eigenvalues are $\lambda_1 = 0$, $\lambda_j = 1$ for $1 < j \leq 5$, and $\lambda_6 = 2$ (i.e., $j^* = 1$ in this case). As shown by the blue dots in Fig. 3.2(c), we have $\Psi' = \max_{1 < j \leq 6} \psi(\lambda_j) < 0$ for this heterogeneous system. We thus see that $\Psi' \geq 0$ (i.e., the synchronous state is not asymptotically stable) for both homogeneous systems and

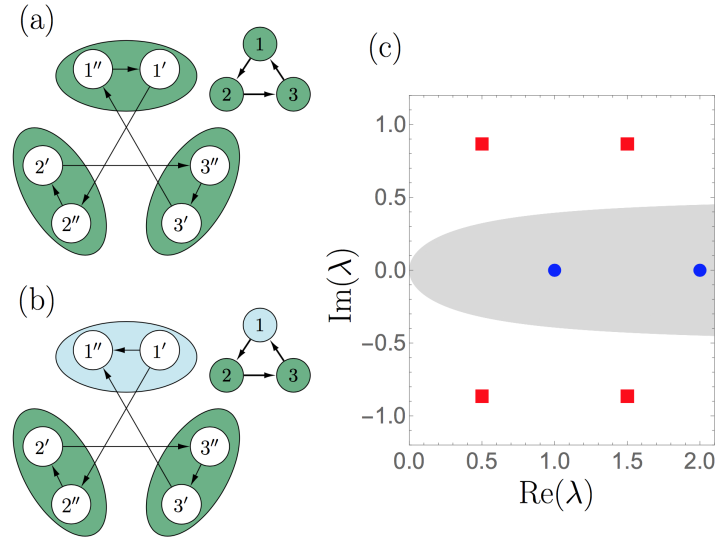


Figure 3.2. Example of consensus system showing AISync. (a) Symmetric network of $N = 3$ homogeneous nodes, each with $L = 2$ subnodes coupled by a directed link (from subnode i'' to i'). (b) The same network but with heterogeneous nodes, in which the direction of the internal sublink in the (light) cyan node is the opposite of that in the (dark) green nodes. In both (a) and (b) we show the corresponding node-level visualization of the network at the top right. (c) Stability region (shaded gray) for the consensus dynamics. All the transverse modes for the homogeneous system in (a) are unstable (red squares), while those for the heterogeneous system in (b) are stable (blue dots).

$\Psi' < 0$ (i.e., the synchronous state is asymptotically stable) for a heterogeneous system, establishing AISync: the agents can reach consensus only when some of them are different from the others.

3.5.2. Coupled Lorenz oscillators

An example of nonlinear system exhibiting AISync is shown in Fig. 3.3. The network structure is symmetric and has $N = 3$ nodes and $K = 2$ types of links representing sublink patterns in the clockwise and counterclockwise directions in Fig. 3.3(a). Each

node consists of $L = 2$ subnodes, each of which is a chaotic Lorenz oscillator. The two subnodes are connected by a sublink, the direction of which determines the node type. This gives rise to two node types, and there are four possible distinct combinations of node types for the network—two homogeneous and two heterogeneous. The system has two parameters, a and b , representing the coupling strength of internal and external sublinks, respectively. We seek to determine for which values of a and b the system exhibits AISync.

In Fig. 3.3(b), we show Ψ_+ (red) and Ψ_- (blue) as functions of a and b , where Ψ_+ (Ψ_-) are defined to be the smaller value of Ψ between the two possible homogeneous (heterogeneous) systems. In the region shaded purple (where $\Psi_- > 0$ and $\Psi_+ < 0$), the synchronous state $\mathbf{x}_\ell^{(i)}(t) = \mathbf{s}(t)$, $\forall i, \ell$ is stable for at least one of the heterogeneous systems, but unstable for both homogeneous systems. We further verify in this region that the other possible forms of synchronous states, $\mathbf{x}_\ell^{(i)}(t) = \mathbf{s}_\ell(t)$, $\forall i, \ell$, are unstable for both homogeneous systems (through extensive numerical simulation—see Appendix B.5 for details). This establishes conditions (C1) and (C2), thus confirming that the system exhibits AISync in the purple region. The AISync behavior of the system for a specific combination of a and b is illustrated by the sample trajectory in Fig. 3.3(c), which diverges from synchrony while the nodes are kept homogeneous, but re-synchronizes spontaneously after the nodes are made heterogeneous.

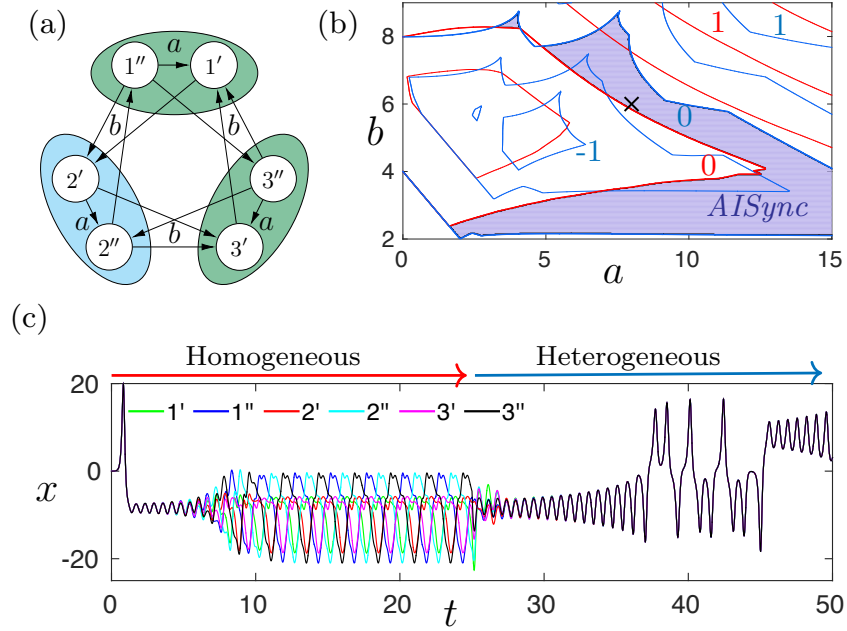


Figure 3.3. Example of coupled Lorenz systems showing AISync. (a) Symmetric network of $N = 3$ nodes, each with $L = 2$ directionally coupled subnodes of Lorenz oscillators. Here we show an instance of a heterogeneous system in which the sublink direction in one node (cyan) is different from the other two (green). (b) Contour plots of $\Psi_{=}$ (red) for the case of homogeneous nodes (all-green or all-cyan nodes) and Ψ_{\neq} (blue) for heterogeneous nodes (one or two green nodes). The shaded region corresponds to AISync systems, for which $\Psi_{=} > 0$ and $\Psi_{\neq} < 0$. (c) Sample trajectory of the system for $a = 8$ and $b = 6$ [cross symbol in (b)], exhibiting AISync. The first component x_1 of the Lorenz oscillator state vector is shown for all $n = 6$ subnodes.

3.5.3. Coupled electro-optic systems

We now present an experimentally testable AISync system based on the discrete-time model of the electro-optic system implemented in Refs. [104, 219] and given by

$$(3.6) \quad x_i^{t+1} = \left[f(x_i^t) - \sum_j \tilde{L}_{ij} f(x_j^t) + \delta \right] \text{ mod } 2\pi,$$

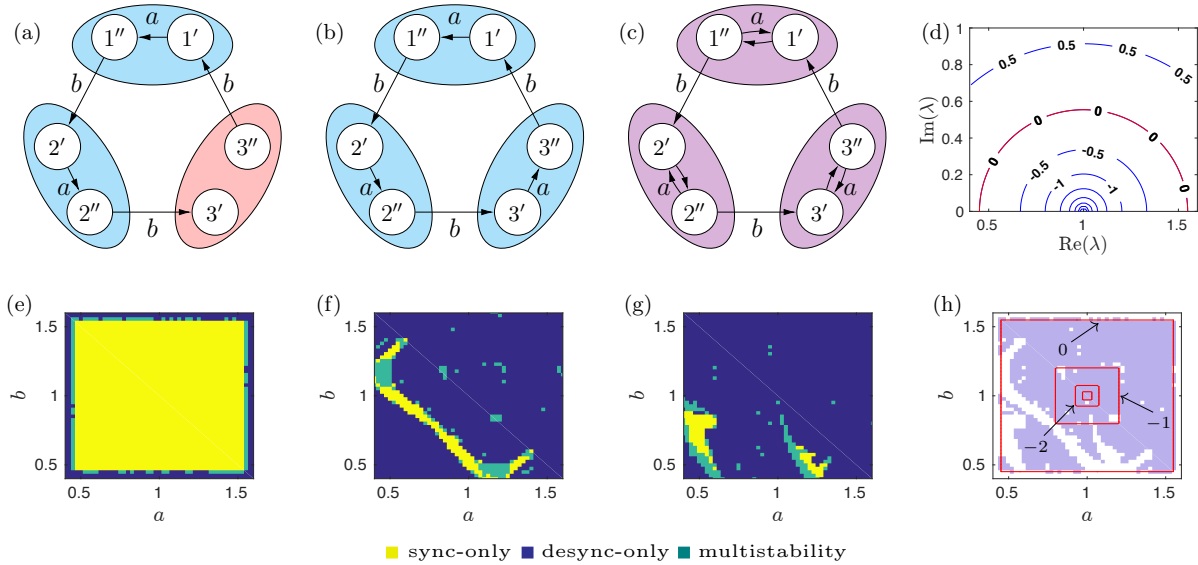


Figure 3.4. Example of coupled electro-optic systems showing AISync. (a–c) Networks with heterogeneous (a) and homogeneous nodes (b,c). (d) Stability function $\psi(\lambda)$ for the electro-optic system. (e–g) Numerical results indicating where each system in (a–c) is synchronizable in the parameter space. Each pixel is categorized into three classes according to 24 independent simulations from random initial conditions (see text for details). (h) The AISync region (shaded purple), which is the union of yellow and green regions in (e) minus the analogous unions in (f) and (g). The red contours encode the MTLE for the heterogeneous system.

where $f(x) = \beta I(x)$ determines the isolated subnode dynamics and also serves as the coupling function. Here, $I(x) = (1 - \cos x)/2$ is the normalized optical intensity, $\beta = 1.7\pi$ is the self-feedback strength, $\delta = 0.2$ is the offset introduced to suppress the trivial solution $x_i = 0$, and \tilde{L}_{ij} is the weighted graph Laplacian [weights controlled by parameters a and b , as shown in Fig. 3.4(a–c)].

Figure 3.4 shows an example of AISync using these electro-optic maps as subnodes. The internal connections are chosen from the quaternary set (no sublink, one directed sublink in either direction, and directed sublinks in both directions). When the same choice is made for all internal connections, this leads to four different homogeneous systems, but

two of them have $\lambda_2 = 0$ (not synchronizable), leaving only two homogeneous systems to consider [Figs. 3.4(b) and (c)]. For comparison, we take the heterogeneous system in Fig. 3.4(a), which forms a directed chain network in its monolayer representation. Each of the three systems [Figs. 3.4(a–c)] has a companion plot showing under what parameters the nodes are synchronizable [Figs. 3.4(e–g)]. In the latter panels, each pixel is generated from 24 independent simulations run from random initial conditions. The pixels are then color-coded according to how many times a fully synchronized state was reached after 2500 iterations (“sync-only”: 24 times; “desync-only”: 0 times; “multistability”: all other cases). Here we consider a trajectory to be fully synchronized if the synchronization error e defined in Eq. (B.7) and averaged over the last 100 iterations falls below 10^{-3} . It is worth noting that, in this example, when a homogeneous system is synchronizable the synchronous state is always in the form of cluster synchronization among subnodes (those indexed with prime and double prime form two separate synchronized clusters), since complete synchronization among subnodes is always unstable for both homogeneous systems.

Figure 3.4(d) shows the stability function $\psi(\lambda)$ for the electro-optic subnode dynamics and coupling function, which has a bounded stable region. The lines are quite dense inside the stable region, meaning that the stability landscape is steep there and the function reaches very deep negative values. This is confirmed in Fig. 3.4(h), where the AISync regions are shaded purple, with the MTLE of the synchronous state for the heterogeneous system shown as red contour lines.

3.6. Propensity for AISync

But how often does a network structure support AISync? To systematically address this question, we use the spread σ of the eigenvalues of the Laplacian matrix \tilde{L} for the monolayer network representation, which is a measure of synchronizability [191] defined by $\sigma^2 := \sum_{j=2}^n |\lambda_j - \bar{\lambda}|^2 / [d^2(n-1)]$, where $d := \sum_{j=1}^n \tilde{L}_{jj} / n$ and $\bar{\lambda} := \sum_{j=2}^n \lambda_j / (n-1)$. A smaller σ indicates higher synchronizability. Given an external sublink structure corresponding to a symmetric network, we compare the minimum spread $\sigma_{=}$ among all systems with homogeneous $F^{(i)}$ to the corresponding minimum σ_{\neq} among all systems with strictly heterogeneous $F^{(i)}$. We call the structure *AISync-favoring* if $\sigma_{\neq} < \sigma_{=}$, which indicates that heterogeneous $F^{(i)}$ can make the system easier to synchronize than any homogeneous $F^{(i)}$. As a measure of how strongly the structure supports AISync, we define $r := 1 - \sigma_{\neq} / \sigma_{=} \leq 1$, where $r > 0$ indicates an AISync-favoring structure, and $r = 1$ implies $\sigma_{\neq} = 0$ (i.e., there is a heterogeneous system with optimal synchronizability). For example, the structure in Fig. 3.3 has $\sigma_{=} \approx 0.56$ and $\sigma_{\neq} \approx 0.33$, and $r \approx 0.41$.

Using this AISync strength r , we first enumerate all networks of a given size supporting AISync (Table 3.1). For each N , we generate one or more diagrams representing all N -node symmetric networks, which are shown in the first row of Table 3.1 for $N = 3, 4, 5$. In these diagrams, each color indicates a set of links that, in any given symmetric network, must all exist together and be of the same type or not exist at all (noting that links from different sets can be of the same type). For example, there are three distinct symmetric networks for $N = 3$: a directed ring (cyan or black links), an undirected ring (cyan and black links of the same type), and the superposition of two directed rings in opposite directions (cyan and black links of different types; as in Fig. 3.3). For a given symmetric

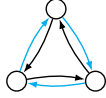
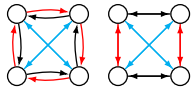
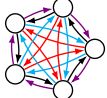
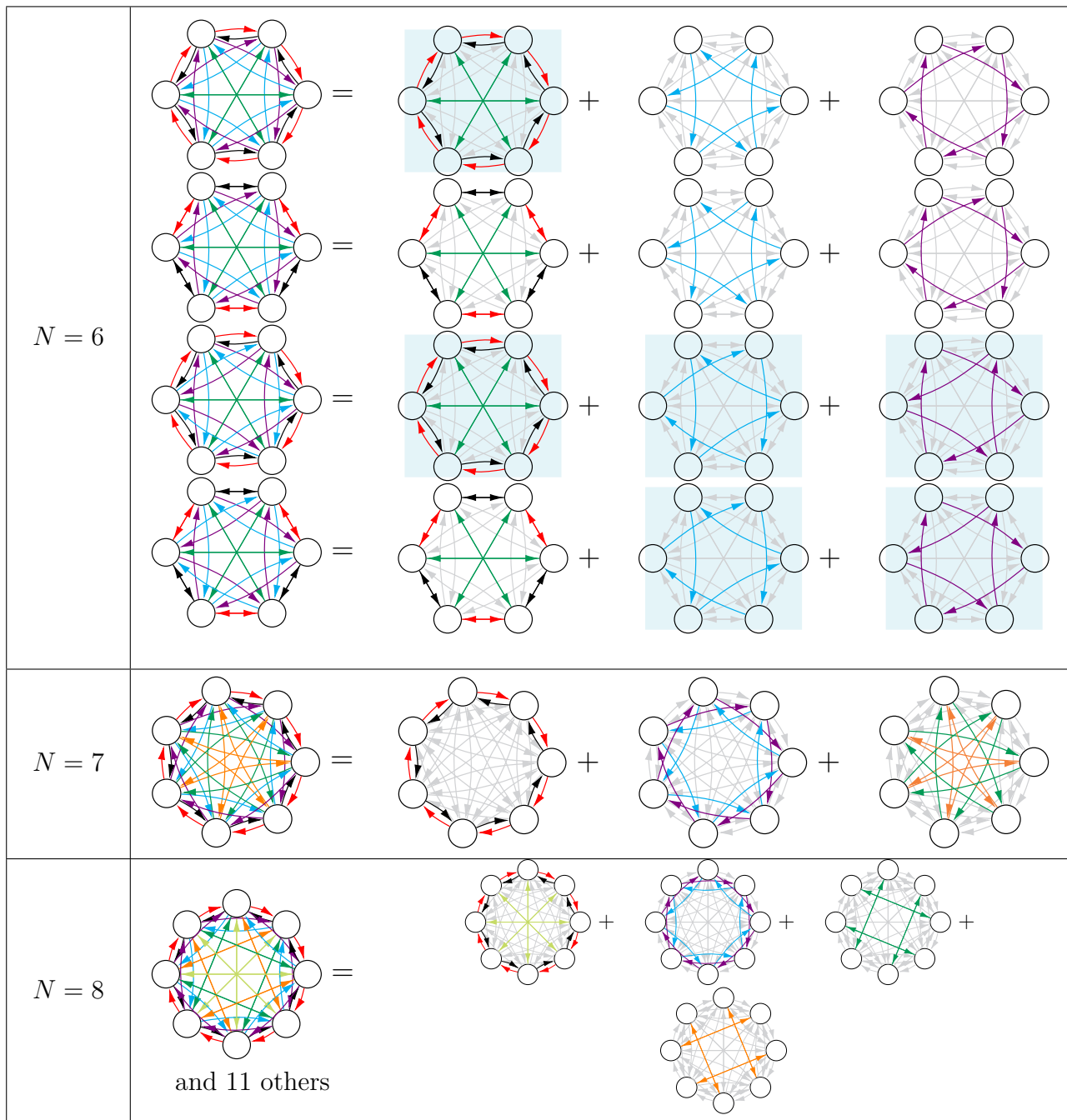
	$N = 3$	$N = 4$	$N = 5$
symmetric networks			
Q (optimal)	9	14	21
Q ($r > 0.2$)	11	81	254
Q ($r > 0.05$)	29	318	2154
B ($r > 0.2$)	11	101	204
B ($r > 0.05$)	31	400	2406

Table 3.1. Number of isomorphically distinct AISync-favoring networks, listed for $N = 3, 4, 5$ nodes and $L = 2$ layers (with $a = b = 1$ to enable counting). The numbers are given for both binary (B) and quaternary (Q) choices of internal sublink configurations, as well as for different AISync strength (as measured by r defined in the text). The network diagrams encode all possible symmetric networks of a given size.

network derived from these diagrams, we choose the external sublink pattern for each link type from all possible ways of connecting a subnode pair to another. For the internal sublink patterns, we use either the binary or quaternary choices, where each node has one directed sublink (in either direction) in the binary case, while all four possibilities are allowed in the quaternary case. The rest of Table 3.1 lists the total numbers of isomorphically distinct external sublink structures with $r > 0.05$, $r > 0.2$, and (optimal) $r = 1$.

Table 3.2 extends the first row in Table 3.1, showing the symmetric network diagrams for $N = 6, 7$, and 8. In each row, the leftmost diagram is the full representation as in Table 3.1, which is decomposed into multiple components (the partial diagrams in the same row) to make them more clearly visible. The partial diagrams with the same background color indicate identical components appearing in multiple rows. Thus, for $N = 6$, we have four different diagrams (rows), each with a different combination of components. There is only

Table 3.2. Diagrams of symmetric networks with $N = 6, 7,$ and 8 nodes.

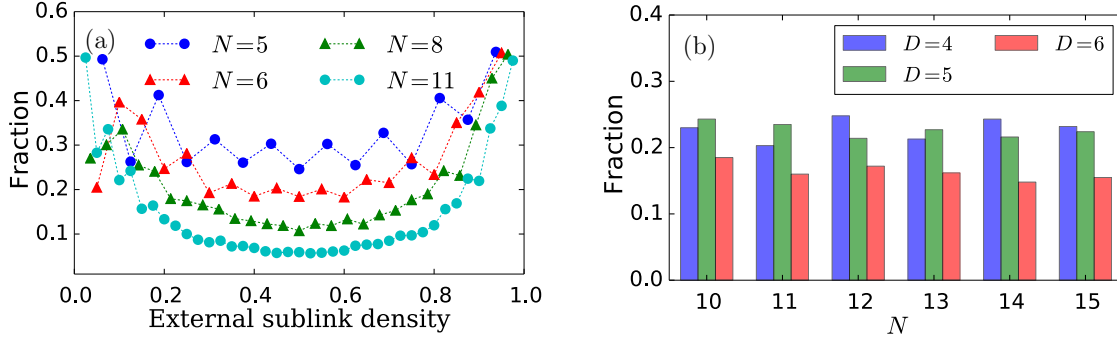


Figure 3.5. Statistics on the prevalence of AISync-favoring networks. Shown as functions of (a) external sublink density and (b) network size N . Both panels show the fraction of systems with AISync strength $r > 0.05$ among those with circulant network structures, where the external sublink density is given by $D/[L^2(N-1)]$, and D is the number of external sublinks received by a node (which is the same for all nodes).

one diagram for $N = 7$, while we show one representative diagram out of twelve in the case of $N = 8$.

Figure 3.5 shows the statistics of AISync-favoring networks. For numerical feasibility, we focus on those systems whose network structure is a directed circulant graph with multiple link types (which covers all symmetric networks if N is a prime number). Sampling uniformly within this class (Appendix B.6), we observe that significant fraction of external sublink structures are AISync-favoring over a range of external sublink densities [Fig. 3.5(a)] and network sizes [Fig. 3.5(b)]. We also observe that sparse and dense structures favor AISync more often than medium-density ones, despite the expectation that the effect of internal sublink heterogeneity would be smaller with higher external sublink density. This phenomenon is further explored in Appendix B.7 by establishing the approximate left-right symmetry in Fig. 3.5(a).

3.7. Concluding remarks

Given a symmetric network of identical oscillators, it is instructive to compare our results above in which the symmetry is broken by making the oscillators nonidentical with the alternative scenario in which the symmetry is broken by making the network structure asymmetric. For directed unweighted networks of diffusively-coupled identical oscillators, it can be shown that: 1) with the exception of the complete graphs, all topologies that optimize synchronizability (i.e., those with $\sigma = 0$) are asymmetric; 2) any network topology that can be spanned from a node (i.e., $\min_{i \geq 2} \text{Re}(\lambda_i) > 0$) embeds optimally synchronizable subnetworks generated by deleting a subset of links [190, 191]. For example, a synchronous state that is not stable for a directed ring network may become stable for a directed chain formed by removing a link. More generally, introducing structural heterogeneity (breaking the symmetry of the network) can stabilize otherwise unstable homogeneous (symmetric) states.

Finally, we note that the defining characteristic of AISync considered here—that preserving the symmetry of a stable state requires breaking the symmetry of the system—can bear analogs in oscillator networks whose structure is not necessarily symmetric. Such a network can always be partitioned into symmetric subnetwork clusters (structurally equivalent subsets of nodes) that are candidates for cluster synchronization [96, 219, 187]. Synchronization of one of these clusters plays the role of complete synchronization in a symmetric network, which opens the possibility of exploiting AISync to tune cluster synchronization patterns through oscillator heterogeneity in arbitrary complex networks. We

hope that our findings, and future theoretical and experimental studies they will stimulate, will significantly advance understanding of the interplay between symmetry and network dynamics.

CHAPTER 4

Identical Synchronization of Nonidentical Oscillators

An outstanding problem in the study of networks of heterogeneous dynamical units concerns the development of rigorous methods to probe the stability of synchronous states when the differences between the units are not small. Here, we address this problem by presenting a generalization of the master stability formalism that can be applied to heterogeneous oscillators with large mismatches. Our approach is based on the simultaneous block diagonalization of the matrix terms in the variational equation, and it leads to dimension reduction that simplifies the original equation significantly. This new formalism allows the systematic investigation of scenarios in which the oscillators need to be nonidentical in order to reach an identical state, where all oscillators are completely synchronized. In the case of networks of identically coupled oscillators, this corresponds to breaking the symmetry of the system as a means to preserve the symmetry of the dynamical state—a recently discovered effect termed asymmetry-induced synchronization (AISync). Our framework enables us to identify communication delay as a new and potentially common mechanism giving rise to AISync, which we demonstrate using networks of delay-coupled Stuart-Landau oscillators. The results also have potential implications for control, as they reveal oscillator heterogeneity as an attribute that may be manipulated to enhance the stability of synchronous states.

This chapter is based on the joint work with Adilson E. Motter. The presentation closely follows Ref. [313].

4.1. Background

The study of synchronization phenomena in networks of coupled dynamical systems has traditionally focused on either the partial synchronization of nonidentical oscillators, such as in the Kuramoto model [131], or the complete synchronization of identical ones, as in the Pecora-Carroll model [216, 217]. The first concerns primarily studies in the limit of large population sizes and uses approaches that stem from statistical physics, while the second emphasizes the study of finite-size systems using dynamical systems methods to characterize the stability of synchronous states [2]. Until recently, little attention was given to the possibility of complete synchronization of nonidentical oscillators. This was the case because, on the one hand, there has been a lack of rigorous dynamical systems approaches that can be used to study complete synchronization in networks of nonidentical oscillators; on the other hand, it was not appreciated that complete synchronization could occur for nonidentical oscillators, let alone that it would lead to interesting new effects. The latter has changed with the recent discovery of so-called asymmetry-induced synchronization (AISync) [192, 317], where complete synchronization becomes stable in networks of nonidentical oscillators because of (not despite) the differences between the oscillators. This was demonstrated for networks of identically coupled oscillators, meaning that the symmetry of the system had to be broken to preserve the symmetry of the stable solution—a property that corresponds to the converse of symmetry breaking (hence of chimera states [210]) and after which the effect is named.

Motivated by that discovery, in this chapter we first present a rigorous framework to analyze complete synchronization in the most general class of coupled nonidentical

oscillators that permits complete synchronization, and then apply this formalism to characterize a new mechanism through which AISync can occur. This class includes networks of nonidentical oscillators with arbitrary differences, provided that they admit at least one common orbit when coupled. Our framework consists of a generalization of the master stability function (MSF) formalism [217], which can be applied to this class of nonidentical oscillators and several forms of coupling. The new mechanism for AISync identified here is mediated by delay-coupling and is demonstrated for networks of Stuart-Landau oscillators.

Complete (or identical) synchronization refers to the scenario in which all oscillators converge to the same dynamical state (with respect to all of their variables). In a network of N oscillators, where the d -dimensional state of the i -th oscillator is denoted \mathbf{x}_i , complete synchronization corresponds to

$$(4.1) \quad \mathbf{x}_1(t) = \mathbf{x}_2(t) = \dots = \mathbf{x}_N(t) \equiv \mathbf{s}(t)$$

for all t , where $\mathbf{s}(t)$ denotes the synchronous state⁴. This should be contrasted with cases in which a condition of the form (4.1) is satisfied for only some of the variables or a function of the variables, as in the cases of identical-frequency (but not identical-phase) synchronization in power-grid networks [175, 73, 236] and output-function synchronization in output consensus dynamics [255, 147].

It is instructive to first recall the previous main mechanisms through which AISync has been demonstrated:

⁴For notational simplicity, throughout the text (but not in equations) the synchronization orbit of individual oscillators $\mathbf{s}(t)$ will also be used to denote the synchronization orbit of the full network, as a short for the $N \times d$ -dimensional vector $(\mathbf{s}(t), \dots, \mathbf{s}(t))$

- Amplitude-dependent coupling in networks of phase-amplitude oscillators [192], where suitable heterogeneity in the amplitude term stabilizes the otherwise unstable state of complete synchronization.
- Subnode coupling in multilayer networks [317], where heterogeneity is required in the internal couplings between different variables of the oscillators in order to stabilize complete synchronization.

In the mechanism considered here, on the other hand, the oscillator heterogeneity is in the angular term of delay-coupled Stuart-Landau oscillators. This heterogeneity stabilizes the complete synchronization state that would otherwise become unstable in the presence of coupling delay. While we exemplify our results on a selection of representative networks, the oscillator model we consider can be tested for AISync (using our formalism) in any network of identically coupled nodes, which includes the rich class of vertex-transitive graphs. We also demonstrate the analog of AISync in a broader class of networks by showing that oscillator heterogeneity can stabilize synchronization when the oscillators are not necessarily identically coupled. For the oscillators that we explicitly consider, the latter includes arbitrary regular graphs.

The generalization of the MSF formalism presented in this work applies to oscillators that are not necessarily similar to each other. This should be contrasted with previous generalizations of the MSF formalism to systems with small parameter mismatches in the oscillators [276, 4] and systems with small mismatches in the oscillators and coupling functions [266], where the focus is on approximate (rather than complete) synchronization. Other approaches, such as the dichotomy technique used in Ref. [220], are also designed for approximate synchronization of nearly identical oscillators. Here, while we

Table 4.1. Necessary and sufficient conditions for the existence of a complete synchronization state $\mathbf{s}(t)$. Here, \mathbf{F}_i is the intrinsic dynamics of the i -th oscillator, \mathbf{H} is the interaction function, μ_i is the indegree of the i -th node (denoted by μ when equal for all nodes), σ is the coupling strength, and τ is the communication delay. In each case, the conditions are to be satisfied for all t .

Coupling type	Networks with arbitrary indegrees	Networks with common indegrees
Laplacian-matrix coupling (Sec. 4.2.1)	$\mathbf{F}_i(\mathbf{s}(t))$ independent of i $\dot{\mathbf{s}}(t) = \mathbf{F}_i(\mathbf{s}(t))$	$\mathbf{F}_i(\mathbf{s}(t))$ independent of i $\dot{\mathbf{s}}(t) = \mathbf{F}_i(\mathbf{s}(t))$
Adjacency-matrix coupling (Sec. 4.2.2)	$\mathbf{F}_i(\mathbf{s}(t)) + \sigma\mu_i\mathbf{H}(\mathbf{s}(t))$ independent of i $\dot{\mathbf{s}}(t) = \mathbf{F}_i(\mathbf{s}(t)) + \sigma\mu_i\mathbf{H}(\mathbf{s}(t))$	$\mathbf{F}_i(\mathbf{s}(t))$ independent of i $\dot{\mathbf{s}}(t) = \mathbf{F}_i(\mathbf{s}(t)) + \sigma\mu\mathbf{H}(\mathbf{s}(t))$
Delay coupling (Sec. 4.2.3)	$\mathbf{F}_i(\mathbf{s}(t)) + \sigma\mu_i[\mathbf{H}(\mathbf{s}(t-\tau)) - \mathbf{H}(\mathbf{s}(t))]$ independent of i $\dot{\mathbf{s}}(t) = \mathbf{F}_i(\mathbf{s}(t)) + \sigma\mu_i[\mathbf{H}(\mathbf{s}(t-\tau)) - \mathbf{H}(\mathbf{s}(t))]$	$\mathbf{F}_i(\mathbf{s}(t))$ independent of i $\dot{\mathbf{s}}(t) = \mathbf{F}_i(\mathbf{s}(t)) + \sigma\mu[\mathbf{H}(\mathbf{s}(t-\tau)) - \mathbf{H}(\mathbf{s}(t))]$

consider oscillators that can differ by more than a small mismatch, our focus is on the case of complete synchronization. A notable exception in the existing literature to also have considered complete synchronization in a non-perturbative parameter regime comes from the control community [318], where it has been shown that sufficient conditions for the global stability of a state of complete synchronization among nonidentical oscillators can be given based on a Lyapunov function approach. Those conditions are expressed through equations with the dimension of the individual oscillators, but their verification requires finding time-varying matrices that satisfy matrix inequalities for all t ; moreover, like other Lyapunov function methods, such an approach has limitations when applied to multi-stable systems. The approach we present, on the other hand, gives verifiable necessary and sufficient conditions for the linear stability of states of complete synchronization in networks with any number of stable states or attractors (including chaotic ones).

The chapter is organized as follows. In Sec. 4.2, we first develop our framework for non-identical oscillators in the context of Laplacian-matrix (diffusive) coupling (Sec. 4.2.1). We then discuss the conditions under which the framework also applies to two classes of non-diffusively coupled systems, namely networks with adjacency-matrix coupling (Sec. 4.2.2) and networks with delay coupling (Sec. 4.2.3). Table 4.1 summarizes the conditions for nonidentical oscillators to admit complete synchronization for each of the three types of couplings we consider. In Sec. 4.3, we elaborate on the theoretical background and algorithmic implementation of our approach, which is based on the irreducible decomposition of an algebraic structure known as matrix $*$ -algebra. In Sec. 4.4, we present our application of the formalism to establish networks of delay-coupled Stuart-Landau oscillators as a new class of systems that exhibit AISync. To that end, following a brief discussion of the delay-coupled dynamics (Sec. 4.4.1), we show that oscillator heterogeneity can stabilize an otherwise unstable state of complete synchronization on representative networks (Sec. 4.4.2). We also demonstrate the analogs of AISync for networks in which the oscillators are not identically coupled (Sec. 4.4.3) and for networks with unrestricted oscillator parameters (Sec. 4.4.4). We show that delay is a key ingredient leading to this effect in the class of systems we consider, which suggests that AISync may be common in physical systems, where delay is often significant. Concluding remarks are presented in Sec. 4.5.

4.2. Generalized master stability analysis for nonidentical oscillators

The MSF formalism was originally introduced to study the stability of states of complete synchronization in networks of diffusively coupled identical oscillators [217]. Applied to the linearized dynamics around the synchronization manifold, it effectively reduces the dimension of the variational equation from the dimension $N \times d$ of the full system to the dimension d of the local dynamics. This is achieved by simultaneously diagonalizing the Laplacian matrix and the identity matrix, which can always be done when the Laplacian matrix is diagonalizable, as in the case of undirected networks. The approach has also been adapted to directed networks in which the Laplacian matrix is not diagonalizable by replacing the diagonalization with a transformation into a Jordan canonical form [189].

The main difficulty in extending this powerful formalism to the case of nonidentical oscillators is that the identity matrix is then replaced by a set of more complicated matrices that, in general, cannot be simultaneously diagonalized with the coupling matrix. We address this problem by instead finding the finest simultaneous block diagonalization of this set of matrices and the coupling matrix, corresponding to the largest possible dimension reduction from the original system that can be achieved by an orthogonal transformation matrix. Our approach is partially inspired by the framework of irreducible representation previously used to study cluster synchronization in networks of identical oscillators [219], which leads to dimension reduction in that context. As shown below, our extension of the MSF formalism has the advantage of being applicable to both diffusive and non-diffusive coupling forms, and independently of whether the coupling matrix is diagonalizable or not, provided the conditions for complete synchronization are satisfied.

4.2.1. Networks with diffusive coupling

We consider a network of N nonidentical dynamical units coupled diffusively as

$$(4.2) \quad \dot{\mathbf{x}}_i = \mathbf{F}_i(\mathbf{x}_i) - \sigma \sum_{j=1}^N L_{i,j} \mathbf{H}(\mathbf{x}_j),$$

where \mathbf{x}_i is the d -dimensional state vector, $\mathbf{F}_i : \mathbb{R}^d \rightarrow \mathbb{R}^d$ is the vector field governing the uncoupled dynamics of the i -th oscillator, \mathbf{L} the graph Laplacian encoding the (possibly weighted and directed) network structure, \mathbf{H} is the interaction function, and σ is the coupling strength. The Laplacian matrix \mathbf{L} is defined as $L_{i,j} = \delta_{i,j} \mu_i - A_{i,j}$, where $\delta_{i,j}$ is the Kronecker delta, $A_{i,j}$ is the entry of the adjacency matrix representing the connection from node j to node i , and $\mu_i = \sum_j A_{i,j}$ is the (weighted) indegree of node i . The vector field functions \mathbf{F}_i are chosen from a set of M nonidentical functions $\{\mathbf{F}^{(\beta)}\}$. In a state of complete synchronization, the condition in equation (4.1) holds for some orbit $\mathbf{s}(t)$, which, together with equation (4.2), implies that $\dot{\mathbf{s}}(t) = \mathbf{F}_i(\mathbf{s}(t))$ for all i and thus that $\mathbf{F}_1(\mathbf{s}(t)) = \mathbf{F}_2(\mathbf{s}(t)) = \dots = \mathbf{F}_N(\mathbf{s}(t))$. Therefore, the necessary and sufficient condition for complete synchronization of diffusively coupled nonidentical oscillators is that all oscillators coincide on some common orbit $\mathbf{s}(t)$ that is a solution of each uncoupled oscillator (which in this case is equivalent to being a common orbit of the coupled oscillators). Assuming this condition is satisfied, the question we address next is how to establish an easily verifiable condition for the stability of such complete synchronization states.

The equation governing the evolution of a perturbation from the state of complete synchronization can be obtained by linearizing equation (4.2):

$$(4.3) \quad \delta \dot{\mathbf{X}} = \left(\sum_{\beta=1}^M \mathbf{D}^{(\beta)} \otimes J\mathbf{F}^{(\beta)}(\mathbf{s}) - \sigma \mathbf{L} \otimes J\mathbf{H}(\mathbf{s}) \right) \delta \mathbf{X},$$

where $\delta \mathbf{X} = (\delta \mathbf{x}_1^\top, \dots, \delta \mathbf{x}_N^\top)^\top = ((\mathbf{x}_1 - \mathbf{s})^\top, \dots, (\mathbf{x}_N - \mathbf{s})^\top)^\top$ is the perturbation vector, \otimes denotes the Kronecker product, J is the Jacobian operator, and $^\top$ indicates matrix transpose. Denoting by \mathcal{N}_β the set of nodes equipped with the β -th vector field function $\mathbf{F}^{(\beta)}$, the $\mathbf{D}^{(\beta)}$ are $N \times N$ diagonal matrices given by

$$(4.4) \quad D_{i,i}^{(\beta)} = \begin{cases} 1, & \text{if } i \in \mathcal{N}_\beta, \\ 0, & \text{otherwise.} \end{cases}$$

Note that $\sum_{\beta=1}^M \mathbf{D}^{(\beta)} = \mathbf{1}_N$, where $\mathbf{1}_N$ denotes the identity matrix. It is generally impossible to find a basis of eigenvectors that would simultaneously diagonalize the matrices $\{\mathbf{D}^{(\beta)}\}$ and \mathbf{L} . Thus, to generalize the MSF formalism to the case of nonidentical oscillators starting from equation (4.3), we must abandon the hope of completely decoupling the perturbation modes in general. Indeed, the class of systems is too broad to allow a simple reduced form as in the original MSF formalism (this is the case also for previous generalizations applied to the problems of cluster synchronization [219] and nonidentical interaction functions [67]). Informally, because a transformation that simplifies some of these matrices would generally complicate others, the key is to find the best balance between the competing goals of simplifying different matrices.

We now establish a formalism able to exploit partial decoupling among the perturbation modes in equation (4.3). This is achieved through a transformation of equation (4.3) by a matrix \mathbf{P} that implements the finest simultaneous block diagonalization (SBD)

of all $\mathbf{D}^{(\beta)}$ and \mathbf{L} (the notion of finest is defined rigorously below). This transformation will be referred to as the SBD transformation, and the corresponding coordinates as the SBD coordinates. The transformation matrix \mathbf{P} can be defined as an orthogonal matrix (generally not unique) that decomposes the matrix $*$ -algebra generated by $\{\mathbf{D}^{(1)}, \mathbf{D}^{(2)}, \dots, \mathbf{D}^{(M)}, \mathbf{L}\}$ into the direct sum of (possibly multiple copies of) lower dimensional irreducible matrix $*$ -algebras. For clarity, we defer to Sec. 4.3 the discussion on the construction of matrix \mathbf{P} and proceed for the moment assuming that this matrix has been calculated.

The transformation matrix \mathbf{P} applied to equation (4.3) leads to

$$(4.5) \quad \dot{\boldsymbol{\eta}} = \left(\sum_{\beta=1}^M \tilde{\mathbf{D}}^{(\beta)} \otimes J\mathbf{F}^{(\beta)}(\mathbf{s}) - \sigma \tilde{\mathbf{L}} \otimes J\mathbf{H}(\mathbf{s}) \right) \boldsymbol{\eta},$$

where $\boldsymbol{\eta} = (\mathbf{P}^\top \otimes \mathbf{1}_d) \delta \mathbf{X}$ is the perturbation vector expressed in the SBD coordinates. Here, the set of matrices $\{\tilde{\mathbf{D}}^{(\beta)}\} = \{\mathbf{P}^\top \mathbf{D}^{(\beta)} \mathbf{P}\}$ and $\tilde{\mathbf{L}} = \mathbf{P}^\top \mathbf{L} \mathbf{P}$ are block diagonal matrices with the *same* block structure. It is instructive to notice that the effect of the nonidentical Jacobians $\{J\mathbf{F}^{(\beta)}(\mathbf{s})\}$ on the variational equation (4.5) is analogous to that of the Jacobians $\{J\mathbf{F}(\mathbf{s}_m)\}$ associated with different synchronization states \mathbf{s}_m of different clusters in the cluster synchronization systems studied in Ref. [265]. A key difference is that the assignment of $\{J\mathbf{F}(\mathbf{s}_m)\}$ in cluster synchronization is linked to \mathbf{L} by symmetries of the network, whereas here $\{J\mathbf{F}^{(\beta)}(\mathbf{s})\}$ can be assigned arbitrarily (through the choice of the matrices $\{\mathbf{D}^{(\beta)}\}$). This implies a more flexible relation among the matrices in equation (4.5), whose SBD transformation is in general not an irreducible representation transformation.

It is also instructive to notice that the original MSF formalism is recovered when $M = 1$ and the network is undirected (i.e., the Laplacian matrix is symmetric). In this case $\mathbf{D}^{(1)} = \tilde{\mathbf{D}}^{(1)} = \mathbf{1}_N$, matrix \mathbf{P} can be constructed from the eigenvectors of \mathbf{L} , and $\tilde{\mathbf{L}}$ is a diagonal matrix with the eigenvalues v_i of \mathbf{L} as diagonal elements. Letting $\mathbf{F} = \mathbf{F}^{(1)}$, equation (4.5) reduces to N decoupled equations,

$$(4.6) \quad \dot{\boldsymbol{\eta}}_i = (J\mathbf{F}(\mathbf{s}) - \sigma v_i J\mathbf{H}(\mathbf{s})) \boldsymbol{\eta}_i,$$

from which the MSF can be calculated as the maximal Lyapunov exponent (MLE) for different values of $v = \sigma v_i$.

Numerical algorithms are available for the calculation of \mathbf{P} given a set of matrices. Here, we adopt the method introduced in Ref. [151], which we discuss in some detail in Sec. 4.3. As an example, we simultaneously block diagonalize three 16×16 matrices: \mathbf{L} , $\mathbf{D}^{(1)}$, and $\mathbf{D}^{(2)}$. Matrix \mathbf{L} is the Laplacian of an undirected 16-node wheel network (figure 4.1(a)), which is a ring network with additional connections between opposite nodes; matrices $\mathbf{D}^{(1)}$ and $\mathbf{D}^{(2)}$ encode alternating arrangements of two kinds of oscillators (figure 4.1(b)-(c)). The matrices are simultaneously transformed into seven 2×2 blocks and two 1×1 blocks (figure 4.1(d)-(f)). Thus, the original equation of $16d$ dimensions can be reduced to seven equations of dimension $2d$ and two equations of dimension d , which significantly simplifies the stability analysis.

Equation (4.5) is partially decoupled according to the block structure of $\{\tilde{\mathbf{D}}^{(\beta)}\}$ and $\tilde{\mathbf{L}}$. Therefore, we can calculate the Lyapunov exponents of the equations corresponding to each block separately. The block structure does not depend on the synchronization state $\mathbf{s}(t)$, but equation (4.5) itself does, and so do the associated Lyapunov exponents.

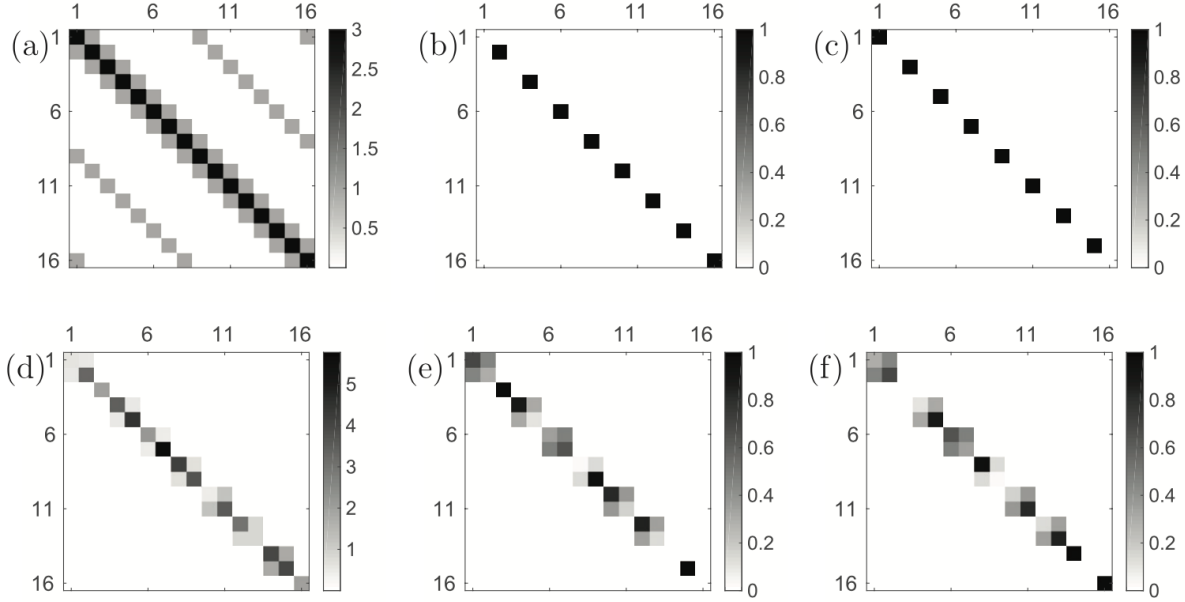


Figure 4.1. (a) Matrix L , (b) matrix $D^{(1)}$, and (c) matrix $D^{(2)}$ representing an undirected wheel network with an alternating arrangement of two kinds of oscillators. (d-f) The corresponding matrices after the SBD transformation, showing that all transformed matrices share the same block structure. The grayscale indicates the absolute value of each element in the matrices.

One of the Lyapunov exponents corresponds to perturbations along the synchronization orbit $\mathbf{s}(t)$, and is zero whether this orbit is periodic or chaotic. The primary question of interest concerns the stability of the synchronization state $\mathbf{s}(t)$, which is determined by the maximal transverse Lyapunov exponent (MTLE). The MTLE always excludes the (null) Lyapunov exponent along $\mathbf{s}(t)$. However, in contrast with the case of identical oscillators, more general perturbations of the form $\delta\mathbf{X} = (\delta\mathbf{x}^\top, \dots, \delta\mathbf{x}^\top)^\top$ usually do not preserve synchronization and cannot be excluded upfront in the stability analysis in the case of non-identical oscillators. This is because the condition $\mathbf{F}_1(\mathbf{s}(t) + \delta\mathbf{x}_1(t)) = \dots = \mathbf{F}_N(\mathbf{s}(t) + \delta\mathbf{x}_N(t))$ is generally not satisfied for all t even when $\delta\mathbf{x}_1(0) = \dots = \delta\mathbf{x}_N(0)$.

Our approach takes this into account automatically since, unlike the MSF formalism, it does not discard the contribution from such perturbation modes in the calculation of the MTLE (instead it only excludes Lyapunov exponents associated with perturbations satisfying $\delta \mathbf{x}_1(t) = \dots = \delta \mathbf{x}_N(t)$ for all t).

Systems in which the synchronization orbit $\mathbf{s}(t)$ is not unique may synchronize even when the individual orbits are unstable. This is the case when the distinct oscillators in the system share common dynamics in a neighborhood of a chaotic attractor, and thus share all the (uncountably many) orbits of the attractor as synchronization orbits. Due to chaos, those orbits are necessarily unstable, but parallel perturbations of the form $\delta \mathbf{X} = (\delta \mathbf{x}^\top, \dots, \delta \mathbf{x}^\top)^\top$ may merely change synchronization trajectory without destroying long-term synchronization. An example in which a full synchronization manifold $\mathbf{x}_1 = \dots = \mathbf{x}_N$ is invariant for nonidentical oscillators is given in Sec. 4.2.2.

Finally, we note that our approach also applies to systems with nonidentical interaction functions by simultaneously block diagonalizing the set of Laplacian matrices that represent different types of interactions. In particular, by finding the finest simultaneous block diagonalization of the set of all matrices in the $*$ -algebra associated with the variational equation, our method can provide a more significant dimension reduction than the coordinates proposed in Ref. [67] in the study of networks with multiple interaction layers, where partial diagonalization was implemented by choosing as a basis the eigenvectors of one of the Laplacian matrices from the set. For identical oscillators, the utility of the SBD transformation in this context has been demonstrated in a separate study [118]. Our formulation, however, applies to systems in which both the interactions and the oscillators are allowed to be nonidentical (provided they satisfy the conditions for

complete synchronization). Another advantage of the approach is that, because it does not require the graph Laplacians to be diagonalizable, its use extends to systems with directed couplings in general.

4.2.2. Networks with adjacency-matrix coupling

The method developed in Sec. 4.2.1 also applies to oscillator networks with adjacency-matrix coupling:

$$(4.7) \quad \dot{\mathbf{x}}_i = \mathbf{F}_i(\mathbf{x}_i) + \sigma \sum_{j=1}^N A_{i,j} \mathbf{H}(\mathbf{x}_j),$$

where \mathbf{A} represents the adjacency matrix of the network and the other symbols are defined as in equation (4.2). This form of coupling has been considered for the case of identical oscillators (i.e., identical \mathbf{F}_i for all i) in the study of cluster (hence partial) synchronization [219]. In order to consider complete synchronization for nonidentical \mathbf{F}_i , we first note that the necessary and sufficient condition for the existence of a synchronous state $\mathbf{s}(t)$ as defined by equation (4.1) is that $\mathbf{F}_i(\mathbf{s}(t)) + \sigma \mu_i \mathbf{H}(\mathbf{s}(t)) = \dot{\mathbf{s}}(t)$ holds for all i , where we recall that μ_i denotes the indegree of node i .

Following the same procedure used for diffusive coupling, we obtain an equation analogous to equation (4.5),

$$(4.8) \quad \dot{\boldsymbol{\eta}} = \left(\sum_{\beta=1}^M \tilde{\mathbf{D}}^{(\beta)} \otimes J\mathbf{F}^{(\beta)}(\mathbf{s}) + \sigma \tilde{\mathbf{A}} \otimes J\mathbf{H}(\mathbf{s}) \right) \boldsymbol{\eta},$$

where $\tilde{\mathbf{A}} = \mathbf{P}^\top \mathbf{A} \mathbf{P}$ is the adjacency matrix \mathbf{A} after the orthogonal transformation \mathbf{P} . As in the case of diffusive coupling, this transformation reduces the dimension of the problem by partially decoupling the perturbation modes in the original equation. The stability

of the synchronization orbit $\mathbf{s}(t)$ is now determined by considering the MTLE associated with equation (4.8), which always excludes the (null) Lyapunov exponent associated with the perturbation mode along this orbit (and it often excludes only this exponent, but see an exception below).

As an example, consider N nonidentical Rössler oscillators coupled through an undirected chain network. The equation for an isolated Rössler oscillator $\dot{\mathbf{x}}_i = \mathbf{F}_i(\mathbf{x}_i)$ is given by

$$(4.9) \quad \begin{cases} \dot{x}_{i1} = -x_{i2} - x_{i3}, \\ \dot{x}_{i2} = x_{i1} + a_i x_{i2}, \\ \dot{x}_{i3} = b_i + (x_{i1} - c_i)x_{i3}, \end{cases}$$

and the coupling function is taken to be $\mathbf{H}(\mathbf{x}_j) = (0, x_{j2}, 0)^\top$. For the two end nodes, $i = 1$ and N , we set the oscillator parameters to be $(a_i, b_i, c_i) = (0.1, 0.2, 9)$; for all the other nodes, $1 < i < N$, the parameters are $(a_i, b_i, c_i) = (0, 0.2, 9)$. Since $\mu_i = 1$ for $i = 1$ and N , and $\mu_i = 2$ for all other i , there exist common orbits $\mathbf{s} = (s_1, s_2, s_3)$ such that $\mathbf{F}_i(\mathbf{s}(t)) + \sigma\mu_i\mathbf{H}(\mathbf{s}(t))$ do not depend on i and are equal to $(-s_2 - s_3, s_1 + 0.2s_2, 0.2 + (s_1 - 9)s_3)^\top$ for the coupling strength $\sigma = 0.1$. In this case, the synchronization manifold is invariant and $\mathbf{s}(t)$ is any orbit in the chaotic attractor of an isolated Rössler oscillator for parameters $(a, b, c) = (0.2, 0.2, 9)$; thus, perturbations parallel to the synchronization manifold do not lead to desynchronization. (An *undirected* ring network of identical Rössler oscillators with parameters $(a_i, b_i, c_i) = (0, 0.2, 9)$ also admits the same $\mathbf{s}(t)$ as complete synchronization states for the same \mathbf{H} and σ , although the stability can be

different in general.) For the chain of heterogeneous Rössler oscillators, we have

$$(4.10) \quad J\mathbf{F}_i = \begin{pmatrix} 0 & -1 & -1 \\ 1 & a_i & 0 \\ x_{i3} & 0 & x_{i1} - c_i \end{pmatrix} \quad \text{and} \quad J\mathbf{H} = \begin{pmatrix} 0 & 0 & 0 \\ 0 & 1 & 0 \\ 0 & 0 & 0 \end{pmatrix}.$$

For $N = 4$ oscillators, equation (4.8) then leads to the following (non-unique) set of matrices with the same block structure:

$$(4.11) \quad \bar{\mathbf{A}} = \begin{pmatrix} 0.60 & 0.24 & 0 & 0 \\ 0.24 & -1.60 & 0 & 0 \\ 0 & 0 & 1.60 & 0.22 \\ 0 & 0 & 0.22 & -0.60 \end{pmatrix}, \quad \tilde{\mathbf{D}}^{(1)} = \begin{pmatrix} 0.81 & -0.39 & 0 & 0 \\ -0.39 & 0.19 & 0 & 0 \\ 0 & 0 & 0.19 & 0.40 \\ 0 & 0 & 0.40 & 0.81 \end{pmatrix}, \quad \tilde{\mathbf{D}}^{(2)} = \begin{pmatrix} 0.19 & 0.39 & 0 & 0 \\ 0.39 & 0.81 & 0 & 0 \\ 0 & 0 & 0.81 & -0.40 \\ 0 & 0 & -0.40 & 0.19 \end{pmatrix},$$

where we have two matrices $\tilde{\mathbf{D}}^{(\beta)}$ because this example has two types of oscillators.

A scenario of special interest in our application to AISync below is the one in which all *oscillators* are identically coupled, which implies that

$$(4.12) \quad \mu_1 = \mu_2 = \cdots = \mu_N \equiv \mu,$$

for some common indegree μ . In this case, as in the case of diffusive coupling, the condition for the synchronous state to exist is thus that all \mathbf{F}_i coincide on some orbit $\mathbf{s}(t)$. However, in contrast with the case of diffusive coupling, in the case of adjacency-matrix coupling this orbit is generally not a solution of the uncoupled oscillator dynamics, but rather of $\dot{\mathbf{s}}(t) = \mathbf{F}_i(\mathbf{s}(t)) + \sigma\mu\mathbf{H}(\mathbf{s}(t))$.

4.2.3. Networks with delay coupling

An important generalization of equation (4.2) is oscillator networks with delay coupling of the form

$$(4.13) \quad \dot{\mathbf{x}}_i(t) = \mathbf{F}_i(\mathbf{x}_i(t)) + \sigma \sum_{j=1}^N A_{i,j} [\mathbf{H}(\mathbf{x}_j(t - \tau)) - \mathbf{H}(\mathbf{x}_i(t))],$$

where τ is the time delay. Other forms of delay coupling are possible, including those that do not consider the self-feedback term $\mathbf{H}(\mathbf{x}_i(t))$ [80, 116] and those that incorporate processing delay alongside the propagation delay τ [307, 324]. Our framework applies to those scenarios as well, and here we focus on the coupling form in equation (4.13) for concreteness. We first note that, although for $\tau = 0$ this system reduces to the form of equation (4.2), for $\tau > 0$ the coupling is no longer diffusive in the sense that the coupling term does not necessarily vanish in a state of complete synchronization. In this case, the necessary and sufficient condition for the existence of a synchronous state $\mathbf{s}(t)$ is that $\mathbf{F}_i(\mathbf{s}(t)) + \sigma \mu_i [\mathbf{H}(\mathbf{s}(t - \tau)) - \mathbf{H}(\mathbf{s}(t))] = \dot{\mathbf{s}}(t)$ holds for all i . Like in the case of adjacency-matrix coupling, this reduces to all \mathbf{F}_i being equal along the orbit $\mathbf{s}(t)$ when the condition in equation (4.12) is satisfied, which is the case if the oscillators are identically coupled.

We can now extend the formalism established in Sec. 4.2.1 to also include the delay-coupled system (4.13). As a sufficient condition for this extension, we will assume that the matrices $J\mathbf{F}^{(\beta)}(\mathbf{s})$ and $J\mathbf{H}(\mathbf{s})$ do not depend on time. Like in the other cases considered above, the oscillators can in principle be arbitrarily different from each other as long as they coincide on the synchronization orbit $\mathbf{s}(t)$, which is generally not a solution of

the isolated node dynamics. No assumption need to be made about the structure of the network.

Using $\boldsymbol{\mu}$ to denote the diagonal matrix with μ_i in the i -th diagonal entry, the analog of equation (4.3) can be written as

$$(4.14) \quad \delta \dot{\mathbf{X}}(t) = \left(\sum_{\beta=1}^M \mathbf{D}^{(\beta)} \otimes J\mathbf{F}^{(\beta)} - \sigma \boldsymbol{\mu} \otimes J\mathbf{H} \right) \delta \mathbf{X}(t) + \sigma (\mathbf{A} \otimes J\mathbf{H}) \delta \mathbf{X}(t - \tau).$$

The SBD transformation can then be applied to $\{\mathbf{D}^{(\beta)}\}$, $\boldsymbol{\mu}$, and \mathbf{A} , to obtain

$$(4.15) \quad \dot{\boldsymbol{\eta}}(t) = \left(\sum_{\beta=1}^M \tilde{\mathbf{D}}^{(\beta)} \otimes J\mathbf{F}^{(\beta)} - \sigma \tilde{\boldsymbol{\mu}} \otimes J\mathbf{H} \right) \boldsymbol{\eta}(t) + \sigma (\tilde{\mathbf{A}} \otimes J\mathbf{H}) \boldsymbol{\eta}(t - \tau),$$

where $\tilde{\boldsymbol{\mu}}$ is the matrix $\boldsymbol{\mu}$ after the transformation. If we now invoke the assumption that $\{J\mathbf{F}^{(\beta)}\}$ and $J\mathbf{H}$ are constant matrices on the orbit $\mathbf{s}(t)$, it follows that the effect of the time delay τ in $\boldsymbol{\eta}(t - \tau)$ can be represented by the factor $e^{-\Lambda\tau}$ [60], resulting in the following transcendental characteristic equation for the exponent Λ :

$$(4.16) \quad \det \left\{ \sum_{\beta=1}^M \tilde{\mathbf{D}}^{(\beta)} \otimes J\mathbf{F}^{(\beta)} + \sigma (e^{-\Lambda\tau} \tilde{\mathbf{A}} - \tilde{\boldsymbol{\mu}}) \otimes J\mathbf{H} - \Lambda \mathbf{1}_{dN} \right\} = 0.$$

Equation (4.16) can be factorized according to the common block structure of $\{\mathbf{D}^{(\beta)}\}$, $\boldsymbol{\mu}$, and \mathbf{A} . The Lyapunov exponents are then obtained as $\text{Re}(\Lambda)$, where Λ can be calculated efficiently for each block using already available root-finding algorithms. The largest Lyapunov exponent calculated from the decoupled blocks corresponds to the MLE of the original full system. The stability of a synchronization orbit $\mathbf{s}(t)$ is determined by the MTLE associated with equation (4.15), which, as in the previous cases, is determined

by excluding the Lyapunov exponents associated with perturbations satisfying $\delta \mathbf{x}_1(t) = \dots = \delta \mathbf{x}_N(t)$ for all t .

As an example, we note that the block diagonalized structure in figure 4.1 also applies to equation (4.16) if we choose \mathbf{A} to be the adjacency matrix of the same wheel network and the same arrangement of oscillators as represented by $\mathbf{D}^{(1)}$ and $\mathbf{D}^{(2)}$. Since $\boldsymbol{\mu} = \tilde{\boldsymbol{\mu}} = \mu \mathbf{1}_N$ in this case, the only difference between the sets of matrices to be block diagonalized in these two examples is that matrix \mathbf{L} is now replaced by matrix \mathbf{A} . More generally, we can show that when the corresponding adjacency matrix \mathbf{A} is in the matrix $*$ -algebra generated by the Laplacian matrix \mathbf{L} and $\{\mathbf{D}^{(\beta)}\}$, the SBD transformation of \mathbf{A} and $\{\mathbf{D}^{(\beta)}\}$ always yields the same block structure as the one from \mathbf{L} and $\{\mathbf{D}^{(\beta)}\}$. This includes the case of identically coupled oscillators, where $\mathbf{A} = -\mathbf{L} + \mu \mathbf{1}_N$.

4.3. Finding the finest simultaneous block diagonalization

Having established in Sec. 4.2 the usefulness of the SBD transformation in addressing the synchronization of nonidentical oscillators, we now consider this transformation rigorously. Moreover, we put on firm ground the notion of *finest simultaneous block diagonalization* and also discuss an algorithm for the calculation of the transformation matrix \mathbf{P} .

To define the SBD transformation we must first introduce the matrix $*$ -algebra [178], which is an object of study in non-commutative algebra. Denoting by \mathcal{M}_N the set of $N \times N$ real matrices, a subset \mathcal{T} of \mathcal{M}_N is a *matrix $*$ -algebra* over \mathbb{R} if

$$(4.17) \quad \mathbf{B}, \mathbf{C} \in \mathcal{T}; \alpha, \beta \in \mathbb{R} \implies \alpha \mathbf{B} + \beta \mathbf{C}, \mathbf{BC}, \mathbf{B}^\top \in \mathcal{T},$$

and $\mathbf{1}_N \in \mathcal{T}$. This structure is convenient because it is closed under the involution operation defined by the matrix transpose (thus the $*$). We say a subspace \mathcal{W} of \mathbb{R}^N is \mathcal{T} -invariant if $\mathbf{B}\mathcal{W} \subseteq \mathcal{W}$ for every $\mathbf{B} \in \mathcal{T}$. A matrix $*$ -algebra \mathcal{T} is said to be *irreducible* if $\{\mathbf{0}\}$ and \mathbb{R}^N are the only \mathcal{T} -invariant subspaces.

A matrix $*$ -algebra \mathcal{T} can always be decomposed, through an orthogonal matrix \mathbf{P} , into the direct sum of lower dimensional matrix $*$ -algebras that can be further decomposed into irreducible matrix $*$ -algebras \mathcal{T}_j :

$$(4.18) \quad \mathbf{P}^\top \mathcal{T} \mathbf{P} = \bigoplus_{j=1}^{\ell} (\mathbf{1}_{m_j} \otimes \mathcal{T}_j) = \text{diag}\{\mathbf{1}_{m_1} \otimes \mathcal{T}_1, \dots, \mathbf{1}_{m_\ell} \otimes \mathcal{T}_\ell\}.$$

Here \bigoplus denotes direct sum, ℓ is the number of irreducible matrix $*$ -algebras in the decomposition, m_j is the multiplicity of \mathcal{T}_j , and thus ℓ and/or m_j are strictly larger than one unless \mathcal{T} is already irreducible. The existence of such orthogonal matrix \mathbf{P} follows from Artin-Wedderburn type structure theorems (Theorems 3.1 and 6.1 in Ref. [178]). This decomposition implies that, with a single orthogonal matrix \mathbf{P} , all matrices in \mathcal{T} can be transformed simultaneously to a block diagonal form determined by equation (4.18). The orthogonal matrix \mathbf{P} in this equation is not unique, but the irreducible $*$ -algebras \mathcal{T}_j are uniquely determined by \mathcal{T} (up to isomorphism). That is, each diagonal block of the matrices after an SBD transformation is uniquely determined up to an orthogonal transformation.

Now we are in a position to define precisely what we mean by the finest simultaneous block diagonalization of a given set of matrices. An orthogonal matrix \mathbf{P} is said to give the *finest* simultaneous block diagonalization of a set of $N \times N$ real matrices $\mathcal{B} = \{\mathbf{B}_1, \dots, \mathbf{B}_n\}$, if it leads to the irreducible decomposition of the matrix $*$ -algebra

generated by $\{\mathbb{1}_N, \mathbf{B}_1, \dots, \mathbf{B}_n\}$. It follows that the dimension of each diagonal block is finest also in the sense that it cannot be further reduced without violating the condition of it being a simultaneous block diagonalization for all matrices in the $*$ -algebra, even if we allow non-orthogonal similarity transformation matrices.

If we allow non-orthogonal transformation matrices, then there can be a stronger definition of finest simultaneous block diagonalization in the sense that, after the transformation, the i -th common blocks of all matrices in \mathcal{B} only share trivial invariant subspaces for all i . However, in the important case in which all matrices in \mathcal{B} are symmetric, such as the synchronization models of Sec. 4.2 when considered on undirected networks, this stronger definition is equivalent to the one above based on the irreducible decomposition of the matrix $*$ -algebra. Thus, for symmetric matrices, the orthogonal matrix \mathbf{P} in equation (4.18) always gives the finest simultaneous block diagonalization of \mathcal{B} according to both definitions. Henceforth we shall refer to the finest simultaneous block diagonalization exclusively in the sense of matrix $*$ -algebra.

We can now turn to the numerical calculation of the transformation matrix \mathbf{P} . Algorithms for the determination of \mathbf{P} given a set of matrices have been developed in previous studies motivated by their applications in semidefinite programming and independent component analysis. While to the best of our knowledge their potential for synchronization problems remains underexplored, we can in fact benefit quite directly from such algorithms in connection with the SBD transformations we consider. In this work we adopt an implementation of the method introduced in Ref. [151], which considers the commutant algebra of the matrix $*$ -algebra generated by $\{\mathbb{1}_N, \mathbf{B}_1, \dots, \mathbf{B}_n\}$, defined as

the set of matrices that commute with all matrices of that $*$ -algebra; this approach provides a simpler algorithm than those working directly with the original matrix $*$ -algebra [178, 150]. The algorithm finds \mathbf{P} through numerical linear-algebraic computations (i.e., eigenvalue/eigenvector calculations) and does not require any algebraic structure to be known in advance. Using the notation $[\mathbf{B}_k, \mathbf{X}] = \mathbf{B}_k\mathbf{X} - \mathbf{X}\mathbf{B}_k$, we can summarize the algorithm into two steps as follows.

SBD Algorithm. (*Algorithm 3.5 in Ref. [151]*)

- Calculate a symmetric $N \times N$ matrix \mathbf{X} as a generic solution of $[\mathbf{B}_k, \mathbf{X}] = \mathbf{0}$, $k = 1, \dots, n$.
- Calculate an orthogonal matrix \mathbf{P} that diagonalizes matrix \mathbf{X} .

Here, a generic solution means a matrix \mathbf{X} with no accidental eigenvalue degeneracy that is not enforced by $\{\mathbf{B}_k\}$. While the second step is straightforward using standard algorithms, the first step can be addressed by translating it into an eigenvector problem that can then be solved efficiently using the Lanczos method.

The intuition behind this algorithm is that the common invariant subspaces among $\{\mathbf{B}_k\}$ can be captured by \mathbf{X} , and \mathbf{P} automatically decomposes \mathbb{R}^N into the direct sum of those invariant subspaces. Note that, even though \mathbf{X} commutes with all \mathbf{B}_k and \mathbf{P} diagonalizes \mathbf{X} , the matrix \mathbf{P} will generally not diagonalize the matrices \mathbf{B}_k but rather block diagonalize them—this is true even for symmetric matrices. Moreover, since we do not limit ourselves to symmetric matrices, being simultaneously diagonalizable (or even diagonalizable at all) is not implied by having a null commutator.

4.4. AISync in delay-coupled oscillator networks

For the purpose of studying AISync, we require the network structure to be symmetric (i.e., all oscillators to be identically coupled), so that any system asymmetry can be attributed to oscillator heterogeneity. Formally, a (possibly directed and weighted) network is said to be symmetric if all nodes belong to a single orbit under the action of the network's automorphism group, whose elements can be represented by permutation matrices that re-order the nodes while leaving the adjacency matrix invariant. This is a generalization of the (undirected and unweighted) vertex-transitive graphs considered in algebraic graph theory, and makes precise the intuition that all nodes play the same structural role by requiring the existence of symmetry operations that map one node to any other node in the network.⁵

Network symmetry implies the condition in equation (4.12). Thus, for symmetric networks, the condition for complete synchronization of nonidentical oscillators in the cases of adjacency-matrix coupling (4.7) and delay coupling (4.13) is that the vector field functions satisfy $\mathbf{F}_1(\mathbf{s}) = \mathbf{F}_2(\mathbf{s}) = \dots = \mathbf{F}_N(\mathbf{s})$ (as in the case of diffusive coupling (4.2)), where the synchronous state $\mathbf{s} = \mathbf{s}(t)$ is now a common solution of the coupled dynamics of all oscillators. Because the oscillators are nonidentical, these equalities generally do not hold for state-space points outside the orbit $\mathbf{s}(t)$, which can impact the stability of this orbit as a synchronous state solution.

Given $\{\mathbf{F}^{(\beta)}\}$, we say a system exhibits AISync if it satisfies the following two conditions: 1) there are no stable states of complete synchronization for any homogeneous system (i.e., any system for which $\mathbf{F}_1(\mathbf{x}) = \mathbf{F}_2(\mathbf{x}) = \dots = \mathbf{F}_N(\mathbf{x}) \quad \forall \mathbf{x}$); 2) there is

⁵A network being symmetric should not be confused with a network having a symmetric coupling matrix, which is neither sufficient nor necessary for the network to be symmetric.

a heterogeneous system (i.e., a system such that $\mathbf{F}_i \neq \mathbf{F}_j$ for some $i \neq j$) for which a stable synchronous state exists. Using the formalism presented above, now we show that AISync occurs in networks of delay-coupled Stuart-Landau oscillators. We also show that the scenario in which stable synchronization requires oscillators to be nonidentical extends naturally to non-symmetric networks.

4.4.1. Stuart-Landau oscillators sharing a common orbit

We start with N delay-coupled identical (supercritical) Stuart-Landau oscillators, whose equation in complex variable notation reads

$$(4.19) \quad \dot{z}_j(t) = f(z_j(t)) + \sigma \sum_{k=1}^N A_{j,k} [z_k(t - \tau) - z_j(t)],$$

where $z_j = r_j e^{i\psi_j} \in \mathbb{C}$ for τ and σ as in equation (4.13). The adjacency matrix \mathbf{A} represents the structure of a symmetric network and thus has a common row sum $\mu = \sum_k A_{j,k} \forall j$. Because the common row sum condition is equivalent to the condition in equation (4.12) and is thus satisfied by any network with the same indegree for all nodes j , our analysis also applies to arbitrary non-symmetric network structures that satisfy this indegree condition (including all directed regular graphs), as illustrated below in Sec. 4.4.3.

The local dynamics of each oscillator is given by the normal form of a supercritical Hopf bifurcation [132]:

$$(4.20) \quad f(z_j) = [\lambda + i\omega - (1 + i\gamma)|z_j|^2] z_j,$$

where λ , ω , and γ are real parameters. Intuitively, λ relates to the amplitude of the oscillation, ω represents the base angular velocity, and γ controls the amplitude-dependent angular velocity term.

Substituting the limit cycle ansatz $z_j = r_0 e^{i\Omega t}$ into equation (4.19) and assuming $r_0^2 \neq 0$, we obtain the invariant solution

$$(4.21a) \quad r_0^2 = \lambda + \mu\sigma(\cos \Phi - 1),$$

$$(4.21b) \quad \Omega = \omega - \gamma r_0^2 + \mu\sigma \sin \Phi,$$

where we use the notation $\Phi = -\Omega\tau$. This set of equations can be solved for Ω by substituting the r_0^2 in equation (4.21b) with the right hand side of equation (4.21a) and solving numerically the resulting transcendental equation. After determining Ω , the value of r_0^2 can be immediately calculated from equation (4.21a). There can be multiple solutions of Ω (thus also of r_0^2) for certain combinations of parameters (including spurious solutions with $r_0^2 < 0$). Here, we focus on regions where a unique solution of positive r_0^2 exists. In addition, there is always a time-independent solution $r_0 = 0$, corresponding to an amplitude death state, which was excluded in our derivation of equation (4.21) but can be identified directly from equations (4.19) and (4.20).

For identical Stuart-Landau oscillators, a variational equation for the limit cycle synchronous state ($z_j = r_0 e^{i\Omega t}$) is derived in Ref. [60] as

$$(4.22) \quad \dot{\boldsymbol{\xi}}(t) = \mathbb{1}_N \otimes (\mathbf{J}_0 - \mu\sigma\mathbf{R})\boldsymbol{\xi}(t) + \sigma(\mathbf{A} \otimes \mathbf{R})\boldsymbol{\xi}(t - \tau),$$

where $\mathbf{J}_0 = \begin{pmatrix} -2r_0^2 & 0 \\ -2\gamma r_0^2 & 0 \end{pmatrix}$ and $\mathbf{R} = \begin{pmatrix} \cos \Phi & -\sin \Phi \\ \sin \Phi & \cos \Phi \end{pmatrix}$. The $2N$ -dimensional perturbation vector is defined as $\boldsymbol{\xi} = (\boldsymbol{\xi}_1^\top, \dots, \boldsymbol{\xi}_N^\top)^\top$, where $\boldsymbol{\xi}_j = (\delta r_j, \delta \psi_j)^\top$ and $(r_j, \psi_j) = (r_0(1 + \delta r_j), \Omega t + \delta \psi_j)$. Equation (4.22) is a special case of equation (4.14) obtained by setting $M = 1$, $J\mathbf{F}^{(1)} = \mathbf{J}_0$, and $J\mathbf{H} = \mathbf{R}$. Because the oscillators are identical, one can apply the standard MSF formalism to diagonalize \mathbf{A} and obtain decoupled variational equations of the form

$$(4.23) \quad \dot{\boldsymbol{\eta}}_k(t) = \mathbf{J}_0 \boldsymbol{\eta}_k(t) - \sigma \mathbf{R} [\mu \boldsymbol{\eta}_k(t) - v_k \boldsymbol{\eta}_k(t - \tau)],$$

with $\boldsymbol{\eta}_k$ representing the perturbation vector associated with the eigenvalue v_k of \mathbf{A} after diagonalization. In particular, $v_0 = \mu$ corresponds to the perturbation mode (eigenvector) along the synchronization manifold. Since \mathbf{J}_0 and \mathbf{R} are constant matrices, the Lyapunov exponents of the perturbation modes are obtained as $\text{Re}(\Lambda)$, where the exponents Λ can be determined from the characteristic equation

$$(4.24) \quad \det\{\mathbf{J}_0 - \Lambda \mathbf{1}_2 + (-\sigma \mu + \sigma v_k e^{-\Lambda \tau}) \mathbf{R}\} = 0.$$

As usual, the resulting MLE can be interpreted as the MSF and visualized on the complex plane parametrized by the effective coupling parameter $v = \sigma v_k$.

For a given Stuart-Landau oscillator $f(z; \lambda_0, \omega_0, \gamma_0)$ along with fixed parameters $\sigma \mu$ and τ , there exists an entire class of nonidentical Stuart-Landau oscillators $\mathcal{SL}(\lambda_0, \omega_0, \gamma_0)$ characterized by a parameter h , consisting of oscillators of the form $f(z; \lambda_0, \omega_0 + h, \gamma_0 + h/r_0^2)$ for all values of $h \in \mathbb{R}$. All oscillators in this class share the common orbit $s = r_0 e^{i\Omega t}$ according to equation (4.21), and are thus potential candidates for AISync. Moreover, $\gamma = \gamma_0 + h/r_0^2$ enters the variational equation (4.22) through \mathbf{J}_0 , so in general one would

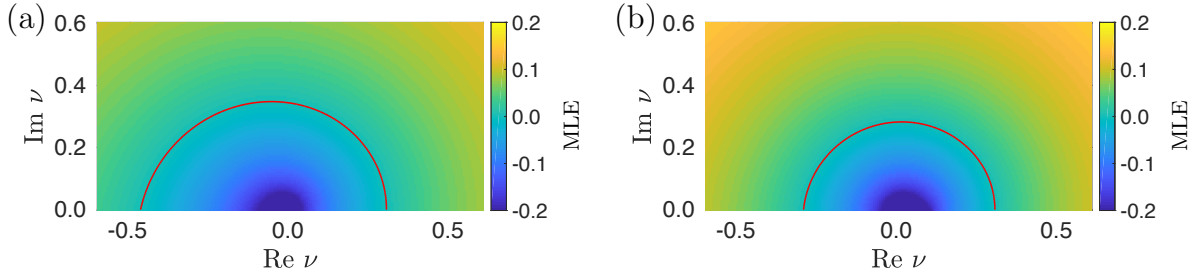


Figure 4.2. MSF calculated from equation (4.24) for (a) $h = 0$ and (b) $h = 0.8$. The red contours mark the boundary of linear stability (i.e., where the MLE changes sign). The other parameters are $\sigma\mu = 0.3$, $\tau = 1.8\pi$, $\lambda_0 = 0.1$, $\omega_0 = 1$, and $\gamma_0 = 0$, which are the values used throughout the rest of the chapter, except when indicated otherwise.

expect different stability of the synchronous solution for oscillators in $\mathcal{SL}(\lambda_0, \omega_0, \gamma_0)$ with different h if the delay τ is nonzero (if $\tau = 0$, then \mathbf{R} becomes diagonal and the off diagonal term $-2\gamma r_0^2$ in \mathbf{J}_0 will not contribute to the characteristic equation). This dependence on h is illustrated in the example of figure 4.2. Note that the amplitude death state, $z_j = 0$ for all j , is also a solution common to all oscillators in $\mathcal{SL}(\lambda_0, \omega_0, \gamma_0)$.

4.4.2. Demonstration of AISync in delay-coupled Stuart-Landau oscillators

We now apply the framework developed thus far to characterize the AISync property in networks of identically coupled Stuart-Landau oscillators. As a concrete example, we consider a directed ring network of $N = 6$ nodes populated with Stuart-Landau oscillators of two kinds: $\mathbf{F}^{(1)}(z) = f(z; \lambda_0, \omega_0 + h, \gamma_0 + h/r_0^2)$ and $\mathbf{F}^{(2)}(z) = f(z; \lambda_0, \omega_0 - h, \gamma_0 - h/r_0^2)$ in the notation of Sec. 4.2, for $\lambda_0 = 0.1$, $\omega_0 = 1$, $\gamma_0 = 0$, and h (which we convention to be positive from this point on) serving as a measure of the heterogeneity among oscillators. The other parameters are set to be $\sigma\mu = 0.3$ and $\tau = 1.8\pi$. Both $\mathbf{F}^{(1)}$ and $\mathbf{F}^{(2)}$ belong

to $\mathcal{SL}(0.1, 1, 0)$ and thus satisfy $\mathbf{F}^{(1)}(s) = \mathbf{F}^{(2)}(s)$. Each of the six nodes in the directed ring network can be chosen as $\mathbf{F}^{(1)}$ or $\mathbf{F}^{(2)}$, which results in two possible homogeneous systems— $\mathbf{F}^{(1)}$ in all nodes (referred to as $+h$) or $\mathbf{F}^{(2)}$ in all nodes (referred to as $-h$)—and 11 distinct heterogeneous systems.

Equation (4.16) with $\boldsymbol{\mu} = \mu \mathbf{1}_N$ can be applied to any of the 13 systems above. The block structure of $\tilde{\mathbf{D}}^{(1)}$, $\tilde{\mathbf{D}}^{(2)}$ and $\tilde{\mathbf{A}}$ varies from system to system. For example, when $\mathbf{F}^{(1)}$ and $\mathbf{F}^{(2)}$ are arranged on the ring such that every other oscillator is identical (corresponding to $\mathbf{D}^{(1)} = \text{diag}\{1, 0, 1, 0, 1, 0\}$ and $\mathbf{D}^{(2)} = \text{diag}\{0, 1, 0, 1, 0, 1\}$), they share a common block structure of one 2×2 block and one 4×4 block. This reduction from an $N \times N$ system of equations may seem small for $N = 6$, but for any directed ring network of an even number of nodes N , the largest block will always be 4×4 , which represents a tremendous simplification from the fully coupled set of equations when N is large.

Figure 4.3 shows results of applying this method to calculate the MTLE of all heterogeneous systems (gray and blue lines) and of the corresponding homogeneous systems $+h$ (cyan line) and $-h$ (red line). Blue marks the most synchronizable heterogeneous system, which has $\mathbf{D}^{(1)} = \text{diag}\{1, 1, 1, 0, 1, 0\}$ and $\mathbf{D}^{(2)} = \text{diag}\{0, 0, 0, 1, 0, 1\}$, and is referred to as $\pm h$. The limit cycle synchronous state of system $\pm h$ is stable for the entire range of h considered. For the homogeneous system $-h$, the synchronous state is stable for $h \in (0, 0.23)$, and for the homogeneous system $+h$ this state is stable for $h \in (0, 0.32)$. This gives rise to a wide AISync region, ranging from $h = 0.32$ all the way to at least $h = 1.0$ (the largest value considered in our calculations). We also verified that the other possible symmetric state—the amplitude death state—is unstable for both homogeneous systems, and we show the corresponding MLEs in the inset of figure 4.3.

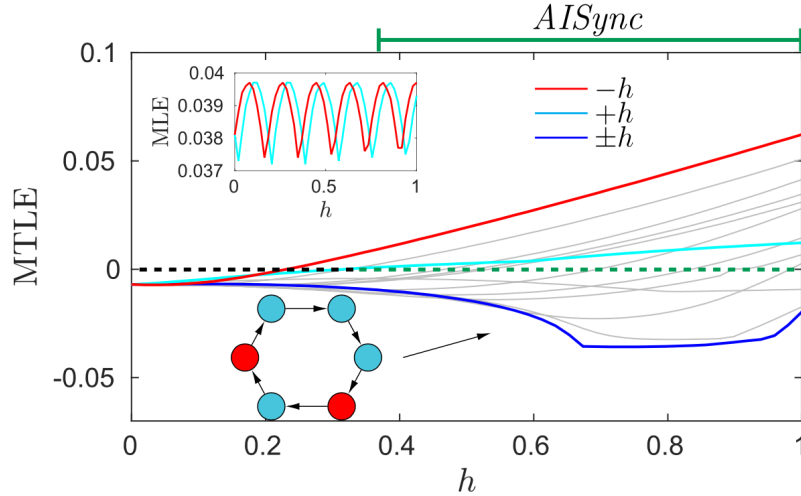


Figure 4.3. Dependence of the MTLE on the heterogeneity h for heterogeneous systems (gray and blue lines) and homogeneous systems ($+h$, cyan line; $-h$, red line). A total of 10 out of 11 heterogeneous systems exhibit AISync for some range of $h \in (0, 1)$. The most synchronizable heterogeneous system is $\pm h$ (highlighted in blue, and accompanied by its network diagram color-coded by oscillator type). The MLE of the amplitude death state is shown as inset for both homogeneous systems. The dashed line at zero marks the boundary of linear stability, and the top green line marks the region $h \in (0.32, 1)$ where AISync occurs.

Figure 4.4 shows the result of direct simulations of systems initiated close to the limit cycle synchronous state with h set to 0.8. In figure 4.4(a) we compare the homogeneous system $+h$ with the heterogeneous system $\pm h$. The upper panel trajectory is produced by system $+h$ alone, which loses synchrony over time due to instability. In the lower panel trajectory, $+h$ is switched to the heterogeneous system $\pm h$ at $t = 100$. This stabilizes the synchronous trajectory and no desynchronization is observed for the course of the simulation. As the effect of this switching in the lower panel trajectory is not very visually distinctive, we also plot the synchronization error δ for $t \in [0, 1000]$, where δ is defined as

the standard deviation among z_j :

$$(4.25) \quad \delta = \sqrt{\frac{1}{N} \sum_{j=1}^N \|z_j - \bar{z}\|^2}, \quad \bar{z} = \frac{1}{N} \sum_{j=1}^N z_j.$$

The error plot clearly shows that δ grows for $t < 100$ and decreases for $t > 100$. Similarly, in figure 4.4(b) we compare the homogeneous system $-h$ with the heterogeneous system $\pm h$. The upper panel trajectory (now produced by system $-h$ alone) quickly loses synchrony and evolves into a high-dimensional incoherent state, while the lower panel trajectory converges to the amplitude death state after switching to $\pm h$. Note that this state is different from the limit cycle state in figure 4.4(a), illustrating that $\pm h$ has two distinct symmetric states that are stabilized by system asymmetry.

We further characterize the AISync property of those systems in terms of the time delay τ . The stability of the homogeneous systems is compared with the heterogeneous system $\pm h$ for a range of τ and h . As shown in figure 4.5, the parameter space is divided into three regions: a region where the heterogeneous system $\pm h$ and at least one of the homogeneous systems are stable (region I); a region where the heterogeneous system $\pm h$ is stable but both homogeneous systems are unstable (region II); and a region where all three systems, $\pm h$, $+h$ and $-h$, are unstable (region III). This figure establishes the occurrence of AISync in the entire region II. We note, moreover, that region II is a conservative estimate of the AISync region as it only considers one out of eleven possible heterogeneous systems and only concerns the limit cycle synchronous state (not accounting for the possibility of a stable amplitude death state for $\pm h$; we have verified that this fixed point is unstable for both $+h$ and $-h$ over the entire range of h and τ considered in our simulations).

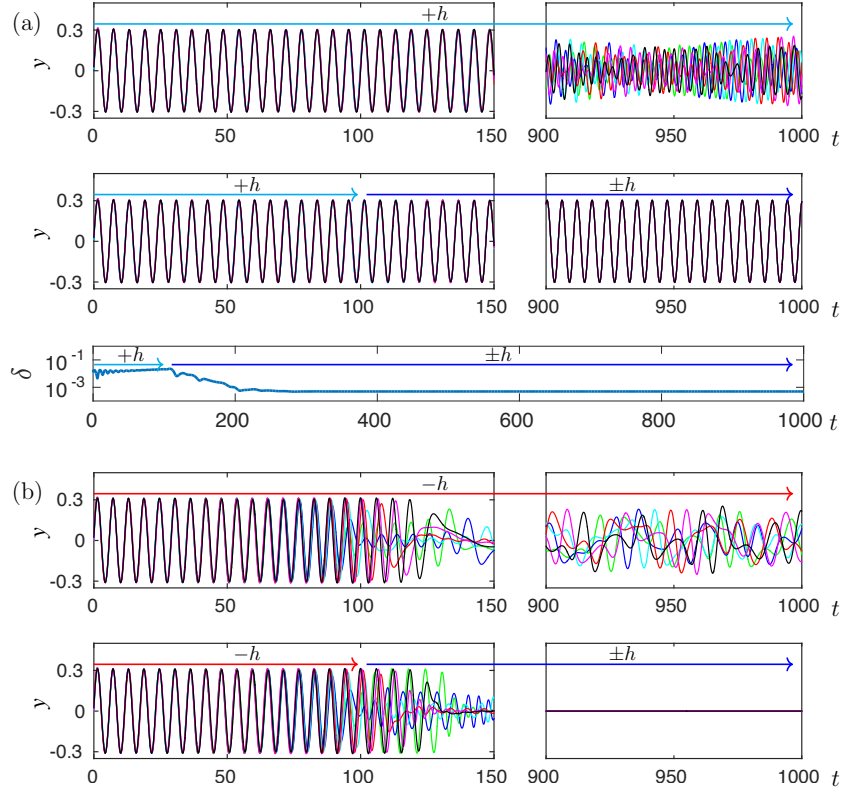


Figure 4.4. (a) Time evolution of typical trajectories of the systems $+h$ and $\pm h$ in figure 4.3 initiated close to the limit cycle synchronous state $z_j = r_0 e^{i\Omega t}$, where the main panels show the imaginary part of $z_j = x_j + iy_j$, $j = 1, \dots, 6$. Top panel: trajectory for the homogeneous system $+h$. Middle panel: trajectory starting from the same initial condition when a switch to the heterogeneous system $\pm h$ is performed at $t = 100$. Bottom panel: time evolution of the synchronization error δ , further demonstrating that the trajectory deviates from the limit cycle state for the homogeneous system but converges to it for the heterogeneous one. (b) Same as in the main panels of (a) but now for the homogeneous system $-h$, where in this case the heterogeneous system $\pm h$ converges to the amplitude death state. In these examples, the heterogeneity h was chosen to be 0.8. To initiate the system close to the limit cycle synchronous state, we extended $z_j = r_0 e^{i\Omega t}$ backward τ time units from $t = 0$, and perturbed the components of each oscillator independently at $t = 0$ with a displacement chosen randomly from the interval $(0, 0.1)$.

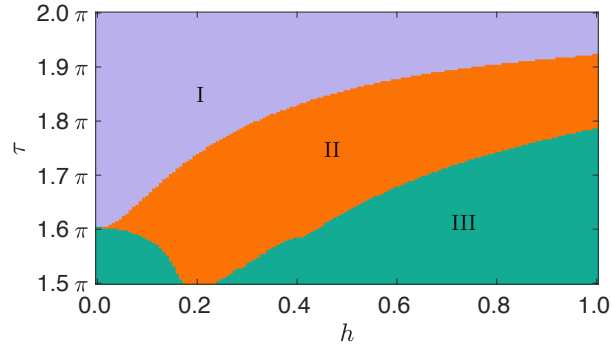


Figure 4.5. Regions in the τ versus h plane categorized by the stability of the limit cycle synchronous state for the 6-node directed ring network in figure 4.3. In region I (purple), the synchronous state is stable for both the heterogeneous system $\pm h$ and at least one homogeneous systems ($-h$ and/or $+h$). In region II (orange), the synchronous state is stable only for the heterogeneous system. Region II is thus part of the AISync region. In region III (green), the synchronous state is unstable for the two homogeneous systems as well as for the heterogeneous one.

Another interesting fact to note is that unlike many other delay-coupled systems [55], here larger delay does not always lead to reduced synchronizability, as both region I and the union of regions I and II expand with increasing time delay τ . This adds to the few existing examples showing time-delay enhanced synchronization [18, 74, 70, 294], which can have implications for phenomena such as the remote synchronization between neurons in distant cortical areas.

Thus far we have focused on Stuart-Landau oscillators coupled through a directed ring network, which is a directed version of a circulant graph. Such graphs have the property of admitting a circulant matrix as their adjacency matrix. Networks of identically coupled oscillators can be much more complex, as most symmetric networks are non-circulant. It is thus natural to ask whether AISync can be observed for Stuart-Landau oscillators coupled through such networks.

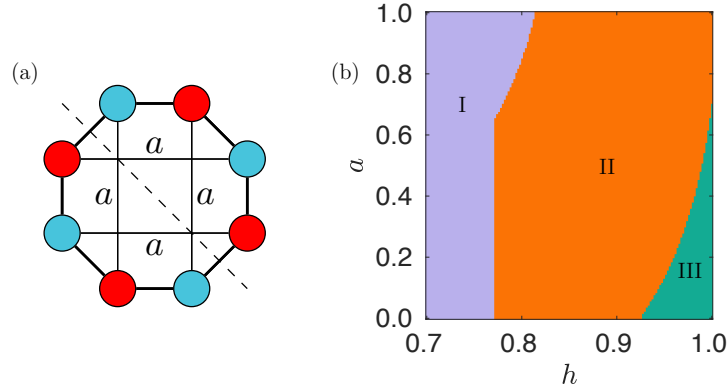


Figure 4.6. AISync in a symmetric non-circulant network. (a) Crown network of $N = 8$ nodes, for outer edges of weight 1 and inner edges of weight a . (b) Illustration in the a versus h plane of the regions categorized by the stability of the limit cycle synchronous state, where the heterogeneous system alternates the two types of oscillators as color-coded in (a). As in the previous example, region II is part of the AISync region, since in this region synchronization is unstable for both homogeneous systems ($+h$ and $-h$) but is stable for the heterogeneous one.

In figure 4.6 we show the example of a (weighted) crown network of 8 nodes, which, when weighted, is the smallest non-circulant vertex-transitive graph [40]. In this illustration, the inner edges have weight a and the outer edges have fixed weight 1. It is intuitively clear that all nodes are identically coupled. This can be verified in figure 4.6(a) by applying 90-degree rotations (which connect nodes of the same color) and reflections with respect to the dashed line (which connects nodes of different colors) to show that all nodes belong to the same orbit under automorphisms of the network.

We calculate the stability of the limit cycle synchronous state for both homogeneous systems (all nodes equipped with $\mathbf{F}^{(1)}$ or all nodes equipped with $\mathbf{F}^{(2)}$) and a representative heterogeneous system. The heterogeneous system has $\mathbf{F}^{(1)}$ and $\mathbf{F}^{(2)}$ arranged alternately, as indicated by the colors in figure 4.6(a), which is a configuration described

by $\mathbf{D}^{(1)} = \text{diag}\{1, 0, 1, 0, 1, 0, 1, 0\}$ and $\mathbf{D}^{(2)} = \text{diag}\{0, 1, 0, 1, 0, 1, 0, 1\}$. These matrices and the adjacency matrix of the crown network can be simultaneously block diagonalized into a block structure composed of four 2×2 blocks, which significantly simplifies the calculation of the MTLE. The results are shown in figure 4.6(b) for a range of inner edge weight a and oscillator heterogeneity h , where the regions I, II, and III are defined as before. We have also verified that, for the entire range of parameters in figure 4.6(b), the amplitude death state is unstable for both homogeneous systems. For the same reasons as in figure 4.5, region II is a conservative estimate of the AISync region. The AISync region extends from $a = 0$, where the network is an unweighted ring, to $a = 1$, where the network is an unweighted crown. Incidentally, this example shows that AISync can also occur for undirected networks (previous examples, both in this chapter and in the literature [192, 317], were limited to directed networks).

4.4.3. Synchronization in non-symmetric networks induced by oscillator heterogeneity

The scenario in which identically coupled oscillators synchronize stably only when the oscillators themselves are nonidentical is, arguably, AISync in its most compelling form, as all the heterogeneity can then be attributed to the oscillators and there is no potential for compensatory heterogeneity to result from the network structure. But the possibility of synchronization induced by oscillator heterogeneity is not restricted to such symmetric networks, and we hypothesize that this effect can be prevalent also in networks that do not have symmetric structure. In examining this hypothesis, it is useful to note that

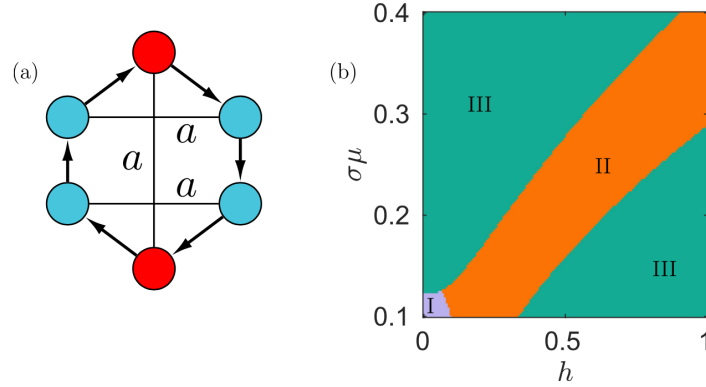


Figure 4.7. Synchronization induced by oscillator heterogeneity in a non-symmetric network. (a) Network of $N = 6$ nodes with outer (directed) edges of weight $+1$ and inner (undirected) edges of weight $a = -0.1$, which has 3 symmetry clusters. (b) Illustration in the $\sigma\mu$ versus h plane of the regions categorized by the stability of the limit cycle synchronous state, where the heterogeneous system has two oscillators of one type and four oscillators of the other type, as indicated by the colors in (a). Once again, region II corresponds to the scenario in which the homogeneous systems $-h$ and $+h$ do not synchronize stably whereas the heterogeneous system does.

our analysis extends naturally to networks that have the same (weighted) indegree for all nodes (as defined in equation (4.12)) but are otherwise arbitrary.

Figure 4.7 shows an example for a 6-node non-symmetric network of Stuart-Landau oscillators. The network, which is directed and has both positive and negative edge weights, is composed of three symmetry clusters, as defined by the orbits of its automorphism group. Each symmetry cluster consists of two nodes that are diagonally opposite and can be mapped to each other by rotations of 180 degrees in the representation of figure 4.7(a). Thus, the oscillators are indeed not identically coupled. As a representative heterogeneous system to be compared with the homogeneous systems ($+h$ and $-h$), we consider four nodes equipped with the dynamics $\mathbf{F}^{(1)}$ and the other two nodes with

$\mathbf{F}^{(2)}$ (as indicated by the colors in figure 4.7(a), where $\mathbf{F}^{(1)}$ and $\mathbf{F}^{(2)}$ are defined as in Sec. 4.4.2). In figure 4.7(b) we show the results of the stability analysis for a range of the effective coupling strength $\sigma\mu$ and oscillator heterogeneity h , with the same definition of regions I, II and III as above. Again, we verified that, for the range of parameters in figure 4.7(b), the amplitude death state is unstable for both homogeneous systems. Region II occupies a sizable portion of the diagram, showing that the scenario in which the oscillators are required to be nonidentical for the network to synchronize stably can also be common for non-symmetric networks.

4.4.4. Generalization to unrestricted parameters

We note that our Stuart-Landau system exhibits even stronger notions of AISync than the one considered thus far. For example, if a mixture of heterogeneous oscillators with parameters $+h$ and $-h$ can synchronize stably, then it may be natural to ask whether the homogeneous systems are all unstable even when the oscillator parameter is chosen from the entire interval $[-h, +h]$, rather than just from the pair $\{-h, +h\}$. The system in equation (4.19) exhibits AISync also in this stronger sense. The region between $\tau = 1.5\pi$ and $\tau = 1.6\pi$ in figure 4.5 provides one such example, where both homogeneous systems $+h$ and $-h$ are unstable for any $h \in [0, 1]$, while the heterogeneous system $\pm h$ is stable for a range of h in this interval. A similar result holds for heterogeneity-induced synchronization in non-symmetric networks, as illustrated by the example in figure 4.7 for $\sigma\mu$ larger than 0.13.

One can further ask whether it is possible for a heterogeneous system to be stable for some h while the homogeneous systems are unstable for any $h \in (-\infty, +\infty)$. We have

extended the range of h in figure 4.5 to verify numerically that no homogeneous system can synchronize for any h in the region $1.5\pi < \tau < 1.6\pi$ (and, similarly, in figure 4.7 for any h in the region $\sigma\mu > 0.13$). Thus, these are scenarios in which the oscillators need to be nonidentical for the system to synchronize even if the homogeneous system has unrestricted access to the values of the parameter h .

Naturally, we can also imagine heterogeneous systems in which each oscillator is allowed to take an independent value of the parameter h in the full interval $(-\infty, +\infty)$. Computational challenges aside, this would only show that the phenomenon of AISync is even more common, since there would then be a larger set of heterogeneous systems to choose from.

4.5. Concluding remarks

Motivated by the recent discovery of *asymmetry-induced synchronization*, here we established a general stability analysis method for demonstrating and examining identical synchronization among nonidentical oscillators. This can be seen as a generalization of the standard master stability analysis to non-perturbative regimes of parameter mismatches, and is illustrated for systems with Laplacian- and adjacency-matrix coupling as well as time-delay coupling. In establishing our formalism, we first characterized the most general conditions under which nonidentical oscillators can synchronize completely for the various coupling schemes. When the coupling is non-diffusive, the balanced input conditions required for the synchronization of identical oscillators [96, 6] is replaced by conditions that involve both the node dynamics and the coupling term. We then established our

approach to simultaneously block diagonalize the matrices in the variational equation, which reduces dimension and facilitates stability analysis.

This new framework was applied to networks of heterogeneous delay-coupled Stuart-Landau oscillators and reveals AISync as a robust behavior. We identify coupling delay as a new key ingredient leading to AISync in this class of systems, which suggests that AISync may be more common than previously anticipated in real systems, where delay is ubiquitous [128, 188]. The possibility of AISync, along with the conditions we establish for complete synchronization, has the potential to lead to new optimization and control approaches focused on creating or enhancing synchronization stability in networks that may not synchronize spontaneously when the dynamical units are identical. By tuning the oscillators to suitable nonidentical parameters, such approaches promise to be useful specially when the network structure is fixed, since they could rely solely on nonstructural degrees of freedom associated with the local (node) dynamics.

Our analysis of the heterogeneous Stuart-Landau system is far from exhaustive, as we explored only slices of its vast parameter space and our parameter choices were not fine-tuned. In particular, we only considered real coupling strength σ , while complex coupling strength (known as conjugate coupling) has been shown to have significant impact on stability [60]; the effect of the oscillation amplitude parameter λ , not varied here, also warrants further investigation. Moreover, we focused mainly on heterogeneous systems of only two kinds of oscillators, while more diverse populations of oscillators are yet to be explored in detail. Another promising future direction concerns the underlying network structure, as it is still an open question whether there exist ways to characterize a system's potential to exhibit AISync on the basis of its network structure. In particular,

it would be desirable to identify algebraic indexes determined by the coupling matrix that could provide such a characterization (similar to the way matrix eigenvalues determine synchronizability of certain coupled-oscillator systems).

Finally, we emphasize that while we have explicitly developed our framework for three widely adopted forms of coupling, complete synchronization can be investigated through a similar formulation whenever necessary and sufficient conditions analogous to those in Table 4.1 can be derived. In particular, this may include systems with different types of coupling matrices, other forms of time delay, heterogeneous interaction functions, and explicit periodic time dependence in the coupling terms. Another area for future research concerns extending this work to systems in which the synchronization applies to some (but not all) dynamical variables or to functions of the variables (but not the variables themselves), as found in various applications. Such systems are candidates to exhibit yet new synchronization phenomena, which we hope will be revealed by future research.

CHAPTER 5

Outperforming Design with Random Heterogeneity in Network Synchronization

A fundamental and widely held assumption on network dynamics is that similar components are more likely to exhibit similar behavior than dissimilar ones and that generic differences among them are necessarily detrimental to synchronization. Here, we show that this assumption does not hold in oscillator networks when communication delays are present. We demonstrate, in particular, that random parameter mismatches among oscillators can consistently rescue the system from losing synchrony. This finding is supported by electrochemical oscillator-experiments performed under realistic conditions. Remarkably, at intermediate levels, random mismatches are far more effective in promoting synchronization than differences specially designed to facilitate identical synchronization. Our results suggest that, rather than being eliminated or ignored, intrinsic disorder in technological and biological systems can be harnessed to help maintain coherent dynamics required for function.

This chapter is based on the joint work with Jorge L. Ocampo-Espindola, István Z. Kiss, and Adilson E. Motter.

5.1. Background

Heterogeneity among interacting components is usually seen as detrimental to the emergence of uniform dynamics in networks, including consensus [198, 155] and synchronization [274, 13]. For networks of coupled oscillators, the implicit assertion is that global synchronization would be hindered by parameter mismatches among oscillators. This assertion, which has been established rigorously for Kuramoto models [274], remains under-substantiated for more general classes of oscillator networks [301, 145, 196], especially those studied using variants of the master stability function formalism [217, 190, 60, 280]. This lack of theoretical understanding can be partially attributed to the mathematical difficulties involved in the study of nonidentical oscillators. In the relatively few theoretical studies that have explicitly considered oscillator heterogeneity beyond the context of Kuramoto models, the focus has been on small parameter mismatches and the persistence of synchronization among nearly-identical oscillators [233, 276, 220, 5, 264]. These results have further reinforced the perception that disorder, in the form of random oscillator heterogeneity, is undesirable for synchronization.

Yet, a few exceptions to the above perception exist in the literature. In particular, it was shown that disorder can sometimes enhance synchronization and/or spatiotemporal order in arrays of driven dissipative pendulums with free boundary conditions [50, 49, 51]. For example, for initially identical oscillators in a chaotic regime, heterogeneity was shown to suppress chaos, giving rise to more regular spatiotemporal patterns [50]. Still, in such cases disorder does not stabilize the system around the original synchronization orbit present in the homogeneous system. More recently, it was realized that certain oscillator heterogeneity can stabilize the original synchronization orbit that is unstable in the

homogeneous system [193, 314]. In those findings the heterogeneity must be judiciously designed to preserve at least one common orbit among the nonidentical oscillators, which may be difficult to achieve in practice.

Here, we show that *generic* differences among individual oscillators can *consistently* stabilize the dynamics around an otherwise unstable global synchronization orbit of the homogeneous system. We demonstrate the phenomenon for random heterogeneity in delay-coupled Stuart-Landau oscillators, which is a canonical model for limit-cycle oscillations close to a Hopf bifurcation. Stuart-Landau oscillators have been used to describe diverse processes, ranging from electrochemical reactions [323] to plant circadian rhythms [83]. Importantly, we establish the surprising result that random heterogeneity can be more effective than judiciously designed heterogeneity in preserving system-level coherence. To support the theoretical and numerical results, we performed experiments using coupled electrochemical oscillators. The experimental results confirm our predictions and further extend the effect to systems that are not limited to the vicinity of a Hopf bifurcation. Thus, our findings are expected to have implications for a broad class of technological and biological systems, whose function depends on the synchronization of heterogeneous components.

5.2. Modeling the dynamics of heterogeneous oscillators

We consider a network of N delay-coupled nonidentical Stuart-Landau oscillators, whose dynamics is governed by

$$(5.1) \quad \dot{z}_j(t) = f_j(z_j(t)) + K \sum_{k=1}^N A_{jk} [z_k(t - \tau) - z_j(t)],$$

where $z_j = r_j e^{i\psi_j} = x_j + iy_j$ is a complex variable representing the state of the j th oscillator, and K is the coupling strength. The adjacency matrix $\mathbf{A} = \{A_{jk}\}$ represents a network with a common indegree $d = \sum_k A_{jk}$ for all oscillators j . The coupling delay τ models the finite speed of signal propagation in real systems, which is often significant in biological [74, 52, 292], physical [78, 79, 39], and control systems [227, 102]. The local dynamics f_j is the canonical form for systems born out of a Hopf bifurcation [132],

$$(5.2) \quad f_j(z_j) = [\lambda_j + i\omega_j - (1 + i\gamma_j)|z_j|^2] z_j,$$

where λ_j , ω_j , and γ_j are real parameters associated with the amplitude, base frequency, and amplitude-dependent frequency of the underlying limit-cycle oscillations.

The oscillators are identical when $\lambda_j = \lambda$, $\omega_j = \omega$, and $\gamma_j = \gamma$ for all j . For identical oscillators, the amplitude r_0 and angular velocity Ω_0 of the limit-cycle synchronous solution

$$(5.3) \quad z_j = r_0 e^{i\Omega_0 t}, \quad j = 1, \dots, N$$

can be found by solving the transcendental equations

$$(5.4a) \quad r_0^2 = \lambda + dK(\cos \Phi - 1),$$

$$(5.4b) \quad \Omega_0 = \omega - \gamma r_0^2 + dK \sin \Phi,$$

where $\Phi = -\Omega_0 \tau$ [60]. When random heterogeneity is introduced through one or more oscillator parameters, the identical synchronization state [5.3] no longer exists. Nonetheless, we show that heterogeneous systems can still admit states that are synchronized in the

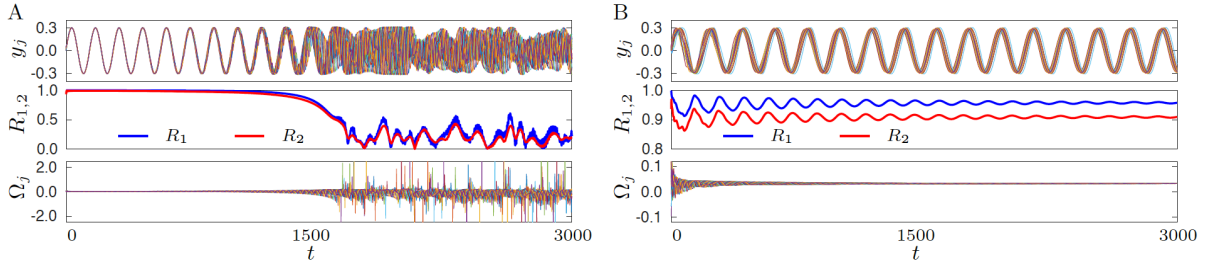


Figure 5.1. Impact of oscillator heterogeneity on the synchronization dynamics of Stuart-Landau oscillators. The different panels show the time evolution of the imaginary components y_j (top), order parameters R_1 and R_2 (middle), and angular velocities $\Omega_j = \dot{\psi}_j$ (bottom), for trajectories in a 18-node ring network initialized close to the identical synchronization state. (A) Homogeneous system for the parameters defined in the text. (B) Heterogeneous system for the same parameters, except for base angular velocities $\{\omega_j\}$, which are drawn from a Gaussian distribution with standard deviation $\sigma = 0.1$. The trajectories show that synchronization is unstable in the homogeneous system but becomes stable in the heterogeneous one.

sense of exhibiting cohesive phase and amplitude dynamics, as formalized below. Here, we consider synchronization in this sense and ask whether it can be stabilized by random oscillator heterogeneity.

We start by considering a homogeneous system of $N = 18$ identical Stuart-Landau oscillators coupled through a directed ring network for $\lambda = 0.1$, $\omega = -0.28$, $\gamma = -4.42$, $K = 0.3$, $d = 1$ and $\tau = 1.8\pi$. Under this parameter choice, the limit-cycle synchronous solution [5.3] is unstable, and the system evolves into a symmetry-broken state exhibiting incoherent chaotic dynamics. As an example of a heterogeneous system, we draw each base frequency ω_j from a Gaussian distribution, then linearly shift and rescale them so the set $\{\omega_j\}$ has mean equal to $\omega = -0.28$, as in the homogeneous system, and standard deviation $\sigma = 0.1$.

In Fig. 5.1, we show typical trajectories of the imaginary components y_j , order parameters R_1 and R_2 , and angular velocities $\Omega_j = \dot{\psi}_j$ for the homogeneous and heterogeneous systems. Here, two order parameters are introduced to measure the cohesiveness of the dynamics: the phase order parameter $R_1 = \left| \sum_j e^{i\psi_j} / N \right|$, which is the one typically used in the study of Kuramoto oscillators; the phase-amplitude order parameter $R_2 = \frac{1}{\max(r_j)} \left| \sum_j r_j e^{i\psi_j} / N \right|$, which measures the coherence in both phases and amplitudes. It follows that both R_1 and R_2 are constant for frequency-synchronized states. For the trajectories shown, the two systems were initialized close to the limit-cycle synchronous state and evolved for 3000 time units. The homogeneous system loses synchrony at $t \approx 1500$ and transitions to an incoherent state with both R_1 and R_2 fluctuating around 0.2. Remarkably, despite having different base frequencies, the heterogeneous oscillators converge to a stable cohesive state with high order parameters ($R_1 > R_2 > 0.9$) and identical angular velocities. That is, the oscillators are not only approximately synchronized in phase and amplitude—they are also exactly synchronized in frequency (i.e., phase-locked).

5.3. Synchronization states and stability conditions

To gain theoretical understanding of the observation in Fig. 5.1 and its prevalence, we characterize the synchronization states of interest in the presence of heterogeneity and derive analytical conditions for their stability. These results are established for delay-coupled Stuart-Landau oscillators with arbitrary heterogeneity.

Inspired by the fact that the heterogeneous system in Fig. 5.1 settles into a frequency-synchronized state, for which the frequencies of all oscillators are equal and the phase

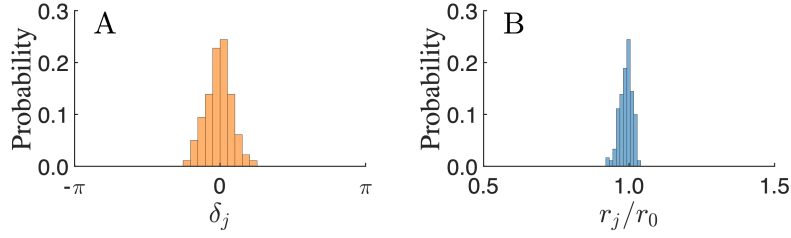


Figure 5.2. Distribution of the phase lags δ_j and the normalized amplitudes r_j/r_0 for $\sigma = 0.06$. The data are obtained by solving Eqs. 5.6 for 10 independent realizations of heterogeneous ω_j . The network and the other parameters are the same as in Fig. 5.1.

differences and amplitudes are constant, we employ the following ansatz:

$$(5.5) \quad z_j = r_j e^{i(\Omega t + \delta_j)},$$

where each oscillator has amplitude r_j and phase lag δ_j but all oscillators share the same angular velocity Ω . Substituting the ansatz into Eq. 5.1, we obtain $2N$ nonlinear algebraic equations with $2N$ unknowns:

$$(5.6a) \quad r_j^2 = \lambda_j + K \sum_{k=1}^N A_{jk} \frac{r_k}{r_j} \cos \Phi_{jk} - dK,$$

$$(5.6b) \quad \Omega = \omega_j - \gamma_j r_j^2 + K \sum_{k=1}^N A_{jk} \frac{r_k}{r_j} \sin \Phi_{jk},$$

for $j = 1, \dots, N$, where $\Phi_{jk} = \delta_k - \delta_j - \Omega\tau$. Taking $\delta_1 = 0$, which can be done without loss of generality, the solution of Eqs. 5.6 determines $\delta_2, \dots, \delta_N, r_1, \dots, r_N$, and Ω . As shown in Fig. 5.2, when parameter heterogeneity is not too large, this gives us frequency-synchronized states that are close to the identical synchronization state of the homogeneous system given by Eqs. (5.3) and (5.4).

We can analyze the stability of the frequency-synchronized state through the variational equation that governs the evolution of small deviations $\delta r_j(t)$ and $\delta\psi_j(t)$ from the frequency-synchronized state. Letting $z_j(t) = r_j[1 + \delta r_j(t)]e^{i[\Omega t + \delta_j + \delta\psi_j(t)]}$, $\boldsymbol{\eta}_j = (\delta r_j, \delta\psi_j)^\top$, and $\boldsymbol{\eta} = (\boldsymbol{\eta}_1, \dots, \boldsymbol{\eta}_N)^\top$, the variational equation reads

$$(5.7) \quad \dot{\boldsymbol{\eta}}(t) = \oplus (\mathbf{J}_j - K\mathbf{P}_j) \boldsymbol{\eta}(t) + K(\mathbf{A} \otimes \mathbf{R}_{jk}) \boldsymbol{\eta}(t - \tau),$$

where $\mathbf{J}_j = \begin{pmatrix} -2r_j^2 & 0 \\ -2\gamma_j r_j^2 & 0 \end{pmatrix}$, $\mathbf{R}_{jk} = \frac{r_k}{r_j} \begin{pmatrix} \cos \Phi_{jk} & -\sin \Phi_{jk} \\ \sin \Phi_{jk} & \cos \Phi_{jk} \end{pmatrix}$, $\oplus (\mathbf{J}_j - K\mathbf{P}_j) = \text{diag}(\mathbf{J}_1 - K\mathbf{P}_1, \dots, \mathbf{J}_N - K\mathbf{P}_N)$, $\mathbf{P}_j = \sum_k A_{jk} \mathbf{R}_{jk}$, and $\mathbf{A} \otimes \mathbf{R}_{jk}$ is a $2N \times 2N$ matrix obtained by replacing each entry A_{jk} in \mathbf{A} with 2×2 block $A_{jk} \mathbf{R}_{jk}$.

Since all the matrices in Eq. 5.7 are time independent, the stability calculation boils down to finding the eigenvalues v of the following characteristic equation:

$$(5.8) \quad \det\{\oplus (\mathbf{J}_j - K\mathbf{P}_j) + K(\mathbf{A} \otimes \mathbf{R}_{jk})e^{-v\tau} - v\mathbb{1}_{2N}\} = 0.$$

To obtain Eq. 5.8 we have replaced $\boldsymbol{\eta}(t - \tau)$ in Eq. 5.7 by $e^{-v\tau} \boldsymbol{\eta}(t)$. The real part of the eigenvalues v gives us the Lyapunov exponents of Eq. 5.7. After removing the eigenvalue $v = 0$ (which corresponds to perturbing the phase of each oscillator by the same amount and thus does not affect the synchronization state), we can take the maximum among the remaining $\text{Re}(v)$ to obtain Λ —the maximum transverse Lyapunov exponent (MTLE) relative to the frequency-synchronization manifold. The sign of Λ determines the stability of the frequency-synchronized state.

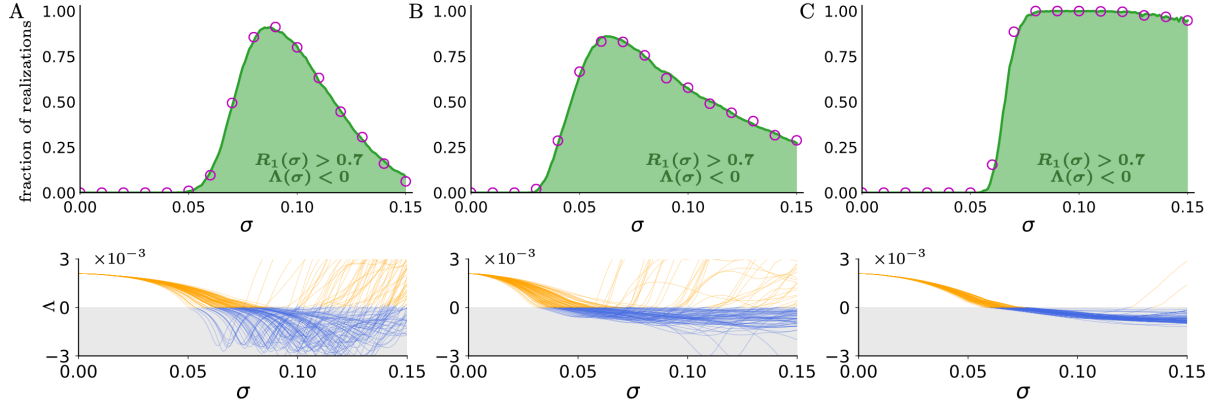


Figure 5.3. Statistics on the synchronizing effect of disorder for systems with (A) nonidentical ω_j , (B) nonidentical λ_j , and (C) nonidentical γ_j . For each upper panel, we generate 1000 realizations of disorder in the corresponding parameter and then, for each realization, calculate $R_1(\sigma)$ and $\Lambda(\sigma)$ of the frequency-synchronized state as σ is increased from 0 to 0.15. The filled green curves show the percentage of realizations that successfully stabilize a frequency-synchronized state with order parameter $R_1 > 0.7$, which are validated by direct simulations shown as purple circles. To visualize the differences between different realizations and their characteristics as an ensemble, each lower panel shows $\Lambda(\sigma)$ for 100 independent realizations of disorder. The stable portions are highlighted in blue. The network and other parameters are the same as in Fig. 5.1.

5.4. Disorder consistently promotes synchronization

Next, we examine the phenomenon systematically and, in particular, address key questions underlying its prevalence. For example, what is the effect of the magnitude of parameter mismatches? Do the results change significantly depending on which parameters are made heterogeneous? And, most importantly, can different realizations of random heterogeneity consistently induce synchronization?

In Fig. 5.3, we start with the same homogeneous system as in Fig. 5.1 and introduce heterogeneity in $\{\omega_j\}$, $\{\lambda_j\}$, and $r_0^2\{\gamma_j\}$, respectively. (Here, the factor r_0^2 is introduced to scale σ for γ_j because the influence of γ_j in Eq. 5.2 is scaled by the square of the oscillation

amplitude. The constant r_0 can be found by solving Eqs. 5.4 for the corresponding homogeneous system.) In all cases, the standard deviation is σ and the mean is taken to be the same as the corresponding parameter in the homogeneous system. For each realization of heterogeneity, as σ increases from zero, the identical synchronization state progressively changes into a phase-locked state with high order parameters. The stability of this state is measured by $\Lambda(\sigma)$, which we obtain by solving Eq. (5.8) for each realization of heterogeneity. The filled green curves in the upper panels show the probability that synchronization is stabilized by random heterogeneity in each parameter. These results are verified by direct simulations of Eqs. (5.1) and (5.2) for various σ , shown as purple circles. In the lower panels, we plot $\Lambda(\sigma)$ for a representative subset of realizations of heterogeneity in each parameter, visualizing their impact on stability as an ensemble.

One can see from Fig. 5.3 that there is always a sweet spot of optimal heterogeneity at an intermediate value of σ . Around that sweet spot, the green curves stay very close to 1, indicating that intermediate heterogeneity can consistently induce synchronization, largely independent of its particular realization. It is interesting to note from the lower panels that small heterogeneity *always* improves stability, as reflected in the monotonic decrease of $\Lambda(\sigma)$ at small σ . Disorder can also consistently stabilize synchronization when all three parameters are allowed to be heterogeneous, as demonstrated in Appendix C.1. Furthermore, we verified that the same effect can be observed for a wide range of network sizes and different network structures (see Appendices C.2 and C.3).

5.5. Disorder is better than design

It is important to compare the effect of random and nonrandom heterogeneities. When the heterogeneity is judiciously designed, Stuart-Landau oscillators can synchronize identically (i.e., all phase differences are identically zero and all amplitudes are equal) even when they are nonidentical. This is most easily seen from Eqs. 5.4, whose solution remains invariant under the transformation $\omega \rightarrow \omega + h$, $\gamma \rightarrow \gamma + h/r_0^2$ for any $h \in \mathbb{R}$. Thus, any given Stuart-Landau oscillator belongs to a continuous family of nonidentical Stuart-Landau oscillators parameterized by h , within which the oscillators can synchronize identically with each other. Moreover, as shown in Ref. [314], mixing different oscillators from the same family can stabilize identical synchronization that would otherwise be unstable.

By designing heterogeneity to preserve identical synchronization, can we do better than by relying on randomness and disorder? Once again we start with the homogeneous system studied in Figs. 5.1 and 5.3. The oscillators are then made heterogeneous by sampling from the identically synchronizable family, with h drawn from a Gaussian distribution. More concretely, $\omega_j = \omega + h_j$ and $\gamma_j = \gamma + h_j/r_0^2$, where $\{h_j\}$ has standard deviation σ and mean zero. This can be seen as a special subset of oscillators with random heterogeneity in both parameters $\{\omega_j\}$ and $\{\gamma_j\}$, the only difference being that $\omega_j - \omega$ and $\gamma_j - \gamma$ are independent when heterogeneity is random.

In Fig. 5.4, we compare the ensemble average MTLE and order parameters between systems with random heterogeneity and systems with designed heterogeneity. Consistent with Fig. 5.3, random heterogeneity is most effective for intermediate magnitudes σ , ranging from 0.05 to 0.1. On the other hand, designed heterogeneity is effective for much

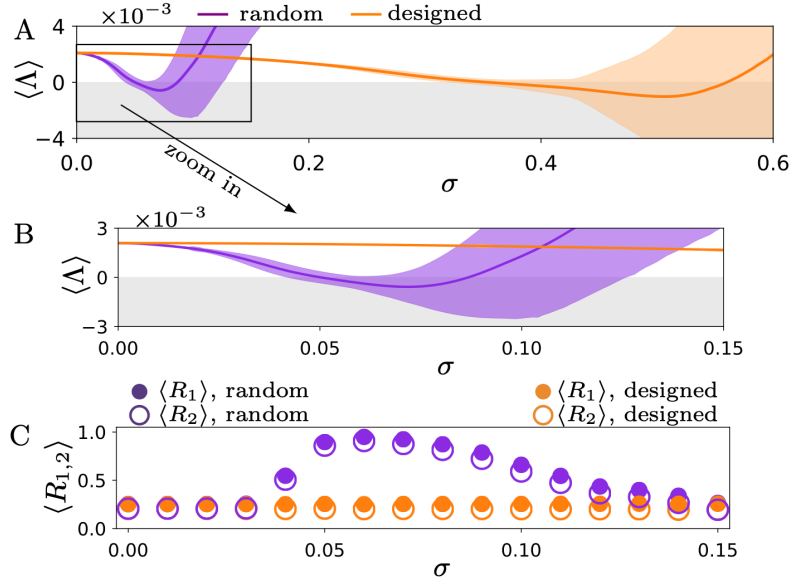


Figure 5.4. Comparing systems with random and designed heterogeneity in $\{\omega_j\}$ and $\{\gamma_j\}$, where the latter preserves a common orbit among heterogeneous oscillators. (A) Average MTLE of systems with random heterogeneity (purple line) and designed heterogeneity (orange line). The shades indicate the standard deviation among 1000 independent realizations. Designed heterogeneity stabilizes synchronization when σ is large, but fails to do so for intermediate σ , where random heterogeneity is effective. (B) Magnification of the marked portion of A, highlighting the effectiveness of random heterogeneity of intermediate magnitude. (C) Average order parameters of systems with random and designed heterogeneities. Each data point is averaged over 1000 independent realizations of heterogeneity and also averaged over time for steady states that are not frequency synchronized. The network and other parameters are the same as in Fig. 5.1.

larger σ , from about 0.4 to 0.6, which may be interpreted as a consequence of the identical synchronization solution being preserved in this case. Remarkably, no system with designed heterogeneity is stable within the range for which random heterogeneity is effective. This implies that at intermediate magnitude, random heterogeneity can outperform those designed to preserve identical synchronization.

5.6. Insight from a minimal system

To gain further understanding, in Fig. 5.5 we focus on a minimal system formed by three nonidentical Stuart-Landau oscillators coupled through a directed ring network. The j th oscillator has parameters $\{\lambda_j, \omega_j, \gamma_j\} = \{\lambda, \omega + h, \gamma + (h + \Delta_j)/r_0^2\}$, with the constraint that $\sum_{j=1}^3 \Delta_j = 0$. The parameter h is introduced to vary the synchronization stability of the homogeneous system without altering the synchronous solution. This enables us to investigate all possible realizations of heterogeneous γ_j for different levels of instability by sweeping the Δ_1 - Δ_2 plane.

In Figs. 5.5A and B, the origin is the only point corresponding to a homogeneous system, and the differences among oscillators increase as one moves away from the origin along the radial directions. Stability analysis indicates that regions of stability appear for intermediate magnitude of the disorder, as shown in Fig. 5.5A ($\Lambda < 0$, blue belts). The phase-locked state is unstable for weak disorder ($\Lambda > 0$, red areas) and ceases to exist for strong disorder (blank areas). A complementary perspective is offered by direct simulations, as shown in Fig. 5.5B. Because order parameters averaged over time is a poor indicator of coherence for systems with a small number of oscillators, we quantify the level of coherence using the minimum of R_2 over a period of 10000 time units after the initial transient. For zero and small heterogeneity, the three oscillators are in an incoherent state with $\min R_2 \approx 0$. As σ is increased further, the oscillators first settle into an approximate synchronization state with $\min R_2$ ranging from 0.6 to 0.9 (light purple regions). The level of coherence continues to improve until it plateaus at $\min R_2 \approx 0.96$ for phase-locked states (dark purple regions), which correspond to the stable states marked by the blue belts in Fig. 5.5A. Finally, once we cross the stability boundary,

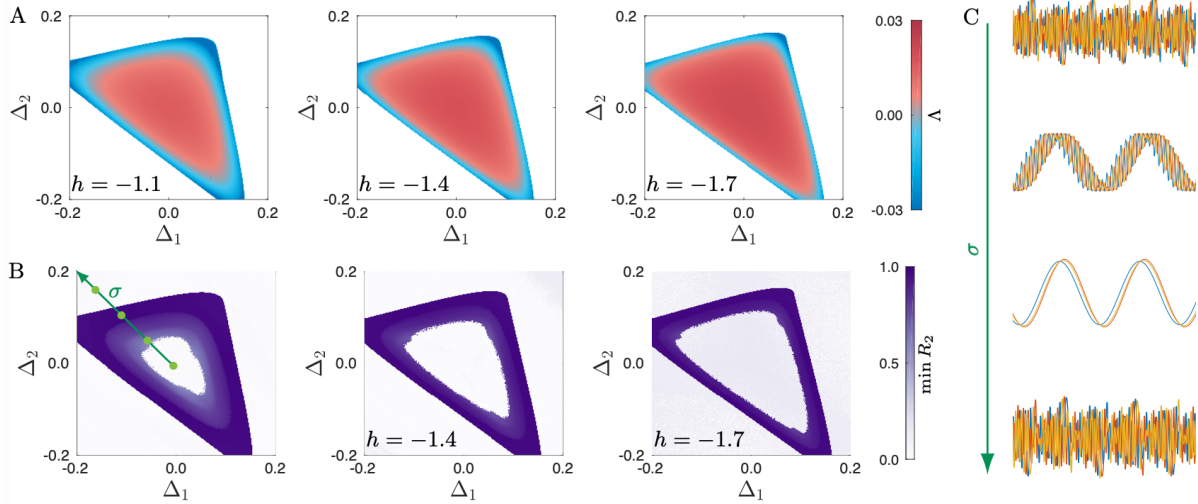


Figure 5.5. Synchronization among three nonidentical Stuart-Landau oscillators coupled through a directed ring network. (A) MTLE of the phase-locked state in the Δ_1 - Δ_2 plane. The homogeneous system lies at the origin of each panel, and its instability increases as h changes from -1.1 to -1.7 . For small Δ_1 and Δ_2 , heterogeneity is not strong enough to tame the instability (red regions). At intermediate Δ_1 and/or Δ_2 , a stability belt emerges (blue regions), demonstrating the stabilizing effect of heterogeneity. When heterogeneity becomes too strong, however, the phase-locked solution no longer exists (blank regions). (B) Minimum of the order parameter R_2 over 10000 time units in a steady state. As one moves along the green line for increasing σ , we observe the incoherence-coherence-incoherence transitions predicted by the stability analysis. (C) Time evolution of y_j (colored by oscillator) for representative states corresponding to the parameters marked by the dots in the left panel in B. In all panels, the other parameters are $\lambda = 0.1$, $\omega = 1$, $\gamma = 0$, $K = 0.3$, $d = 1$, and $\tau = 1.8\pi$.

synchrony is lost again and the value of $\min R_2$ falls back to approximately 0. This incoherence-coherence-incoherence transition is illustrated in Fig. 5.5C with representative trajectories from each stage. It is worth noting that even before the phase-locked state is fully stabilized, disorder can already induce approximate synchronization states with well-defined rhythms, as illustrated by the second trajectory.

Figure 5.5 demonstrates two competing effects of disorder: when heterogeneity is too small, it cannot tame synchronization instability; when it is too large, it destroys the synchronization state. In other words, there is a trade-off between synchronizability and stability, and stable synchronization naturally emerges at intermediate levels of disorder. Another interesting observation is that the stable belts are contiguous in all cases in Fig. 5.5A and completely surround the unstable regions in the middle, which explains why intermediate disorder can consistently stabilize synchronization. It also demonstrates that the effect is robust against increasing instability (controlled by h) in the homogeneous system.

5.7. Electrochemical experiments

A natural question at this point is whether the described phenomenon is robust and general enough to be observed in real systems. To provide an answer, we perform experiments using chemical reaction oscillators based on the electrochemical dissolution of nickel in sulfuric acidic media [323]. The experimental apparatus consist of a counter electrode, a reference electrode, a potentiostat, and N nickel wires submerged in the same sulfuric acidic media, each attached to a resistor (Fig. 5.6A). At constant circuit potential ($V_0 = 1.240$ V relative to the reference electrode) and with the resistance of resistors set to $\xi_j = 1.06$ k ohm, the dissolution rate of each nickel wire, measured as its current, exhibits periodic oscillations [125]. The oscillatory dynamics originate from a Hopf bifurcation at $V_0 = 1.070$ V. Compared to the voltage used in some of the previous studies [39], the system here is farther away from the bifurcation point. When the wires are placed

sufficiently far from each other, the current oscillations do not show noticeable synchronization, confirming that the interactions through the solution are negligible. Coupling among the wires can be introduced through external feedback [323, 39], in which the circuit potential of the wires $V_j(t)$ are set based on the measured currents $I_j(t)$ as

$$(5.9) \quad V_j(t) = V_0 + K \sum_{k=1}^N A_{jk} [I_j(t - \tau) - I_k(t)]$$

for $j = 1, \dots, N$, where K and τ are the experimental coupling strength and delay, respectively. Here, we investigate $N = 16$ wires with oscillatory currents arranged in an undirected 4-by-4 lattice network with periodic boundary conditions, which can be seen as a 2-dimensional variant of the ring networks considered above. For details of the experimental setup and procedure, see Appendix C.4.

With relatively strong coupling ($K \approx -0.10$ V/mA) and no delay ($\tau = 0$ s), the system exhibits in-phase synchronization [310]. Similar in-phase synchronization exists for large delay ($\tau \approx 2.4$ s) that corresponds to the mean period of the uncoupled oscillations. When τ is set to about 1.2 s (about half of the oscillation period), the system exhibits a two-cluster state where every other elements on the grid are in phase, and the neighboring elements are in anti-phase. When the delay is set between these two regions ($\tau \approx 1.75$ s), the system exhibits a desynchronized state. Parametric heterogeneity was introduced by setting the resistance of each oscillator to a different value ξ_j while keeping the mean resistance fixed to $\bar{\xi} = 1.06$ k ohm. The level of parametric heterogeneity is measured by the standard deviation σ among all ξ_j .

First, we randomly pick one heterogeneity profile and experimentally test its effect on the collective dynamics at different heterogeneity level σ . Each experiment starts close to

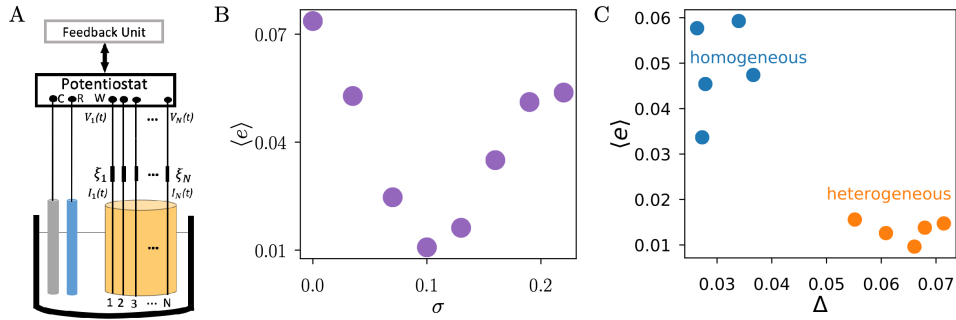


Figure 5.6. Electrochemical oscillator experiments showing that random heterogeneity promotes synchronization. (A) Diagram illustrating the setup of the experimental system, where C is the counter electrode, R is the reference electrode, and W are the working electrodes. (B) Time-averaged synchronization error $\langle e \rangle$ as a function of the parametric heterogeneity σ for one realization of heterogeneous resistances. (C) Time-averaged synchronization error $\langle e \rangle$ vs. dynamical heterogeneity Δ , where each dot represents a different realization of heterogeneous (orange) and homogeneous (blue) systems for $\sigma = 0.13$ kohm and $\sigma = 0$ kohm, respectively.

the in-phase synchronization state and consists of running the system for 600 seconds. The level of coherence is measured by the synchronization error $e(t)$, defined as the standard deviation among currents at time t . Here, the synchronization error is a more straightforward coherence measure than order parameters because the experimental systems are not in the vicinity of a Hopf bifurcation and the dynamics of the amplitude variables are nontrivial. (Nevertheless, we have verified that the order parameters of phases extracted using either Hilbert transform or peak detection algorithms give similar results as the ones obtained using synchronization error.) The experimental results summarized in Fig. 5.6B reveal a well-defined minimum of the average synchronization error $\langle e \rangle$ (averaged over the last 200 seconds of each experimental run) for an intermediate level of parametric heterogeneity $\sigma = 0.1$ kohm. This is consistent with what we observed numerically for delay-coupled Stuart-Landau oscillators.

Unlike the idealized systems used in simulations, experimental systems come with unavoidable imperfections and uncertainties. As a result, the electrochemical oscillators in our system have slightly different dynamics even when resistances are all set to the same nominal value. These relatively small intrinsic heterogeneities can arise because of unavoidable differences in the metal wires (e.g., in composition and size) and surface conditions (oxide film layer thickness and composition, localized corrosion, etc.). To account for such intrinsic heterogeneity, we use peak detection algorithms⁶ to extract the natural frequency and amplitude of each uncoupled oscillator, and we use that information to measure the dynamical heterogeneity Δ for systems both with homogeneous ξ_j and with heterogeneous ξ_j . Here, $\Delta = \bar{\rho}_T + \bar{\rho}_A$, where $\bar{\rho}_T$ ($\bar{\rho}_A$) is the standard deviation of the average oscillation periods (amplitudes) of the uncoupled oscillators normalized by the mean. In Fig. 5.6C, we show results for five sets of independent experiments. Each experiment corresponds to a different realization of heterogeneous resistances (for σ fixed at 0.13 kohm), and of the homogeneous system (corresponding to $\sigma = 0$ kohm). It can be seen that when uncoupled, all heterogeneous systems have a much higher dynamical heterogeneity Δ than homogeneous systems. In contrast, when coupled, the heterogeneous systems achieve significantly better coherence than the homogeneous systems, which is reflected by consistently smaller $\langle e \rangle$.

The contrast between the homogeneous and heterogeneous systems is further visualized in Fig. 5.7. There, we compare the first data point ($\sigma = 0$ kohm) and the fifth data point ($\sigma = 0.13$ kohm) from Fig. 5.6B. The time series of the homogeneous system (Fig. 5.7A) is very much incoherent compared to that of the heterogeneous system

⁶Peak detection algorithms in SciPy: https://docs.scipy.org/doc/scipy/reference/generated/scipy.signal.find_peaks.html.

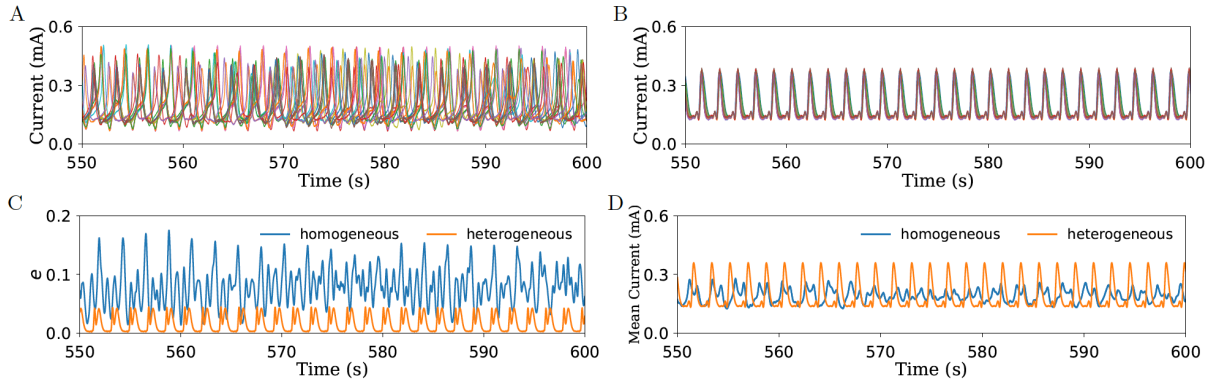


Figure 5.7. Comparison between the dynamics of homogeneous and heterogeneous systems in the electrochemical oscillator experiment. (A) Time series of the currents in the homogeneous system, which shows desynchronized dynamics. (B) Time series of the currents in the heterogeneous system, showing that they remain synchronized throughout the experiment. (C–D) Evolution of synchronization error e (C) and mean-field current (D) for the two systems. In all panels, we show the last 50 s of trajectories of 600 s, initialized close to a synchronized state for $\sigma = 0$ kohm (homogeneous system) and $\sigma = 0.13$ kohm (heterogeneous system).

(Fig. 5.7B). Accordingly, the heterogeneous system exhibits a smaller synchronization error and a more regular rhythm, as demonstrated in Figs. 5.7C and D.

5.8. Concluding remarks

It is often challenging, if not impossible, to completely eliminate component mismatches in coupled systems. Our results suggest that, instead of trying to erase these imperfections (often to no avail), one may be able to take advantage of them to promote synchronization required for the system to function. Indeed, our theory, simulations, and experiments consistently show that synchronization can be stabilized by intermediate levels of random oscillator heterogeneity. The fact that no fine-tuning of the heterogeneity profile is needed to induce synchronization can be valuable for controlling synchronization

in both technological and biological systems. For example, it is often important in applications to generate high power, high frequency voltage oscillations in electric circuits. A single Josephson junction can achieve oscillations as fast as a terahertz, but only with low power output [235]. It is thus desirable to couple many Josephson junctions together and use their synchronized oscillations to increase power. While in practice no two junctions are perfectly identical, our results indicate that it might be possible to boost the performance of coupled Josephson junctions by amplifying rather than reducing the existing mismatches.

In physiology, many important rhythmic processes also depend on the coordination and coherence among a diverse population of cells [91]. The heartbeat, for example, is generated by the mutual entrainment of thousands of pacemaker cells in the sinoatrial node [170, 154], whereas the sleep-wake cycle is regulated by the rhythmic and synchronized oscillation of circadian cells in the suprachiasmatic nucleus [141, 99, 286]. Our findings thus raise the question of whether the heterogeneity among pacemaker or circadian cells is a fundamental limitation of the biology, or, instead, a feature selected by nature to promote synchronization and stabilize vital rhythms in living organisms.

The effect of disorder is also one of the central focus in condensed matter physics [181]. For example, exotic materials such as topological insulators have attracted vast amount of attention over the past decade [110, 228]. A defining property of topological insulators is the existence of edge states that are protected by time-reversal symmetry, which makes the states robust to weak disorder. In the context of oscillator networks, we have been able to go one step further and show that synchronization states may not only be immune to but also thrive on disorder.

It is worth pointing out connections between the phenomenon described here and noise-induced synchronization previously reported in the literature [319, 289]. It has been found that spatially correlated (i.e., common) noise can enhance synchronization both when the oscillators are coupled [179] and uncoupled [282, 180], even if the noise is temporally uncorrelated (i.e., white). In contrast, the disorder we consider here are spatially *uncorrelated* and temporally *quenched*. It was recently shown that uncorrelated noise can even outperform common noise in increasing coherence when oscillators are nonidentical [186]. Thus, understanding the interplay between noise and oscillator heterogeneity poses an intriguing challenge for future research.

Bringing the analogy one step further, stochastic resonance [33, 169, 300, 86] and coherence resonance [87, 229, 225, 295] are also phenomena for which order can emerge from disorder. In those cases, the signal-to-noise ratio is maximized for intermediate noise intensity. Just as noise-induced synchronization and the resonance phenomena have found abundant biological and engineering applications, we believe the relation between disorder and coherence uncovered here should play an important role in numerous natural and man-made systems. Future studies further exploring this relation in specific systems will undoubtedly deepen our understanding of collective behaviors in general and lead to new ways to control the dynamics of interconnected components.

CHAPTER 6

Synchronizing Chaos with Imperfections

Previous research on nonlinear oscillator networks has shown that chaos synchronization is attainable for identical oscillators but deteriorates in the presence of parameter mismatches. Here, we identify regimes for which the opposite occurs and show that oscillator heterogeneity can synchronize chaos for conditions under which identical oscillators cannot. This effect is not limited to small mismatches and is observed for random oscillator heterogeneity on both homogeneous and heterogeneous network structures. The results are demonstrated experimentally using networks of Chua's oscillators and are further supported by numerical simulations and theoretical analysis. Since individual differences are ubiquitous and often unavoidable in real systems, it follows that such imperfections can be an unexpected source of synchronization stability.

This chapter is based on the joint work with Yoshiki Sugitani and Adilson E. Motter.

6.1. Background

Synchronization in networks of chaotic oscillators is a remarkable phenomenon that is now well established theoretically and experimentally [218], with implications for numerous biological and technological systems [290, 174, 75]. Two conditions are generally assumed for this phenomenon to occur: (i) that the coupling strength be sufficiently large and (ii) that the oscillators be sufficiently identical. If the coupling is too weak, the oscillators evolve mostly independently from each other, and their trajectories tend to

diverge due to sensitive dependence on initial conditions—a hallmark of chaos [204]. On the other hand, if the oscillators are not sufficiently identical, their trajectories tend to diverge due to sensitive dependence on parameters—another hallmark of chaos [204]—even if the initial conditions are exactly the same and the coupling strength is otherwise suitably strong.

Previous analyses of synchronization of nonidentical chaotic oscillators have focused mainly on cluster synchronization [26, 62] and phase synchronization [237, 69, 124, 321, 262]. For example, oscillator heterogeneity has been shown to mediate relay synchronization [78] and to induce frequency locking by suppressing chaos [50]. Global chaos synchronization of nonidentical oscillators, on the other hand, has only been explored for strong coupling and small parameter mismatches [234, 191, 266, 4], with an emphasis on the extent to which synchrony persists when the oscillators are slightly different [277, 220]. These previous results consistently show that global synchronization degrades as heterogeneity is increased.

A different body of work has recently shown that, for periodic oscillators, heterogeneity can in fact facilitate synchronization [193, 173]. A natural question is then whether a similar effect would be possible for chaotic oscillators despite the fact that their dynamics exhibit sensitive dependence on parameters and that a well-defined synchronization manifold no longer exists for nonidentical chaotic oscillators. This question is especially relevant in weak coupling regimes, in which synchronization is unstable for identical chaotic oscillators.

In this chapter, we experimentally demonstrate that oscillator heterogeneity can enable synchronization of weakly coupled chaotic oscillators that would otherwise not synchronize. This surprising result is demonstrated using Chua’s oscillators diffusively coupled through their x components, which leads to a semi-infinite stability region for identical oscillators. The robustness of the effect is established by showing that it occurs consistently for *random* parameter heterogeneity and for *different* parameters respectively associated with temporal and state variable scales. The effect is demonstrated across different network structures and is further supported by simulations and theoretical analysis. The role of *oscillator* heterogeneity is isolated by showing the persistence of the effect for structurally homogeneous networks of identically coupled oscillators. These results have immediate implications for real systems, where heterogeneity is ubiquitous. They also have foundational consequences for establishing an unanticipated relation between network coupling, oscillator heterogeneity, and sensitive dependence on initial conditions. In particular, although condition (i) cannot be violated in isolation without causing desynchronization, our results show that the violation of (ii) (albeit detrimental by itself) can mitigate the effect of infringing (i), and thus the synchronization of chaotic oscillators can persist if *both* (i) and (ii) are violated together.

6.2. Experimental setup

We start by considering networks of N diffusively coupled oscillators described by

$$(6.1) \quad \tau_i \dot{\mathbf{x}}_i = F(\mathbf{x}_i) - k \sum_{j=1}^N L_{ij} H(\mathbf{x}_j),$$

where τ_i denotes the time scale and \mathbf{x}_i is the state variable of the i th oscillator. The functions F and H describe the dynamics of a single oscillator and their interactions, respectively. The Laplacian matrix $\mathbf{L} = (L_{ij})$ represents the network structure and k is the coupling strength.

The oscillators and coupling are implemented in our experiment using electrical circuits, as shown in Fig. 6.1. The oscillators consist of x -coupled Chua's circuits [165] given by

$$(6.2) \quad F(\mathbf{x}) = \begin{bmatrix} \eta\{y - x - g(x)\} \\ x - y + z \\ -y/\gamma \end{bmatrix}, \quad H(\mathbf{x}) = \begin{bmatrix} x \\ 0 \\ 0 \end{bmatrix},$$

$$(6.3) \quad g(x) = bx + \frac{1}{2}(b - a)(|x - 1| - |x + 1|),$$

where x , y , and z are the state variables and η , γ , a , and b are parameters. The variables correspond respectively to the voltages v_x and v_y across the capacitors C_x and C_y and the current i_L through the inductor L (which is implemented using a generalized impedance converter circuit). The parameters a and b are determined by a nonlinear resistor (NR) with a piecewise linear characteristic made from op-amps (TL084) and resistors [122]. The tunable parameters of the oscillators are controlled through tunable capacitors. The oscillators are coupled through the voltage v_x , where the directionality of the coupling is implemented using voltage followers. A light-emitting diode (LED) is attached to each oscillator so as to monitor the oscillation visually, with the diode turning on for $v_x > 0$ and off for $v_x < 0$. The voltage $v_x^{(i)}$ for each oscillator is recorded in a computer through an analog-to-digital converter (ADC) attached to the circuit.

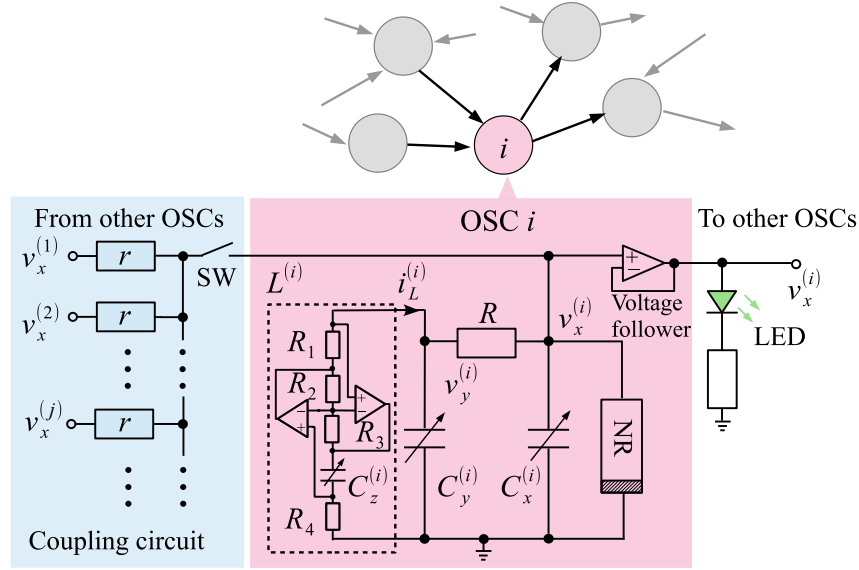


Figure 6.1. Circuit diagram of coupled Chua's oscillators in our experiment. The individual oscillators are coupled through their voltage $v_x^{(i)}$, and an LED is attached to each oscillator to visualize the voltage oscillations. The capacitors are tunable and control the heterogeneity across the oscillators.

The circuit parameters and variables are associated with the dimensionless quantities in Eqs. (6.1)-(6.3) as follows:

$$\tau_i = \frac{C_y^{(i)}}{\bar{C}_y}, \quad k = \eta \frac{R}{r}, \quad \eta = \frac{C_y^{(i)}}{C_x^{(i)}}, \quad \gamma = \frac{C_z^{(i)} R_1 R_3 R_4}{C_y^{(i)} R^2 R_2},$$

$$a = m_1 R, \quad b = m_0 R, \quad x^{(i)} = \frac{v_x^{(i)}}{B_p}, \quad y^{(i)} = \frac{v_y^{(i)}}{B_p}, \quad z^{(i)} = \frac{i_L^{(i)} R}{B_p},$$

where $\bar{C}_y = \frac{1}{N} \sum_{i=1}^N C_y^{(i)}$, m_1 and m_0 are determined by the NR, and B_p depends on both the saturation voltage of the op-amps and the resistors connected to them [122]. The dimensionless time used in Eq. (6.1) is defined as $t' = t/(R\bar{C}_y)$ and, without loss of generality, it follows that the mean time scale is $\bar{\tau} = \frac{1}{N} \sum_{i=1}^N \tau_i \equiv 1$ (this condition is also imposed in our simulations and analysis). Unless noted otherwise, the oscillator

parameters are fixed at $\eta = 10$, $\gamma = 0.056$, $a = -1.44$, and $b = -0.72$, which gives rise to a double-scroll chaotic attractor in the absence of coupling [161]. These parameters are realized in the experiment by setting $R_1 = R_2 = R_3 = 1\text{k}\Omega$, $R = R_4 = 1.8\text{k}\Omega$, $\bar{C}_y = 5.7\mu\text{F}$, $B_p = 1.3\text{V}$, $m_0 = -0.4\text{m}\Omega^{-1}$, and $m_1 = -0.8\text{m}\Omega^{-1}$, and keeping the capacitance ratios as

$$(6.4) \quad C_y^{(i)} = 10C_x^{(i)}, \quad C_z^{(i)} = C_x^{(i)},$$

which ensure the same η and γ values across all oscillators. The capacitors $C_y^{(i)}$, which control the time scales τ_i , are tuned to vary the heterogeneity among the oscillators, and the resistors r are changed to modify the coupling strength k .

6.3. Synchronization emerges from random oscillator heterogeneity

We first analyze in Fig. 6.2(a) the experimental time series of $v_x^{(i)}$ for a directed ring network of five oscillators, where the coupling strength is below the synchronization transition threshold for the identical oscillators. The upper panel confirms that, for homogeneous time scales, the trajectories of the oscillators diverge from each other and the system moves away from the synchronous chaotic state. In the lower panel, we introduce a random perturbation to the time scales, as indicated on the network image. Although the synchronization manifold $\mathbf{x}_1 = \dots = \mathbf{x}_N$ is no longer invariant, the heterogeneous system remains closely synchronized for the duration of the experiment and, collectively, exhibits double-scroll chaotic dynamics comparable to those of the uncoupled oscillators. Figure 6.2(b) shows similar result for a random network with nonuniform indegrees. Once again, for the subcritical coupling strength considered, the synchronization is lost in the homogeneous system but persists in the heterogeneous system.

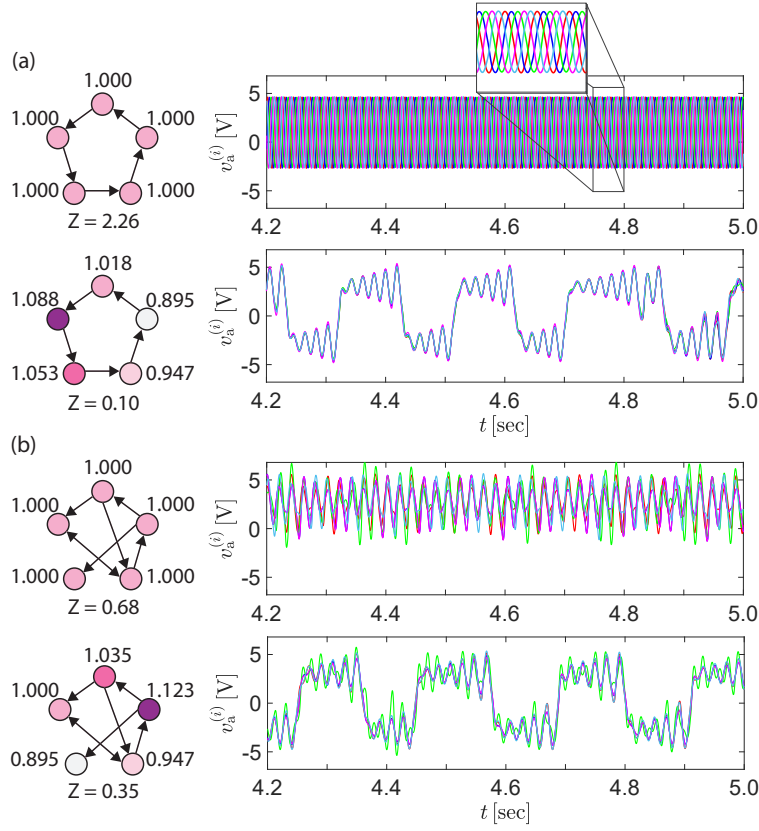


Figure 6.2. Experimental time series of the voltage $v_x^{(i)}$ in two different networks: (a) directed ring for $k = 8.18$ and (b) random network for $k = 5$. Left: network structures, where each node is labeled with the time scale τ_i , and the corresponding synchronization errors Z . Right: time series after the initial transient colored by oscillator for initial conditions close to the synchronous state, showing that chaos synchronization is stable in the heterogeneous system but not in the homogeneous one.

The degree of synchronization in our experiment is further quantified by calculating the synchronization error Z . We first define

$$(6.5) \quad e_{v_x} = \left\langle \sqrt{\frac{1}{N} \sum_{i=1}^N [v_x^{(i)}(t) - \bar{v}_x(t)]^2} \right\rangle,$$

where $\bar{v}_x(t)$ is the average of $v_x^{(i)}(t)$ over the oscillators at time t , and $\langle \cdot \rangle$ denotes the time average over a period of 5 seconds after the initial transient. The synchronization error Z is then calculated as the average of e_{v_x} over the experimental trials (taken to be 5 in Fig. 6.2). In Fig. 6.2(a), for example, the synchronization error for the homogeneous system is $Z = 2.26$, whereas for the heterogeneous system it is $Z = 0.10$.

To explore the effect of random heterogeneity more systematically, we focus on a minimal system of three circuit oscillators. Figure 6.3(a) shows the synchronization error Z in the (τ_1, τ_2) parameter space, for τ_3 satisfying $\tau_3 = 3 - \tau_1 - \tau_2$. The center of the image $(\tau_1, \tau_2, \tau_3) = (1, 1, 1)$ corresponds to the homogeneous system, which is characterized by a large synchronization error. As we move away from the center, regardless of the direction, Z eventually decreases to a value closer to zero. The contours in the figure show the standard deviation σ among the τ_i . We see that in almost all directions Z decreases abruptly when σ becomes larger than 0.05, which indicates that the oscillator heterogeneity consistently promotes chaos synchronization in our system.

To further substantiate these results, we perform numerical simulations for the same network and parameters using the model in Eqs. (6.1)-(6.3). In our experiments, the saturation of the output from the op-amps limits the amplitude of the voltages v_x and v_y . However, because this aspect of the experiment is not explicitly accounted for in the model, desynchronization in the numerical simulations would cause the divergence of the state variables to infinity due to the lack of saturation. Thus, in the numerical results presented in Fig. 6.3(b), we use $P(e_x > 0.5/B_p)$ as the measure of synchronization, which denotes the probability that $e_x \equiv e_{v_x}/B_p$ is larger than $0.5/B_p$ and is calculated based on 36 independent trials for each parameter set. Compared with the experiments,

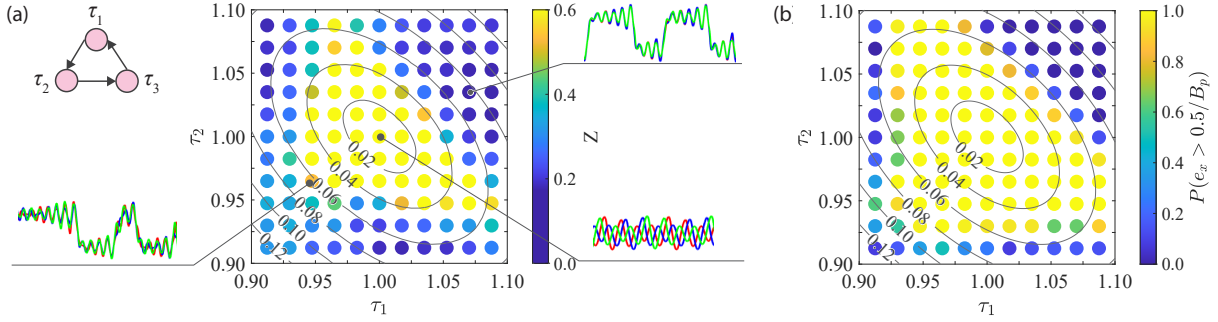


Figure 6.3. Experimental and numerical results for a directed ring network of three oscillators. (a) Synchronization error Z from the experiments, where the contour lines indicate the standard deviation of τ_i . The insets show representative examples of the time series of $v_x^{(i)}$ for the corresponding parameters. (b) Results from numerical simulations, which are in qualitative agreement with the experimental data. Each data point is determined from 10 experimental trials in (a) and 36 simulated trials in (b), each corresponding to a random initial condition. The coupling strength is set to $k = 5$.

our numerical simulations show qualitatively similar transitions to synchronization in all directions of the parameter space (τ_1, τ_2) as the heterogeneity is increased but for a slightly larger value of σ . Given the idealized nature of the model in Eqs. (6.1)-(6.3), the agreement between the experiments and simulations is impressive, and it indicates that the model successfully captures the essence of the experimental system.

Having shown experimentally that random parameter heterogeneity facilitates synchronization, we turn to the analytically tractable case of small mismatches to provide insight into this counter-intuitive observation. To this end, we adapt the extended master stability approach originally developed in Ref. [277], which enables the stability analysis of synchronization in networks of nearly-identical dynamical systems. Equation (6.1) can

be rewritten as,

$$(6.6) \quad \dot{\mathbf{x}}_i = \hat{F}(\mathbf{x}_i, \tau_i) - k \sum_{j=1}^N L_{ij} \hat{H}(\mathbf{x}_j, \tau_i),$$

where $\hat{F}(\mathbf{x}_i, \tau_i) = F(\mathbf{x}_i)/\tau_i$ and $\hat{H}(\mathbf{x}_j, \tau_i) = H(\mathbf{x}_j)/\tau_i$. Assuming that the parameter mismatches $\delta_i = \tau_i - \bar{\tau}$ are small, we can derive an extended master stability function $\Lambda(\alpha, \beta)$ to determine the synchronization stability. The function $\Lambda(\alpha, \beta)$ is the largest Lyapunov exponent of the variational equation

$$(6.7) \quad \dot{\boldsymbol{\xi}} = \left[\mathbf{D}_{\mathbf{x}} \hat{F}(\bar{\mathbf{x}}, \bar{\tau}) - \alpha \mathbf{D}_{\mathbf{x}} \hat{H}(\bar{\mathbf{x}}, \bar{\tau}) \right] \boldsymbol{\xi} + \left[\mathbf{D}_{\tau} \hat{F}(\bar{\mathbf{x}}, \bar{\tau}) - \alpha \mathbf{D}_{\tau} \hat{H}(\bar{\mathbf{x}}, \bar{\tau}) \right] \beta,$$

where \mathbf{D} represents the Jacobian operator and $\bar{\mathbf{x}}$ is the trajectory of a single oscillator with the time scale set to the mean time scale $\bar{\tau}$. Here, $\boldsymbol{\xi}$ is the perturbation mode that corresponds to the eigenvalue λ_i of the modified graph Laplacian $\mathbf{G} = (G_{ij})$ defined by $G_{ij} = L_{ij} - \frac{1}{N} \sum_{i=1}^N L_{ij}$. The parameter $\alpha = k\lambda_i$ is determined by the coupling strength k and the eigenvalue λ_i , and $\beta = \mathbf{w}_i^T \boldsymbol{\delta}$ is the inner product of the parameter mismatch vector $\boldsymbol{\delta} = [\delta_1, \dots, \delta_N]^T$ and the left eigenvector \mathbf{w}_i of \mathbf{G} corresponding to λ_i . Thus, the extended master stability function $\Lambda(\alpha, \beta)$ depends on the coupling strength and network structure encoded in α as well as the oscillator heterogeneity encoded in β .

Figure 6.4 shows $\Lambda(k\lambda, \beta)$ as a function of β for different values of k , and λ corresponding to the most unstable mode of the system in Fig. 6.3. As we increase the heterogeneity, measured as $|\beta|$, the function Λ decreases and reaches a minimum for $|\beta| \geq 0.06$ for all relevant k . This theoretical result confirms that synchronization stability can be improved

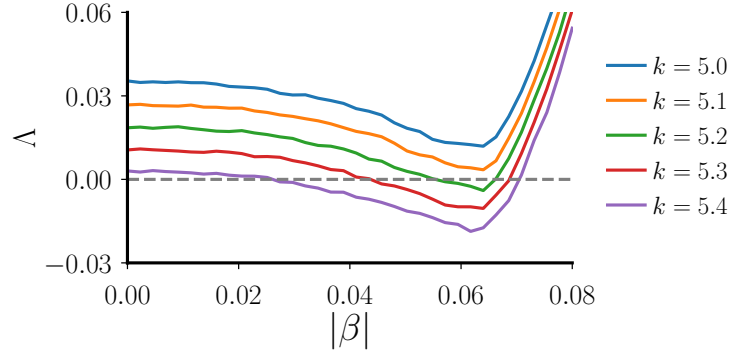


Figure 6.4. Dependence of Λ on $|\beta|$ for the oscillator network considered in Fig. 6.3 and a range of values of the coupling strength k . In all cases, the stability is predicted to improve as heterogeneity is increased from zero, reaching an optimum for intermediate values of $|\beta|$.

by increasing oscillators heterogeneity, in further support of the experimental results in Fig. 6.3.

There are two approximations involved when assessing stability using the formalism above. First, because the analysis is perturbative, the δ_i are assumed to be small. Second, the synchronization trajectory of the heterogeneous oscillators is assumed to be well represented by the trajectory of a single oscillator with $\tau = \bar{\tau}$ (the mean time scale in the network). Because these approximations become increasingly less reliable as heterogeneity increases, the accuracy of the prediction tends to deteriorate for large heterogeneity. For $k = 5$, for example, the experimental system synchronizes for sufficiently large heterogeneity despite the fact that the corresponding Λ calculated using Eq. (6.7) never becomes negative. This result suggests that the predictions generated using the extended master stability function are conservative for our system.

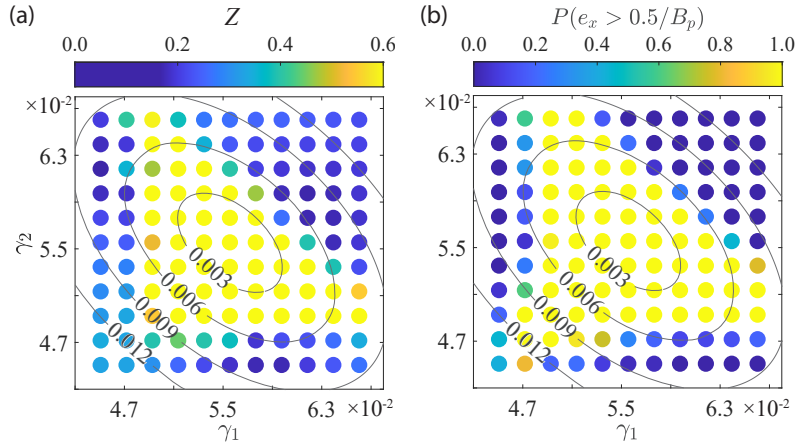


Figure 6.5. Synchronizing effect of heterogeneity in γ_i from (a) experiments and (b) numerical simulations. In each panel, the network, undeclared parameters, and plotted quantities are the same as in Fig. 6.3.

Thus far we have focused on the effect of heterogeneity in the time scales τ_i . While the time scale is a natural parameter to consider, as it allows probing the effect of heterogeneity when the chaotic properties of the dynamics are manifestly preserved, the phenomenon reported here is not limited to τ_i and can also be observed for other parameters. This is illustrated in Fig. 6.5, both experimentally and numerically, where we relax the second condition in Eq. (6.4) to allow the parameter γ to take different values γ_i across different oscillators. The network and parameters are the same as in Fig. 6.3, except that in this case all τ_i are set to 1 and the γ_i are individually varied under the constraint that the average among the oscillators is kept fixed as $\bar{\gamma} = 0.056$. Our numerical simulations indicate that similar results also hold when the parameter η is heterogeneous across oscillators. It follows that generic parameter mismatches can consistently improve synchronization in networks of Chua's oscillators, and we believe the same phenomenon should be observed in other networks of coupled chaotic systems.

6.4. Concluding remarks

For the oscillators and coupling function considered in this study, the stability region is semi-infinite as a function of the coupling strength, which in particular shows that the effect described is not reminiscent of a compromise between short and long wavelength instabilities. For different oscillators and/or coupling functions, the stability region can be finite [217], and for such systems there is a limit on the number of identical oscillators that can remain stably synchronized in specific network configurations, such as ring and star networks. It is a natural question for future research to consider whether systems with a finite stability region can exhibit the effect described here and, if so, whether heterogeneity would allow for a larger number of oscillators to remain stably synchronized in the same network configuration.

Our demonstration that parameter heterogeneity can enable rather than halt synchronization has several implications. In particular, it completes a full circle in revealing the interplay between chaos and coupling interactions. Early work on synchronization between coupled oscillators showed that sufficiently strong coupling can mitigate sensitive dependence on initial conditions. By demonstrating that parameter heterogeneity can enable synchronization below the synchronization transition of identical oscillators, this work shows that even weak coupling can mitigate sensitive dependence on parameter assignment—and thus on initial conditions—and lead to convergence rather than divergence between the trajectories of mismatched systems. Thus, our findings show that oscillator heterogeneity can consistently reduce the effective coupling threshold for synchronization. In man-made systems, this has the important implication that experimental imperfections may become an unexpected source of synchronization stability. In

natural systems that rely on synchronization, it also suggests the possibility of observed mismatches being the result from evolutionary pressure to favor synchronization.

CHAPTER 7

Critical Switching in Globally Attractive Chimeras

We report on a new type of chimera state that attracts almost all initial conditions and exhibits power-law switching behavior in networks of coupled oscillators. Such *switching chimeras* consist of two symmetric configurations, which we refer to as subchimeras, in which one cluster is synchronized and the other is incoherent. Despite each subchimera being linearly stable, switching chimeras are extremely sensitive to noise: Arbitrarily small noise triggers and sustains persistent switching between the two symmetric subchimeras. The average switching frequency scales as a power law with the noise intensity, which is in contrast with the exponential scaling observed in typical stochastic transitions. Rigorous numerical analysis reveals that the power-law switching behavior originates from intermingled basins of attraction associated with the two subchimeras, which, in turn, are induced by chaos and symmetry in the system. The theoretical results are supported by experiments on coupled optoelectronic oscillators, which demonstrate the generality and robustness of switching chimeras.

This chapter is based on the joint work with Zachary G. Nicolaou, Joseph D. Hart, Rajarshi Roy, and Adilson E. Motter. The presentation closely follows Ref. [316].

7.1. Background

The relationship between symmetry and synchronization underlies many recent discoveries in network dynamics. Symmetries influence the possible dynamical patterns in a

network [219, 96] and can either facilitate [187, 197, 311] or inhibit [192, 241, 109] synchronization. A particularly interesting symmetry phenomenon in networks is the coexistence of coherent and incoherent clusters in populations of identically coupled identical oscillators [133, 121]—the so-called chimera states [3]. Since chimeras have less symmetry than the system itself, they represent symmetry-broken states [61] of the network dynamics. Over the years, different forms of chimera states have been discovered [252, 1, 157, 139, 308, 309, 305, 249, 256], which has been accompanied by new results on robustness [104, 285, 159, 39, 287] and existence conditions [202, 251, 17, 158, 185, 201, 22].

Early work on chimera states focused mainly on networks of phase oscillators in the limit of a large system size [210], where dimension reduction is often possible by employing the Ott-Antonsen ansatz [206, 207, 215]. For finite-size systems, some chimera states have been shown to be long transients [304], while others have been shown to be stable [224, 211] using the Watanabe-Strogatz ansatz [296, 160]. Recent research has placed an increased emphasis on chimeras in finite-size networks of chaotic oscillators [199, 200, 250, 106, 59], which are important given the prevalence of chaos in physical systems [44]. In that context, it has been shown that the stability of chimera states can be studied rigorously using cluster synchronization techniques [106, 59].

Even for permanently stable chimeras, an important question is how carefully one has to prepare the initial conditions in order to observe them. Early examples of chimera states required specially prepared initial conditions [3, 1, 156], while more recent examples include chimera states that emerge from a wide range of initial conditions [202, 253, 246, 308, 245, 129]. In the presence of global feedback control, some chimeras have

even been observed to attract almost all initial conditions [48, 258]. However, whether globally attractive chimeras can emerge in the absence of control is still an open problem.

Because of the symmetry-broken nature of chimera states, another important question concerns the coexistence of multiple chimeras [156] and the possibility of transitions between them [148]. When multiple chimeras coexist, adding fluctuation or mismatch terms may induce switching events between them. This phenomenon has been studied under the name of “alternating chimeras” [135, 54, 249]. In previous studies, finite transition barriers must be overcome for transitions between otherwise persistent chimeras to occur. Accordingly, the transition rates are expected to scale exponentially with noise intensity.

Here, we report on switching chimeras, which are chimera states that both exhibit power-law dependence of the switching frequency on noise intensity and attract almost all initial conditions in the absence of control. A switching chimera is comprised of two symmetric metastable states—referred to as subchimeras—between which the switching occurs. The power-law switching dynamics is a signature of critical behavior and stems from a vanishing quasipotential barrier between the two metastable states. It follows that the switching persists indefinitely for any nonzero noise intensity. Strikingly, when the noise intensity is strictly zero, the symmetric subchimeras are linearly stable. Thus, the deterministic dynamics settle into one of the two subchimeras, and, as in the original studies of chimeras, the state symmetry is broken. For any nonzero noise intensity, however, the long-term dynamical symmetry is restored due to the persistent switching between the two subchimeras. This dependence on noise intensity shares similarities with singular limits [36], in that the asymptotic network dynamics are qualitatively different for zero

and small noise. Our analytical and numerical results are further validated by an experimental demonstration of switching chimeras in networks of optoelectronic oscillators. We suggest that switching chimeras can find applications in the study of intermittently alternating dynamics in biological systems and the development of approaches to measure small experimental noise.

The chapter is organized as follows. In Sec. 7.2, we introduce a representative system exhibiting switching chimeras. The power-law dependence between the average switching period and noise intensity is presented in Sec. 7.3.1. This critical switching behavior is then established and explained from various angles in the subsequent subsections. In Sec. 7.3.2, we show that it arises robustly in a first-exit model derived from an extension of the Freidlin-Wentzell theory. In Sec. 7.3.3, we further elucidate the mechanism underlying the switching dynamics by describing the dominant transition paths and the role of invariant saddles. In Sec. 7.3.4, we relate the scaling in the switching dynamics with the existence of transition paths of arbitrarily small action and compare it to critical phenomena in phase transitions. In Sec. 7.3.5, we establish a connection between power-law switching and intermingled basins of attraction. Experiments confirming switching chimeras and their power-law scaling in a network of optoelectronic oscillators are presented in Sec. 7.4. In Sec. 7.5, we discuss connections between switching chimeras and other phenomena in physical and biological systems. Finally, we present our concluding remarks in Sec. 7.6.

7.2. Computational observation of switching chimeras

We consider $2n$ -node networks formed by two rings of n nodes, with nearest-neighbor coupling of strength σ in each ring. The two rings are all-to-all coupled by weaker links

of strength $c\sigma$ for some $0 < c < 1$. In this way, all the nodes are identically coupled, as shown by the network diagram in Fig. 7.1(a). We assume the oscillators are diffusively coupled, so the network can be represented through a Laplacian matrix in the dynamical equation. Adding to each node an uncorrelated Gaussian noise term of zero mean and tunable standard deviation ξ (which we refer to as the noise intensity) and writing down the coupling explicitly, the resulting stochastic dynamical equation for the first ring reads:

$$\begin{aligned}
 (7.1) \quad x_i^{(1)}[t+1] = & \left\{ \underbrace{r f(x_i^{(1)}[t])}_{\text{intrinsic dynamics}} \right. \\
 & + \underbrace{\sigma \left(f(x_{i-1}^{(1)}[t]) + f(x_{i+1}^{(1)}[t]) - 2f(x_i^{(1)}[t]) \right)}_{\text{intracluster coupling}} \\
 & + \underbrace{c\sigma \sum_{j=1}^n \left(f(x_j^{(2)}[t]) - f(x_i^{(1)}[t]) \right)}_{\text{intercluster coupling}} \\
 & \left. + \underbrace{\xi N_i^{(1)}[t]}_{\text{Gaussian noise}} \right\} \bmod 1, \quad 1 \leq i \leq n,
 \end{aligned}$$

where $N_i^{(1)}$ is Gaussian noise with unit standard deviation and the superscripts indicate which ring the variables are associated with. The dynamical equation for the second ring can be expressed similarly. (We note that it is not essential for the dynamics to be discrete; an example of switching chimeras in systems with continuous-time dynamics is presented in Appendix D.1.)

We first assume that the dynamics of each node is governed by a logistic map $f(x) = x(1-x)$. For concreteness, we also set $n = 6$ and $c = 0.2$ unless mentioned otherwise. Using a generalization of the master stability function formalism developed in Ref. [109],

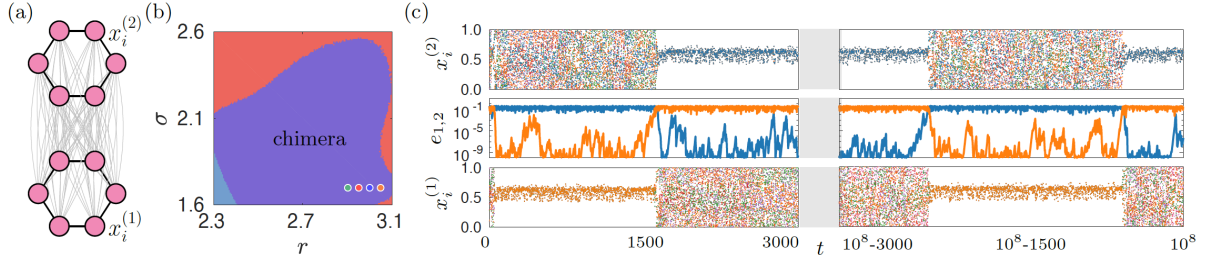


Figure 7.1. Globally attractive chimera state whose coherent and incoherent clusters switch under extremely small noise. (a) Network system, formed by two rings of logistic maps mutually coupled through weaker links [Eq. (7.1)]. (b) Parameter space color coded according to the linear stability of the possible states, namely, whether both rings can synchronize (cyan), only one ring can synchronize (purple), or neither ring can synchronize (red). The four dots mark the parameters used in Fig. 7.2. (c) Direct simulation of the system for $\sigma = 1.7$ and $r = 3.05$ [orange dot in (b)] for noise intensity $\xi = 10^{-10}$, illustrating the dynamics of a switching chimera. The top and bottom panels show the oscillator states in each of the two rings (color coded by oscillator, where single-color segments indicate synchronization), while the center panel shows the synchronization error [defined in Eq. (7.2)] in each ring.

we can calculate the maximum transverse Lyapunov exponent associated with chimera states efficiently (Appendix D.2). In particular, we find parameters under which

- i) the two clusters cannot be simultaneously in stable synchronous states (i.e., any solution satisfying $x_i^{(1)}[t] = s_1[t]$, $x_i^{(2)}[t] = s_2[t]$ for all i is linearly unstable);
- ii) one of the clusters can be in a stable synchronous state if the other cluster is not.

Inside the region where both conditions are satisfied, *coherence is induced by incoherence*, meaning that synchronization in one cluster is stabilized by desynchronization in the other cluster. Figure 7.1(b) shows that the system in Fig. 7.1(a) has a large parameter region (purple) in which these two conditions are satisfied. In that region, chimera states are linearly stable and do not coexist with stable globally synchronized states.

To confirm that the desynchronized ring is indeed in an incoherent state, we run direct simulations⁷ from random initial conditions for 10^8 iterations under noise of intensity $\xi = 10^{-10}$. Figure 7.1(c) shows representative trajectories and associated synchronization errors for $\sigma = 1.7$ and $r = 3.05$. The synchronization error in the j -th cluster is defined as

$$(7.2) \quad e_j := \sqrt{\frac{\sum_{i=1}^n \|x_i^{(j)} - \bar{x}^{(j)}\|^2}{n}},$$

where $\|x\| = \min(|x|, 1 - |x|)$ and $\bar{x}^{(j)}$ is the mean of $x_i^{(j)}$ over all i .

The system exhibits not only chimera dynamics but also persistent transitions in which the coherent and incoherent rings switch roles: As one ring loses synchrony and becomes incoherent, the other ring synchronizes. Moreover, as we show below, the switching observed here is critical—the transition rate depends on the noise intensity as a power law and switching can be triggered by arbitrarily small noise. This power-law dependence distinguishes switching chimeras from previously reported “alternating chimeras,” in which the transitions either are forced by large fluctuation terms [148, 135, 54, 249] or rely on heteroclinic dynamics [112, 37, 94]. In the first case, there are finite barriers separating the different states, while in the second case each state is inherently unstable and switching occurs in the absence of noise.

The persistence of switching chimeras under many transition cycles suggests it is globally attractive. To verify that this is indeed the case, we evolve the system for 10^4 iterations starting from 10^6 different random initial conditions for $\sigma = 1.7$ and

⁷Simulation code available at <https://github.com/y-z-zhang/switching-chimeras>

$r = 2.9, 2.95, 3.0,$ and 3.05 [dots in Fig. 7.1(b)]. In all tests, the oscillators are swiftly attracted to the chimera state and no other attractors are observed.

7.3. Power-law switching

7.3.1. Extreme sensitivity to noise

Next, we present numerical results characterizing the effect of noise intensity ξ on the average switching period \bar{T} . Figure 7.2 shows that, as one approaches the boundary of the chimera region [from the green dot to the orange dot in the bottom right of Fig. 7.1(b)], \bar{T} decreases and switching becomes more frequent. For each fixed value of r , the average switching period increases as the noise intensity decreases, with scaling that follows a power law. It is remarkable that even noise of intensity as small as $\xi = 10^{-15}$ (the resolution limit of computers using double-precision floating-point format) can induce frequent switching.

This switching between the coherent and incoherent clusters does not contradict the fact that synchronization in one cluster is linearly stable if the other cluster is incoherent. This is the case because linear stability analysis assumes the perturbations to be infinitesimally small, whereas finite-size perturbations, no matter how small, can still grow large enough along the unstable portions of a chaotic attractor to disrupt synchrony in the coherent ring and induce switching.

The power-law scaling of the average switching period and, consequently, the extreme noise sensitivity of chimera states, makes the switching behavior observed here “anomalous” in the sense that it appears to contradict the Freidlin-Wentzell theory [81]. According to that theory, for a stochastic system with deterministic dynamics \mathbf{F} and a

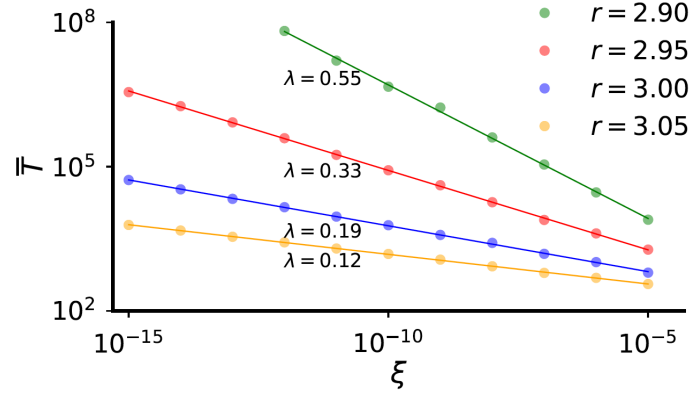


Figure 7.2. Average switching period \bar{T} as a function of the noise intensity ξ for $\sigma = 1.7$ and various values of r [dots in Fig. 7.1(b)]. The switching periods are extracted from long time series of switching chimeras obtained by simulating Eq. (7.1) for different values of ξ . The numbers indicate the scaling exponents and are obtained through least-square fit (slopes of the solid lines).

noise term of intensity ξ ,

$$(7.3) \quad \mathbf{x}[t+1] = \mathbf{F}(\mathbf{x}[t]) + \xi \mathbf{N}[t],$$

the rate of transition from one metastable⁸ state \mathcal{A} to another metastable state \mathcal{B} scales as $\exp(-S_{\mathcal{A} \rightarrow \mathcal{B}}/\xi^2)$, and the first exit time scales as $\exp(S_{\mathcal{A} \rightarrow \mathcal{B}}/\xi^2)$ [297]. Here, $S_{\mathcal{A} \rightarrow \mathcal{B}}$ is the infimum of the Freidlin-Wentzell action among all paths \mathbf{X} connecting state \mathcal{A} to state \mathcal{B} :

$$(7.4) \quad S_{\mathcal{A} \rightarrow \mathcal{B}} := \frac{1}{2} \inf_{\substack{\mathbf{X} \\ \mathbf{X}[0] \in \mathcal{A} \\ \mathbf{X}[m] \in \mathcal{B}}} \sum_{t=0}^{m-1} \|\mathbf{X}[t+1] - \mathbf{F}(\mathbf{X}[t])\|^2.$$

⁸We consider a state to be metastable if it is linearly stable in the absence of noise but only has a finite lifetime when noise is present.

The infimum of the action measures how much one has to work against the deterministic part of the dynamics to induce a transition from \mathcal{A} to \mathcal{B} . This quantity is also known in the literature as a quasipotential barrier [322] and is analogous to a potential barrier for transitions in gradient systems.

7.3.2. First-exit problem in log-error space

Although the power-law scaling observed for switching chimeras and the exponential scaling predicted by the Freidlin-Wentzell theory seem incompatible at first glance, we can establish a connection between them. We first note that the synchronization error inside the coherent ring usually fluctuates close to an error floor determined by the noise intensity, but switching can be triggered by rare events that drive the error all the way to an error ceiling determined by the synchronization error of the incoherent ring [for an example, see the middle panel of Fig. 7.1(c)]. Moreover, since the variational equation acts multiplicatively on the synchronization error (see Appendix D.2), the error naturally evolves on a log scale as long as the linearization around the synchronization manifold is still valid.

Motivated by these observations, we focus on an attribute ϵ , defined as the logarithm of the synchronization error inside the coherent ring:

$$(7.5) \quad \epsilon := \ln(\min\{e_1, e_2\}).$$

As a first approximation, the dynamics of ϵ can be modeled as a biased one-dimensional random walk confined within two boundaries, corresponding to the error floor and the error ceiling. At each step, ϵ has probability p of moving up a fixed distance d_1 and

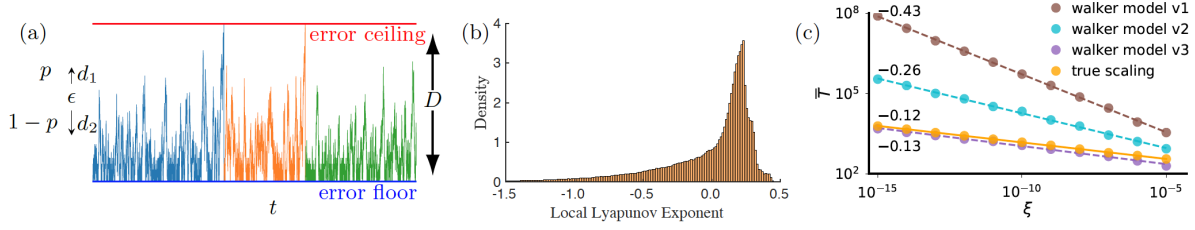


Figure 7.3. Modeling transitions in switching chimeras. (a) Illustration of a random walk model in the log-error space, where a switching event is triggered when the walker reaches the error ceiling. The time series is colored differently after each switching event. (b) Distribution of the local Lyapunov exponents associated with Eq. (7.1) for $\sigma = 1.7$ and $r = 3.05$, which is used to refine the random walk model for the switching chimeras. (c) Power-law scalings predicted by the random walk model and its refined versions (dashed lines). The scaling obtained from direct simulations of Eq. (7.1) is also shown for comparison (solid orange line).

probability $1 - p$ of moving down a distance d_2 . The random walker starts from the error floor, and it never goes below that boundary. Every time ϵ reaches the error ceiling, we consider that a switching event has occurred and reset ϵ to the lower boundary. An illustration of this process can be found in Fig. 7.3(a).

To derive a relation between the average switching period \bar{T} and the interboundary distance D in the random walk model, we note that when $pd_1 < (1 - p)d_2$ and $D \gg d_{1,2}$ this is a first-exit problem. Thus, according to the Freidlin-Wentzell theory,

$$(7.6) \quad \bar{T} \propto \exp(\lambda D),$$

where λ is some constant determined by p , d_1 , and d_2 . Now recall that D is determined by the distance between the error floor and error ceiling. The error floor is given by $\ln(\xi)$, and, without loss of generality, we set the error ceiling to be 1. Thus, $D = \ln(1) - \ln(\xi) =$

$\ln(\xi^{-1})$, and Eq. (7.6) becomes

$$(7.7) \quad \bar{T} \propto \xi^{-\lambda}.$$

This scaling reproduces the power-law relation between the average switching period \bar{T} and the noise intensity ξ observed in Fig. 7.2.

We now turn to a more quantitative analysis to support the idea that the switching events in the original system can be inferred from the one-dimensional attribute ϵ . Starting with the system in Eq. (7.1), we compute the growth rate of the synchronization error in the coherent ring $\epsilon[t+1] - \epsilon[t]$ at each iteration. The distribution of this quantity, which we call the *local* Lyapunov exponent, is shown in Fig. 7.3(b) for $\sigma = 1.7$ and $r = 3.05$. Of all the local Lyapunov exponents sampled, 35% are negative, with a mean of -0.46 ; the remaining 65% of the exponents are positive, with a mean of 0.19 . Because e is a one-dimensional variable, the Lyapunov exponent that determines its asymptotic stability at 0 is given by averaging over the local Lyapunov exponents from $t = 0$ to $t = \infty$. Since $-0.46 \times 0.35 + 0.19 \times 0.65 < 0$, although 65% of the chaotic attractor is repelling, the chimera state is actually linearly stable. From the above information, we can set $p = 0.65$, $d_1 = 0.19$, and $d_2 = 0.46$ in our random walk model and calculate the relation between the average switching period \bar{T} and the noise intensity ξ .

The brown circles in Fig. 7.3(c) indicate how \bar{T} scales with ξ for this random walk model; they follow a well-defined power law, as expected from Eq. (7.7). But it is also clear that a random walk is not a very accurate picture for the dynamics of ϵ , since the predicted average switching periods are much larger than the ones obtained from simulating Eq. (7.1) (orange circles). This discrepancy is partially due to the crude

approximation we made when fixing the step sizes of the random walk to be constants. If we choose the step size as well as the direction of the random walk according to the distribution in Fig. 7.3(b), we observe the scaling indicated by cyan circles in Fig. 7.3(c), which is closer to the true scaling. However, the predicted exponent of -0.26 is not yet close to the true value of -0.12 , which indicates that something is still missing.

The approach we just took is equivalent to shuffling the time series of the local Lyapunov exponents and using the shuffled sequence to generate the random walk. This shuffling preserves the information of the full distribution but ignores temporal correlations. Because the stable and unstable portions of a chaotic attractor are usually not well mixed, the actual evolution of ϵ is a non-Markovian process, and we expect the temporal information to be relevant. This effect tends to correlate the upward movements of ϵ , which, in turn, makes it more likely for ϵ to reach the error ceiling and shortens the average switching period for small noise. When the temporal information is incorporated into the model (by using the original sequence of local Lyapunov exponents rather than randomly sampling them), we arrive at a more realistic model for the switching dynamics, which takes the form of a deterministic walker. The prediction of this refined model (purple circles) is in excellent agreement with the true scaling (orange circles).

It is important to note that the power-law scaling is preserved even after we allow variable step sizes and strong correlation between steps in our model. We thus suggest that Eq. (7.7) is robust and that power-law switching is expected for a general class of systems. Transitions in such systems can be modeled as a first-exit problem in which the distance to the exit increases linearly with the logarithm of the inverse of noise intensity.

7.3.3. Transition pathways

We can gain a deeper understanding of the switching dynamics by investigating the transition paths connecting the two symmetric subchimeras. One natural question concerns whether there is a single pathway or multiple pathways for the switching. If multiple pathways exist, do they intersect at key intermediate states? For the system in Fig. 7.1(a), with $n = 6$, it turns out that there is only one dominant pathway when noise is small. We illustrate the key transitions (T1 to T4) and intermediate states of this pathway in Fig. 7.4. We later analyze an explicit realization of this pathway in Fig. 7.5, which provides strong numerical support for the following transition sequence:

(T1) Starting from one of the subchimeras, the incoherent ring occasionally visits near-synchronized states (referred to as temporary clustering in Fig. 7.4).

(T2) The temporary clustering in the incoherent ring strongly correlates with the instability windows in the coherent ring. This correlation is not surprising, since states with both rings synchronized are unstable. Within those short windows, small noise or perturbations applied to the coherent ring are amplified and lead to a short-wavelength bifurcation. That is, the coherent ring partially desynchronizes and splits into two alternating groups with different dynamics (oscillators in the same group remain synchronized). Reaching this “activated state” is the only stage in which noise is needed, even though it can be arbitrarily small.

(T3, T4) The state between T3 and T4 lives in an invariant subspace induced by the rotational symmetry in each ring. In fact, the state is an invariant saddle and serves as the key intermediate state connecting the two subchimeras. During T3, the system moves along the stable manifold of the invariant saddle, and the six oscillators in the upper ring

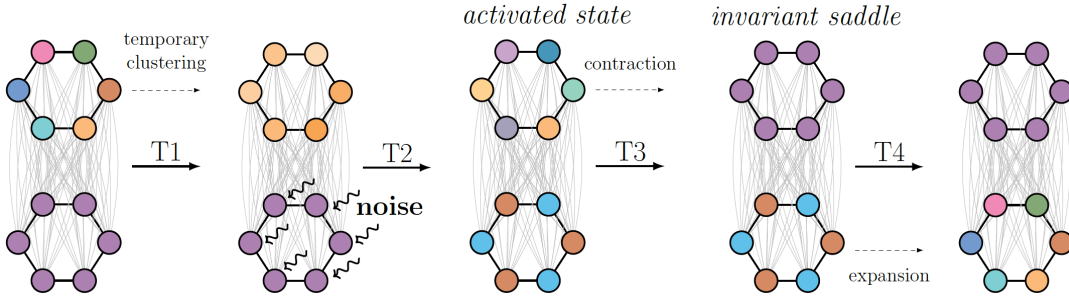


Figure 7.4. Dominant transition pathway between the two symmetric subchimeras, which consists of the intermediary stages T1 to T4. Only T2 requires activation from noise, which can be arbitrarily small but not strictly zero; all other transitions follow directly from the deterministic dynamics of Eq. (7.1). In particular, T3 and T4 follow the stable and unstable manifolds of the invariant saddle, respectively.

converge to a synchronized state. During T4, the system moves away from the saddle following its unstable manifold, where the partially desynchronized state in the lower ring evolves into an incoherent state. The roles of the rings are now reversed, thus concluding the entire sequence of transitions from one subchimera to the other.

The short-wavelength perturbation

$$(7.8) \quad \Delta_{sw}(\delta) = \frac{1}{\sqrt{6}}(\delta, -\delta, \delta, -\delta, \delta, -\delta),$$

where the i -th component of this vector is to be interpreted as a perturbation to the i -th node in the ring, is the dominant instability in the coherent ring according to our linear stability analysis and is the one being excited by noise during transition T2. To further support this claim, we run direct simulations of Eq. (7.1), but with Δ_{sw} filtered out from the noise applied to each ring. This time, for noise intensity $\xi \leq 10^{-9}$, the average switching period \bar{T} becomes independent of ξ and always equals the average switching period induced by round-off errors, as shown in Appendix D.3. These simulations confirm

that the overwhelming majority of the switching events must be initiated through a short-wavelength bifurcation in the coherent ring when noise is small⁹.

To better visualize the subchimeras and the invariant saddles, we project them onto the mean state of each ring: $\bar{x}^{(1)} = \sum x_i^{(1)}/n$ and $\bar{x}^{(2)} = \sum x_i^{(2)}/n$. Figure 7.5(a) shows the projection of the two symmetric subchimeras colored in blue and orange, respectively. We can see the fine structure of the subchimeras under this projection, which is indicative of their fractal nature. In Fig. 7.5(b), we show the projection of the two invariant saddles (red and green).

We now try to explicitly find a least-action path connecting the two subchimeras, which can be challenging even for transitions between fixed points or periodic orbits [297, 322]. In our case, the high dimensionality and the chaotic nature of the subchimeras make the optimization of the transition path extremely difficult when using traditional methods. Fortunately, the mechanism presented in Fig. 7.4 points to an efficient way of finding paths of arbitrarily low action connecting the two subchimeras. We simply wait for the incoherent ring to visit a near-synchronized state and then introduce a one-time perturbation in the form of $\Delta_{sw}(\delta)$ to excite the short-wavelength bifurcation in the coherent ring. If a transition is successfully triggered, the action of the transition path is simply $\frac{1}{2}\delta^2$.

Using this strategy, we can easily find a transition path with action as small as 10^{-28} (i.e., δ around 10^{-14}), which is shown in Fig. 7.5(c) and Fig. 7.5(d) for different projections. The coordinate e'_1 (e'_2) in Fig. 7.5(c) is defined as the sum of the synchronization error

⁹The same result holds for all $n > 2$. A ring network with n nodes has eigenvalues $\lambda_k = 4 \sin^2(k\pi/n)$ and eigenvectors $\boldsymbol{\eta}_k = (1, e^{\frac{2\pi i}{n}k}, e^{\frac{2\pi i}{n}2k}, \dots, e^{\frac{2\pi i}{n}(n-1)k})/\sqrt{n}$. For Eq. (7.1), the leading instability is associated with the largest eigenvalue. This corresponds to $\boldsymbol{\eta}_{n/2} = (1, -1, 1, -1, \dots, 1, -1)/\sqrt{n}$ for n even and to both $\boldsymbol{\eta}_{(n-1)/2}$ and $\boldsymbol{\eta}_{(n+1)/2}$ for n odd.

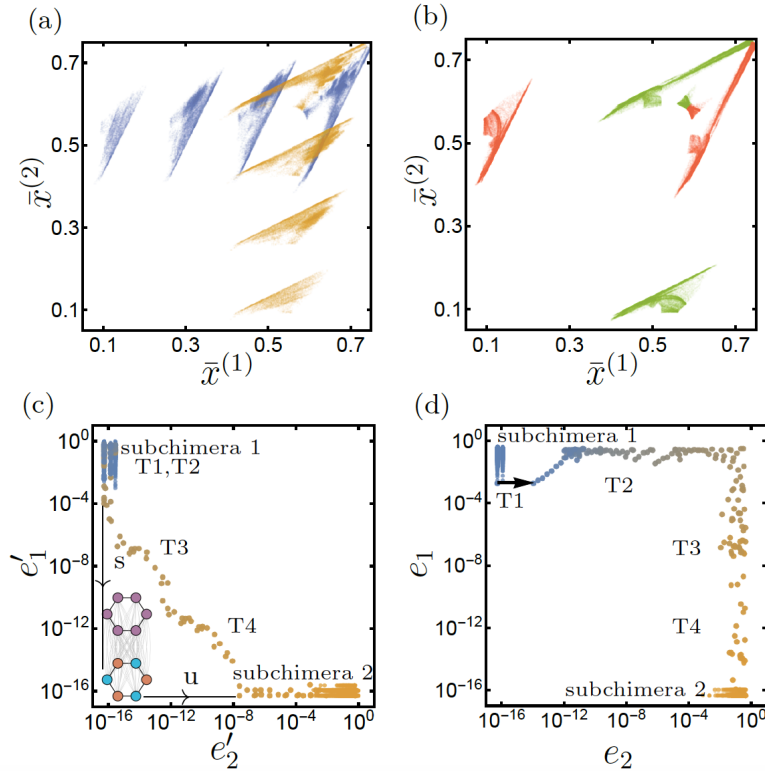


Figure 7.5. Projections of invariant sets and transition paths. (a) Symmetric subchimeras when projected onto the mean state of each ring. Each subchimera is indicated by a different color. (b) Invariant saddle in Fig. 7.4 (and its symmetric counterpart) projected onto the mean state of each ring. (c) Transition path with an action of 10^{-28} projected onto coordinates e'_1 and e'_2 . Under this projection, the invariant saddle is projected onto the lower left corner. The stable and unstable manifolds of the invariant saddle are marked by s and u , respectively. The path starts at the blue subchimera in the upper left corner and ends at the orange subchimera in the lower right corner. (d) Same transition path as in (c) projected onto e_1 and e_2 . The perturbation that initiates the transition is marked by an arrow.

among the odd oscillators and the synchronization error among the even oscillators in the first (second) ring. For this projection, the two subchimeras are found in the upper left and the lower right corners, while the key invariant saddle connecting the two subchimeras is projected onto the lower left corner ($e'_1 = e'_2 = 0$). It is informative to view the

projected transition path in Fig. 7.5(c) in light of the pathway shown in Fig. 7.4: The first two transitions (T1 and T2) correspond to the upper left corner, while the other two transitions (T3 and T4) loop around the lower left corner as they follow the stable and unstable manifolds of the invariant saddle closely. Conversely, the projected path provides strong numerical support for the pathway illustrated in Fig. 7.4. However, the evidence is not yet conclusive, as states with both rings synchronized also project onto the lower left corner for the coordinates in Fig. 7.5(c). Could the two subchimeras be connected by an unstable synchronized state instead of the invariant saddles in Fig. 7.4? The projection to the synchronization errors e_1 and e_2 in Fig. 7.5(d) excludes this possibility, since the path goes through the upper right corner (both rings desynchronized) rather than the lower left corner (each ring synchronized). Multiple transition paths with action ranging from 10^{-30} to 10^{-10} are tested, and they are all qualitatively identical to each other under both projections. This evidence further supports the existence of a dominant transition pathway for the observed switching between subchimeras.

7.3.4. Connections with critical phenomena

The fact that switching can be induced by arbitrarily small noise but not in the absence of noise implies that (i) no matter how small the action of a transition path, we can always find another path with even smaller action, and (ii) there is no zero-action path of finite length connecting the two subchimeras. Thus, a least-action path does not exist in our system. Instead, given an arbitrarily small upper bound on the available action, there are always finite-length transition paths that meet that constraint. It follows that the infimum of the action over all transition paths (i.e., the quasipotential barrier S separating the two

subchimeras) vanishes. In Fig. 7.6(a), we show that the quasipotential barrier does indeed vanish by applying a single perturbation $\Delta_{sw}(\delta)$ to the coherent ring, with δ ranging from 10^{-5} to 10^{-15} . The distribution of the number of times a transition path is found through this procedure shows that the landscape is highly nontrivial for paths of small action: Transition barriers of all heights exist, and the height distribution follows a power law. This claim is further supported by Fig. 7.6(b), where we show the action for 1000 different transition paths, each obtained by applying $\Delta_{sw}(\delta)$ at a different time t (the same initial condition is used for all simulations). One can see that the landscape varies wildly and the associated action spans many decades. As we include more transition paths, deeper and deeper valleys can be found, bringing the smallest action ever closer to zero.

The power-law distribution of barrier heights, in turn, gives rise to the power-law scaling of the average switching periods shown in Fig. 7.2. This relationship follows because the only transition paths that matter are the ones with action comparable to the square of noise intensity. Although there are many more higher-action paths, the probability of crossing those barriers is exponentially smaller. The argument is further supported by the scaling exponents in Figs. 7.2 and 7.6, which differ only by a negative sign.

There are intriguing parallels between what we find here and critical phenomena in second-order phase transitions [269, 268]. For instance, in site percolation models, the correlation (which quantifies the likelihood of two sites being connected) decays exponentially with distance when the occupation probability is $p < p_c$, but the decay changes to a power law at the critical point $p = p_c$. Here, the average switching period scales exponentially with the inverse square of noise intensity, ξ^{-2} , when the quasipotential barrier

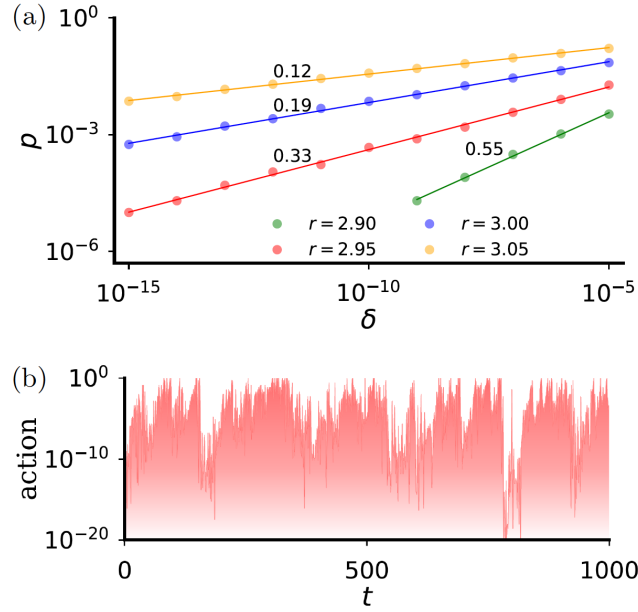


Figure 7.6. Action profile for transition paths. (a) Probability p of finding small-action transition paths by introducing a short-wavelength perturbation of magnitude δ in a single iteration. The simulations are performed for $\xi = 0$ and the other parameters are the same as in Fig. 7.2. Paths with arbitrarily small action exist but small-action paths become increasingly more difficult to find as the available action is decreased, resulting in power-law relationships between the probability p and the perturbation size δ . Notice that the scaling exponents here match those in Fig. 7.2. (b) Minimum action ($\frac{1}{2}\delta^2$) needed to induce a transition by applying $\Delta_{sw}(\delta)$ at a given time t , for $\xi = 0$, $\sigma = 1.7$, and $r = 2.95$. This highly structured profile can be regarded as a visualization of the transition-barrier landscape for switching chimeras.

has $S > 0$, but it is replaced by a power law when $S = 0$. There are finite barriers of all heights between the two subchimeras when $S = 0$; similarly, in percolation, there are finite clusters of all sizes at the critical point $p = p_c$. The power laws uncovered here, however, are more robust than those from the percolation theory. The latter happens only at the critical point and requires fine-tuning, whereas here the power-law switching persists for a wide range of parameters. In this sense, the analogy is perhaps closer with

self-organized criticality [20, 21, 71], in which scale-invariance emerges in the absence of fine-tuning.

7.3.5. Intermingled basins

By now, we have explained the “anomalous” power-law switching behavior from a first-exit model in log-error space (Sec. 7.3.2) as well as by characterizing the action landscape of transition paths (Sec. 7.3.4). In those characterizations, one can catch glimpses of chaos lurking in the background, but its exact role is still unclear. In this section, we establish a direct connection between power-law switching and riddled basins [8, 209, 208, 113, 205, 15, 152, 7, 242], which is possible only for chaotic attractors [16], thus bringing the fundamental importance of the chaotic dynamics to the forefront.

Chaos has long been known to produce power laws by generating fractal structures in state space [204]. For example, in the presence of fractal basin boundaries, a small uncertainty ε in the initial conditions translates to an uncertainty of $A\varepsilon^\alpha$ percent on the final states, where prefactor A is a constant and α is the uncertainty exponent given by the difference between the state-space dimension and the box-counting dimension of the basin boundary [167]. In the case of riddled basins, the entire basin is its own (fractal) boundary and $\alpha = 0$. This means that, for any ε , the ε -neighborhood of an arbitrary point in a riddled basin will always include points that are in the basin of some other attractor [204].

In Fig. 7.7, we show a two-dimensional section of the twelve-dimensional state space to visually illustrate that the attraction basin of each subchimera is riddled. Because the two basins are mutually riddled, they are referred to as *intermingled basins*. In this

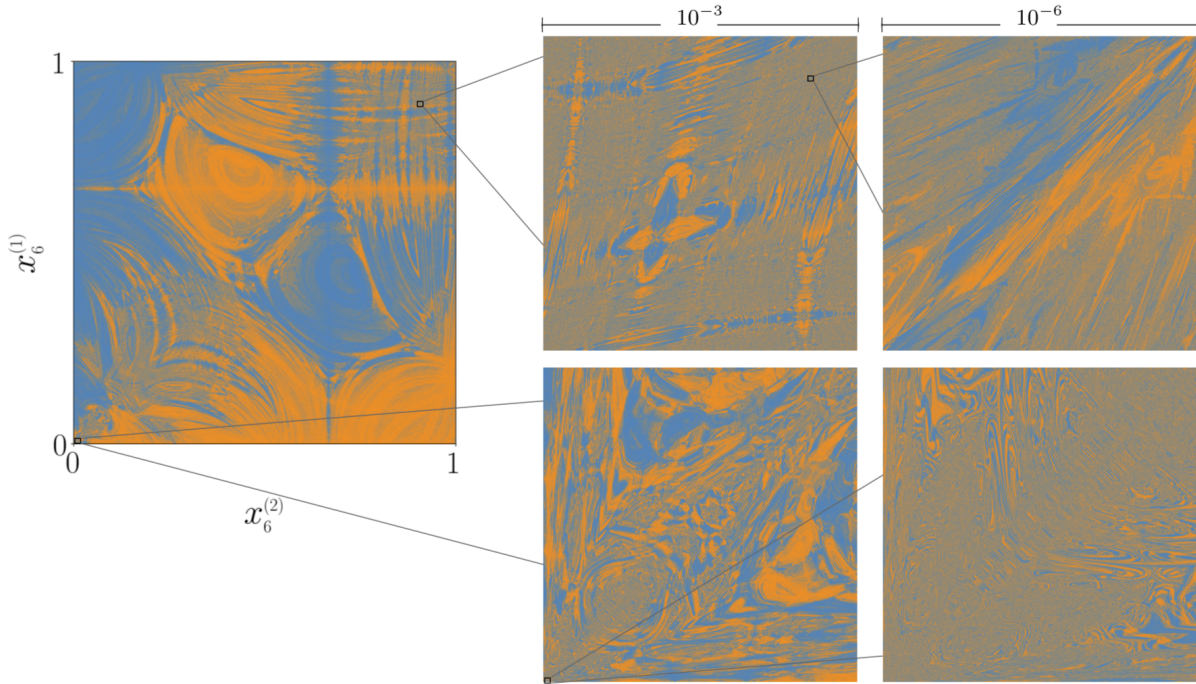


Figure 7.7. Two-dimensional section of the state space showing intermingled basins of the two subchimera. The two basins, shown in blue and orange, are fat fractals [204] intermingled with each other everywhere. Orange points are attracted to the subchimera where the first ring is synchronized, and the blue ones converge to the subchimera with the second ring synchronized. There is a symmetry between the two basins with respect to reflections across the diagonal, which originates from the reflection symmetry of the network. The areas marked for magnification are intentionally oversized to facilitate visualization. The choice of state-space section and system parameters are specified in the text.

figure, the initial conditions for $x_6^{(1)}$ and $x_6^{(2)}$ are sampled independently from the interval $[0, 1]$, while the initial conditions for the other oscillators are specified as $x_i^{(1)} = x_6^{(1)}/2$ and $x_i^{(2)} = x_6^{(2)}/2$, where $1 \leq i \leq 5$. We then simulate Eq. (7.1) for $\sigma = 1.7$ and $r = 2.95$ in the absence of noise and record the subchimera attractor each trajectory is attracted to. (There is nothing special about the choice of the parameters or the section of the state space, since other choices lead to similar results.) One can observe intricate fractal-like

structures in all parts of the two-dimensional section, for all resolutions considered (up to pixels of size $10^{-10} \times 10^{-10}$). There is also a symmetry between the two basins. If an initial condition is in the basin of one subchimera, then its mirror image reflected along the diagonal line must be in the basin of the other subchimera [i.e., if $(x_6^{(1)}, x_6^{(2)}) = (a, b)$ is blue, then $(x_6^{(1)}, x_6^{(2)}) = (b, a)$ is orange]. This is the result of the reflection symmetry between the two rings in Fig. 7.1(a).

Because the basins are intermingled, the basin of one subchimera has points arbitrarily close to the other subchimera attractor, and vice versa, which gives rise to arbitrarily small transition barriers in Fig. 7.6. Thus, the subchimeras are attractors in the sense of Milnor [172] (i.e., attracts initial conditions of nonzero measure) but not in the sense of attracting an open neighborhood of initial conditions containing the attractor.

Apart from the Freidlin-Wentzell action, the perturbation magnitude δ in Fig. 7.6 can also be interpreted as a distance from the closest subchimera attractor. The probability p then measures the fraction of the state space that converges to the opposite subchimera when at distance δ from the subchimera attractor. As the initial conditions are taken further away from one subchimera, it becomes more likely for the system to land in the basin of the other subchimera. Conversely, as $\delta \rightarrow 0$, the probability of escaping to the opposite subchimera approaches zero algebraically. This property is visualized using a transverse section of the intermingled basins that directly connects the two subchimera attractors, as shown in Appendix D.4.

Although arbitrarily small perturbations can drive the system out of a subchimera attractor, both subchimeras are transversally stable according to linear stability analysis. While seemingly incompatible, these two conditions can coexist when an attractor is

transversally stable for the natural measure but unstable for some other invariant ergodic measure. In fact, transversal stability for the natural measure and instability for at least one other invariant ergodic measure are necessary conditions for riddled basins to occur [16]. This mathematical statement is, in its core, similar to the intuitive explanation given in Sec. 7.3.1 on why a system can be driven away from a linearly stable state by arbitrarily small perturbations.

7.4. Experimental observation of switching chimeras

Thus far, we have focused on the theoretical analysis of networks of logistic maps, which reveals remarkable features of a new chimera state, including intermingled basins and switching triggered by arbitrarily small noise. To demonstrate that the theoretical results can be observed under realistic conditions and for different oscillator dynamics, we perform experiments on networks of coupled optoelectronic oscillators. As we show next, our experiments confirm the existence of switching chimeras in physical systems.

The experimental setup is schematically shown in Fig. 7.8(a). A single optoelectronic oscillator draws nonlinearity from a Mach-Zehnder modulator, which takes voltage x as an input and outputs light of intensity $\sin^2(x + \phi)$. The operation point ϕ is fixed at $\pi/4$ throughout the experiments. Time multiplexing and delays are used to realize multiple oscillators from a single time-delayed feedback loop, which reduces apparatus costs and allows for the realization of a large number of truly identical oscillators. The oscillators are coupled together by a digital filter implemented electronically on a field-programmable gate array (FPGA) according to a predetermined Laplacian matrix $\mathbf{L} = \{L_{ij}\}$. In this

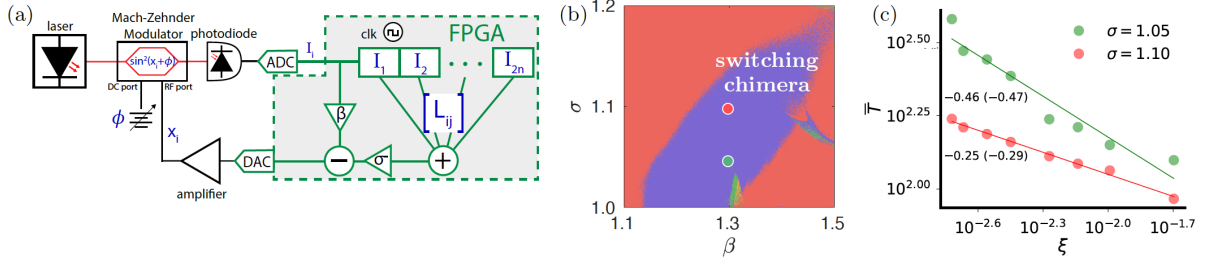


Figure 7.8. Experimental realization of globally attractive switching chimeras. (a) Schematic diagram of the optoelectronic system, where the dashed box depicts our implementation of the coupling scheme. (b) Parameter space color coded according to direct simulations of Eq. (7.9). The regions shown include switching chimeras (purple), nonswitching chimeras (green), chimera death [309] (yellow), and incoherence (red). (c) Experimentally measured average switching period \bar{T} as a function of the noise intensity ξ for $\beta = 1.3$ and two values of σ [dots in (b)]. The scaling exponents annotated on the figure are obtained through linear least-square fitting applied to the relationship between $\log(\bar{T})$ and $\log(\xi)$. The exponents obtained from experiments are in good agreement with those predicted from simulations (shown in parentheses).

case, \mathbf{L} describes the two-cluster network shown in Fig. 7.1(a). Further details of the optoelectronic system can be found in Refs. [108, 107].

The main source of intrinsic noise comes from the measurement of light intensity, including the noise introduced by the analog-to-digital converter (ADC) due to its finite resolution. To best model the experimental system, we introduce independent Gaussian noise to the oscillators at each iteration: $I(x_i^{(1,2)}[t]) = \sin^2(x_i^{(1,2)}[t] + \phi) + \xi N_i^{(1,2)}[t]$. The dynamical equation describing the optoelectronic oscillator network can then be written

as

$$\begin{aligned}
 (7.9) \quad x_i^{(1,2)}[t+1] &= \beta I(x_i^{(1,2)}[t]) \\
 &+ \sigma \left(I(x_{i-1}^{(1,2)}[t]) + I(x_{i+1}^{(1,2)}[t]) - 2I(x_i^{(1,2)}[t]) \right) \\
 &+ c\sigma \sum_{j=1}^n \left(I(x_j^{(2,1)}[t]) - I(x_i^{(1,2)}[t]) \right),
 \end{aligned}$$

where the noise term is implicitly included in I . In our experiments, we again set $c = 0.2$ and $n = 6$.

We first sweep the parameter space of feedback strength β and coupling strength σ using direct simulations of Eq. (7.9). As shown in Fig. 7.8(b), switching chimeras are predicted to occupy a significant portion of this space. Inside the switching chimera region (purple), the red and green dots denote the parameters to be systematically investigated in the experiments.

The dynamics exhibited by the experimental system is in many ways qualitatively similar to that of coupled logistic maps. In particular, a clear pattern of irregular switching between two subchimeras is observed for suitable parameters, as shown in Fig. 7.9(b). To characterize the experimental dynamics quantitatively, we first test whether the power-law relationship between the average switching time \bar{T} and noise intensity ξ holds in the experimental data. An important step in the data analysis is to estimate the level of the intrinsic experimental noise, which we do by simulating Eq. (7.9) under different ξ to extract \bar{T} for a range of noise intensities. The simulation results are then compared with the \bar{T} observed in the experiments. For both parameter sets ($\beta = 1.3$, $\sigma = 1.05$ and $\beta = 1.3$, $\sigma = 1.1$), the simulations with noise intensity 0.0019 agree best with the experiments. We thus choose Gaussian noise of intensity ξ_1 to approximate the base-noise

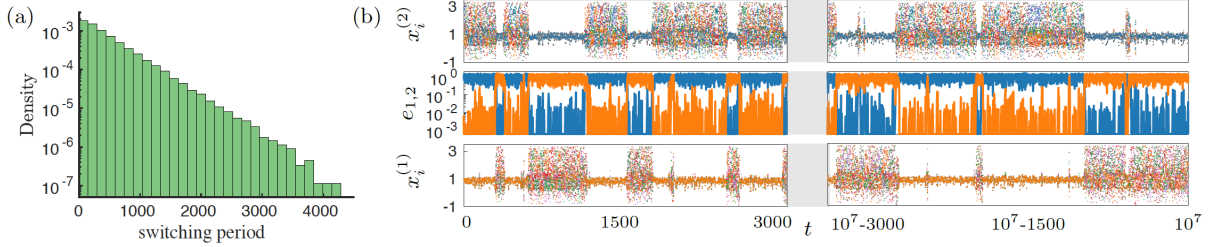


Figure 7.9. Statistics and dynamics of a switching chimera in the experiments. (a) Distribution of switching periods for $\beta = 1.3$ and $\sigma = 1.05$ [green dot in Fig. 7.8(b)]. (b) Portion of the experimentally measured time series used to generate (a). These measurements are performed at the base-noise level of the system, which is estimated to be 0.0019.

level intrinsic to the experimental system. It is worth noting that this technique can, in principle, be extended to estimate the level of intrinsic noise in other oscillators, even when the noise is extremely small—an outstanding problem for which, to the best of our knowledge, no general approach currently exists.

To implement variable noise in the experiments, we introduce an additional Gaussian noise term of tunable intensity ξ_2 via the FPGA. Assuming that the intrinsic and external noise terms are independent, the experimental system is effectively subject to a Gaussian noise of intensity $\xi = \sqrt{\xi_1^2 + \xi_2^2}$. Figure 7.8(c) summarizes the experimentally measured \bar{T} for different ξ from the lower bound 0.0019 all the way to 0.02. Each data point is averaged over at least 20000 experimentally observed switching events. It can be seen that the power-law relationship holds under realistic noise levels and is robust against the imperfections typical of an experimental system. In addition, we also perform systematic simulations to further confirm that the power-law scaling persists in the presence of a small amount of heterogeneity among the oscillators (Appendix D.5).

Figure 7.9(a) shows the distribution of the switching periods T extracted from 45000 switching events, for data collected from multiple experimental runs with $\beta = 1.3$, $\sigma = 1.05$, and $\xi_2 = 0$. The distribution of periods is clearly exponential. This is a consequence of the fact that, although the evolution of the synchronization errors e_1 and e_2 is non-Markovian (Sec. 7.3.2), the switching events themselves are described by a Poisson process. In particular, the experimental data show that the waiting period until the next switching event is independent of the previous switching events. For such a memoryless process with a constant transition rate, the time between switching events is guaranteed to be exponentially distributed [240].

Our experimental results are further visualized using an animated spatiotemporal representation of the time-series data presented in Fig. 7.9(b) (Appendix D.6). As in the case of coupled logistic maps, the underlying state-space structure giving rise to this dynamics is the intermingled nature of the attraction basins. Indeed, direct simulations of Eq. (7.9) confirm that the basins of the two symmetric subchimeras are intermingled (Appendix D.7).

7.5. Connections with biological and other physical systems

A switching chimera can be seen as a chimera state whose symmetry is not broken when considering the long-term dynamics—asymptotically, one cannot distinguish between the behavior of the two clusters. With this observation in mind, we can establish an intriguing parallel between the switching chimera and the symmetry-breaking phenomenon of dipole inversion [11]. Many small molecules, such as ammonia, have more than one (symmetry-broken) ground state with nonvanishing dipole moments. However, due to quantum

tunneling, an ammonia molecule switches rapidly between its two ground states, canceling out the opposite dipole moments and restoring the broken symmetry. The same can be stated for switching chimeras, since each of the two symmetric subchimeras has a broken parity symmetry but the switching between them restores that symmetry. For larger and heavier molecules, such as sugars or phosphorus trifluoride, dipole inversion is no longer likely to be excited by quantum tunneling or even thermal fluctuations, and, thus, the symmetry is spontaneously broken and nonvanishing dipole moments persist. We observe that the tendency for transitioning between subchimeras also decreases in larger systems, with the average switching period growing exponentially as the number of nodes is increased (Appendix D.8).

It is instructive to notice that an exponential dependence of the average switching period on system size is also observed for the magnetized states in the Ising model for any nonzero temperature below the critical point [123, 140]. However, because there is a finite energy barrier to overcome for transitions between the magnetized states, the dependence of the average switching period on the inverse temperature (the analog of the inverse square of noise intensity in our systems) is not power law but instead exponential.

Switching between symmetry-broken states are not limited to physical systems. In particular, switching chimeras may have implications for aperiodic lateral switching in biological systems, of which interhemispheric switching in songbirds during vocal production is an example [293]. Other examples of lateral switching include alternating eye movement in chameleons and fish [223], switching in neural activity inside the two sinuses of leech hearts [271], and unihemispheric sleep in dolphins, birds, and other animals [230, 164]. A common aspect of these various processes is that they involve alternations

in the activity between two approximately symmetrical lateral sides. Despite previous progress [247], the underlying mechanism of lateral switching remains elusive. This is especially the case for aperiodic lateral switching, since such cases cannot be easily modeled by hypothesizing the existence of a central pattern generator or propagating wave dynamics, as in previous alternating chimeras [148, 112, 37]. In the case of the songbird zebra finches, for instance, the interhemispheric switching between song-control areas of the brain is highly irregular, characterized by switching intervals ranging from 4 to 150 ms [293]. Switching chimeras offer a simple mechanism by which a wide range of switching intervals can emerge naturally, and, thus, suggest the possibility that aperiodic lateral switching could be generated spontaneously (as opposed to, for example, being forced by neurotransmitter release [138]).

7.6. Concluding remarks

The theoretical, computational, and experimental results presented here offer a comprehensive characterization of a novel class of chimera states that are globally attractive and exhibit power-law switching dynamics. We extended the Freidlin-Wentzell theory to derive the observed power-law scaling, and we demonstrated that there is no finite quasipotential barrier separating the two symmetric subchimeras. This unexpected scaling behavior, which should be contrasted with the exponential scaling observed for typical noise-induced transitions [105, 47], was confirmed under realistic conditions in our experiments using networks of optoelectronic oscillators. We also established a connection between switching chimeras and intermingled basins, which provides insight into both

phenomena. In particular, the latter explains why switching between subchimeras occurs for arbitrarily small noise despite each subchimera being linearly stable.

We expect switching chimeras to be a common phenomenon in multilayer networks with symmetry. These networks are generalizations of the two-layer networks considered in Ref. [1]. In particular, switching between symmetric subchimeras is expected to be possible for networks formed by any number of identically coupled identical layers, where the layers themselves can have an arbitrary structure. Thus, while we focused on networks with two subchimeras, our analysis extends naturally to other states and to a larger number of switching configurations. From the dynamical perspective, we point to the following conditions for the emergence of power-law switching behavior: (i) There are two or more attractors and they are embedded in manifolds of dimension lower than that of the state space; (ii) each attractor is chaotic and has transversally unstable periodic orbits embedded within. If the transitions are not restricted to chimera states, the requirement on the network structure can be further relaxed, as these conditions are often satisfied even by single-layer oscillator networks.

Finally, we note that the observed high noise sensitivity of the switching dynamics has far-reaching implications. It can be exploited, for instance, to detect small intrinsic noise in oscillator systems—e.g., by using time multiplexing to create a network of such systems that exhibits power-law switching. It also offers a potential explanation for irregular switching noticed in biological systems, which suggests that the dynamical behavior described here may be observed in naturally evolved processes.

CHAPTER 8

Mechanism for Strong Chimeras

Chimera states have attracted significant attention as symmetry-broken states exhibiting the unexpected coexistence of coherence and incoherence. Despite the valuable insights gained from analyzing specific systems, an understanding of the general physical mechanism underlying the emergence of chimeras is still lacking. Here, we show that stable chimeras can arise because coherence in part of the system is sustained by incoherence in the rest of the system. This mechanism may be regarded as a deterministic analog of the phenomenon of noise-induced synchronization and is shown to underlie a broad class of *strong* chimeras, which are chimera states with identically synchronized coherence as a defining property. Recognizing this mechanism offers a new meaning to the interpretation that chimeras are a natural link between coherence and incoherence.

This chapter is based on the joint work with Adilson E. Motter.

8.1. Background

Chimera states are a remarkable phenomenon in which coherence and incoherence coexist in a system of identically-coupled identical oscillators [210, 201]. Initially regarded as a state that requires specific nonlocal coupling structure [133, 3] and/or specially prepared initial conditions [1, 156], chimeras have since been shown to be a general phenomenon that can occur robustly as a system (upon parameter changes) transitions from coherence to incoherence [202, 48, 104, 253, 246, 158, 39]. Despite numerous efforts

to elucidate the underlying principles [159, 251, 308, 250, 245, 249, 185, 129], including irregular forcing in globally-coupled Kuramoto-Sakaguchi oscillators with delayed self-feedback [308], currently no system-independent mechanistic explanation exists that can provide broad physical insight into the emergence of chimeras.

Our goal is to bridge this gap by proposing a general mechanism for chimeras that is not tied to specific node dynamics, network structure, or coupling scheme. We consider the important class of *permanently stable* chimera states whose coherent part is *identically* synchronized, which have been observed for both periodic [308, 246, 211] and chaotic oscillators [106, 59, 316]. We also focus on parameter regions where global coherence is *unstable*, so the chimeras may be observed without the need of specially prepared initial conditions [202, 258, 308, 246, 245, 129, 59, 316]. Here, chimera states that i) are permanently stable, ii) exhibit identically synchronized coherence, and iii) do not co-occur with stable global synchronization are referred to as *strong* chimeras.

In this chapter, we characterize strong chimeras that emerge between a globally synchronized state and a globally incoherent state as a bifurcation parameter is varied (Fig. 8.1). In such chimera states, the coexistence of a synchronous and an incoherent cluster challenges the intuition that inputs from the incoherent cluster would inevitably desynchronize the other cluster. Yet, our analysis shows that incoherence in part of the system in fact stabilizes the otherwise unstable coherence in the rest of the system, thus preventing a direct transition from coherence to incoherence when the former becomes unstable. This incoherence-stabilized coherence effect can be seen as a deterministic analog of synchronization induced by common noise [321, 93, 179, 226] and serves as a general mechanism giving rise to strong chimeras.

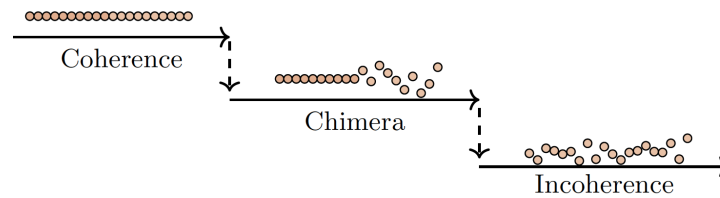


Figure 8.1. Example scenario considered in this chapter. As a bifurcation parameter is varied and the system transitions from coherence to incoherence, an intermediate chimera region emerges.

We first note that strong chimeras can be observed for both periodic and chaotic node dynamics, and in networks with either diffusive or non-diffusive coupling. In all cases, the necessary and sufficient condition for the coherent cluster to admit an identical synchronization solution is that each of its oscillators receives the same input from the incoherent cluster. This condition translates generically to the coherent cluster belonging to an equitable partition and not being intertwined with the rest of the network, although intertwined clusters are still allowed elsewhere in the network. (For diffusive coupling, the partition can be further relaxed to be *externally* equitable [244].) This structure allows the oscillators in the coherent cluster to synchronize identically regardless of the state in the rest of the network, but such a synchronous state may be unstable. A strong chimera will emerge if synchronization in the coherent cluster can be stable while synchronization in the rest of the network is necessarily unstable. This characterization of strong chimeras is not limited to networks of a particular structure and extends immediately to chimera states consisting of multiple coherent and incoherent clusters as well as to generalized chimeras on arbitrary networks [210].

8.2. Incoherence-stabilized coherence

The impact of the rest of the network on the coherent cluster of a strong chimera can be analyzed by considering a network of N coupled oscillators described by

$$(8.1) \quad x_i^{t+1} = \beta f(x_i^t) + K \sum_{j=1}^N M_{ij} h(x_j^t), \quad i = 1, \dots, N,$$

where x_i^t is the state of the i -th oscillator at time t , function f governs the dynamics of the uncoupled oscillators, β denotes the self-feedback strength of the oscillators, $\mathbf{M} = (M_{ij})$ is the coupling matrix representing the network structure, h is the coupling function, and K is the overall coupling strength. We assume the oscillators to be time-discrete and one-dimensional for simplicity, but the analysis extends straightforwardly to continuous-time and high-dimensional systems. The matrix \mathbf{M} can be rather general, including both diffusive and non-diffusive coupling schemes. Now, suppose that C is the coherent cluster and that it consists of n nodes numbered from 1 to n . For oscillators in this cluster, the dynamical equation takes the form

$$(8.2) \quad x_i^{t+1} = \beta f(x_i^t) + K \sum_{j=1}^n M_{ij} h(x_j^t) + I(t), \quad i = 1, \dots, n,$$

where $I(t) = K \sum_{j=n+1}^N M_{ij} h(x_j^t)$ is the input from the rest of the network, which does not depend on i since the cluster must belong to a partition that is at least externally equitable. Thus, the function $I(t)$ is common across all nodes in C and the identical synchronization state s^t in this cluster is given by

$$(8.3) \quad s^{t+1} = \beta f(s^t) + K \mu h(s^t) + I(t),$$

where $\mu = \sum_{j=1}^n M_{ij}$ is a constant not depending on i for any $1 \leq i \leq n$. The stability of this state is determined by the largest transverse Lyapunov exponent (LTLE) Λ specified by the variational equations

$$(8.4) \quad \eta_i^{t+1} = \left[\beta f'(s^t) + K \widehat{\lambda}_i h'(s^t) \right] \eta_i^t, \quad i = 2, \dots, n,$$

where $\widehat{\lambda}_i$ is the i -th eigenvalue of the $n \times n$ sub-coupling matrix $\widehat{\mathbf{M}} = (M_{ij})_{1 \leq i, j \leq n}$ and η_i is the corresponding perturbation mode. The mode associated with $\widehat{\lambda}_1 = \mu$ is excluded as it corresponds to perturbations parallel to the synchronization manifold. Equation (8.4) implicitly assumes that $\widehat{\mathbf{M}}$ is diagonalizable, but this assumption can be lifted using the Jordan canonical form of this matrix [189, 109], and all conclusions extend immediately to all cases.

We explicitly examine the two most widely studied coupling schemes, namely diffusive coupling defined by the Laplacian matrix \mathbf{L} and non-diffusive coupling defined by adjacency matrix \mathbf{A} . For Laplacian coupling, $\mathbf{M} = -\mathbf{L}$ and thus μ is the negative of the indegree of nodes in C due to connections from the rest of the network. The eigenvalue $\widehat{\lambda}_i$ is given by $\widehat{\lambda}_i = -\lambda_i + \mu$, where λ_i is the eigenvalue of the Laplacian matrix of C in isolation (i.e., consisting of intracluster connections only). For adjacency-matrix coupling, $\mathbf{M} = \mathbf{A}$, the factor μ is the indegree of nodes in C when the cluster is considered in isolation, and the eigenvalues are $\widehat{\lambda}_i = \lambda_i$, where λ_i are the eigenvalues of the adjacency matrix of C in isolation.

We first consider Laplacian coupling and, for concreteness, focus on networks composed of two *identical* clusters with all-to-all intercluster coupling. These networks are known to exhibit chimera states, which have been extensively studied in the literature

[1, 285, 159, 211]. Assume that as a bifurcation parameter q is increased, the coherent state of a two-cluster network becomes unstable at a critical value q_c . Because this point marks the end of coherence, at least one cluster must become incoherent when q is further increased. Since both clusters are identical, one might expect that both will become unstable at q_c and that the system will thus transition directly from coherence (both clusters synchronized) into incoherence (both clusters incoherent). That is, due to the symmetry between the two clusters, both clusters are expected to lose synchrony at the same time. Nevertheless, chimera states often emerge right at the instability transition, breaking the symmetry between the clusters, with only one cluster becoming incoherent while the other remains perfectly synchronized. So, what prevents the system from evolving directly into global incoherence? The short answer is that, beyond q_c , incoherence in one cluster stabilizes synchronization in the other cluster, delaying the onset of global incoherence and instead giving rise to a chimera.

To further investigate this question, we focus on the node dynamics and coupling function given by

$$(8.5) \quad f(x) = h(x) = \sin^2(x + \pi/4),$$

which model optoelectronic oscillators that have been realized in synchronization experiments [108, 316]. While the intracluster coupling structure can be arbitrary in general, for clarity we focus on a network consisting of two ring clusters of $n = 3$ nodes. The clusters have internal coupling of strength K and are connected to each other by all-to-all

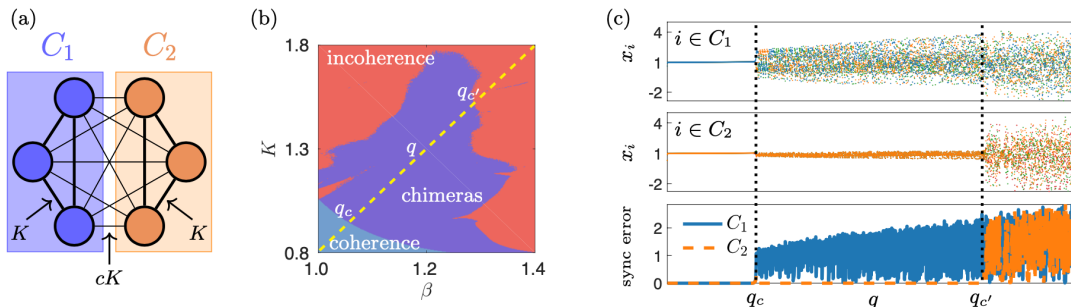


Figure 8.2. Strong chimeras in a network of diffusively coupled oscillators given by Eq. (8.5). (a) Network consisting of two identical clusters, C_1 and C_2 . (b) Diagram in the $\beta-K$ parameter space marking the regions for which the system exhibits coherence (cyan), chimeras (purple), and incoherence (red) for $c = 0.2$. (c) State transitions as parameter q is varied quasi-statically along the dashed line in (b), showing the abrupt change from coherence to a chimera at q_c and then from the chimera to incoherence at $q_{c'}$. The individual panels show the states in each cluster colored by the individual oscillators (top and middle) and the synchronization error in each cluster defined by the standard deviation among the oscillator states (bottom).

coupling of strength cK [Fig. 8.2(a)], where c is included in matrix \mathbf{M} in the representation of Eq. (8.1). There is nothing special about this choice of dynamics and cluster structure, and we anticipate that our conclusions hold for other functions and networks.

Figure 8.2(b) shows the corresponding state diagram in the $\beta-K$ parameter space for $c = 0.2$. The classification of states in the diagram is based on the linear stability analysis of the coherent and chimera states as determined by the corresponding LTLE. A generic bifurcation scenario is depicted in Fig. 8.2(c): as a linear combination of the parameters β and K is increased [dashed line in Fig. 8.2(b)], the system transitions from global coherence to a chimera state, and then from the chimera state to global incoherence. In this example, the chimera is defined by incoherence in cluster C_1 and coherence in cluster C_2 . Starting from random initial conditions, it is equally likely for the clusters to exhibit

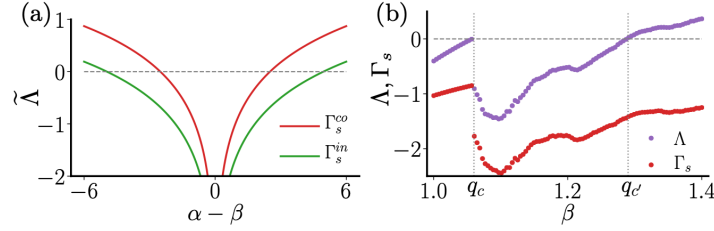


Figure 8.3. Impact of the incoherent cluster on the stability of the coherent one. (a) MSF for the coherent cluster before (red) and after (green) the other cluster transitions to incoherence, showing a widening of the stable region. (b) LTLE of the coherent cluster (purple) as the parameter $q = q(\beta)$ in Fig. 8.2(b) is varied, showing a discontinuous transition at q_c and a continuous one at q_c' due to the corresponding changes in Γ_s (red). The system and other parameters are as in Fig. 8.2.

swapped states, corresponding to a chimera in $q_c < q < q_c'$ that has incoherence in C_2 and coherence in C_1 .

We can now establish a theoretical foundation for the mechanism underlying the onset of such chimeras by examining Eqs. (8.3)-(8.4) in the most general case of arbitrary networks and coupling matrices. Crucially, the input from the rest of the network is irregular temporally but uniform spatially and does not affect the variational equations of C directly, since $I(t)$ does not appear in Eq. (8.4). Yet, it indirectly impacts synchronization stability by changing the synchronous state s^t according to Eq. (8.3). It is entirely through the change it causes to s^t that incoherence in the rest of the network stabilizes coherence in C , giving rise to a stable chimera.

To establish this rigorously we note that the Lyapunov exponents of Eq. (8.4) can be written as $\Lambda^{(i)} = \ln | -K\hat{\lambda}_i - \beta | + \Gamma_s$, where $\Gamma_s = \lim_{T \rightarrow \infty} \ln \left| \prod_{t=1}^T f'(s^t) \right|^{\frac{1}{T}}$ for $f'(x) = h'(x)$ as in the systems explicitly examined here. Since Γ_s is generally finite, the associated master stability function (MSF) $\tilde{\Lambda}(\alpha, \beta) = \ln |\alpha - \beta| + \Gamma_s$ defines a finite stability region,

and synchronization in C is stable if and only if

$$(8.6) \quad | -K\hat{\lambda}_i - \beta | < e^{-\Gamma_s}, \quad i = 2, \dots, n.$$

This equation explains what happens at the interface between global coherence and a chimera state. As the bifurcation parameter q is varied and the transition is approached from the coherent region, the condition in Eq. (8.6) is violated by at least one mode and $\Lambda = \max_{i \geq 2} \{\Lambda^{(i)}\}$ vanishes at $q = q_c$. But past this point, $K\mu h(s^t) + I(t)$ becomes nonzero and Γ_s changes (abruptly) from Γ_s^{co} to Γ_s^{in} according to its dependence on Eq. (8.3). If $\Gamma_s^{in} < \Gamma_s^{co}$, the stability region defined by Eq. (8.6) expands (i.e., Λ becomes negative again for $q > q_c$), and a chimera region then emerges due to stabilization caused by the incoherent input $I(t)$. In the example of Fig. 8.2(b), in particular, $\Gamma_s^{co} = -0.92$ and $\Gamma_s^{in} = -1.6$, confirming our phenomenological observation that incoherence in C_1 stabilizes coherence in C_2 . Figure 8.3 shows the impact of this change on $\tilde{\Lambda}$ [Fig. 8.3(a)] as well as the co-dependence of Λ and Γ_s as the bifurcation parameter is varied [Fig. 8.3(b)].

8.3. Relation with noise-induced synchronization

To further validate the hypothesis that the synchronization stability in the coherent cluster can be induced by the incoherent driving, we model the *effective* input $K\mu h(s^t) + I(t)$ in Eq. (8.3) as a driving noise term $\xi(t)$. The synchronization trajectory s^t in the coherent cluster is then

$$(8.7) \quad s^{t+1} = f(s^t) + \xi(t),$$

with the corresponding variational equations given by Eq. (8.4) for $\hat{\lambda}_i = -\lambda_i - cn$. Figure 8.4(a) shows the result of our stability analysis for $\beta = 1.2$, $K = 1.2$, and $c = 0.2$. We see that synchronization in the coherent cluster is unstable ($\Lambda > 0$) in the absence of external driving ($\nu = \sigma = 0$), but it can be stabilized ($\Lambda < 0$) by a Gaussian noise effective input over a range of mean ν and standard deviation σ . Direct simulation of the corresponding chimera state shows that the effective input from the incoherent cluster has $\nu = -0.30$ and $\sigma = 0.15$, which is inside the stable region in Fig. 8.4(a). On the other hand, the scenario in which both clusters are synchronized corresponds to $\nu = \sigma = 0$ for diffusive coupling, which is equivalent to not having external driving, and is thus unstable for the given parameters. More generally, for diffusive coupling, wherever the coherent state takes the form of identical synchronization, coherence in one cluster can benefit from common driving only when the other cluster is not in the same state.

For a more systematic understanding of the interaction between the two clusters, we vary the intercluster coupling strength by varying c while the other parameters are kept fixed. Figure 8.4(b) shows the resulting LTLE for synchronization in the coherent cluster [modeled by Eq. (8.7)] when this cluster is subject to noise input or input from the incoherent cluster. For each value of c , the mean and standard deviation of the input are set respectively to the values of $\nu = \nu(c)$ and $\sigma = \sigma(c)$ calculated from direct simulation of the dynamics. Both forms of input lead to the stabilization of synchronization for intermediate intercluster coupling strength, which is to be contrasted with the unstable state obtained if the other cluster is set to the same coherent state (shown in Fig. 8.4(b) as a reference). This suggests that the stabilization effect of a common driving signal is

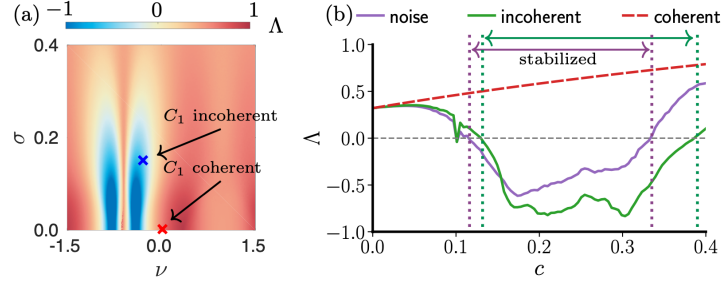


Figure 8.4. Incoherence-stabilized coherence for the influence of the incoherent cluster modeled as a noise effective input. The system is the same as in Fig. 8.2 for $\beta = 1.2$, $K = 1.2$, and C_2 as the coherent cluster. (a) LTLE of the coherent cluster for $c = 0.2$ and the input drawn from a Gaussian distribution of mean ν and standard deviation σ . Also marked are the corresponding (ν, σ) from direct simulation of the dynamics when the other cluster is incoherent (blue cross) or coherent (red cross). (b) LTLE of the coherent cluster as a function of c for noise input (purple), input from direct simulation of the incoherent cluster (green), and input from an identical coherent state (red).

relatively insensitive to the form of the signal, as long as the mean and standard deviation of the signal are suitable.

8.4. Insight into previously-studied chimera systems

We now turn to adjacency matrix coupling for

$$(8.8) \quad f(x) = h(x) + (\pi/6)/\beta = [1 - \cos(x)]/2 + (\pi/6)/\beta,$$

which is a closely-related class of optoelectronic oscillators for which this type of coupling has been implemented experimentally [219]. Here, the dynamical variables are constrained to the interval $[0, 2\pi)$ by taking mod 2π at each iteration. Our primary goal with this model is to illustrate a coupling scheme for which the intercluster coupling term

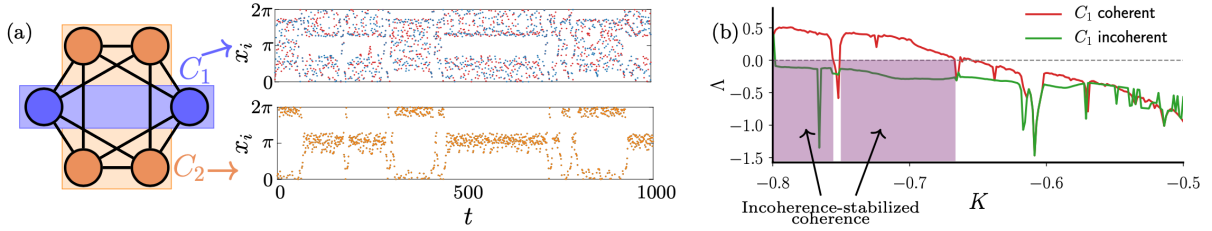


Figure 8.5. Strong chimeras in a network of non-diffusively coupled oscillators given by Eq. (8.8). (a) Network of identically-coupled oscillators organized into an incoherent (C_1) and a coherent (C_2) cluster. Right: representative chimera trajectory for $K = -0.72$. (b) LTLE of the coherent cluster as a function of K from direct simulation when the other cluster is taken to be in an identical coherent state (red) or an incoherent one (green). In the shaded region, coherence in C_2 is stabilized by incoherence in C_1 .

does not vanish in the coherent state. But we also want to show that our results do not depend on the coherent and incoherent clusters being equal. To facilitate comparison with the literature, we adopt a network and parameter setting for the system in Eq. (8.8) first considered in Ref. [59]. The network consists of a ring of six nodes coupled to their first and second nearest neighbors [Fig. 8.5(a)], and the parameters are set to $\beta = 2\pi/3 - 4K$. For $-0.65 < K < -0.53$, synchronization in cluster C_1 (comprising two oscillators) is unstable while synchronization in cluster C_2 (comprising four oscillators) is stable [59]. Thus, for coupling strength in this range, a chimera state with two asymmetric clusters is expected to exist. However, this prediction is derived by assuming that C_1 and C_2 are both in a synchronized state when performing the stability analysis. Once C_1 becomes incoherent and the system transitions from global coherence into a chimera state, this assumption is no longer valid. Thus, incoherence in C_1 should be taken into account when estimating the range of parameters for which the chimera can be stable.

In Fig. 8.5(b), we perform a comparative analysis and plot the LTLE for coherence in C_2 when C_1 is assumed to be coherent and incoherent, respectively. We see that incoherence in C_1 significantly delays the instability transition in C_2 from $K = -0.65$ to $K = -0.80$ and, as a consequence, gives rise to a much wider chimera region than initially expected. A representative time series for the chimera state at $K = -0.72$, whose coherent cluster is stabilized by the incoherent one, is shown in Fig. 8.5(a).

8.5. Concluding remarks

The analysis presented above reveals a physical mechanism underlying the emergence of strong chimeras. The self-consistency of such states was partially elucidated by the previous demonstration that desynchronization in one cluster does not necessarily lead to the concurrent desynchronization in another cluster [219, 59]. Here, we have been able to go one step further and demonstrate that incoherence in one cluster can in fact stabilize coherence in the other cluster. This incoherence-stabilized coherence adds a new dimension to the proposition that chimera states are the natural link between coherent and incoherent states [202, 199, 200]. As a promising direction for future research, we note that chimera states not meeting the conditions for strong chimeras have been studied in the literature, including those with coherent clusters that are not identically synchronized [3, 104, 39, 46] and those that co-occur with stable global coherence [1, 156, 251, 129]. It remains to be shown how the mechanism uncovered for strong chimeras may provide insight into those states. Given the prevalence of related phenomena such as noise-induced synchronization [319, 282, 180, 289], we believe the cooperative relation

between incoherence and coherence revealed by our analysis can be a general mechanism giving rise to a wide range of chimera states.

CHAPTER 9

Symmetry-Independent Stability Analysis of Synchronization Patterns

The field of network synchronization has seen tremendous growth following the introduction of the master stability function (MSF) formalism, which enables the efficient stability analysis of synchronization in large oscillator networks. However, to make further progress we must overcome the limitations of this celebrated formalism, which focuses on global synchronization and requires both the oscillators and their interactions to be identical, while many systems of interest are inherently heterogeneous and exhibit complex synchronization patterns. Here, we establish a generalization of the MSF formalism that can characterize the stability of any cluster synchronization pattern, even when the oscillators and/or their interactions are nonidentical. The new framework is based on finding the finest simultaneous block diagonalization of matrices and does not rely on information about network symmetry. This leads to an algorithm that is error-tolerant and orders of magnitude faster than existing symmetry-based algorithms. As an application, we rigorously characterize the stability of chimera states in networks with multiple types of interactions.

This chapter is based on the joint work with Adilson E. Motter. The presentation closely follows Ref. [315].

9.1. Background

Coupled oscillator networks have been extensively studied as a fundamental model of collective behavior in complex systems [274, 44, 184, 45, 13, 55, 2]. The field is unique in its close interaction between theoretical developments [216, 237, 283, 206, 6] and practical applications [299, 77, 27, 145, 175]. A central theme of current research is how to characterize the stability of increasingly complex synchronization patterns in arbitrary network structures. Such patterns can be regarded as forms of cluster synchronization, in which the oscillators form one or more internally synchronized clusters that exhibit mutually distinct dynamics [29, 97, 30, 62, 238, 302, 203, 108]. The stability of a synchronization pattern is important because it usually cannot be observed if it is unstable, and thus a bifurcation leading to the loss or restoration of stability has significant ramifications in various biological and technological systems.

In order to perform efficient stability analysis for large networks of coupled oscillators, the key is to first divide the full state space of the variational equation into minimal flow-invariant subspaces (defined below) and then calculate the maximum Lyapunov exponent in each flow-invariant subspace to determine whether perturbations within that subspace would grow. To achieve this for the global synchronization of identical oscillators, the MSF formalism [217] finds a coordinate transformation that diagonalizes the coupling matrix, which in turn decouples the high-dimensional variational equation of the full network into low-dimensional equations describing the evolution of independent perturbation modes. The full equation has a dimension that grows linearly with the network size, while the decoupled equations all have a fixed dimension equal to that of an individual oscillator, irrespective of the network size.

However, when one considers cluster synchronization states, nonidentical oscillators, or disparate interactions, all of which common in real systems, there are in general two or more non-commuting matrices in the variational equation. Since non-commuting matrices cannot be diagonalized simultaneously (even when the individual matrices can), the MSF formalism is not applicable to these cases. The goal of the current chapter is to introduce an extension of the MSF formalism and propose a fundamentally new framework based on the theory of matrix $*$ -algebra that addresses these important cases. In particular, we present a highly scalable algorithm that finds a finest simultaneous block diagonalization (SBD) of any given set of self-adjoint matrices, leading to an optimal separation of the perturbation modes and efficient stability analysis of arbitrary synchronization patterns.

Our framework applies to the general class of network dynamical systems described by

$$(9.1) \quad \dot{\mathbf{x}}_i = \mathbf{F}_i(\mathbf{x}_i) + \sum_{r=1}^R \sigma_r \sum_{j=1}^n \mathbf{C}_r(i, j) \mathbf{H}_r(\mathbf{x}_i, \mathbf{x}_j), \quad i = 1, \dots, n,$$

where \mathbf{x}_i is the d -dimensional state vector of the i -th oscillator, n is the number of oscillators, R is the number of interaction types, and overdot represents time derivative. Here, $\mathbf{F}_i : \mathbb{R}^d \rightarrow \mathbb{R}^d$ is the vector field governing the uncoupled dynamics of the i -th oscillator and \mathbf{C}_r is a self-adjoint coupling matrix representing interactions of the form \mathbf{H}_r and strength σ_r . The synchronization patterns we study can be derived from any balanced equivalence relation [97, 120], which is the most general class of patterns for which oscillators in the same cluster can admit equal dynamics for generic \mathbf{F}_i and \mathbf{H}_r . In general, nodes in a cluster can be separated by nodes from other clusters and do not necessarily form a connected component of the network. The resulting synchronization

patterns describe a wide range of network dynamics, including remote synchronization and chimera states.¹⁰

A related extension of the MSF formalism to study cluster synchronization patterns was previously proposed by Pecora and colleagues [219]. That framework was originally developed for networks with adjacency-matrix coupling and has since been extended to diffusively coupled networks [265] and multilayer networks [41]. In those studies, the authors simplified the stability analysis using the machinery of irreducible representations (IRR) [284], which decouples the variational equation according to symmetries present in the system.

Both the IRR framework and our SBD framework reduce to the MSF formalism for global synchronization of identical oscillators with a single type of interaction. The key difference between the two frameworks is that the former relies on network symmetry to perform stability analysis, whereas the latter does not.¹¹ As a result, the IRR framework has to resort to ad hoc modifications when a cluster synchronization pattern is not induced by network symmetry [265, 257]. In contrast, our SBD framework does not require any symmetry information to be known in advance and is directly applicable to all cluster synchronization patterns. Moreover, it forgoes the calculation on irreducible representations of network symmetry, which becomes computationally prohibitive very quickly as the number of symmetries grow. This leads to a faster, simpler, and more

¹⁰For the ease of presentation, we ground our discussions in this chapter on Eq. (9.1), but we note that it is straightforward to generalize our methods beyond ODE settings. For instance, it is possible to introduce coupling delay into the interaction functions and the resulting delay differential equations can still be analyzed within our framework. Naturally, the framework also applies to discrete-time dynamical systems.

¹¹We note that it is computationally inexpensive to identify synchronization patterns when compared to the cost of determining their stabilities. We thus assume that the synchronization patterns of interest are given before stability analysis are performed.

robust algorithm than existing ones based on the IRR framework and enables the study of complex synchronization patterns in large networks.

The chapter is organized as follows. In Section 9.2, we present the concept of matrix $*$ -algebra and a fast algorithm for finding a finest simultaneous block diagonalization for any set of self-adjoint matrices. Then, in Section 9.3, we develop a symmetry-independent framework for the stability analysis of arbitrary cluster synchronization patterns and compare our algorithm with state-of-the-art algorithms based on irreducible representations. We further show in Section 9.4 that our algorithm can be applied to analyze cluster synchronization patterns of nonidentical oscillators and oscillators with multiple types of interactions. The strength of this unified framework is demonstrated with the characterization of permanently stable chimera-like states in multilayer networks. A discussion on open problems and future directions is presented in Section 9.5.

9.2. Finest simultaneous block diagonalization

Given a set of $n \times n$ matrices $\mathcal{B} = \{\mathbf{B}_1, \dots, \mathbf{B}_K\}$, we say that a subspace \mathcal{W} of \mathbb{C}^n is *invariant* under \mathcal{B} if $\mathbf{B}_k \mathcal{W} \subseteq \mathcal{W}$ for every $\mathbf{B}_k \in \mathcal{B}$. Further, an invariant subspace \mathcal{W} is *minimal* if no proper subspace of \mathcal{W} other than $\mathbf{0}$ is invariant under \mathcal{B} . An invertible matrix \mathbf{T} is said to give a *finest simultaneous block diagonalization* of the matrix set \mathcal{B} if it brings all matrices in \mathcal{B} into a common block-diagonal form that cannot be further refined. Equivalently, \mathbf{T} decomposes \mathbb{C}^n into minimal invariant subspaces under \mathcal{B} , such that the j -th common blocks in $\mathbf{T}^{-1} \mathcal{B} \mathbf{T}$ only have $\mathbf{0}$ and \mathbb{C}^{n_j} as invariant subspaces, where n_j is the dimension of the j -th blocks.

To make progress in finding a finest simultaneous block diagonalization, it is beneficial to consider an algebraic structure called matrix $*$ -algebra. Letting \mathcal{M}_n denote the set of all $n \times n$ matrices with complex entries, a subset \mathcal{T} of \mathcal{M}_n is said to be a *matrix $*$ -algebra* over \mathbb{C} if the identity matrix \mathbf{I}_n belongs to \mathcal{T} and

$$(9.2) \quad \mathbf{B}, \mathbf{C} \in \mathcal{T}; \alpha, \beta \in \mathbb{C} \implies \alpha\mathbf{B} + \beta\mathbf{C}, \mathbf{BC}, \mathbf{B}^* \in \mathcal{T},$$

where $*$ denotes conjugate transpose.¹² Matrix $*$ -algebras enjoy better properties than matrix algebras because they are closed under the conjugate transpose operation. This makes matrix $*$ -algebras semisimple and thus characterizable by the Artin-Wedderburn theorem [136].

According to structure theorems based on the Artin-Wedderburn theorem (Theorem 3.1 and Theorem 6.1 in Ref. [178]), a matrix $*$ -algebra \mathcal{T} can always be decomposed through a unitary transformation \mathbf{P} into the direct sum of ℓ irreducible matrix $*$ -algebras \mathcal{T}_j :

$$(9.3) \quad \mathbf{P}^*\mathcal{T}\mathbf{P} = \bigoplus_{j=1}^{\ell} (\mathbf{I}_{m_j} \otimes \mathcal{T}_j) = \text{diag}\{\mathbf{I}_{m_1} \otimes \mathcal{T}_1, \dots, \mathbf{I}_{m_\ell} \otimes \mathcal{T}_\ell\},$$

where $\mathcal{T}_j \subseteq \mathcal{M}_{n_j}$, m_j is the multiplicity of \mathcal{T}_j , and $\sum_{j=1}^{\ell} n_j m_j = n$. The \otimes symbol denotes the tensor product of matrices (i.e., the Kronecker product), the summand $\mathbf{I}_{m_j} \otimes \mathcal{T}_j = \{\bigoplus_{k=1}^{m_j} \mathbf{B} : \mathbf{B} \in \mathcal{T}_j\}$ represents m_j copies of the irreducible matrix $*$ -algebra \mathcal{T}_j arranged diagonally (not to be confused with $\bigoplus_{k=1}^{m_j} \mathcal{T}_j$). We say that a matrix $*$ -algebra

¹²The results remain applicable if the matrix $*$ -algebras are over \mathbb{R} , as in various examples considered throughout the chapter. However, working in \mathbb{C} both allows complex coupling matrices, which arise for oscillator networks that are naturally expressed using complex vector fields (such as coupled Stuart-Landau oscillators), and can lead to finer block structures when networks are directed.

\mathcal{T}_j is *irreducible* if it contains matrices that only share trivial invariant subspaces (i.e., $\mathbf{0}$ and \mathbb{C}^{n_j}). Equation (9.3) is the canonical form of an irreducible decomposition of a matrix $*$ -algebra, which is unique up to block permutations and unitary transformations localized within each block. As a consequence, all the matrices in \mathcal{T} can be transformed simultaneously into a block-diagonal form of $\sum_{j=1}^{\ell} m_j$ blocks through a single unitary matrix \mathbf{P} .

A matrix $*$ -algebra \mathcal{T} is said to be *generated by* a set of matrices \mathcal{B} if $\mathcal{B} \subseteq \mathcal{T}$ and every matrix in \mathcal{T} can be constructed from \mathbf{I}_n and \mathcal{B} using the operations of matrix $*$ -algebras (i.e., scalar multiplication, matrix addition, matrix multiplication, and conjugate transpose). In order to calculate a transformation matrix \mathbf{P} that gives a finest simultaneous block diagonalization of all matrices in \mathcal{T} , we propose a new algorithm (Algorithm 1) and refer to the corresponding coordinate transformation as an SBD transformation. The algorithm involves only numerical linear-algebraic calculations and does not require any algebraic structure (e.g., symmetries) to be known in advance.

The idea behind the algorithm is simple. First, pick an eigenvector \mathbf{v}_1 of a self-adjoint matrix $\mathbf{B} = \sum_{k=1}^K [c_k(\mathbf{B}_k + \mathbf{B}_k^*) + id_k(\mathbf{B}_k - \mathbf{B}_k^*)]$, where c_k and d_k are random coefficients drawn from a Gaussian distribution. This eigenvector lies inside one of the minimal invariant subspaces of \mathcal{B} with probability 1. Furthermore, all the images of \mathbf{v}_1 under $\{\mathbf{B}_k\}$ and $\{\mathbf{B}_k^*\}$ must also be inside the same minimal invariant subspace. By running the Gram-Schmidt process on $\{\mathbf{v}_1, \mathbf{B}_1\mathbf{v}_1, \mathbf{B}_1^*\mathbf{v}_1, \dots, \mathbf{B}_K\mathbf{v}_1, \mathbf{B}_K^*\mathbf{v}_1\}$ and discarding the linearly redundant vectors, we can obtain a set of orthonormal vectors all inside the same minimal invariant subspace. If these vectors span the entire invariant subspace, then we have discovered a common block and can repeat the process starting from another eigenvector

Algorithm 1 Finding an SBD transformation for a matrix $*$ -algebra generated by a set of $n \times n$ matrices $\mathcal{B} = \{\mathbf{B}_k\}$ in $\mathcal{O}(n^3)$. (A MATLAB implementation is available as a Github repository at <https://github.com/y-z-zhang/net-sync-sym/>.)

- ▷ step 1: generate a self-adjoint matrix \mathbf{B} from combining matrices in \mathcal{B} with random coefficients c_k and d_k
 - 1: $\mathbf{B} = \sum_{k=1}^K [c_k(\mathbf{B}_k + \mathbf{B}_k^*) + id_k(\mathbf{B}_k - \mathbf{B}_k^*)]$
 - 2: find the eigenvectors $\{\mathbf{v}_j\}$ of \mathbf{B}
 - ▷ steps 3 to 9: find (a basis of) the minimal invariant subspace that contains \mathbf{v}_1
 - 3: perform Gram-Schmidt orthonormalization on $\{\mathbf{v}_1, \mathbf{B}_k \mathbf{v}_1, \mathbf{B}_k^* \mathbf{v}_1\}$, $k = 1, \dots, K$ to obtain a set of orthonormal vectors \mathcal{V}
 - 4: let \mathbf{v} be a random linear combination of the vectors from \mathcal{V}
 - 5: **while** the images $\{\mathbf{B}_k \mathbf{v}, \mathbf{B}_k^* \mathbf{v}\}$, $k = 1, \dots, K$ include vectors that are linearly independent from \mathcal{V} **do**
 - 6: make these new vectors orthonormal to \mathcal{V} and to each other
 - 7: expand \mathcal{V} to include the new vectors
 - 8: let \mathbf{v} be a random combination of the vectors from the expanded \mathcal{V}
 - 9: **end while**
 - 10: let \mathbf{P} be a matrix whose columns are made of vectors from \mathcal{V}
 - ▷ steps 11 to 16: find the rest of the minimal invariant subspaces
 - 11: **while** the matrix \mathbf{P} has less than n columns **do**
 - 12: find an eigenvector \mathbf{v}_j outside the span of \mathbf{P} 's column vectors
 - 13: make \mathbf{v}_j orthonormal to the column vectors of \mathbf{P}
 - 14: repeat step 3 to 9 with \mathbf{v}_1 replaced by \mathbf{v}_j
 - 15: add the vectors from \mathcal{V} to \mathbf{P} as additional columns
 - 16: **end while**
-

of \mathbf{B} outside the discovered minimal invariant subspace. Otherwise, we generate a random linear combination \mathbf{v} of the existing orthonormal vectors and “explore” the invariant subspace further by generating images of \mathbf{v} under $\{\mathbf{B}_k\}$ and $\{\mathbf{B}_k^*\}$. It is easy to see that a complete basis for a minimal invariant subspace can always be reached after no more than n such iterations. The computational complexity of the algorithm scales as $\mathcal{O}(n^3)$ —it can easily handle $n \times n$ matrices with n in the range of thousands.¹³ This distinguishes Algorithm 1 from the best competing algorithms available [178, 150, 151],

¹³It takes $\mathcal{O}(n^2)$ operations to calculate the image of \mathbf{v} under \mathbf{B}_k , and $\mathcal{O}(n)$ such images need to be computed to discover the transformation matrix \mathbf{P} .

which run in $\mathcal{O}(n^4)$ time and are already slow at $n \approx 100$. Moreover, applications of those algorithms to network synchronization have been limited to the study of global synchronization [118, 313], while our framework enables application of the new algorithm to general synchronization patterns.

In most cases, we are interested in a given set of matrices instead of the full matrix $*$ -algebra. When is Algorithm 1 guaranteed to find a finest simultaneous block diagonalization for a given matrix set \mathcal{B} ? A sufficient condition is that the matrices in \mathcal{B} are self-adjoint.

Proposition 1. *Given a set of $n \times n$ self-adjoint matrices $\mathcal{B} = \{\mathbf{B}_1, \dots, \mathbf{B}_K\}$, let \mathcal{T} be the matrix $*$ -algebra generated by \mathcal{B} . If a unitary matrix \mathbf{P} leads to an irreducible decomposition of \mathcal{T} , then it also gives rise to a finest simultaneous block diagonalization of \mathcal{B} .*

Proof. Assume that an invertible matrix \mathbf{T} yields a finest simultaneous block diagonalization of the set of self-adjoint matrices \mathcal{B} . Since

$$\mathbf{T}^{-1}(\alpha\mathbf{B}_j + \beta\mathbf{B}_k)\mathbf{T} = \alpha\mathbf{T}^{-1}\mathbf{B}_j\mathbf{T} + \beta\mathbf{T}^{-1}\mathbf{B}_k\mathbf{T},$$

$$\mathbf{T}^{-1}\mathbf{B}_j\mathbf{B}_k\mathbf{T} = (\mathbf{T}^{-1}\mathbf{B}_j\mathbf{T})(\mathbf{T}^{-1}\mathbf{B}_k\mathbf{T}),$$

$$\mathbf{T}^{-1}\mathbf{B}_j^*\mathbf{T} = \mathbf{T}^{-1}\mathbf{B}_j\mathbf{T} \text{ for self-adjoint } \mathbf{B}_j,$$

all matrices in $\mathbf{T}^{-1}\mathcal{T}\mathbf{T}$ can admit the same block structure shared by the matrices in its generating set $\mathbf{T}^{-1}\mathcal{B}\mathbf{T}$. Since this block structure is finest in \mathcal{B} , it is also finest in \mathcal{T} . By definition, the unitary matrix \mathbf{P} yields a finest simultaneous block diagonalization of the

matrices in \mathcal{T} . Because \mathcal{B} and \mathcal{T} have the same finest common block structure, \mathbf{P} also generates a finest simultaneous block diagonalization of the matrix set \mathcal{B} . \square

Taken together, Proposition 1 and Algorithm 1 establish a powerful framework for finding a finest simultaneous block diagonalization for any set of self-adjoint matrices. In the sections below, we show how SBD transformations can be used to characterize the stability of synchronization patterns in an efficient and unified fashion. We will focus mainly on oscillators coupled through undirected networks (i.e., self-adjoint coupling matrices). The possibility of extending the current framework to directed networks will be discussed in Section 9.5.

9.3. Cluster synchronization from a symmetry-independent perspective

Consider a network of n identical d -dimensional oscillators forming a synchronization pattern of M clusters. The cluster synchronization subspace can be defined as an Md -dimensional subspace of the full nd -dimensional state space, in which oscillators from the same cluster have exactly the same dynamics. *Parallel perturbations* are perturbations inside the cluster synchronization subspace—they do not destroy the cluster synchronization pattern. *Transverse perturbations* are the ones that are perpendicular to the cluster synchronization subspace—all of them must have negative Lyapunov exponents under the evolution of the variational equation in order for the cluster synchronization pattern to be stable.

One key step in analyzing the stability of a synchronization pattern amounts to finding a coordinate system that separates the evolution of transverse and parallel perturbation modes. The coordinate transformation should also decouple the transverse perturbation

modes as much as possible. The current state-of-the-art method exploits symmetries in the network structure and uses the machinery of group representation theory [219]. In this section, we establish a symmetry-independent framework based on SBD transformations and compare Algorithm 1 with symmetry-based algorithms in terms of speed, simplicity, and error tolerance.

9.3.1. The symmetry perspective

A network of n identical oscillators with adjacency-matrix coupling can be described as the following special case of Eq. (9.1):

$$(9.4) \quad \dot{\mathbf{x}}_i = \mathbf{F}(\mathbf{x}_i) + \sigma \sum_{j=1}^n A(i, j) \mathbf{H}(\mathbf{x}_j),$$

where $\mathbf{A} = \{A(i, j)\}$ is the self-adjoint adjacency matrix encoding the structure of the underlying network.

To study the stability of cluster synchronization states, it is necessary to first identify possible synchronization patterns supported by Eq. (9.4), a subset of which is determined by the symmetries of the network. The network symmetries, described by the graph automorphism group $\text{Aut}(\mathbf{A})$, can be computed using discrete algebra softwares [270]. The nodes can be partitioned into disjoint clusters: two nodes belong to the same cluster if there is a symmetry operation (i.e., node permutations that respect the adjacency matrix) from the automorphism group that maps one node to the other. In other words, nodes are partitioned according to the orbits under the action of $\text{Aut}(\mathbf{A})$ [219]. This is the coarsest synchronization pattern that can be derived from network symmetry. If one instead considers a subgroup G of $\text{Aut}(\mathbf{A})$, the nodes can then be partitioned into finer

clusters according to the orbits under the action of G . We call these partitions the *orbital partitions* of the network and refer to the corresponding clusters as *symmetry clusters*. Each element $g \in G$ can be represented by a permutation matrix \mathbf{R}_g , upon whose action the adjacency matrix \mathbf{A} stays invariant, i.e., $\mathbf{R}_g^* \mathbf{A} \mathbf{R}_g = \mathbf{A}$. The set of matrices $\{\mathbf{R}_g\}$ form a *permutation representation* of the subgroup G . As a result of network symmetry, nodes in each symmetry cluster receive the same input from other clusters and admit equal dynamics. In other words, cluster synchronization patterns based on symmetry clusters are guaranteed to be *flow invariant* (i.e., subspaces of the state space that are invariant under time evolution of the system).

Once a subgroup G and the corresponding orbital partition have been identified, one can find the associated cluster synchronization manifold by evolving the dynamical equation on a quotient network in which each symmetry cluster is represented by a single node. Equation (9.4) can then be linearized around the cluster synchronization manifold, leading to a variational equation that determines the stability of the corresponding synchronization pattern:

$$\begin{aligned}
 (9.5) \quad \delta \dot{\mathbf{X}} &= \left(\sum_{m=1}^M \mathbf{E}_m \otimes J\mathbf{F}(\mathbf{s}_m) + \sigma (\mathbf{A} \otimes \mathbf{I}_d) \sum_{m=1}^M \mathbf{E}_m \otimes J\mathbf{H}(\mathbf{s}_m) \right) \delta \mathbf{X}, \\
 &= \left(\sum_{m=1}^M \mathbf{E}_m \otimes J\mathbf{F}(\mathbf{s}_m) + \sigma \sum_{m=1}^M \mathbf{A} \mathbf{E}_m \otimes J\mathbf{H}(\mathbf{s}_m) \right) \delta \mathbf{X},
 \end{aligned}$$

where \mathbf{s}_m is the synchronization trajectory of the m -th cluster, $\delta \mathbf{X} = (\delta \mathbf{x}_1^\top, \dots, \delta \mathbf{x}_n^\top)^\top$ is the nd -dimensional perturbation vector, and J is the Jacobian operator. Let \mathcal{C}_m denote

the set of nodes in the m -th cluster. Then

$$\mathbf{E}_m(i, i) = \begin{cases} 1, & \text{if } i \in \mathcal{C}_m, \\ 0, & \text{otherwise,} \end{cases}$$

is an $n \times n$ diagonal matrix encoding the nodes in the m -th cluster. It follows that $\sum_{m=1}^M \mathbf{E}_m = \mathbf{I}_n$.

A key insight from Ref. [219] is that there exists a coordinate choice under which the transformed adjacency matrix $\tilde{\mathbf{A}} = \mathbf{Q}^* \mathbf{A} \mathbf{Q}$ has a block-diagonal form that matches the cluster structure. They termed it the IRR coordinates since the transformation matrix \mathbf{Q} decomposes the permutation representation $\{\mathbf{R}_g\}$ into the direct sum of irreducible representations of G . In particular,

$$(9.6) \quad \tilde{\mathbf{R}}_g = \mathbf{Q}^* \mathbf{R}_g \mathbf{Q} = \bigoplus_{j=1}^{\ell} (\tilde{\mathbf{R}}_g^{(j)} \otimes \mathbf{I}_{n_j}), \quad \tilde{\mathbf{A}} = \mathbf{Q}^* \mathbf{A} \mathbf{Q} = \bigoplus_{j=1}^{\ell} (\mathbf{I}_{m_j} \otimes \tilde{\mathbf{A}}^{(j)}),$$

where ℓ is the number of distinct IRRs present in $\{\tilde{\mathbf{R}}_g\}$, the j -th block $\tilde{\mathbf{A}}^{(j)}$ is an $n_j \times n_j$ matrix with n_j equal to the multiplicity of the j -th IRR $\{\tilde{\mathbf{R}}_g^{(j)}\}$, and m_j is the multiplicity of $\tilde{\mathbf{A}}^{(j)}$ as well as the dimension of $\tilde{\mathbf{R}}_g^{(j)}$. The trivial IRR (which maps every $g \in G$ to 1) is always present with multiplicity M , so there is always an $M \times M$ block in $\tilde{\mathbf{A}}$ corresponding to the dynamics inside the cluster synchronization subspace [219]. In this way, \mathbf{Q} completely decouples the transverse perturbations from the parallel ones and also separates the transverse perturbation modes.

9.3.2. The symmetry-independent perspective

The IRR transformation decouples Eq. (9.5) by exploiting the network symmetry and its irreducible representations. The end result of this transformation is a block diagonalization of the matrix set $\mathcal{A} = \{\mathbf{E}_1, \dots, \mathbf{E}_M, \mathbf{A}\}$. But is finding the irreducible representations the most effective way to block diagonalize these matrices? Below we show that the answer is negative.

The readers might have noticed the parallel between the block forms in Eq. (9.3) and Eq. (9.6), which hints at a deep connection between the IRR and the SBD transformations. We now make this parallel precise by looking at the IRR transformation through the lens of matrix $*$ -algebras.

To proceed, we introduce the *commutant algebra* \mathcal{T}' of a matrix $*$ -algebra $\mathcal{T} \subseteq \mathcal{M}_n$, which is the set of all matrices $\mathbf{C} \in \mathcal{M}_n$ that commute with every element in \mathcal{T} . Letting $[\mathbf{B}, \mathbf{C}] = \mathbf{BC} - \mathbf{CB}$, one has

$$(9.7) \quad \mathcal{T}' = \{\mathbf{C} \in \mathcal{M}_n \mid [\mathbf{B}, \mathbf{C}] = \mathbf{0}, \forall \mathbf{B} \in \mathcal{T}\}.$$

\mathcal{T}' is also a matrix $*$ -algebra and enjoys the following dual relations with \mathcal{T} [151]:

- (a) $\mathcal{T}'' = \mathcal{T}$, known as the double commutant property.
- (b) If the irreducible decomposition of \mathcal{T} has blocks of sizes n_j and multiplicities m_j , then the irreducible decomposition of \mathcal{T}' is the direct sum of blocks of sizes m_j and multiplicities n_j .

Given a subgroup G of $\text{Aut}(\mathbf{A})$, let \mathcal{S} be the set of all $n \times n$ matrices over \mathbb{C} that are invariant under the action of G . That is,

$$(9.8) \quad \mathcal{S} = \{\mathbf{S} \in \mathcal{M}_n \mid \mathbf{R}_g^* \mathbf{S} \mathbf{R}_g = \mathbf{S}, \forall g \in G\}.$$

First, we note that \mathcal{S} is a matrix $*$ -algebra. Second, we make a key observation involving the commutant algebra \mathcal{S}' . It is clear from Eq. (9.8) that \mathcal{S} is the commutant algebra of the matrix $*$ -algebra \mathcal{R} generated by $\{\mathbf{R}_g\}$. According to the double commutant property, we have $\mathcal{S}' = \mathcal{R}'' = \mathcal{R}$, and hence $\{\mathbf{R}_g\}$ is a generating set of \mathcal{S}' . Since the IRR transformation \mathbf{Q} decomposes $\{\mathbf{R}_g\}$ into the form $\tilde{\mathbf{R}}_g = \mathbf{Q}^* \mathbf{R}_g \mathbf{Q} = \bigoplus_{j=1}^{\ell} (\tilde{\mathbf{R}}_g^{(j)} \otimes \mathbf{I}_{n_j})$, the irreducible decomposition of \mathcal{S}' has blocks of sizes m_j and multiplicities n_j .¹⁴

Next, we utilize the relation $\mathbf{S} \mathbf{R}_g = \mathbf{R}_g \mathbf{S}$, or equivalently,

$$\tilde{\mathbf{S}} \tilde{\mathbf{R}}_g = \mathbf{Q}^* \mathbf{S} \mathbf{Q} \mathbf{Q}^* \mathbf{R}_g \mathbf{Q} = \mathbf{Q}^* \mathbf{R}_g \mathbf{Q} \mathbf{Q}^* \mathbf{S} \mathbf{Q} = \tilde{\mathbf{R}}_g \tilde{\mathbf{S}}$$

to show that \mathbf{Q} performs the irreducible decomposition of \mathcal{S} . Writing out $\tilde{\mathbf{R}}_g$ and $\tilde{\mathbf{S}}$ more explicitly,

$$\tilde{\mathbf{R}}_g = \begin{pmatrix} \tilde{\mathbf{R}}_g^{(1)} \otimes \mathbf{I}_{n_1} & & \cdots & \mathbf{0} \\ & \tilde{\mathbf{R}}_g^{(2)} \otimes \mathbf{I}_{n_2} & & \vdots \\ \vdots & & \ddots & \\ \mathbf{0} \cdots & & & \tilde{\mathbf{R}}_g^{(\ell)} \otimes \mathbf{I}_{n_\ell} \end{pmatrix}, \quad \tilde{\mathbf{S}} = \begin{pmatrix} \tilde{\mathbf{S}}_{11} & \tilde{\mathbf{S}}_{12} & \cdots & \tilde{\mathbf{S}}_{1\ell} \\ \tilde{\mathbf{S}}_{21} & \tilde{\mathbf{S}}_{22} & \cdots & \tilde{\mathbf{S}}_{2\ell} \\ \vdots & \vdots & \ddots & \vdots \\ \tilde{\mathbf{S}}_{\ell 1} & \tilde{\mathbf{S}}_{\ell 2} & \cdots & \tilde{\mathbf{S}}_{\ell\ell} \end{pmatrix},$$

¹⁴For any pairs of square matrices \mathbf{X} and \mathbf{Y} there exists a permutation matrix \mathbf{O} such that $\mathbf{X} \otimes \mathbf{Y} = \mathbf{O}^\top (\mathbf{Y} \otimes \mathbf{X}) \mathbf{O}$.

one can see that the commutativity relation implies $(\tilde{\mathbf{R}}_g^{(i)} \otimes \mathbf{I}_{n_i})\tilde{\mathbf{S}}_{ij} = \tilde{\mathbf{S}}_{ij}(\tilde{\mathbf{R}}_g^{(j)} \otimes \mathbf{I}_{n_j})$. According to Schur's Lemma [284, 136], $\tilde{\mathbf{S}}_{ij} = \mathbf{0}$ when $i \neq j$ (i.e., when the irreducible representations $\{\tilde{\mathbf{R}}_g^{(i)}\}$ and $\{\tilde{\mathbf{R}}_g^{(j)}\}$ are non-isomorphic); and $\tilde{\mathbf{S}}_{ij} = \mathbf{I}_{m_j} \otimes \tilde{\mathbf{S}}^{(j)}$ when $i = j$, where $\tilde{\mathbf{S}}^{(j)}$ is an $n_j \times n_j$ complex matrix. Taken together,

$$(9.9) \quad \tilde{\mathbf{S}} = \mathbf{Q}^* \mathbf{S} \mathbf{Q} = \bigoplus_{j=1}^{\ell} (\mathbf{I}_{m_j} \otimes \tilde{\mathbf{S}}^{(j)}).$$

Thus, \mathbf{Q} simultaneously block diagonalizes all matrices in \mathcal{S} into blocks of sizes n_j , each of multiplicity m_j . Based on the dual relation (b) between the commutant algebras, we see that this is the irreducible decomposition of \mathcal{S} .

Accordingly, the IRR transformation can be interpreted within the framework of matrix $*$ -algebra: it performs the irreducible decomposition of the matrix $*$ -algebra \mathcal{S} formed by all $n \times n$ matrices satisfying the symmetry condition Eq. (9.8). This interpretation explains the parallel between Eqs. (9.3) and (9.6). However, \mathcal{S} may not always be the best matrix $*$ -algebra to work with for the stability analysis of synchronization patterns.

In particular, notice that the matrix $*$ -algebra \mathcal{T} generated by the matrix set $\mathcal{A} = \{\mathbf{E}_1, \dots, \mathbf{E}_M, \mathbf{A}\}$ is always a subalgebra of \mathcal{S} , as \mathbf{E}_m and \mathbf{A} all share the symmetries defined by the subgroup G :

$$\mathbf{R}_g^* \mathbf{A} \mathbf{R}_g = \mathbf{A}, \quad \mathbf{R}_g^* \mathbf{E}_m \mathbf{R}_g = \mathbf{E}_m, \quad \forall g \in G \text{ and } 1 \leq m \leq M.$$

This means that the IRR transformation could be considering the simultaneous block diagonalization of an unnecessarily large set of matrices, and \mathcal{S} might have a coarser irreducible decomposition than its subalgebra \mathcal{T} . Thus, an SBD transformation applied

directly to \mathcal{A} will always give a block structure on par or finer than the one found by the IRR transformation.

9.3.3. Optimal separation of perturbation modes

Next, we further characterize the decoupling among perturbation modes achieved by an SBD transformation. Given an adjacency matrix \mathbf{A} and a flow-invariant synchronization pattern described by $\{\mathbf{E}_m\}$, we divide the perturbation modes into three classes according to their dynamical characteristics:

- (I) perturbation modes inside the cluster synchronization subspace;
- (II) perturbation modes transverse to the cluster synchronization subspace and belonging to a d -dimensional (the dimension of a single oscillator) flow-invariant subspace under the variational equation Eq. (9.5);
- (III) perturbation modes transverse to the cluster synchronization subspace and that do not belong to a d -dimensional flow-invariant subspace under the variational equation Eq. (9.5).

Class I perturbation modes do not destroy the cluster synchronization pattern, while those from classes II and III do.

From an algebraic point of view, the class I perturbation modes correspond to the M -dimensional invariant subspace spanned by the diagonal vectors of matrices in $\{\mathbf{E}_m\}$. Perturbation modes of class II are associated with a one-dimensional invariant subspace under the matrix set \mathcal{A} , whereas perturbation modes of class III are induced by higher-dimensional invariant subspaces.

In particular, perturbation modes in Class II are localized inside individual clusters and each of them is decoupled from all other perturbation modes. This is the basis of the so-called *isolated desynchronization* [219], in which an individual cluster can desynchronize without destroying synchronization in other clusters despite their mutual influence through inter-cluster coupling. Class III perturbation modes arise from *intertwined clusters* [219, 59]. Two clusters are intertwined if there exists transverse perturbations inside one cluster that are coupled to transverse perturbations in the other. It is worth noting that not all transverse perturbations inside intertwined clusters belong to Class III, as some of them form d -dimensional invariant subspaces on their own and are thus Class II.

An SBD transformation finds the optimal separation of perturbation modes that can be inferred from the network structure and cluster patterns. In particular, it is guaranteed to separate the parallel perturbations (Class I) from the transverse ones (Class II and III), completely decouple the perturbation modes in Class II, and separate the ones in Class III as much as possible. This separation is “robust” in the sense that it works for any intrinsic dynamics \mathbf{F} and coupling function \mathbf{H} , since it is induced solely by the algebraic structure of the system. For some special \mathbf{F} and \mathbf{H} , the flow-invariant subspaces (under the variational equation) induced by the minimal invariant subspaces (under the matrix set \mathcal{A}) may not be minimal and can be further decomposed.¹⁵ But such special flow-invariant subspaces are not robust and will be destroyed by small changes to \mathbf{F} and/or \mathbf{H} .

¹⁵A flow-invariant subspace is said to be *minimal* if it does not contain proper subspaces that are flow invariant.

9.3.4. Treating clusters not induced by symmetry

The strength of the SBD framework becomes even more evident when the oscillators are diffusively coupled, which is another natural class of coupling schemes [217, 187] featured prominently in real systems, such as consensus networks [145, 198]. This class of systems is a special case of Eq. (9.1) and can be described by

$$(9.10) \quad \dot{\mathbf{x}}_i = \mathbf{F}(\mathbf{x}_i) - \sigma \sum_{j=1}^n L(i, j) \mathbf{H}(\mathbf{x}_j),$$

where the Laplacian matrix $\mathbf{L} = \{L(i, j)\}$ is defined as $L(i, j) = \delta_{ij}\mu_i - A(i, j)$, for δ_{ij} denoting the Kronecker delta and $\mu_i = \sum_j A(i, j)$ representing the indegree of node i . The main difference of systems with Laplacian-matrix coupling from those with adjacency-matrix coupling is that the interaction between two oscillators vanishes when they synchronize.

As a consequence of the diffusive coupling, additional flow-invariant synchronization patterns can emerge that are not predicted by network symmetry. These additional patterns are called *Laplacian clusters*, and they can be formed by merging some of the symmetry clusters [265]. Since an adjacency matrix and its corresponding Laplacian matrix have exactly the same symmetry (i.e., $\text{Aut}(\mathbf{A}) = \text{Aut}(\mathbf{L})$), the original IRR transformation cannot distinguish the systems described by equations Eqs. (9.4) and (9.10). Thus, it fails to decouple the parallel and transverse perturbations if applied directly. In Ref. [265], it was proposed that one can apply the IRR transformation to the adjacency matrix of the diffusive network first, then perform additional local coordinate transformations to account for the merging of symmetry clusters induced by the diffusive coupling.

This method provides valuable insight, but at the same time it adds an additional layer of complexity on top of the irreducible representation calculations. In fact, all necessary information for the separation of perturbation modes is already encoded in the Laplacian matrix \mathbf{L} and Laplacian clusters $\{\mathcal{C}_m\}$. Accordingly, neither network symmetry nor local coordinate transformations are needed in order to properly decouple the variational equation.

What the IRR transformation misses is the diffusive nature of the Laplacian-matrix coupling. Due to the IRR transformation’s inability to detect non-symmetry features (e.g., the zero-row-sum of the Laplacian matrix), one has to perform local coordinate transformations to “manually” incorporate that information. An SBD transformation, on the other hand, does not assume any symmetry a priori. It can thus be applied directly to the matrix set $\mathcal{L} = \{\mathbf{E}_1, \dots, \mathbf{E}_M, \mathbf{L}\}$ and automatically takes the additional features of \mathbf{L} into account. As in the case of adjacency-matrix coupling, an SBD transformation can find the optimal separation of perturbation modes for any flow-invariant synchronization pattern under the Laplacian-matrix coupling.

More recently, Ref. [244] introduced the concept of *external equitable partition* as a new way of finding flow-invariant synchronization patterns in Laplacian-matrix coupled systems. An external equitable partition splits a network into *input clusters* such that each node inside a cluster connects to the same number of nodes in another cluster. This definition guarantees that any external equitable partition corresponds to a flow-invariant synchronization pattern and is more general than orbital partitions. One example of an external equitable partition that is not an orbital partition is presented in Fig. 9.1(a). Ref. [244] also proposed the only other widely known symmetry-independent method for

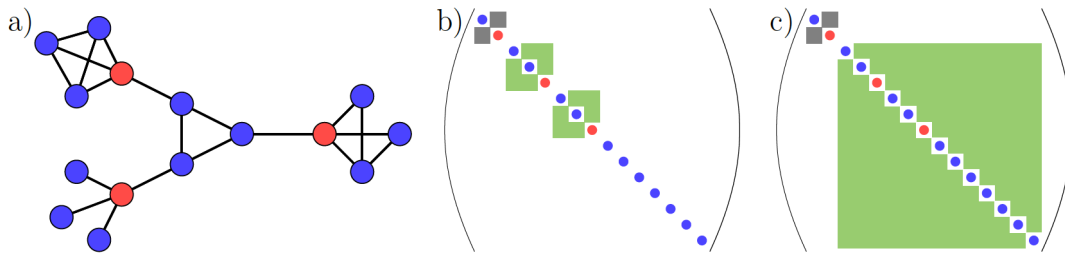


Figure 9.1. Input clusters not induced by network symmetry. (a) External equitable partition that is not an orbital partition. The partition consists of two clusters—colored red and blue, respectively. The corresponding synchronization pattern is flow invariant under Laplacian-matrix coupling despite there being no symmetry between the blue nodes from different cliques or between the three red nodes. (b) Common block structure of $\{\mathbf{E}_1, \mathbf{E}_2, \mathbf{L}\}$ found by an SBD transformation. Colored circles indicate the cluster each perturbation mode belongs to. Gray squares mark the block associated with the parallel perturbations while green squares indicate transverse blocks that are not 1×1 . (c) Common block structure produced by the transformation proposed in Ref. [244].

the stability analysis of cluster synchronization patterns, which is based on the concept of quotient graphs and uses results from algebraic graph theory. While it succeeds in decoupling the parallel and transverse perturbations, it in general fails to further separate the transverse perturbation modes. In contrast, an SBD transformation not only separates the parallel perturbations from the transverse ones but also optimally decouples the transverse perturbations (compare Fig. 9.1(b) to Fig. 9.1(c)). It is still possible to modify the symmetry-based IRR framework for the stability analysis of input clusters by introducing additional local coordinate transformations [257]. However, the SBD framework can be applied more directly to the problem and, as we show below, leads to a much more scalable algorithm.

9.3.5. Computational efficiency and error tolerance

An SBD transformation is not only directly applicable to more synchronization patterns but is also demonstrably more efficient to compute. The computational complexity of the SBD algorithm (Algorithm 1) scales with the network size as $\mathcal{O}(n^3)$. Moreover, the computational cost is independent of the number of symmetries in the network, as demonstrated in Fig. 9.2(a). This gives the SBD algorithm a huge computational advantage over the algorithm based on the IRR transformation [103], which relies on the computation of irreducible group representations and becomes inefficient when a large number of symmetries is present. Since the complete graph with n nodes has the *symmetric group* S_n as its automorphism group and $|S_n| = n!$, the number of symmetries can grow as the factorial of network size n . Combined with the observation that the CPU time scales with the number of symmetries as a power law for the IRR algorithm (orange dots in Fig. 9.2(a)), it follows that the computational cost of the IRR algorithm can grow super-exponentially with the network size. This is further illustrated in Fig. 9.2(b), where the gap between the worst-case CPU time for the two algorithms grows rapidly with n , and the IRR algorithm can be more than six orders of magnitude slower than the SBD algorithm even for networks of moderate sizes (e.g., $n = 14$). We note that another polynomial-time algorithm exists, which applies to symmetry clusters [59]. However, that algorithm was designed to separate clusters that synchronize independently of each other, and thus is not intended to have the same decoupling power as the IRR and SBD algorithms for intertwined clusters and their generalizations.

Another aspect in which the SBD algorithm excels is its error tolerance. Algorithm 1 can be easily adapted to treat cases in which the coupling matrices contain small errors.

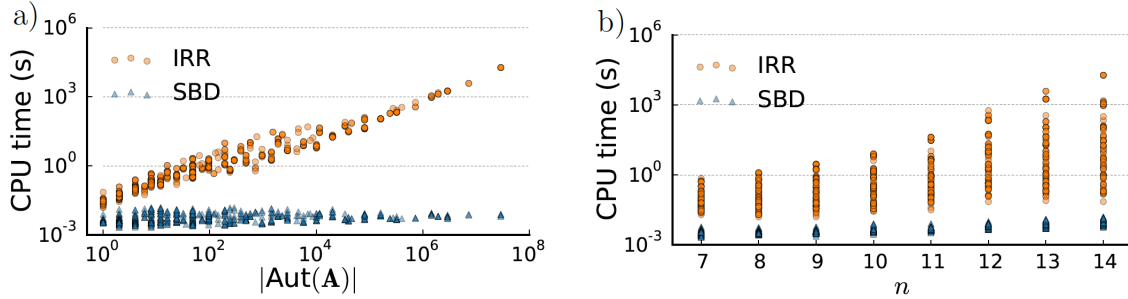


Figure 9.2. Comparing the efficiency of the SBD algorithm (Algorithm 1) and the IRR algorithm [103]. The tests are done using networks of varying sizes formed by randomly removing 2–10 edges from complete graphs. (a) CPU time required to find the IRR transformations (orange) and the SBD transformations (blue) for the symmetry clusters produced by the orbital partition of $\text{Aut}(\mathbf{A})$, plotted against the number of network symmetries. (b) Same data with CPU time plotted as functions of the network size. All tests are done on an Intel Xeon E5-2680 v3 Processor.

In this case one can simply replace the linear dependence tests by approximate linear dependence tests. That is, a vector can be regarded as being linearly independent from a set of vectors if it cannot be expressed as a linear combination of the existing vectors within some preset tolerance. Unlike the IRR algorithm, which works best when the entries in the adjacency matrix are exact, the SBD algorithm, with its error control capability, has the flexibility to deal with noises and uncertainties in real data.

As an example, we consider a 30-node network generated by deleting 6 randomly selected edges from a complete graph. For each entry of the otherwise binary adjacency matrix, we add a mismatch term drawn from a normal distribution with zero mean and a standard deviation of 10^{-3} . These mismatches can model hardware imperfections and measurement errors in real systems. We then equip each node with the dynamics of an electro-optic oscillator used for the first experimental demonstration of chimera states

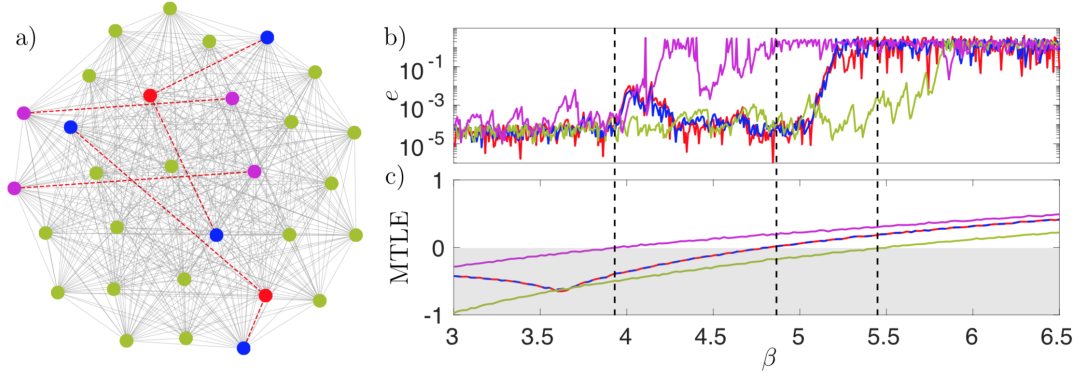


Figure 9.3. Symmetry-breaking bifurcations of cluster synchronization patterns in a dense random network. (a) 30-node network (generated by removing the 6 red dashed edges from a complete graph) colored according to the orbital partition induced by $\text{Aut}(\mathbf{A})$. (b) Synchronization error for each cluster as the bifurcation parameter β is increased slowly from 3 to 6.5. (c) MTLLE for individual clusters calculated from the SBD coordinates. Both (b) and (c) show a sequence of three desynchronization bifurcations as β increases, which are indicated by vertical dashed lines.

[104], described by

$$(9.11) \quad \theta_i(t+1) = \left[\beta I(\theta_i(t)) + \sigma \sum_{j=1}^n A(i,j) I(\theta_j(t)) + \xi_i(t) + \delta \right] \bmod 2\pi,$$

where θ_i is the phase for the i -th oscillator, β is the strength of the self-feedback coupling, and $\delta = 0.525$ is introduced to suppress the trivial solution at the origin. The nonlinear function $I(\theta) = [1 - \cos(\theta)]/2$ models the dynamics of individual oscillators as well as their interaction function. To demonstrate the robustness of our approach in the context of Eq. (9.4), here we also introduce noise terms ξ_i to mimic experimental conditions. The noise terms are Gaussian, have intensity of 10^{-5} , and are independent for each oscillator.

The network admits a flow-invariant synchronization pattern of 4 clusters, as shown in Fig. 9.3 (clusters are indicated by node colors), which is induced by the orbital partition of $\text{Aut}(\mathbf{A})$. The IRR algorithm is not practical for this system due to the mismatch terms in

the adjacency matrix and the huge number of symmetries present, which is generally the case for dense random networks. This particular network has approximately 1.557×10^{20} symmetries, and thus extrapolation from Fig. 9.2 suggests around a billion years of CPU time for the IRR algorithm to find the right transformation. In contrast, Algorithm 1 finds an SBD transformation of $\{\mathbf{E}_1, \dots, \mathbf{E}_4, \mathbf{A}\}$ within one CPU second. Under the SBD coordinates, the matrices share one 4×4 block corresponding to class I perturbation modes, twenty-four 1×1 blocks corresponding to class II perturbation modes, and one 2×2 block corresponding to class III perturbation modes (the red and blue clusters are intertwined)¹⁶.

Based on this decomposition, we calculate the maximal transverse Lyapunov exponent (MTLE) for each cluster over a range of parameter β . We further verify their stabilities by directly simulating equation Eq. (9.11) for β slowly increasing from 3 to 6.5 and calculating the synchronization error in each cluster. We define the synchronization error e_m in the m -th cluster \mathcal{C}_m with n_m nodes as the standard deviation of the phases θ_i in that cluster:

$$e_m = \sqrt{\sum_{j \in \mathcal{C}_m} (\theta_j - \bar{\theta})^2 / n_m},$$

where $\bar{\theta} = \sum_{j \in \mathcal{C}_m} \theta_j / n_m$. Fig. 9.3(b) and (c) show a sequence of three symmetry-breaking bifurcations as β is increased: it starts with the isolated desynchronization of the magenta cluster around $\beta = 3.9$, followed by the concurrent loss of stability of the red and blue clusters around $\beta = 4.9$, and ends with a transition to incoherence in the green cluster just below $\beta = 5.5$.

¹⁶See Section 9.3.3 for the definition of the perturbation classes.

9.4. Extension to nonidentical oscillators and coupling functions

The techniques developed in the previous sections can be easily extended to study cluster synchronization of nonidentical oscillators with disparate coupling functions. In this section, we establish such a generalized formalism and use it to discover permanently stable chimera states in multilayer networks.

A system of (possibly nonidentical) oscillators diffusively coupled through a multilayer network with R different types of interactions can be described by

$$(9.12) \quad \dot{\mathbf{x}}_i = \mathbf{F}_{k(i)}(\mathbf{x}_i) - \sum_{r=1}^R \sigma_r \sum_{j=1}^n \mathbf{L}_r(i, j) \mathbf{H}_r(\mathbf{x}_j),$$

where $\mathbf{F}_{k(i)} : \mathbb{R}^d \rightarrow \mathbb{R}^d$ is the vector field governing the uncoupled dynamics of the i -th oscillator, k indexes the K different functions $\{\mathbf{F}_k\}$ that can be assigned to each oscillator, and \mathbf{L}_r is the Laplacian matrix representing the r -th type of interaction \mathbf{H}_r . Other special cases of Eq. (9.1), corresponding to different choices of the coupling matrices in Eq. (9.12), can be treated similarly, as outlined below.

For any flow-invariant synchronization pattern, a variational equation governing the evolution of $\delta \mathbf{X} = (\delta \mathbf{x}_1^\top, \dots, \delta \mathbf{x}_n^\top)^\top$ can be obtained by linearizing Eq. (9.12) around the corresponding cluster synchronization manifold:

$$(9.13) \quad \delta \dot{\mathbf{X}} = \left(\sum_{m,k} \mathbf{E}_m \mathbf{D}_k \otimes J\mathbf{F}_k(\mathbf{s}_m) - \sum_{m,r} \sigma_r \mathbf{L}_r \mathbf{E}_m \otimes J\mathbf{H}_r(\mathbf{s}_m) \right) \delta \mathbf{X},$$

where \mathbf{s}_m is the synchronization trajectory of the m -th cluster. Recall that \mathbf{E}_m is an $n \times n$ diagonal matrix encoding the nodes inside the m -th cluster. Similarly, let \mathcal{N}_k be the set

of nodes equipped with the k -th function \mathbf{F}_k . Then

$$\mathbf{D}_k(i, i) = \begin{cases} 1, & \text{if } i \in \mathcal{N}_k, \\ 0, & \text{otherwise,} \end{cases}$$

are $n \times n$ diagonal matrices encoding the assignment of heterogeneous nodes, whose sum satisfies $\sum_{k=1}^K \mathbf{D}_k = \mathbf{I}_n$. In order to find the coordinates that optimally decouple Eq. (9.13), one can apply Algorithm 1 to the following matrix set: $\{\mathbf{E}_1, \dots, \mathbf{E}_M, \mathbf{D}_1, \dots, \mathbf{D}_K, \mathbf{L}_1, \dots, \mathbf{L}_R\}$.

Our formalism can be used, in particular, to search for permanently stable chimera states in multilayer networks. Broadly speaking, chimera states and their generalizations refer to states in which coherence and incoherence coexist in a system. In the context of coupled oscillators, a network in a chimera state splits into one group of synchronized oscillators and one group of incoherent oscillators [210, 201]. Over the past two decades, chimera states have been shown to be a general phenomenon [121, 133, 3, 1, 202, 308, 251, 245, 17, 249] that arises robustly in physical systems [104, 285, 159, 39, 287]. Meanwhile, multilayer and multiplex networks have recently emerged as suitable descriptions of many real systems [126, 42]. In the synchronization community, such networks are often used to represent oscillators coupled through multiple types of interactions [263, 118, 254, 67, 41, 280].

Given the relevance of these developments, it is of interest to consider chimera and chimera-like states in networks with two or more types of interactions. There has been previous reports of chimera states in multiplex networks based on numerical simulations

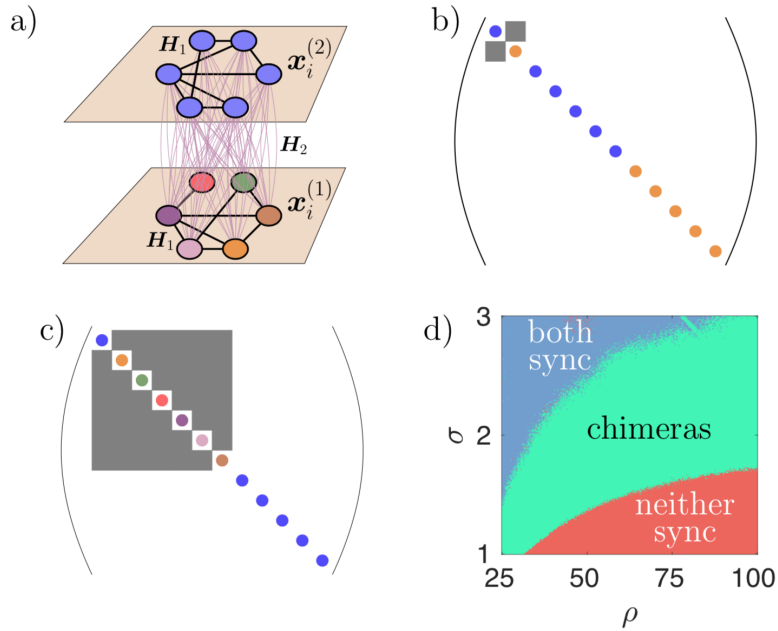


Figure 9.4. Chimera states in a multilayer network. (a) Two-layer network of Lorenz oscillators with different intralayer and interlayer interactions, given by $\mathbf{H}_1 = (0, 0, z)^\top$ and $\mathbf{H}_2 = (0, 0, x)^\top$, respectively. The color coded nodes represent a chimera state in which the first layer is incoherent and the second layer is synchronized. (b) Finest common block structure for the two-cluster state in which both layers are synchronized, which is obtained through an SBD transformation. (c) Finest common block structure for the seven-cluster state depicted in (a), also obtained through an SBD transformation. (d) Diagram in the ρ - σ plane characterizing the stability of the two patterns. The three regions correspond to parameters for which both patterns are unstable (red), both patterns are stable (blue), and only the seven-cluster pattern (i.e., chimera state) is stable (green).

[89, 153]. However, an analytical treatment of their stability is still lacking. The formalism developed here bridges this gap, since many chimera and chimera-like states can be seen as special cluster synchronization patterns [106, 59].

As an example, we consider a multilayer network depicted in Fig. 9.4(a). Each layer consists of six identical Lorenz oscillators interacting through eight connections with the coupling function $\mathbf{H}_1 = (0, 0, z)^\top$. We represent the intralayer connections in the first

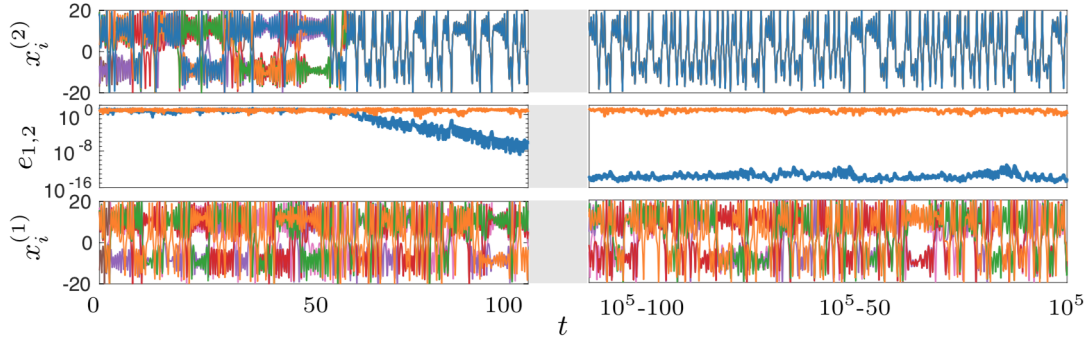


Figure 9.5. Trajectories converging to a chimera state in which layer 2 synchronizes and layer 1 remains incoherent for the system in Fig. 9.4. Top and bottom panels: trajectories for oscillators in each layer. Each oscillator in one layer is assigned a different color. When a layer is synchronized, only one color is visible since all trajectories overlap. Middle panel: synchronization errors e_1 for the first layer (orange) and e_2 for the second layer (blue). The parameters used are $\rho = 60$ and $\sigma = 2$.

(second) layer using the Laplacian matrix $\mathbf{L}_1^{(1)}$ ($\mathbf{L}_1^{(2)}$). In addition, the two layers are all-to-all coupled through the coupling function $\mathbf{H}_2 = (0, 0, x)^\top$. The oscillators in the first layer are thus described by the equations

$$\begin{aligned}
 \dot{x}_i^{(1)} &= \alpha(y_i^{(1)} - x_i^{(1)}), \\
 \dot{y}_i^{(1)} &= x_i^{(1)}(\rho - z_i^{(1)}) - y_i^{(1)}, \\
 \dot{z}_i^{(1)} &= x_i^{(1)}y_i^{(1)} - \beta z_i^{(1)} - \sigma_1 \sum_j \mathbf{L}_1^{(1)}(i, j)z_j^{(1)} + \sigma_2 \sum_j (x_j^{(2)} - x_i^{(1)}),
 \end{aligned}
 \tag{9.14}$$

where we set $\alpha = 10$, $\beta = 2$, $\sigma_1 = \sigma$, and $\sigma_2 = 0.2\sigma$, leaving the parameters ρ and σ to be varied. The oscillators in the second layer are described by similar equations.

To search for chimera states where one layer is synchronized and the other is incoherent, we need to analyze the linear stability of two different cluster synchronization patterns (both formed by input clusters). Specifically, the two-cluster state in which both

layers are coherent ($\mathbf{x}_1^{(1)} = \dots = \mathbf{x}_6^{(1)}, \mathbf{x}_1^{(2)} = \dots = \mathbf{x}_6^{(2)}$) should be unstable while the seven-cluster state $\mathbf{x}_1^{(1)} \neq \dots \neq \mathbf{x}_6^{(1)}, \mathbf{x}_1^{(2)} = \dots = \mathbf{x}_6^{(2)}$ (each cluster represented by a different color in Fig. 9.4(a)) should be stable. In both cases, the cluster synchronization manifold can be found by simulating Lorenz oscillators coupled through the corresponding quotient network. Applying the SBD algorithm to the two-cluster state leads to a common block structure for the matrices in the variational equation Eq. (9.13), as shown in Fig. 9.4(b), where a diagonal entry is colored orange if the corresponding perturbation mode belongs to the first layer and is colored blue if the mode belongs to the second layer. In this case, the transverse perturbation modes are fully decoupled and the 2×2 block corresponds to perturbations inside the cluster synchronization subspace. Similarly, the common block structure for the seven-cluster state is shown in Fig. 9.4(c). In this case, we have a 7×7 block representing the parallel perturbations and five 1×1 blocks related to the transverse perturbation modes for the coherent layer. It is straightforward to perform stability analysis under these SBD coordinates. We show the results in the ρ - σ diagram of Fig. 9.4(d). Red indicates parameters for which both patterns are unstable while blue indicates where both patterns are stable. Chimera states are found in the green region, where only the seven-cluster pattern is stable.

A representative trajectory of the chimera state for $\rho = 60$ and $\sigma = 2$ is shown in Fig. 9.5. The lower and upper panels show the dynamics of x variables for oscillators in each layer, while the middle panel shows their respective synchronization error. This chimera state is permanently stable and can emerge from random initial conditions.

9.5. Concluding remarks

The framework established here utilizes the finest simultaneous block diagonalization of matrices to study cluster synchronization patterns in complex networks. This framework has its theoretical foundation rooted in the theory of matrix $*$ -algebra and does not rely on symmetry information in the system. This results in an algorithm that is faster, simpler, and more robust than the state-of-the-art algorithm based on irreducible representations of network symmetry. In particular, the SBD framework enjoys the following advantages over the IRR framework and its variants:

- (1) It applies straightforwardly to *any* flow-invariant synchronization pattern, including those formed by symmetry clusters, Laplacian clusters, and input clusters.
- (2) It can easily treat nonidentical oscillators and oscillators coupled through multiple types of interactions.
- (3) It is highly scalable because the SBD transformations can be calculated much more efficiently than the IRR transformations, which enables the stability analysis of complex synchronization patterns in large networks and in networks with a high degree of symmetry.
- (4) It is especially suited for practical applications because Algorithm 1 is robust against uncertainties in the network structure typical of real systems.

A Matlab implementation of Algorithm 1 is available online and comes with illustrative examples of use.¹⁷ The utility of this algorithm is not limited to network synchronization problems. It can be applied, for instance, to reduce the complexity of many problems in

¹⁷See <https://github.com/y-z-zhang/net-sync-sym/>.

which multiple matrices are involved, such as in the control of network systems and in semidefinite programming [178].

An important open problem for future research concerns the case of directed networks. When considering cluster synchronization patterns in directed networks, two complications arise. The first concerns the identification of valid clusters. Directed networks support many flow-invariant synchronization patterns that do not result from orbital partitions. Thus, it is often the case that a synchronization pattern of interest will not be identified by a software based on computational group theory. Indeed, any partition of the nodes that satisfies the balanced equivalence relations [95, 272] gives rise to a flow-invariant cluster synchronization pattern.

The second difficulty involves finding an optimal coordinate system to separate perturbation modes in the stability analysis. Since in directed networks the coupling matrices are no longer self-adjoint, one must consider the corresponding matrix algebra (as opposed to the matrix $*$ -algebra) to obtain a finest simultaneous block diagonalization of matrices in the variational equation. Unlike matrix $*$ -algebras, matrix algebras are no longer closed under the conjugate transpose operation and are generally not semisimple algebras. This renders the Artin-Wedderburn theorem inapplicable and introduces “bad” elements called radicals [136] such that, in general, matrix algebras cannot be decomposed into the direct sum of irreducible matrix algebras. Thus, a promising direction for future research is to generalize the current algorithm to find a finest simultaneous block diagonalization for matrices that are not necessarily self-adjoint.

CHAPTER 10

Unified Treatment of Dynamical Processes on Higher-Order and Temporal Networks

For the past two decades, networks have emerged as a versatile description of interconnected complex systems. However, it is also increasingly clear that the original formulation of a static network representing a single type of pairwise interaction has its limitations. For this reason, the original formulation has been generalized in different directions, including hypergraphs that account for higher-order interactions, multilayer networks that accommodate multiple types of interactions, and temporal networks for interaction patterns that change over time. Naturally, with the increased descriptive power comes increased analytical complexity, especially for dynamical processes on those generalized networks. This renders many of the traditional tools, such as master stability functions, inapplicable in the new settings. Here, we first establish a natural generalization of master stability functions that enables analysis of arbitrary synchronization patterns in hypergraphs. It simplifies the stability analysis to the fullest extent possible by finding the finest simultaneous block diagonalization (SBD) of matrices in the variational equation. We demonstrate the utility of the SBD framework by applying it to real datasets describing the macaque brain connectome and to characterize chimera states arising from nonpairwise interactions. By exploiting similar underlying mathematical

structure, our results can be easily extended to other dynamical processes (diffusion, random walk, etc.) and other generalized networks (e.g., temporal networks). Such a unified framework will facilitate a deeper understanding of dynamical processes on generalized networks frequently encountered in the real world.

This chapter is based on the joint work with Vito Latora and Adilson E. Motter.

10.1. Background

Many biological and technological networks show intricate synchronization patterns, where one or more internally coherent but mutually independent clusters coexist [272, 30, 62, 187, 302, 238, 82]. Maintaining the desired dynamical patterns is critical to the function of those networked systems [248]. For instance, long-range synchronization between the prefrontal cortex and the temporal cortex has been shown to improve working memory in older adults [232]. Whether a synchronization pattern can persist ultimately depends on its stability, which is determined by the Lyapunov exponents transverse to the cluster synchronization manifold. The case of globally synchronization was readily simplified by the master stability function (MSF) formalism [217], which separates the effect of local dynamics and network structure through the diagonalization of the coupling matrix. The analysis of complex dynamical patterns beyond global synchronization, however, is much more challenging due to the existence of additional nontrivial matrices in the variational equation, which precludes its decoupling through simple diagonalization of any single matrix. This issue was partially addressed with the introduction of sophisticated methods utilizing irreducible representations of network symmetry [219] and was further

resolved using simpler and more versatile methods based on matrix $*$ -algebras (which are not encumbered by symmetry restrictions) [315].

Up until now, these endeavors have focused exclusively on networks with pairwise interactions. However, many real-world systems cannot be adequately described by these traditional networks [137]. Very often, three or more nodes can influence each other in a nonlinear fashion such that the many-body interaction cannot be broken down into the sum of pairwise interactions [25]. Examples include scientific collaborations [214], random walks and diffusion [243, 56, 64], social and biological contagion [221, 117, 162, 63, 267], ecological communities [19, 166, 143], functional brain networks [222, 90, 231, 259], gene, drug, and protein interaction networks [134, 281, 76], and consensus dynamics [182]. In these cases, hypergraphs [34] or simplicial complexes [111] are needed to accurately describe the higher-order interactions.

Recently, phase oscillators coupled through non-pairwise interactions have received significant attention [279, 38, 260, 261, 306, 57, 146, 171], partly driven by the fact that such systems arise naturally from phase reduction beyond the first order [142] and have been observed in experiments [163]. However, the dynamics of more general oscillators with non-pairwise interactions, especially when the collective dynamical pattern is more complex than global synchronization, remains underexplored. This is in no small part due to the technical difficulties associated with such analysis in the context of hypergraphs.

In this chapter, we generalize the simultaneous block diagonalization (SBD) framework first developed in Ref. [315] to simplify the stability analysis of synchronization patterns

formed by general oscillators on hypergraphs. Furthermore, we show that the same technique can be easily extended to temporal networks, providing a unified framework for the treatment of dynamical processes on many generalized networks.

10.2. Simplifying master stability functions for hypergraphs

Hypergraphs and simplicial complexes provide general languages to study networks with higher-order interactions and have been widely adopted in the literature [32, 31]. However, the associated tensors describing those higher-order structures are much more cumbersome to work with than matrices, especially when combined with the analysis of dynamical processes. Naturally, there have been several attempts to generalize the MSF formalism to those settings, for which different variants of an aggregated Laplacian have been proposed [177, 146, 57, 64]. The aggregated Laplacian captures the interactions of all orders in a single matrix, whose spectral decomposition allows the stability analysis to be decoupled into structural and dynamical components, just like the MSF in traditional networks. However, such powerful reduction comes with inevitable cost—simplifying assumptions must be made about the network structure (e.g., all-to-all coupling), node dynamics (e.g., fixed points), and/or interaction functions (e.g., linear) in order for the aggregation to a single matrix to be valid.

Here, for the ease of presentation and without loss of generality, we first focus on networks with interactions that involve up to three oscillators simultaneously:

$$(10.1) \quad \dot{\mathbf{x}}_i = \mathbf{F}(\mathbf{x}_i) + \sigma_1 \sum_{j=1}^N A_{ij}^{(1)} \mathbf{H}^{(1)}(\mathbf{x}_i, \mathbf{x}_j) + \sigma_2 \sum_{j=1}^N \sum_{k=1}^N A_{ijk}^{(2)} \mathbf{H}^{(2)}(\mathbf{x}_i, \mathbf{x}_j, \mathbf{x}_k).$$

The adjacency matrix $\mathbf{A}^{(1)}$ and adjacency tensor $\mathbf{A}^{(2)}$ represent the pairwise and the three-body interactions, respectively. The coupling is assumed to be diffusive, that is, $\mathbf{H}^{(1)}(\mathbf{x}^s, \mathbf{x}^s) = 0$ and $\mathbf{H}^{(2)}(\mathbf{x}^s, \mathbf{x}^s, \mathbf{x}^s) = 0$ for any synchronous state \mathbf{x}^s . The challenges posed by the higher-order interactions are demonstrated through the analysis presented in Ref. [84], where Eq. (10.1) is considered without the aforementioned restrictions. A key insight in that study is that one can define the generalized Laplacian for the adjacency tensor

$$(10.2) \quad L_{ij}^{(2)} = \begin{cases} -\sum_k A_{ijk}^{(2)} & \text{for } i \neq j, \\ -\sum_{j \neq i} L_{ij}^{(2)} & \text{for } i = j, \end{cases}$$

so that the variational equation for the global synchronization state can be written as

$$(10.3) \quad \dot{\boldsymbol{\delta}} = \left(\mathbf{I}_d \otimes J\mathbf{F} - \sigma_1 \mathbf{L}^{(1)} \otimes J\mathbf{H}^{(1)} - \sigma_2 \mathbf{L}^{(2)} \otimes J\mathbf{H}^{(2)} \right) \boldsymbol{\delta}.$$

Here, $\boldsymbol{\delta}$ is the deviation from the synchronization trajectory \mathbf{x}^s , \mathbf{I}_d is an identity matrix, \otimes is the Kronecker product,

$$J\mathbf{H}^{(1)} = \partial_{\mathbf{x}_j} \mathbf{H}^{(1)}(\mathbf{x}_i, \mathbf{x}_j) |_{(\mathbf{x}^s, \mathbf{x}^s)},$$

and

$$J\mathbf{H}^{(2)} = \partial_{\mathbf{x}_j} \mathbf{H}^{(2)}(\mathbf{x}_i, \mathbf{x}_j, \mathbf{x}_k) |_{(\mathbf{x}^s, \mathbf{x}^s, \mathbf{x}^s)} + \partial_{\mathbf{x}_k} \mathbf{H}^{(2)}(\mathbf{x}_i, \mathbf{x}_j, \mathbf{x}_k) |_{(\mathbf{x}^s, \mathbf{x}^s, \mathbf{x}^s)}.$$

One can then seek to separate the parallel and transverse perturbations by diagonalizing $\mathbf{L}^{(1)}$. However, this often does not lead to the optimal decoupling of Eq. (10.3), whose

transverse perturbations can potentially be further divided into lower-dimensional flow-invariant subspaces. This is especially true for simplicial complexes, whose generalized Laplacians are not independent from each other. In fact, $\mathbf{L}^{(m)}$ for $m \geq 2$ are entirely determined by $\mathbf{L}^{(1)}$ for simplicial complexes.

We solve this problem by finding coordinates that block diagonalize $\mathbf{L}^{(1)}$ and $\mathbf{L}^{(2)}$ simultaneously. For this purpose, we developed an algorithm to find an orthogonal transformation matrix \mathbf{P} that reveals the *finest* SBD of any given set of symmetric matrices, which in turn gives rise to the optimal separation of perturbation modes in Eq. (10.3). Given a set of matrices $\mathcal{B} = \{\mathbf{B}^{(1)}, \mathbf{B}^{(2)}, \dots, \mathbf{B}^{(M)}\}$, the SBD Algorithm consists of two simple steps:

- i) Find the eigenvectors \mathbf{v}_i of a symmetric matrix $\mathbf{L} = \sum_m \xi_m (\mathbf{B}^{(m)} + (\mathbf{B}^{(m)})^\top)$, where ξ_m are independent random numbers drawn from a Gaussian distribution.
- ii) Order \mathbf{v}_i to form a basis (i.e., the orthogonal transformation matrix \mathbf{P}) such that the base vectors corresponding to the same common block are next to each other.

This strategy is based on the fact that each \mathbf{v}_i has probability 1 to be inside a minimal invariant subspace under the action of \mathcal{B} . The SBD algorithm proposed here is either simpler or faster than existing algorithms [150, 151, 315] and is available online as Matlab and Python packages¹⁸.

To establish the utility of SBD transformations, we apply it to simplicial complexes built on random networks with varying degrees of symmetry. We measure the reduction in complexity achieved through SBD transformations using $r(\alpha) = \sum_i n_i^\alpha / N^\alpha$, where n_i is the size of the i th common block between $\mathbf{P}\mathbf{L}^{(1)}\mathbf{P}^\top$ and $\mathbf{P}\mathbf{L}^{(2)}\mathbf{P}^\top$. If the computational

¹⁸<https://github.com/y-z-zhang/SBD>

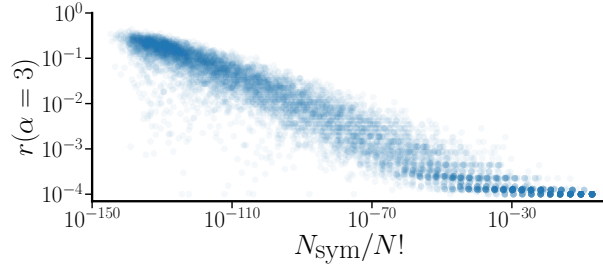


Figure 10.1. Applying SBD transformations to the first two generalized Laplacians of simplicial complexes generated from 8000 random networks of size $N = 100$. Each dot represents a network realization. Larger concentration of dots is naturally reflected through darker shades. The reduction in complexity, as measured by $r(\alpha) = \sum_i n_i^\alpha / N^\alpha$, scales algebraically with the number of symmetries N_{sym} in a network.

complexity of analyzing Eq. (10.3) in its original form scales as $\mathcal{O}(N^\alpha)$, then $r(\alpha)$ gives the fraction of time needed to analyze Eq. (10.3) in its SBD decoupled form. In Fig. 10.1, we set¹⁹ $\alpha = 3$ and plot it against the number of network symmetries N_{sym} normalized by the maximal number of possible symmetries $N!$. From 8000 independent network realizations for $N = 100$, we see that SBD transformations generally reduce more complexity when there is more symmetry in the network and can speed up computations by up to four orders of magnitudes already for modest network size.

To demonstrate our framework on a real dataset, we apply SBD transformations to a macaque brain connectome [239]. Since the network data includes directional binary links, we construct a directed simplicial complex using the following rule: $A_{ijk} = 1$ if and only if $A_{ij} = 1$, $A_{ik} = 1$, and $A_{jk} = 1$. This dataset is particularly challenging since the generalized Laplacians are non-diagonalizable. Figure 10.2 shows that SBD

¹⁹Given that the computational complexity of finding eigenvalues of an $N \times N$ matrix lies between $\mathcal{O}(N^2)$ and $\mathcal{O}(N^3)$, it is reasonable to assume $\alpha = 3$ when performing stability analysis (i.e., calculating Lyapunov exponents) by solving Eqs. (10.1) and (10.3). Furthermore, our results do not depend sensitively on the choice of α .

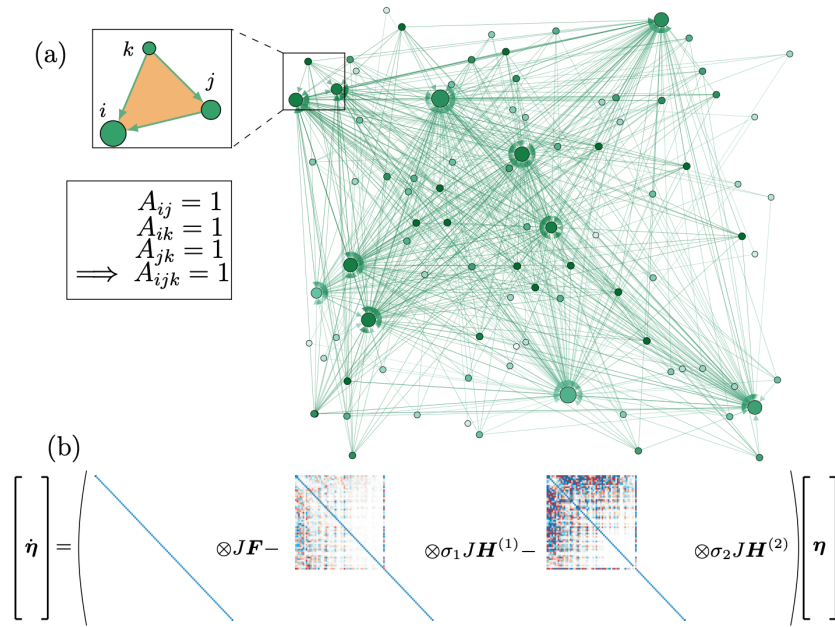


Figure 10.2. SBD transformations applied to a directed simplicial complex constructed from the macaque brain connectome depicted in (a). A visualization of decoupled Eq. (10.3) after the transformation is given in (b), which has been simplified into a 59×59 block and thirty-two 1×1 blocks.

transformations still perform well in this case and give significant reduction in complexity, as evidenced by the common block structure depicted in (b). Other rules of constructing directed simplicial complexes, such as $A_{ij} = 1, A_{jk} = 1, A_{ki} = 1 \implies A_{ijk} = 1$, admits similar reductions.

10.3. Chimera states arising from higher-order interactions

The techniques above can be easily extended from global synchronization to more complex cluster synchronization patterns. This is achieved by adding the following diagonal matrices $\mathbf{D}^{(k)}$ to be simultaneously block diagonalized with the generalized Laplacians

$\mathbf{L}^{(m)}$:

$$(10.4) \quad D_{ii}^{(k)} = \begin{cases} 1, & \text{if node } i \in C_k \\ 0, & \text{otherwise,} \end{cases}$$

where C_k represents the k th cluster. The corresponding variational equation to be block diagonalized then reads (we now consider the most general case involving interactions of any order):

$$(10.5) \quad \dot{\boldsymbol{\delta}} = \left\{ \sum_k \mathbf{D}^{(k)} \otimes J\mathbf{F}(\mathbf{x}^{s_k}) - \sum_{m,k} \sigma_m \mathbf{L}^{(m)} \mathbf{D}^{(k)} \otimes J\mathbf{H}^{(m)}(\mathbf{x}^{s_k}) \right\} \boldsymbol{\delta},$$

where \mathbf{x}^{s_k} is the synchronized state of the oscillators in the k th cluster. Since $\mathbf{D}^{(k)}$ and $\mathbf{L}^{(m)}$ are the only nontrivial matrices in the variational equation, their simultaneous block diagonalization will reveal independent perturbation modes and simplify stability analysis. In particular, SBD transformations can always separate the perturbation modes parallel and transverse to the cluster synchronization manifold, and decouple transverse perturbations to the fullest extent possible.

As an application to nontrivial synchronization patterns, we study chimera states [210, 201] in hypergraphs. The hypergraph in Fig. 10.3(a) consists of two clusters of optoelectronic oscillators. Each cluster is a simplicial complex—a node is coupled to its four nearest neighbors through pairwise interaction of strength σ_1 and it also participates in three-body interaction of strength σ_2 . The two clusters are all-to-all coupled through weaker links of strength $\sigma_1/5$. The individual oscillators are modeled as discrete maps $x_i[t+1] = \beta \sin^2(x_i[t] + \pi/4)$ and have been recently used in the experimental demonstration of globally attractive chimeras with power-law switching dynamics [316]. For the

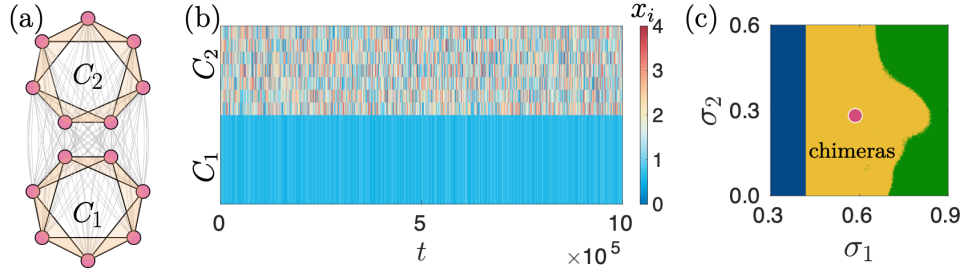


Figure 10.3. Chimera state arising from higher-order interactions. (a) Two coupled simplicial complexes of optoelectronic oscillators. The three-body interactions are indicated by yellow triangles. (b) Simulation of the optoelectronic system for $\sigma_1 = 0.6$ and $\sigma_2 = 0.3$ [purple dot in (c)], illustrating the dynamics of a chimera state. (c) Linear stability analysis of full synchrony and chimera states for a range of pairwise interaction strength σ_1 and three-body interaction strength σ_2 . Blue: stable full synchrony; yellow: stable chimera; green: incoherence.

pairwise interaction, we set $H^{(1)}(x_i, x_j) = \sin^2(x_j + \phi) - \sin^2(x_i + \phi)$. For the three-body interaction, we set $H^{(2)}(x_i, x_j, x_k) = \sin^2(x_j + x_k - 2x_i)$. The full dynamical equation can be summarized as follows:

$$\begin{aligned}
 (10.6) \quad x_i[t+1] &= \beta \sin^2\left(x_i[t] + \frac{\pi}{4}\right) \\
 &+ \sigma_1 \sum_{j=1}^N A_{ij}^{(1)} \left(\sin^2\left(x_j[t] + \frac{\pi}{4}\right) - \sin^2\left(x_i[t] + \frac{\pi}{4}\right) \right) \\
 &+ \sigma_2 \sum_{j=1}^N \sum_{k=1}^N A_{ijk}^{(2)} \sin^2(x_j[t] + x_k[t] - 2x_i[t]),
 \end{aligned}$$

where β is the self-feedback strength of the oscillators.

Figure 10.3(b) shows simulations of Eq. (10.6) for $\beta = 1.1$, $\sigma_1 = 0.6$, and $\sigma_2 = 0.3$. For the chosen initial condition, the system settles into a chimera state in which the first cluster is fully synchronized and the second cluster is incoherent. We then perform stability analysis in the σ_1 - σ_2 parameter space for fixed β to map out the region where chimera

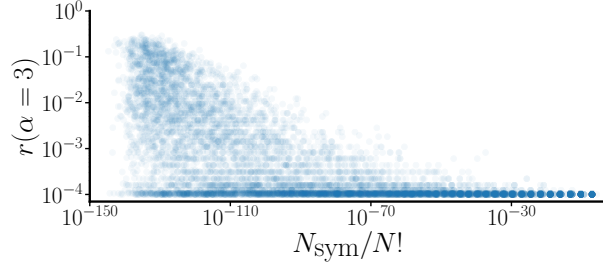


Figure 10.4. Equivalent of Fig. 10.1 for temporal networks. Each of the 8000 dots represents a temporal network of $N = 100$ nodes, in which a single unreliable link turns on and off over time.

states are linearly stable. In this case, the SBD transformation completely decouples the transverse perturbations into 1×1 blocks. As can be seen from Fig. 10.3(c), when σ_1 is small, three-body interaction has no effect on the emergence of chimera states—the boundary between full sync (blue) and chimera (yellow) is independent of σ_2 . On the other hand, for large σ_1 , the three-body interactions become relevant for intermediate σ_2 around 0.3, where it gives rise to chimera states that would otherwise not exist. Such chimera states are unstable when oscillators are coupled only through pairwise interactions.

10.4. The case of temporal networks

Another class of systems that lend itself naturally to the SBD framework are temporal networks [114]. Such networks are ubiquitous in nature and society [9, 212] and their time-varying nature has been shown to significantly alter many dynamical characteristics, including controllability [144] and synchronizability [10, 119]. To keep the formalism to the minimum, we focus on global synchronization, but the same methods can be used to analyze more complex synchronization patterns by including additional diagonal matrices $D^{(k)}$.

Consider a temporal network that switches between M different connection patterns described by $\mathbf{L}^{(m)}$,

$$(10.7) \quad \dot{\mathbf{x}}_i = \mathbf{F}(\mathbf{x}_i) - \sigma \sum_{m=1}^M \Gamma_m(t) \sum_{j=1}^N L_{ij}^{(m)} \mathbf{h}^{(m)}(\mathbf{x}_j),$$

where $\Gamma_m(t)$ are switching functions that encode the temporal evolution of the network. At any given t , we have $\Gamma_m(t) = 1$ for $m = k$, where k is the connection pattern that is active at that time, and $\Gamma_m(t) = 0$ for all $m \neq k$.

Synchronization stability in temporal networks is also governed by variational equations with similar mathematical structure:

$$(10.8) \quad \dot{\boldsymbol{\delta}} = \left(\mathbf{I}_d \otimes J\mathbf{F}(\mathbf{x}^s) - \sigma \sum_{m=1}^M \Gamma_m(t) \mathbf{L}^{(m)} \otimes J\mathbf{h}^{(m)}(\mathbf{x}^s) \right) \boldsymbol{\delta}.$$

Thus, once again the stability analysis can be simplified by simultaneously block diagonalizing $\mathbf{L}^{(m)}$ to optimally decouple Eq. (10.8). This framework generalizes the one developed in Ref. [43], which assumes the set of all $\mathbf{L}^{(m)}$ to be commutative. It also does not require separation of time scales between the evolution of the network structure and the internal dynamics of oscillators (e.g., the fast switching limit), which was assumed in various blinking models in exchange of analytical insight [28, 273]. Therefore, a broad range of systems, including important classes of temporal networks previously considered, can be examined within the same unified framework.

As an application, we consider diffusively-coupled networks that contains a single unreliable connection, which fails from time to time. Such scenarios are frequently encountered in power grids and other engineered systems [58]. This class of temporal networks can be described by two Laplacian matrices: $\mathbf{L}^{(1)}$ for the network with the unreliable link active,

and $\mathbf{L}^{(2)}$ for the network with the unreliable link inactive. In Fig. 10.4, we consider such temporal networks based on random networks with varying degrees of symmetry. Similarly to Fig. 10.1, we observe more significant reduction in complexity in networks that have more symmetries. Although in this case even for networks with few symmetries it is possible to achieve sizable (up to 10000 fold) reduction in computational cost.

10.5. Concluding remarks

In this chapter we established SBD transformations as a versatile tool to analyze complex synchronization patterns in generalized networks with higher-order and/or time-varying interactions. It should be noted that our framework can also be applied in the analysis of other dynamical processes on generalized networks, such as diffusion and random walk. Indeed, the equations describing many such processes often involve several nontrivial matrices, whose simultaneous block diagonalization naturally leads to the decoupling of the equation and simplification of the analysis. In all cases, our SBD approach is highly scalable, whose computational complexity is dominated by the cost of finding the eigenvectors of an $N \times N$ symmetric matrix. Moreover, for a given generalized network, the transformation only needs to be performed once and the same coordinates can be reused for different values of node parameters.

CHAPTER 11

Outlook

As a community that studies complex systems, we have come a long way from the early days of lattice network models and mean-field theories. Along the way, we have gradually incorporated more nuanced features into our models, including network heterogeneity, rich node annotations, higher-order interactions, multilayer structures, and cluster synchronization patterns. At any given time, there will always be systems that are well understood and systems that are out of reach due to their complexity. The most fruitful research opportunities will most likely lie at the boundary between the two, which consists of the *simplest* complex systems into which we can obtain valuable insight. Next we discuss some promising directions for the three main topics covered in this dissertation and where they fit in the broader research landscape.

The differences among interacting nodes, especially for those with dynamics more complex than Kuramoto oscillators, is a feature that presents abundant new opportunities [173]. The work in Chapters 2 to 6 only revealed the tip of the iceberg in terms of the effect of heterogeneity on collective dynamics. In particular, characterizing when and how can such heterogeneity give rise to more synchronized behavior is a key challenge yet to be solved. A system-independent explanation of this phenomenon has the potential to transform our understanding of how order emerges in networked systems.

On the other hand, the chimera states discussed in Chapters 7 and 8 have been the focus of intensive research efforts for quite some time [210]. However, the significance of

chimeras in natural systems is still much debated and needs further elucidation. A fertile ground for this line of research is the brain, where chimera-like states have been observed [12, 22]. What are the physiological and cognitive functions of these chimera-like dynamics? What is driving the switching between chimeras and other partially synchronous states in the brains of dolphins and songbirds? How can we bridge the gap between theoretical models of chimeras and the (much messier) chimera-like states in living organisms? These questions could serve as a driving force for future chimera research.

We have shown in Chapters 4, 9 and 10 that the SBD formalism is versatile enough to analyze complex synchronization patterns in networks with higher-order, multilayer, and temporal interactions. The next frontier to which this formalism could be expanded is adaptive networks, in which the network structure is not only time-varying but its evolution is also coupled to the dynamical states of the nodes [100]. Such two-way influence between the network structure and network dynamics is important for many collective processes, including epidemic spreading [101], consensus seeking [130], and synchronization [35]. A unified framework that can analyze these co-evolutionary dynamics under a general setting would undoubtedly advance our understanding of many adaptive systems.

The interplay between network science and nonlinear dynamics has been fruitful for the past three decades. The cross-fertilization between the two fields, which forms the basis of this dissertation work, will only accelerate moving forward. During this exciting time, it is up to all of us to build new tools and find new connections so that more and more complex systems will eventually become simple.

References

- [1] ABRAMS, D. M., MIROLLO, R., STROGATZ, S. H., AND WILEY, D. A. Solvable model for chimera states of coupled oscillators. *Phys. Rev. Lett.* *101*, 8 (2008), 084103.
- [2] ABRAMS, D. M., PECORA, L. M., AND MOTTER, A. E. Introduction to focus issue: Patterns of network synchronization. *Chaos* *26*, 9 (2016), 094601.
- [3] ABRAMS, D. M., AND STROGATZ, S. H. Chimera states for coupled oscillators. *Phys. Rev. Lett.* *93*, 17 (2004), 174102.
- [4] ACHARYYA, S., AND AMRITKAR, R. Synchronization of coupled nonidentical dynamical systems. *EPL* *99*, 4 (2012), 40005.
- [5] ACHARYYA, S., AND AMRITKAR, R. Synchronization of nearly identical dynamical systems: Size instability. *Phys. Rev. E Review E* *92*, 5 (2015), 052902.
- [6] AGUIAR, M., ASHWIN, P., DIAS, A., AND FIELD, M. Dynamics of coupled cell networks: Synchrony, heteroclinic cycles and inflation. *J. Nonlinear Sci.* *21*, 2 (2011), 271–323.
- [7] AGUIRRE, J., VIANA, R. L., AND SANJUÁN, M. A. F. Fractal structures in nonlinear dynamics. *Rev. Mod. Phys.* *81*, 1 (2009), 333–386.
- [8] ALEXANDER, J., YORKE, J. A., YOU, Z., AND KAN, I. Riddled basins. *Int. J. Bifurcation Chaos* *2*, 04 (1992), 795–813.
- [9] ALMAAS, E., KOVACS, B., VICSEK, T., OLTVAI, Z. N., AND BARABÁSI, A.-L. Global organization of metabolic fluxes in the bacterium *escherichia coli*. *Nature* *427*, 6977 (2004), 839–843.
- [10] AMRITKAR, R., AND HU, C.-K. Synchronized state of coupled dynamics on time-varying networks. *Chaos* *16*, 1 (2006), 015117.
- [11] ANDERSON, P. W. More is different. *Science* *177*, 4047 (1972), 393–396.

- [12] ANDRZEJAK, R. G., RUMMEL, C., MORMANN, F., AND SCHINDLER, K. All together now: Analogies between chimera state collapses and epileptic seizures. *Sci. Rep.* 6 (2016), 23000.
- [13] ARENAS, A., DÍAZ-GUILERA, A., KURTHS, J., MORENO, Y., AND ZHOU, C. Synchronization in complex networks. *Phys. Rep.* 469, 3 (2008), 93–153.
- [14] ARGYRIS, A., BOURMPOS, M., AND SYVRIDIS, D. Experimental synchrony of semiconductor lasers in coupled networks. *Opt. Exp.* 24, 5 (2016), 5600–5614.
- [15] ASHWIN, P., BUDESCU, J., AND STEWART, I. Bubbling of attractors and synchronisation of chaotic oscillators. *Phys. Lett. A* 193, 2 (1994), 126–139.
- [16] ASHWIN, P., BUDESCU, J., AND STEWART, I. From attractor to chaotic saddle: A tale of transverse instability. *Nonlinearity* 9, 3 (1996), 703–737.
- [17] ASHWIN, P., AND BURLYKO, O. Weak chimeras in minimal networks of coupled phase oscillators. *Chaos* 25, 1 (2015), 013106.
- [18] ATAY, F. M., JOST, J., AND WENDE, A. Delays, connection topology, and synchronization of coupled chaotic maps. *Phys. Rev. Lett.* 92, 14 (2004), 144101.
- [19] BAIREY, E., KELSIC, E. D., AND KISHONY, R. High-order species interactions shape ecosystem diversity. *Nat. Commun.* 7, 1 (2016), 1–7.
- [20] BAK, P., TANG, C., AND WIESENFELD, K. Self-organized criticality: An explanation of the $1/f$ noise. *Phys. Rev. Lett.* 59, 4 (1987), 381–384.
- [21] BAK, P., TANG, C., AND WIESENFELD, K. Self-organized criticality. *Phys. Rev. A* 38, 1 (1988), 364–374.
- [22] BANSAL, K., GARCIA, J. O., TOMPSON, S. H., VERSTYNEN, T., VETTEL, J. M., AND MULDOON, S. F. Cognitive chimera states in human brain networks. *Sci. Adv.* 5, 4 (2019), eaau8535.
- [23] BARABÁSI, A.-L., ET AL. *Network science*. Cambridge university press, 2016.
- [24] BARAHONA, M., AND PECORA, L. M. Synchronization in small-world systems. *Phys. Rev. Lett.* 89, 5 (2002), 054101.
- [25] BATTISTON, F., CENCETTI, G., IACOPINI, I., LATORA, V., LUCAS, M., PATANIA, A., YOUNG, J.-G., AND PETRI, G. Networks beyond pairwise interactions: structure and dynamics. *arXiv preprint arXiv:2006.01764* (2020).

- [26] BELYKH, I., BELYKH, V., NEVIDIN, K., AND HASLER, M. Persistent clusters in lattices of coupled nonidentical chaotic systems. *Chaos* 13, 1 (2003), 165–178.
- [27] BELYKH, I., DE LANGE, E., AND HASLER, M. Synchronization of bursting neurons: What matters in the network topology. *Phys. Rev. Lett.* 94, 18 (2005), 188101.
- [28] BELYKH, I. V., BELYKH, V. N., AND HASLER, M. Blinking model and synchronization in small-world networks with a time-varying coupling. *Physica D* 195, 1-2 (2004), 188–206.
- [29] BELYKH, V. N., BELYKH, I. V., AND MOSEKILDE, E. Cluster synchronization modes in an ensemble of coupled chaotic oscillators. *Phys. Rev. E* 63, 3 (2001), 036216.
- [30] BELYKH, V. N., OSIPOV, G. V., PETROV, V. S., SUYKENS, J. A., AND VANDEWALLE, J. Cluster synchronization in oscillatory networks. *Chaos* 18, 3 (2008), 037106.
- [31] BENSON, A. R., ABEBE, R., SCHAUB, M. T., JADBABAIE, A., AND KLEINBERG, J. Simplicial closure and higher-order link prediction. *Proc. Natl. Acad. Sci. U.S.A.* 115, 48 (2018), E11221–E11230.
- [32] BENSON, A. R., GLEICH, D. F., AND LESKOVEC, J. Higher-order organization of complex networks. *Science* 353, 6295 (2016), 163–166.
- [33] BENZI, R., SUTERA, A., AND VULPIANI, A. The mechanism of stochastic resonance. *J. Phys. A* 14, 11 (1981), L453.
- [34] BERGE, C. *Graphs and hypergraphs*. North-Holland, 1973.
- [35] BERNER, R., SAWICKI, J., AND SCHÖLL, E. Birth and stabilization of phase clusters by multiplexing of adaptive networks. *Phys. Rev. Lett.* 124, 8 (2020), 088301.
- [36] BERRY, M. V. Singular limits. *Phys. Today* 55, 5 (2002), 10–11.
- [37] BICK, C. Heteroclinic switching between chimeras. *Phys. Rev. E* 97, 5 (2018), 050201.
- [38] BICK, C., ASHWIN, P., AND RODRIGUES, A. Chaos in generically coupled phase oscillator networks with nonpairwise interactions. *Chaos* 26, 9 (2016), 094814.

- [39] BICK, C., SEBEK, M., AND KISS, I. Z. Robust weak chimeras in oscillator networks with delayed linear and quadratic interactions. *Phys. Rev. Lett.* *119*, 16 (2017), 168301.
- [40] BIGGS, N. *Algebraic Graph Theory*. Cambridge University Press, Cambridge, England, 1993.
- [41] BLAHA, K. A., HUANG, K., DELLA ROSSA, F., PECORA, L. M., HOSSEIN-ZADEH, M., AND SORRENTINO, F. Cluster synchronization in multilayer networks: A fully analog experiment with LC oscillators with physically dissimilar coupling. *Phys. Rev. Lett.* *122*, 1 (2019), 014101.
- [42] BOCCALETTI, S., BIANCONI, G., CRIADO, R., DEL GENIO, C. I., GÓMEZ-GARDENES, J., ROMANCE, M., SENDINA-NADAL, I., WANG, Z., AND ZANIN, M. The structure and dynamics of multilayer networks. *Phys. Rep.* *544*, 1 (2014), 1–122.
- [43] BOCCALETTI, S., HWANG, D.-U., CHAVEZ, M., AMANN, A., KURTHS, J., AND PECORA, L. M. Synchronization in dynamical networks: Evolution along commutative graphs. *Phys. Rev. E* *74*, 1 (2006), 016102.
- [44] BOCCALETTI, S., KURTHS, J., OSIPOV, G., VALLADARES, D., AND ZHOU, C. The synchronization of chaotic systems. *Phys. Rep.* *366*, 1 (2002), 1–101.
- [45] BOCCALETTI, S., LATORA, V., MORENO, Y., CHAVEZ, M., AND HWANG, D.-U. Complex networks: Structure and dynamics. *Phys. Rep.* *424*, 4 (2006), 175–308.
- [46] BOGOMOLOV, S. A., SLEPNEV, A. V., STRELKOVA, G. I., SCHÖLL, E., AND ANISHCHENKO, V. S. Mechanisms of appearance of amplitude and phase chimera states in ensembles of nonlocally coupled chaotic systems. *Comm. Nonlinear Sci. Numer. Simulat.* *43* (2017), 25–36.
- [47] BOLHUIS, P. G., CHANDLER, D., DELLAGO, C., AND GEISLER, P. L. Transition path sampling: Throwing ropes over rough mountain passes, in the dark. *Annu. Rev. Phys. Chem* *53*, 1 (2002), 291–318.
- [48] BORDYUGOV, G., PIKOVSKY, A., AND ROSENBLUM, M. Self-emerging and turbulent chimeras in oscillator chains. *Phys. Rev. E* *82*, 3 (2010), 035205.
- [49] BRAIMAN, Y., DITTO, W., WIESENFELD, K., AND SPANO, M. Disorder-enhanced synchronization. *Phys. Lett. A* *206*, 1-2 (1995), 54–60.

- [50] BRAIMAN, Y., LINDNER, J. F., AND DITTO, W. L. Taming spatiotemporal chaos with disorder. *Nature* 378, 6556 (1995), 465–467.
- [51] BRANDT, S. F., DELLEN, B. K., AND WESSEL, R. Synchronization from disordered driving forces in arrays of coupled oscillators. *Phys. Rev. Lett.* 96, 3 (2006), 034104.
- [52] BRATSUN, D., VOLFSOHN, D., TSIMRING, L. S., AND HASTY, J. Delay-induced stochastic oscillations in gene regulation. *Proc. Natl. Acad. Sci. U.S.A.* 102, 41 (2005), 14593–14598.
- [53] BRUMMITT, C. D., D’SOUZA, R. M., AND LEICHT, E. Suppressing cascades of load in interdependent networks. *Proc. Natl. Acad. Sci. U.S.A.* 109, 12 (2012), E680–E689.
- [54] BUSCARINO, A., FRASCA, M., GAMBUZZA, L. V., AND HÖVEL, P. Chimera states in time-varying complex networks. *Phys. Rev. E* 91, 2 (2015), 022817.
- [55] CAO, Y., YU, W., REN, W., AND CHEN, G. An overview of recent progress in the study of distributed multi-agent coordination. *IEEE Trans. Ind. Informat.* 9, 1 (2013), 427–438.
- [56] CARLETTI, T., BATTISTON, F., CENCETTI, G., AND FANELLI, D. Random walks on hypergraphs. *Phys. Rev. E* 101, 2 (2020), 022308.
- [57] CARLETTI, T., FANELLI, D., AND NICOLETTI, S. Dynamical systems on hypergraphs. *arXiv preprint arXiv:2006.01243* (2020).
- [58] CETINAY, H., KUIPERS, F. A., AND VAN MIEGHEM, P. A topological investigation of power flow. *IEEE Syst J.* 12, 3 (2016), 2524–2532.
- [59] CHO, Y. S., NISHIKAWA, T., AND MOTTER, A. E. Stable chimeras and independently synchronizable clusters. *Phys. Rev. Lett.* 119, 8 (2017), 084101.
- [60] CHOE, C.-U., DAHMS, T., HÖVEL, P., AND SCHÖLL, E. Controlling synchrony by delay coupling in networks: from in-phase to splay and cluster states. *Phys. Rev. E* 81, 2 (2010), 025205.
- [61] CRAWFORD, J. D., AND KNOBLOCH, E. Symmetry and symmetry-breaking bifurcations in fluid dynamics. *Annu. Rev. Fluid Mech.* 23, 1 (1991), 341–387.
- [62] DAHMS, T., LEHNERT, J., AND SCHÖLL, E. Cluster and group synchronization in delay-coupled networks. *Phys. Rev. E* 86, 1 (2012), 016202.

- [63] DE ARRUDA, G. F., PETRI, G., AND MORENO, Y. Social contagion models on hypergraphs. *Phys. Rev. Res.* *2*, 2 (2020), 023032.
- [64] DE ARRUDA, G. F., TIZZANI, M., AND MORENO, Y. Phase transitions and stability of dynamical processes on hypergraphs. *arXiv preprint arXiv:2005.10891* (2020).
- [65] DE DOMENICO, M., GRANELL, C., PORTER, M. A., AND ARENAS, A. The physics of spreading processes in multilayer networks. *Nature Phys.* *12* (2016), 901–906.
- [66] DE DOMENICO, M., SOLÉ-RIBALTA, A., COZZO, E., KIVELÄ, M., MORENO, Y., PORTER, M. A., GÓMEZ, S., AND ARENAS, A. Mathematical formulation of multilayer networks. *Phys. Rev. X* *3*, 4 (2013), 041022.
- [67] DEL GENIO, C. I., GÓMEZ-GARDEÑES, J., BONAMASSA, I., AND BOCCALETTI, S. Synchronization in networks with multiple interaction layers. *Sci. Adv.* *2*, 11 (2016), e1601679.
- [68] DENKER, M., TIMME, M., DIESMANN, M., WOLF, F., AND GEISEL, T. Breaking synchrony by heterogeneity in complex networks. *Phys. Rev. Lett.* *92*, 7 (2004), 074103.
- [69] DESHAZER, D. J., BREBAN, R., OTT, E., AND ROY, R. Detecting phase synchronization in a chaotic laser array. *Phys. Rev. Lett.* *87*, 4 (2001), 044101.
- [70] DHAMALA, M., JIRSA, V. K., AND DING, M. Enhancement of neural synchrony by time delay. *Phys. Rev. Lett.* *92*, 7 (2004), 074104.
- [71] DÍAZ-GUILERA, A. Dynamic renormalization group approach to self-organized critical phenomena. *Europhys. Lett.* *26*, 3 (1994), 177–182.
- [72] DONETTI, L., HURTADO, P. I., AND MUNOZ, M. A. Entangled networks, synchronization, and optimal network topology. *Phys. Rev. Lett.* *95*, 18 (2005), 188701.
- [73] DÖRFLER, F., CHERTKOV, M., AND BULLO, F. Synchronization in complex oscillator networks and smart grids. *Proc. Natl. Acad. Sci. U.S.A.* *110*, 6 (2013), 2005–2010.
- [74] ERNST, U., PAWELZIK, K., AND GEISEL, T. Synchronization induced by temporal delays in pulse-coupled oscillators. *Phys. Rev. Lett.* *74*, 9 (1995), 1570–1573.

- [75] EROGLU, D., LAMB, J. S., AND PEREIRA, T. Synchronisation of chaos and its applications. *Contemp. Phys.* 58, 3 (2017), 207–243.
- [76] ESTRADA, E., AND ROSS, G. J. Centralities in simplicial complexes. applications to protein interaction networks. *J. Theor. Biol.* 438 (2018), 46–60.
- [77] FEKI, M. An adaptive chaos synchronization scheme applied to secure communication. *Chaos, Solitons & Fractals* 18, 1 (2003), 141–148.
- [78] FISCHER, I., VICENTE, R., BULDÚ, J. M., PEIL, M., MIRASSO, C. R., TORRENT, M., AND GARCÍA-OJALVO, J. Zero-lag long-range synchronization via dynamical relaying. *Phys. Rev. Lett.* 97, 12 (2006), 123902.
- [79] FLUNKERT, V., D’HUYS, O., DANCKAERT, J., FISCHER, I., AND SCHÖLL, E. Bubbling in delay-coupled lasers. *Phys. Rev. E* 79, 6 (2009), 065201.
- [80] FLUNKERT, V., YANCHUK, S., DAHMS, T., AND SCHÖLL, E. Synchronizing distant nodes: A universal classification of networks. *Phys. Rev. Lett.* 105, 25 (2010), 254101.
- [81] FREIDLIN, M. I., AND WENTZELL, A. D. *Random Perturbations of Dynamical Systems*. Springer, New York, 1998.
- [82] FU, C., DENG, Z., HUANG, L., AND WANG, X. Topological control of synchronous patterns in systems of networked chaotic oscillators. *Phys. Rev. E* 87, 3 (2013), 032909.
- [83] FUKUDA, H., NAKAMICHI, N., HISATSUNE, M., MURASE, H., AND MIZUNO, T. Synchronization of plant circadian oscillators with a phase delay effect of the vein network. *Phys. Rev. Lett.* 99, 9 (2007), 098102.
- [84] GAMBUZZA, L., DI PATTI, F., GALLO, L., LEPRI, S., ROMANCE, M., CRIADO, R., FRASCA, M., LATORA, V., AND BOCCALETTI, S. The master stability function for synchronization in simplicial complexes. *arXiv preprint arXiv:2004.03913* (2020).
- [85] GAMBUZZA, L. V., FRASCA, M., AND GOMEZ-GARDEÑES, J. Intra-layer synchronization in multiplex networks. *EPL* 110, 2 (2015), 20010.
- [86] GAMMAITONI, L., HÄNGGI, P., JUNG, P., AND MARCHESONI, F. Stochastic resonance. *Rev. Mod. Phys.* 70, 1 (1998), 223.

- [87] GANG, H., DITZINGER, T., NING, C.-Z., AND HAKEN, H. Stochastic resonance without external periodic force. *Phys. Rev. Lett.* 71, 6 (1993), 807.
- [88] GAO, J., BULDYREV, S. V., STANLEY, H. E., AND HAVLIN, S. Networks formed from interdependent networks. *Nature Phys.* 8, 1 (2012), 40–48.
- [89] GHOSH, S., KUMAR, A., ZAKHAROVA, A., AND JALAN, S. Birth and death of chimera: Interplay of delay and multiplexing. *Europhys. Lett.* 115, 6 (2016), 60005.
- [90] GIUSTI, C., GHRIST, R., AND BASSETT, D. S. Two’s company, three (or more) is a simplex. *J Comput Neurosci.* 41, 1 (2016), 1–14.
- [91] GLASS, L. Synchronization and rhythmic processes in physiology. *Nature* 410, 6825 (2001), 277–284.
- [92] GODSIL, C. Eigenvalues of graphs and digraphs. *Linear Algebra Appl.* 46 (1982), 43–50.
- [93] GOLDOBIN, D. S., AND PIKOVSKY, A. S. Synchronization of self-sustained oscillators by common white noise. *Physica A* 351, 1 (2005), 126–132.
- [94] GOLDSCHMIDT, R. J., PIKOVSKY, A., AND POLITI, A. Blinking chimeras in globally coupled rotators. *Chaos* 29, 7 (2019), 071101.
- [95] GOLUBITSKY, M., AND STEWART, I. Nonlinear dynamics of networks: The groupoid formalism. *Bull. Amer. Math. Soc.* 43, 3 (2006), 305–364.
- [96] GOLUBITSKY, M., AND STEWART, I. Rigid patterns of synchrony for equilibria and periodic cycles in network dynamics. *Chaos* 26, 9 (2016), 094803.
- [97] GOLUBITSKY, M., STEWART, I., AND TÖRÖK, A. Patterns of synchrony in coupled cell networks with multiple arrows. *SIAM J. Appl. Dyn. Syst.* 4, 1 (2005), 78–100.
- [98] GOMEZ, S., DIAZ-GUILERA, A., GOMEZ-GARDEÑES, J., PEREZ-VICENTE, C. J., MORENO, Y., AND ARENAS, A. Diffusion dynamics on multiplex networks. *Phys. Rev. Lett.* 110, 2 (2013), 028701.
- [99] GONZE, D., BERNARD, S., WALTERMANN, C., KRAMER, A., AND HERZEL, H. Spontaneous synchronization of coupled circadian oscillators. *Biophys. J* 89, 1 (2005), 120–129.

- [100] GROSS, T., AND BLASIUS, B. Adaptive coevolutionary networks: a review. *J. R. Soc. Interface* 5, 20 (2008), 259–271.
- [101] GROSS, T., D’LIMA, C. J. D., AND BLASIUS, B. Epidemic dynamics on an adaptive network. *Physical review letters* 96, 20 (2006), 208701.
- [102] GU, K., AND NICULESCU, S.-I. Survey on recent results in the stability and control of time-delay systems. *J. Dyn. Sys., Meas., Control* 125, 2 (2003), 158–165.
- [103] HAGERSTORM, A. M. Network symmetries and synchronization: <https://sourceforge.net/projects/networksym/>, 2016.
- [104] HAGERSTROM, A. M., MURPHY, T. E., ROY, R., HÖVEL, P., OMELCHENKO, I., AND SCHÖLL, E. Experimental observation of chimeras in coupled-map lattices. *Nat. Phys.* 8, 9 (2012), 658–661.
- [105] HANGGI, P. Escape from a metastable state. *J. Stat. Phys* 42, 1-2 (1986), 105–148.
- [106] HART, J. D., BANSAL, K., MURPHY, T. E., AND ROY, R. Experimental observation of chimera and cluster states in a minimal globally coupled network. *Chaos* 26, 9 (2016), 094801.
- [107] HART, J. D., LARGER, L., MURPHY, T. E., AND ROY, R. Delayed dynamical systems: Networks, chimeras and reservoir computing. *Philos. Trans. R. Soc. A* 377, 2153 (2019), 20180123.
- [108] HART, J. D., SCHMADEL, D. C., MURPHY, T. E., AND ROY, R. Experiments with arbitrary networks in time-multiplexed delay systems. *Chaos* 27, 12 (2017), 121103.
- [109] HART, J. D., ZHANG, Y., ROY, R., AND MOTTER, A. E. Topological control of synchronization patterns: Trading symmetry for stability. *Phys. Rev. Lett.* 122, 5 (2019), 058301.
- [110] HASAN, M. Z., AND KANE, C. L. Colloquium: Topological insulators. *Rev. Mod. Phys.* 82, 4 (2010), 3045.
- [111] HATCHER, A. *Algebraic topology*. Cambridge University Press, 2002.
- [112] HAUGLAND, S. W., SCHMIDT, L., AND KRISCHER, K. Self-organized alternating chimera states in oscillatory media. *Sci. Rep.* 5 (2015), 9883.

- [113] HEAGY, J. F., CARROLL, T. L., AND PECORA, L. M. Experimental and numerical evidence for riddled basins in coupled chaotic systems. *Phys. Rev. Lett.* *73*, 26 (1994), 3528–3531.
- [114] HOLME, P., AND SARAMÄKI, J. Temporal networks. *Phys. Rep.* *519*, 3 (2012), 97–125.
- [115] HUANG, L., CHEN, Q., LAI, Y.-C., AND PECORA, L. M. Generic behavior of master-stability functions in coupled nonlinear dynamical systems. *Phys. Rev. E* *80*, 3 (2009), 036204.
- [116] HUBER, D., AND TSIMRING, L. Dynamics of an ensemble of noisy bistable elements with global time delayed coupling. *Phys. Rev. Lett.* *91*, 26 (2003), 260601.
- [117] IACOPINI, I., PETRI, G., BARRAT, A., AND LATORA, V. Simplicial models of social contagion. *Nat. Commun.* *10*, 1 (2019), 1–9.
- [118] IRVING, D., AND SORRENTINO, F. Synchronization of dynamical hypernetworks: Dimensionality reduction through simultaneous block-diagonalization of matrices. *Phys. Rev. E* *86*, 5 (2012), 056102.
- [119] JETER, R., AND BELYKH, I. Synchronization in on-off stochastic networks: windows of opportunity. *IEEE Trans. Circuits Syst. I, Reg. Papers* *62*, 5 (2015), 1260–1269.
- [120] KAMEI, H., AND COCK, P. J. Computation of balanced equivalence relations and their lattice for a coupled cell network. *SIAM J. Appl. Dyn. Syst.* *12*, 1 (2013), 352–382.
- [121] KANEKO, K. Clustering, coding, switching, hierarchical ordering, and control in a network of chaotic elements. *Physica D* *41*, 2 (1990), 137–172.
- [122] KENNEDY, M. P. Robust OP amp realization of chua’s circuit. *Frequenz* *46*, 3-4 (Jan. 1992), 11.
- [123] KINDERMANN, R., AND SNELL, J. L. *Markov Random Fields and Their Applications*. American Mathematical Society, Providence, 1980.
- [124] KISS, I. Z., AND HUDSON, J. L. Phase synchronization of nonidentical chaotic electrochemical oscillators. *Phys. Chem. Chem. Phys.* *4*, 12 (2002), 2638–2647.

- [125] KISS, I. Z., WANG, W., AND HUDSON, J. L. Experiments on arrays of globally coupled periodic electrochemical oscillators. *J. Phys. Chem. B* 103 (1999), 11433–11444.
- [126] KIVELÄ, M., ARENAS, A., BARTHELEMY, M., GLEESON, J. P., MORENO, Y., AND PORTER, M. A. Multilayer networks. *J. Complex Netw.* 2, 3 (2014), 203–271.
- [127] KLEINBERG, J. M. Navigation in a small world. *Nature* 406, 6798 (2000), 845–845.
- [128] KOLMANOVSKII, V., AND MYSHKIS, A. *Introduction to the theory and applications of functional differential equations*, vol. 463. Springer Science & Business Media, Berlin, Germany, 2013.
- [129] KOTWAL, T., JIANG, X., AND ABRAMS, D. M. Connecting the kuramoto model and the chimera state. *Phys. Rev. Lett.* 119, 26 (2017), 264101.
- [130] KOZMA, B., AND BARRAT, A. Consensus formation on adaptive networks. *Phys. Rev. E* 77, 1 (2008), 016102.
- [131] KURAMOTO, Y. Self-entrainment of a population of coupled non-linear oscillators. In *International Symposium on Mathematical Problems in Theoretical Physics* (1975), Springer, pp. 420–422.
- [132] KURAMOTO, Y. *Chemical oscillations, waves, and turbulence*, vol. 19. Springer Science & Business Media, 2012.
- [133] KURAMOTO, Y., AND BATTOGTOKH, D. Coexistence of coherence and incoherence in nonlocally coupled phase oscillators. *Nonlinear Phenom. Complex Syst.* 5 (2002), 380–385.
- [134] KUZMIN, E., VANDERSLUIS, B., WANG, W., TAN, G., DESHPANDE, R., CHEN, Y., USAJ, M., BALINT, A., USAJ, M. M., VAN LEEUWEN, J., ET AL. Systematic analysis of complex genetic interactions. *Science* 360, 6386 (2018), eaao1729.
- [135] LAING, C. R. Disorder-induced dynamics in a pair of coupled heterogeneous phase oscillator networks. *Chaos* 22, 4 (2012), 043104.
- [136] LAM, T.-Y. *A First Course in Noncommutative Rings*. Springer Science & Business Media, New York, 2013.
- [137] LAMBIOTTE, R., ROSVALL, M., AND SCHOLTES, I. From networks to optimal higher-order models of complex systems. *Nat. Phys.* 15, 4 (2019), 313–320.

- [138] LAPIERRE, J. L., KOSENKO, P. O., LYAMIN, O. I., KODAMA, T., MUKHAMEDTOV, L. M., AND SIEGEL, J. M. Cortical acetylcholine release is lateralized during asymmetrical slow-wave sleep in northern fur seals. *J. Neurosci.* *27*, 44 (2007), 11999–12006.
- [139] LARGER, L., PENKOVSKY, B., AND MAISTRENKO, Y. L. Virtual chimera states for delayed-feedback systems. *Phys. Rev. Lett.* *111*, 5 (2013), 054103.
- [140] LEBOWITZ, J. L. Statistical mechanics: A selective review of two central issues. *Rev. Mod. Phys.* *71*, 2 (1999), S346–S357.
- [141] LELOUP, J.-C., AND GOLDBETER, A. Toward a detailed computational model for the mammalian circadian clock. *Proc. Natl. Acad. Sci. U.S.A.* *100*, 12 (2003), 7051–7056.
- [142] LEÓN, I., AND PAZÓ, D. Phase reduction beyond the first order: The case of the mean-field complex ginzburg-landau equation. *Phys. Rev. E* *100*, 1 (2019), 012211.
- [143] LEVINE, J. M., BASCOMPTE, J., ADLER, P. B., AND ALLESINA, S. Beyond pairwise mechanisms of species coexistence in complex communities. *Nature* *546*, 7656 (2017), 56–64.
- [144] LI, A., CORNELIUS, S. P., LIU, Y.-Y., WANG, L., AND BARABÁSI, A.-L. The fundamental advantages of temporal networks. *Science* *358*, 6366 (2017), 1042–1046.
- [145] LI, Z., DUAN, Z., CHEN, G., AND HUANG, L. Consensus of multiagent systems and synchronization of complex networks: A unified viewpoint. *IEEE Trans. Circuits Syst. I, Reg. Papers* *57*, 1 (2010), 213–224.
- [146] LUCAS, M., CENCETTI, G., AND BATTISTON, F. A multi-order laplacian framework for the stability of higher-order synchronization. *arXiv preprint arXiv:2003.09734* (2020).
- [147] LUNZE, J. Synchronization of heterogeneous agents. *IEEE Trans. Autom. Control* *57*, 11 (2012), 2885–2890.
- [148] MA, R., WANG, J., AND LIU, Z. Robust features of chimera states and the implementation of alternating chimera states. *Europhys. Lett.* *91*, 4 (2010), 40006.
- [149] MACARTHUR, B. D., SÁNCHEZ-GARCÍA, R. J., AND ANDERSON, J. W. Symmetry in complex networks. *Discr. Appl. Math.* *156*, 18 (2008), 3525–3531.

- [150] MAEHARA, T., AND MUROTA, K. A numerical algorithm for block-diagonal decomposition of matrix *-algebras with general irreducible components. *Jpn. J. Ind. Appl. Math* 27, 2 (2010), 263–293.
- [151] MAEHARA, T., AND MUROTA, K. Algorithm for error-controlled simultaneous block-diagonalization of matrices. *SIAM J. Matrix Anal. Appl.* 32, 2 (2011), 605–620.
- [152] MAISTRENKO, Y. L., MAISTRENKO, V. L., POPOVICH, A., AND MOSEKILDE, E. Transverse instability and riddled basins in a system of two coupled logistic maps. *Phys. Rev. E* 57, 3 (1998), 2713–2724.
- [153] MAJHI, S., PERC, M., AND GHOSH, D. Chimera states in a multilayer network of coupled and uncoupled neurons. *Chaos* 27, 7 (2017), 073109.
- [154] MALTSEV, A. V., MALTSEV, V. A., MIKHEEV, M., MALTSEVA, L. A., SIRENKO, S. G., LAKATTA, E. G., AND STERN, M. D. Synchronization of stochastic ca2+ release units creates a rhythmic ca2+ clock in cardiac pacemaker cells. *Biophys. J* 100, 2 (2011), 271–283.
- [155] MANRIQUE, P. D., AND JOHNSON, N. F. Individual heterogeneity generating explosive system network dynamics. *Phys. Rev. E* 97, 3 (2018), 032311.
- [156] MARTENS, E. A. Bistable chimera attractors on a triangular network of oscillator populations. *Phys. Rev. E* 82, 1 (2010), 016216.
- [157] MARTENS, E. A., LAING, C. R., AND STROGATZ, S. H. Solvable model of spiral wave chimeras. *Phys. Rev. Lett.* 104, 4 (2010), 044101.
- [158] MARTENS, E. A., PANAGGIO, M. J., AND ABRAMS, D. M. Basins of attraction for chimera states. *New J. Phys.* 18, 2 (2016), 022002.
- [159] MARTENS, E. A., THUTUPALLI, S., FOURRIÈRE, A., AND HALLATSCHEK, O. Chimera states in mechanical oscillator networks. *Proc. Natl. Acad. Sci. U.S.A.* 110, 26 (2013), 10563–10567.
- [160] MARVEL, S. A., MIROLLO, R. E., AND STROGATZ, S. H. Identical phase oscillators with global sinusoidal coupling evolve by möbius group action. *Chaos* 19, 4 (2009), 043104.
- [161] MASAMURA, S., IWAMOTO, T., SUGITANI, Y., KONISHI, K., AND HARA, N. Experimental investigation of amplitude death in delay-coupled double-scroll circuits

- with randomly time-varying network topology. *Nonlinear Dyn.* 99 (2020), 3155–3168.
- [162] MATAMALAS, J. T., GÓMEZ, S., AND ARENAS, A. Abrupt phase transition of epidemic spreading in simplicial complexes. *Phys. Rev. Res.* 2, 1 (2020), 012049.
- [163] MATHENY, M. H., EMENHEISER, J., FON, W., CHAPMAN, A., SALOVA, A., ROHDEN, M., LI, J., DE BADYN, M. H., PÓSFAL, M., DUENAS-OSORIO, L., ET AL. Exotic states in a simple network of nanoelectromechanical oscillators. *Science* 363, 6431 (2019), eaav7932.
- [164] MATHEWS, C. G., LESKU, J. A., LIMA, S. L., AND AMLANER, C. J. Asynchronous eye closure as an anti-predator behavior in the western fence lizard (*sceloporus occidentalis*). *Ethology* 112, 3 (2006), 286–292.
- [165] MATSUMOTO, T., CHUA, L., AND KOMURO, M. The double scroll. *IEEE Trans. Circuits Syst.* 32, 8 (Aug. 1985), 797–818.
- [166] MAYFIELD, M. M., AND STOUFFER, D. B. Higher-order interactions capture unexplained complexity in diverse communities. *Nat. Ecol. Evol.* 1, 3 (2017), 1–7.
- [167] McDONALD, S. W., GREBOGI, C., OTT, E., AND YORKE, J. A. Fractal basin boundaries. *Physica D* 17, 2 (1985), 125–153.
- [168] MCKAY, B. D., AND PIPERNO, A. Practical graph isomorphism, II. *J. Symb. Comput.* 60 (2014), 94–112.
- [169] MCNAMARA, B., WIESENFELD, K., AND ROY, R. Observation of stochastic resonance in a ring laser. *Phys. Rev. Lett.* 60, 25 (1988), 2626.
- [170] MICHAELS, D. C., MATYAS, E. P., AND JALIFE, J. Mechanisms of sinoatrial pacemaker synchronization: a new hypothesis. *Circ. Res.* 61, 5 (1987), 704–714.
- [171] MILLÁN, A. P., TORRES, J. J., AND BIANCONI, G. Explosive higher-order kuramoto dynamics on simplicial complexes. *Phys. Rev. Lett.* 124, 21 (2020), 218301.
- [172] MILNOR, J. On the concept of attractor. *Commun. Math. Phys.* 99 (1985), 177–195.
- [173] MOLNAR, F., NISHIKAWA, T., AND MOTTER, A. E. Network experiment demonstrates converse symmetry breaking. *Nat. Phys.* 16, 3 (2020), 351–356.
- [174] MOSEKILDE, E., MAISTRENKO, Y., AND POSTNOV, D. *Chaotic synchronization: applications to living systems*, vol. 42. World Scientific, 2002.

- [175] MOTTER, A. E., MYERS, S. A., ANGHEL, M., AND NISHIKAWA, T. Spontaneous synchrony in power-grid networks. *Nat. Phys.* *9*, 3 (2013), 191–197.
- [176] MOTTER, A. E., ZHOU, C., AND KURTHS, J. Network synchronization, diffusion, and the paradox of heterogeneity. *Phys. Rev. E* *71*, 1 (2005), 016116.
- [177] MULAS, R., KUEHN, C., AND JOST, J. Coupled dynamics on hypergraphs: Master stability of steady states and synchronization. *arXiv preprint arXiv:2003.13775* (2020).
- [178] MUROTA, K., KANNO, Y., KOJIMA, M., AND KOJIMA, S. A numerical algorithm for block-diagonal decomposition of matrix *-algebras with application to semidefinite programming. *Jpn. J. Ind. Appl. Math* *27*, 1 (2010), 125–160.
- [179] NAGAI, K. H., AND KORI, H. Noise-induced synchronization of a large population of globally coupled nonidentical oscillators. *Phys. Rev. E* *81*, 6 (2010), 065202.
- [180] NAKAO, H., ARAI, K., AND KAWAMURA, Y. Noise-induced synchronization and clustering in ensembles of uncoupled limit-cycle oscillators. *Phys. Rev. Lett.* *98*, 18 (2007), 184101.
- [181] NANDKISHORE, R., AND HUSE, D. A. Many-body localization and thermalization in quantum statistical mechanics. *Annu. Rev. Condens. Matter Phys.* *6*, 1 (2015), 15–38.
- [182] NEUHÄUSER, L., MELLOR, A., AND LAMBIOTTE, R. Multibody interactions and nonlinear consensus dynamics on networked systems. *Phys. Rev. E* *101*, 3 (2020), 032310.
- [183] NEWMAN, M. *Networks*. Oxford university press, 2018.
- [184] NEWMAN, M. E. The structure and function of complex networks. *SIAM Rev.* *45*, 2 (2003), 167–256.
- [185] NICOLAOU, Z. G., RIECKE, H., AND MOTTER, A. E. Chimera states in continuous media: Existence and distinctness. *Phys. Rev. Lett.* *119*, 24 (2017), 244101.
- [186] NICOLAOU, Z. G., SEBEK, M., KISS, I. Z., AND MOTTER, A. E. Coherent dynamics enhanced by uncorrelated noise. *Phys. Rev. Lett.* (2020), in press.
- [187] NICOSIA, V., VALENCIA, M., CHAVEZ, M., DÍAZ-GUILERA, A., AND LATORA, V. Remote synchronization reveals network symmetries and functional modules. *Phys. Rev. Lett.* *110*, 17 (2013), 174102.

- [188] NICULESCU, S.-I. *Delay effects on stability: A robust control approach*, vol. 269. Springer Science & Business Media, Berlin, Germany, 2001.
- [189] NISHIKAWA, T., AND MOTTER, A. E. Maximum performance at minimum cost in network synchronization. *Physica D* *224*, 1 (2006), 77–89.
- [190] NISHIKAWA, T., AND MOTTER, A. E. Synchronization is optimal in nondiagonalizable networks. *Phys. Rev. E* *73*, 6 (2006), 065106.
- [191] NISHIKAWA, T., AND MOTTER, A. E. Network synchronization landscape reveals compensatory structures, quantization, and the positive effect of negative interactions. *Proc. Natl. Acad. Sci. U.S.A.* *107*, 23 (2010), 10342–10347.
- [192] NISHIKAWA, T., AND MOTTER, A. E. Symmetric states requiring system asymmetry. *Phys. Rev. Lett.* *117*, 11 (2016), 114101.
- [193] NISHIKAWA, T., AND MOTTER, A. E. Symmetric states requiring system asymmetry. *Phys. Rev. Lett.* *117* (2016), 114101.
- [194] NISHIKAWA, T., MOTTER, A. E., LAI, Y.-C., AND HOPPENSTEADT, F. C. Heterogeneity in oscillator networks: Are smaller worlds easier to synchronize? *Phys. Rev. Lett.* *91*, 1 (2003), 014101.
- [195] NIXON, M., FRIDMAN, M., RONEN, E., FRIESEM, A. A., DAVIDSON, N., AND KANTER, I. Controlling synchronization in large laser networks. *Phys. Rev. Lett.* *108*, 21 (2012), 214101.
- [196] O’KEEFFE, K. P., KRAPIVSKY, P. L., AND STROGATZ, S. H. Synchronization as aggregation: Cluster kinetics of pulse-coupled oscillators. *Phys. Rev. Lett.* *115*, 6 (2015), 064101.
- [197] OKUDA, K., AND KURAMOTO, Y. Mutual entrainment between populations of coupled oscillators. *Prog. Theor. Phys.* *86*, 6 (1991), 1159–1176.
- [198] OLFATI-SABER, R., FAX, A., AND MURRAY, R. M. Consensus and cooperation in networked multi-agent systems. *Proc. IEEE* *95*, 1 (2007), 215–233.
- [199] OMELCHENKO, I., MAISTRENKO, Y. L., HÖVEL, P., AND SCHÖLL, E. Loss of coherence in dynamical networks: Spatial chaos and chimera states. *Phys. Rev. Lett.* *106*, 23 (2011), 234102.

- [200] OMELCHENKO, I., RIEMENSCHNEIDER, B., HÖVEL, P., MAISTRENKO, Y. L., AND SCHÖLL, E. Transition from spatial coherence to incoherence in coupled chaotic systems. *Phys. Rev. E* 85, 2 (2012), 026212.
- [201] OMEL'CHENKO, O. E. The mathematics behind chimera states. *Nonlinearity* 31, 5 (2018), R121–R164.
- [202] OMEL'CHENKO, O. E., MAISTRENKO, Y. L., AND TASS, P. A. Chimera states: The natural link between coherence and incoherence. *Phys. Rev. Lett.* 100, 4 (2008), 044105.
- [203] OROSZ, G. Decomposition of nonlinear delayed networks around cluster states with applications to neurodynamics. *SIAM J. Appl. Dyn. Syst.* 13, 4 (2014), 1353–1386.
- [204] OTT, E. *Chaos in Dynamical Systems*. Cambridge University Press, Cambridge, England, 2002.
- [205] OTT, E., ALEXANDER, J., KAN, I., SOMMERER, J. C., AND YORKE, J. A. The transition to chaotic attractors with riddled basins. *Physica D* 76, 4 (1994), 384–410.
- [206] OTT, E., AND ANTONSEN, T. M. Low dimensional behavior of large systems of globally coupled oscillators. *Chaos* 18, 3 (2008), 037113.
- [207] OTT, E., AND ANTONSEN, T. M. Long time evolution of phase oscillator systems. *Chaos* 19, 2 (2009), 023117.
- [208] OTT, E., AND SOMMERER, J. C. Blowout bifurcations: The occurrence of riddled basins and on-off intermittency. *Phys. Lett. A* 188, 1 (1994), 39–47.
- [209] OTT, E., SOMMERER, J. C., ALEXANDER, J. C., KAN, I., AND YORKE, J. A. Scaling behavior of chaotic systems with riddled basins. *Phys. Rev. Lett.* 71, 25 (1993), 4134–4137.
- [210] PANAGGIO, M. J., AND ABRAMS, D. M. Chimera states: Coexistence of coherence and incoherence in networks of coupled oscillators. *Nonlinearity* 28, 3 (2015), R67–R87.
- [211] PANAGGIO, M. J., ABRAMS, D. M., ASHWIN, P., AND LAING, C. R. Chimera states in networks of phase oscillators: The case of two small populations. *Phys. Rev. E* 93, 1 (2016), 012218.

- [212] PARANJAPE, A., BENSON, A. R., AND LESKOVEC, J. Motifs in temporal networks. In *Proceedings of the Tenth ACM International Conference on Web Search and Data Mining* (2017), pp. 601–610.
- [213] PASTOR-SATORRAS, R., AND VESPIGNANI, A. Epidemic spreading in scale-free networks. *Phys. Rev. Lett.* *86*, 14 (2001), 3200–3203.
- [214] PATANIA, A., PETRI, G., AND VACCARINO, F. The shape of collaborations. *EPJ Data Sci* *6*, 1 (2017), 18.
- [215] PAZÓ, D., AND MONTBRIÓ, E. Low-dimensional dynamics of populations of pulse-coupled oscillators. *Phys. Rev. X* *4*, 1 (2014), 011009.
- [216] PECORA, L. M., AND CARROLL, T. L. Synchronization in chaotic systems. *Phys. Rev. Lett.* *64*, 8 (1990), 821–824.
- [217] PECORA, L. M., AND CARROLL, T. L. Master stability functions for synchronized coupled systems. *Phys. Rev. Lett.* *80*, 10 (1998), 2109–2112.
- [218] PECORA, L. M., AND CARROLL, T. L. Synchronization of chaotic systems. *Chaos* *25*, 9 (2015), 097611.
- [219] PECORA, L. M., SORRENTINO, F., HAGERSTROM, A. M., MURPHY, T. E., AND ROY, R. Cluster synchronization and isolated desynchronization in complex networks with symmetries. *Nat. Commun.* *5* (2014), 4079.
- [220] PEREIRA, T., ELDERING, J., RASMUSSEN, M., AND VENEZIANI, A. Towards a theory for diffusive coupling functions allowing persistent synchronization. *Nonlinearity* *27*, 3 (2014), 501.
- [221] PETRI, G., AND BARRAT, A. Simplicial activity driven model. *Phys. Rev. Lett.* *121*, 22 (2018), 228301.
- [222] PETRI, G., EXPERT, P., TURKHEIMER, F., CARHART-HARRIS, R., NUTT, D., HELLYER, P. J., AND VACCARINO, F. Homological scaffolds of brain functional networks. *J. R. Soc. Interface* *11*, 101 (2014), 20140873.
- [223] PETTIGREW, J. D., COLLIN, S. P., AND OTT, M. Convergence of specialised behaviour, eye movements and visual optics in the sandlance (teleostei) and the chameleon (reptilia). *Curr. Biol.* *9*, 8 (1999), 421–424.
- [224] PIKOVSKY, A., AND ROSENBLUM, M. Partially integrable dynamics of hierarchical populations of coupled oscillators. *Phys. Rev. Lett.* *101*, 26 (2008), 264103.

- [225] PIKOVSKY, A. S., AND KURTHS, J. Coherence resonance in a noise-driven excitable system. *Phys. Rev. Lett.* *78*, 5 (1997), 775.
- [226] PIMENOVA, A. V., GOLDOBIN, D. S., ROSENBLUM, M., AND PIKOVSKY, A. Interplay of coupling and common noise at the transition to synchrony in oscillator populations. *Sci. Rep.* *6* (2016), 38518.
- [227] PYRAGAS, K. Continuous control of chaos by self-controlling feedback. *Phys. Lett. A* *170*, 6 (1992), 421–428.
- [228] QI, X.-L., AND ZHANG, S.-C. Topological insulators and superconductors. *Rev. Mod. Phys.* *83*, 4 (2011), 1057.
- [229] RAPPEL, W.-J., AND STROGATZ, S. H. Stochastic resonance in an autonomous system with a nonuniform limit cycle. *Phys. Rev. E* *50*, 4 (1994), 3249.
- [230] RATTENBORG, N. C., AMLANER, C., AND LIMA, S. Behavioral, neurophysiological and evolutionary perspectives on unihemispheric sleep. *Neurosci. Biobehav. Rev.* *24*, 8 (2000), 817–842.
- [231] REIMANN, M. W., NOLTE, M., SCOLAMIERO, M., TURNER, K., PERIN, R., CHINDEMI, G., DŁOTKO, P., LEVI, R., HESS, K., AND MARKRAM, H. Cliques of neurons bound into cavities provide a missing link between structure and function. *Front. Comput. Neurosci.* *11* (2017), 48.
- [232] REINHART, R. M., AND NGUYEN, J. A. Working memory revived in older adults by synchronizing rhythmic brain circuits. *Nat. Neurosci.* *22*, 5 (2019), 820–827.
- [233] RESTREPO, J. G., OTT, E., AND HUNT, B. R. Spatial patterns of desynchronization bursts in networks. *Phys. Rev. E* *69*, 6 (2004), 066215.
- [234] RIM, S., KIM, I., KANG, P., PARK, Y.-J., AND KIM, C.-M. Routes to complete synchronization via phase synchronization in coupled nonidentical chaotic oscillators. *Phys. Rev. E* *66*, 1 (2002), 015205.
- [235] ROBERTAZZI, R., AND BUHRMAN, R. Josephson terahertz local oscillator. *IEEE Trans. Magn* *25*, 2 (1989), 1384–1387.
- [236] ROHDEN, M., SORGE, A., TIMME, M., AND WITTHAUT, D. Self-organized synchronization in decentralized power grids. *Phys. Rev. Lett.* *109*, 6 (2012), 064101.
- [237] ROSENBLUM, M. G., PIKOVSKY, A. S., AND KURTHS, J. Phase synchronization of chaotic oscillators. *Phys. Rev. Lett.* *76*, 11 (1996), 1804–1807.

- [238] ROSIN, D. P., RONTANI, D., GAUTHIER, D. J., AND SCHÖLL, E. Control of synchronization patterns in neural-like boolean networks. *Phys. Rev. Lett.* *110*, 10 (2013), 104102.
- [239] ROSSI, R., AND AHMED, N. The network data repository with interactive graph analytics and visualization. In *AAAI* (2015).
- [240] ROY, R., SHORT, R., DURIN, J., AND MANDEL, L. First-passage-time distributions under the influence of quantum fluctuations in a laser. *Phys. Rev. Lett.* *45*, 18 (1980), 1486–1490.
- [241] SAA, A. Symmetries and synchronization in multilayer random networks. *Phys. Rev. E* *97*, 4 (2018), 042304.
- [242] SANTOS, V., SZEZECH JR, J. D., BATISTA, A. M., IAROSZ, K. C., BAPTISTA, M. S., REN, H. P., GREBOGI, C., VIANA, R. L., CALDAS, I. L., MAISTRENKO, Y. L., ET AL. Riddling: Chimera’s dilemma. *Chaos* *28*, 8 (2018), 081105.
- [243] SCHAUB, M. T., BENSON, A. R., HORN, P., LIPPNER, G., AND JADBABAIE, A. Random walks on simplicial complexes and the normalized hodge 1-laplacian. *SIAM Rev.* *62*, 2 (2020), 353–391.
- [244] SCHAUB, M. T., O’CLERY, N., BILLEH, Y. N., DELVENNE, J.-C., LAMBIOTTE, R., AND BARAHONA, M. Graph partitions and cluster synchronization in networks of oscillators. *Chaos* *26*, 9 (2016), 094821.
- [245] SCHMIDT, L., AND KRISCHER, K. Clustering as a prerequisite for chimera states in globally coupled systems. *Phys. Rev. Lett.* *114*, 3 (2015), 034101.
- [246] SCHMIDT, L., SCHÖNLEBER, K., KRISCHER, K., AND GARCÍA-MORALES, V. Coexistence of synchrony and incoherence in oscillatory media under nonlinear global coupling. *Chaos* *24*, 1 (2014), 013102.
- [247] SCHMIDT, M. F. Using both sides of your brain: the case for rapid interhemispheric switching. *PLoS Biol.* *6*, 10 (2008), e269.
- [248] SCHNITZLER, A., AND GROSS, J. Normal and pathological oscillatory communication in the brain. *Nat. Rev. Neurosci.* *6*, 4 (2005), 285–296.
- [249] SEMENOVA, N., ZAKHAROVA, A., ANISHCHENKO, V., AND SCHÖLL, E. Coherence-resonance chimeras in a network of excitable elements. *Phys. Rev. Lett.* *117*, 1 (2016), 014102.

- [250] SEMENOVA, N., ZAKHAROVA, A., SCHÖLL, E., AND ANISHCHENKO, V. Does hyperbolicity impede emergence of chimera states in networks of nonlocally coupled chaotic oscillators? *Europhys. Lett.* *112*, 4 (2015), 40002.
- [251] SETHIA, G. C., AND SEN, A. Chimera states: The existence criteria revisited. *Phys. Rev. Lett.* *112*, 14 (2014), 144101.
- [252] SETHIA, G. C., SEN, A., AND ATAY, F. M. Clustered chimera states in delay-coupled oscillator systems. *Phys. Rev. Lett.* *100*, 14 (2008), 144102.
- [253] SETHIA, G. C., SEN, A., AND JOHNSTON, G. L. Amplitude-mediated chimera states. *Phys. Rev. E* *88*, 4 (2013), 042917.
- [254] SEVILLA-ESCOBOZA, R., SENDIÑA-NADAL, I., LEYVA, I., GUTIÉRREZ, R., BULDÚ, J., AND BOCCALETTI, S. Inter-layer synchronization in multiplex networks of identical layers. *Chaos* *26*, 6 (2016), 065304.
- [255] SEYBOTH, G. S., DIMAROGONAS, D. V., JOHANSSON, K. H., FRASCA, P., AND ALLGÖWER, F. On robust synchronization of heterogeneous linear multi-agent systems with static couplings. *Automatica* *53* (2015), 392–399.
- [256] SHENA, J., HIZANIDIS, J., KOVANIS, V., AND TSIRONIS, G. P. Turbulent chimeras in large semiconductor laser arrays. *Sci. Rep.* *7* (2017), 42116.
- [257] SIDDIQUE, A. B., PECORA, L. M., HART, J. D., AND SORRENTINO, F. Symmetry- and input-cluster synchronization in networks. *Phys. Rev. E* *97*, 4 (2018), 042217.
- [258] SIEBER, J., OMEL'CHENKO, O. E., AND WOLFRUM, M. Controlling unstable chaos: Stabilizing chimera states by feedback. *Phys. Rev. Lett.* *112*, 5 (2014), 054102.
- [259] SIZEMORE, A. E., GIUSTI, C., KAHN, A., VETTEL, J. M., BETZEL, R. F., AND BASSETT, D. S. Cliques and cavities in the human connectome. *J Comput Neurosci.* *44*, 1 (2018), 115–145.
- [260] SKARDAL, P. S., AND ARENAS, A. Abrupt desynchronization and extensive multistability in globally coupled oscillator simplexes. *Phys. Rev. Lett.* *122*, 24 (2019), 248301.
- [261] SKARDAL, P. S., AND ARENAS, A. Higher-order interactions in complex networks of phase oscillators promote abrupt synchronization switching. *arXiv preprint arXiv:1909.08057* (2019).

- [262] SKARDAL, P. S., SEVILLA-ESCOBOZA, R., VERA-ÁVILA, V., AND BULDÚ, J. M. Optimal phase synchronization in networks of phase-coherent chaotic oscillators. *Chaos* 27, 1 (2017), 013111.
- [263] SORRENTINO, F. Synchronization of hypernetworks of coupled dynamical systems. *New J. Phys.* 14, 3 (2012), 033035.
- [264] SORRENTINO, F., AND PECORA, L. M. Approximate cluster synchronization in networks with symmetries and parameter mismatches. *Chaos: An Interdisciplinary Journal of Nonlinear Science* 26, 9 (2016), 094823.
- [265] SORRENTINO, F., PECORA, L. M., HAGERSTROM, A. M., MURPHY, T. E., AND ROY, R. Complete characterization of the stability of cluster synchronization in complex dynamical networks. *Sci. Adv.* 2, 4 (2016), e1501737.
- [266] SORRENTINO, F., AND PORFIRI, M. Analysis of parameter mismatches in the master stability function for network synchronization. *EPL* 93, 5 (2011), 50002.
- [267] ST-ONGE, G., THIBEAULT, V., ALLARD, A., DUBÉ, L. J., AND HÉBERT-DUFRESNE, L. Master equation analysis of mesoscopic localization in contagion dynamics on higher-order networks. *arXiv preprint arXiv:2004.10203* (2020).
- [268] STANLEY, H. E. *Introduction to Phase Transitions and Critical Phenomena*. Oxford University Press, New York, 1971.
- [269] STAUFFER, D., AND AHARONY, A. *Introduction to Percolation Theory, revised second ed.* CRC Press, Boca Raton, FL, 2014.
- [270] STEIN, W., ET AL. Sage: Open source mathematical software, www.sagemath.org, 2008.
- [271] STEWART, I. Networking opportunity. *Nature (London)* 427, 6975 (2004), 601–604.
- [272] STEWART, I., GOLUBITSKY, M., AND PIVATO, M. Symmetry groupoids and patterns of synchrony in coupled cell networks. *SIAM J. Appl. Dyn. Syst.* 2, 4 (2003), 609–646.
- [273] STILWELL, D. J., BOLLT, E. M., AND ROBERSON, D. G. Sufficient conditions for fast switching synchronization in time-varying network topologies. *SIAM J. Appl. Dyn. Syst.* 5, 1 (2006), 140–156.
- [274] STROGATZ, S. H. From Kuramoto to Crawford: Exploring the onset of synchronization in populations of coupled oscillators. *Physica D* 143, 1 (2000), 1–20.

- [275] STROGATZ, S. H. Exploring complex networks. *Nature* 410, 6825 (2001), 268–276.
- [276] SUN, J., BOLLT, E. M., AND NISHIKAWA, T. Master stability functions for coupled nearly identical dynamical systems. *EPL* 85, 6 (2009), 60011.
- [277] SUN, J., BOLLT, E. M., AND NISHIKAWA, T. Master stability functions for coupled nearly identical dynamical systems. *EPL* 85, 6 (Apr. 2009), 60011.
- [278] TAKAMATSU, A., TANAKA, R., YAMADA, H., NAKAGAKI, T., FUJII, T., AND ENDO, I. Spatiotemporal symmetry in rings of coupled biological oscillators of physarum plasmodial slime mold. *Phys. Rev. Lett.* 87, 7 (2001), 078102.
- [279] TANAKA, T., AND AOYAGI, T. Multistable attractors in a network of phase oscillators with three-body interactions. *Phys. Rev. Lett.* 106, 22 (2011), 224101.
- [280] TANG, L., WU, X., LÜ, J., LU, J.-A., AND D'SOUZA, R. M. Master stability functions for complete, intralayer, and interlayer synchronization in multiplex networks of coupled rössler oscillators. *Phys. Rev. E* 99, 1 (2019), 012304.
- [281] TEKIN, E., WHITE, C., KANG, T. M., SINGH, N., CRUZ-LOYA, M., DAMOISEAUX, R., SAVAGE, V. M., AND YEY, P. J. Prevalence and patterns of higher-order drug interactions in escherichia coli. *NPJ Syst Biol App* 4, 1 (2018), 1–10.
- [282] TERAMAE, J.-N., AND TANAKA, D. Robustness of the noise-induced phase synchronization in a general class of limit cycle oscillators. *Phys. Rev. Lett.* 93, 20 (2004), 204103.
- [283] TIMME, M., WOLF, F., AND GEISEL, T. Prevalence of unstable attractors in networks of pulse-coupled oscillators. *Phys. Rev. Lett.* 89, 15 (2002), 154105.
- [284] TINKHAM, M. *Group Theory and Quantum Mechanics*. Courier Corporation, 2003.
- [285] TINSLEY, M. R., NKOMO, S., AND SHOWALTER, K. Chimera and phase-cluster states in populations of coupled chemical oscillators. *Nat. Phys.* 8, 9 (2012), 662–665.
- [286] TO, T.-L., HENSON, M. A., HERZOG, E. D., AND DOYLE III, F. J. A molecular model for intercellular synchronization in the mammalian circadian clock. *Biophys. J* 92, 11 (2007), 3792–3803.
- [287] TOTZ, J. F., RODE, J., TINSLEY, M. R., SHOWALTER, K., AND ENGEL, H. Spiral wave chimera states in large populations of coupled chemical oscillators. *Nat. Phys.* 14, 3 (2018), 282–285.

- [288] TOTZ, J. F., SNARI, R., YENGI, D., TINSLEY, M. R., ENGEL, H., AND SHOWALTER, K. Phase-lag synchronization in networks of coupled chemical oscillators. *Phys. Rev. E* 92, 2 (2015), 022819.
- [289] ULLNER, E., BUCETA, J., DÍEZ-NOGUERA, A., AND GARCÍA-OJALVO, J. Noise-induced coherence in multicellular circadian clocks. *Biophys. J.* 96, 9 (2009), 3573–3581.
- [290] VANWIGGEREN, G. D., AND ROY, R. Communication with chaotic lasers. *Science* 279, 5354 (1998), 1198–1200.
- [291] VARDI, R., TIMOR, R., MAROM, S., ABELES, M., AND KANTER, I. Synchronization with mismatched synaptic delays: A unique role of elastic neuronal latency. *Europhys. Lett.* 100, 4 (2012), 48003.
- [292] VICENTE, R., GOLLO, L. L., MIRASSO, C. R., FISCHER, I., AND PIPA, G. Dynamical relaying can yield zero time lag neuronal synchrony despite long conduction delays. *Proc. Natl. Acad. Sci. U.S.A.* 105, 44 (2008), 17157–17162.
- [293] WANG, C. Z., HERBST, J. A., KELLER, G. B., AND HAHNLOSER, R. H. Rapid interhemispheric switching during vocal production in a songbird. *PLoS Biol.* 6, 10 (2008), e250.
- [294] WANG, Q., CHEN, G., AND PERC, M. Synchronous bursts on scale-free neuronal networks with attractive and repulsive coupling. *PLoS One* 6, 1 (2011), e15851.
- [295] WANG, Y., CHIK, D. T., AND WANG, Z. Coherence resonance and noise-induced synchronization in globally coupled hodgkin-huxley neurons. *Phys. Rev. E* 61, 1 (2000), 740–746.
- [296] WATANABE, S., AND STROGATZ, S. H. Constants of motion for superconducting Josephson arrays. *Physica D* 74, 3-4 (1994), 197–253.
- [297] WELLS, D. K., KATH, W. L., AND MOTTER, A. E. Control of stochastic and induced switching in biophysical networks. *Phys. Rev. X* 5, 3 (2015), 031036.
- [298] WHALEN, A. J., BRENNAN, S. N., SAUER, T. D., AND SCHIFF, S. J. Observability and controllability of nonlinear networks: The role of symmetry. *Phys. Rev. X* 5, 1 (2015), 011005.
- [299] WIESENFELD, K., COLET, P., AND STROGATZ, S. H. Synchronization transitions in a disordered Josephson series array. *Phys. Rev. Lett.* 76, 3 (1996), 404–407.

- [300] WIESENFELD, K., AND MOSS, F. Stochastic resonance and the benefits of noise: from ice ages to crayfish and squids. *Nature* 373, 6509 (1995), 33.
- [301] WILEY, D. A., STROGATZ, S. H., AND GIRVAN, M. The size of the sync basin. *Chaos* 16, 1 (2006), 015103.
- [302] WILLIAMS, C. R., MURPHY, T. E., ROY, R., SORRENTINO, F., DAHMS, T., AND SCHÖLL, E. Experimental observations of group synchrony in a system of chaotic optoelectronic oscillators. *Phys. Rev. Lett.* 110, 6 (2013), 064104.
- [303] WOLF, A., SWIFT, J. B., SWINNEY, H. L., AND VASTANO, J. A. Determining lyapunov exponents from a time series. *Physica D* 16, 3 (1985), 285–317.
- [304] WOLFRUM, M., AND OMEL'CHENKO, O. E. Chimera states are chaotic transients. *Phys. Rev. E* 84, 1 (2011), 015201.
- [305] XIE, J., KNOBLOCH, E., AND KAO, H.-C. Multicluster and traveling chimera states in nonlocal phase-coupled oscillators. *Phys. Rev. E* 90, 2 (2014), 022919.
- [306] XU, C., WANG, X., AND SKARDAL, P. S. Bifurcation analysis and structural stability of simplicial oscillator populations. *Phys. Rev. Res.* 2, 2 (2020), 023281.
- [307] YAO, C., MA, J., LI, C., AND HE, Z. The effect of process delay on dynamical behaviors in a self-feedback nonlinear oscillator. *Commun. Nonlinear Sci. Numer. Simulat.* 39 (2016), 99–107.
- [308] YELDESBAI, A., PIKOVSKY, A., AND ROSENBLUM, M. Chimeralike states in an ensemble of globally coupled oscillators. *Phys. Rev. Lett.* 112, 14 (2014), 144103.
- [309] ZAKHAROVA, A., KAPELLER, M., AND SCHÖLL, E. Chimera death: Symmetry breaking in dynamical networks. *Phys. Rev. Lett.* 112, 15 (2014), 154101.
- [310] ZHAI, Y., KISS, I. Z., AND HUDSON, J. L. Control of complex dynamics with time-delayed feedback in populations of chemical oscillators: Desynchronization and clustering. *Ind. Eng. Chem. Res.* 47, 10 (2008), 3502–3514.
- [311] ZHANG, L., MOTTER, A. E., AND NISHIKAWA, T. Incoherence-mediated remote synchronization. *Phys. Rev. Lett.* 118, 17 (2017), 174102.
- [312] ZHANG, X., BOCCALETTI, S., GUAN, S., AND LIU, Z. Explosive synchronization in adaptive and multilayer networks. *Phys. Rev. Lett.* 114, 3 (2015), 038701.

- [313] ZHANG, Y., AND MOTTER, A. E. Identical synchronization of nonidentical oscillators: When only birds of different feathers flock together. *Nonlinearity* 31, 1 (2018), R1–R23.
- [314] ZHANG, Y., AND MOTTER, A. E. Identical synchronization of nonidentical oscillators: when only birds of different feathers flock together. *Nonlinearity* 31 (2018), R1–R23.
- [315] ZHANG, Y., AND MOTTER, A. E. Symmetry-independent stability analysis of synchronization patterns. *arXiv preprint arXiv:2003.05461* (2020).
- [316] ZHANG, Y., NICOLAOU, Z. G., HART, J. D., ROY, R., AND MOTTER, A. E. Critical switching in globally attractive chimeras. *Phys. Rev. X* 10, 1 (2020), 011044.
- [317] ZHANG, Y., NISHIKAWA, T., AND MOTTER, A. E. Asymmetry-induced synchronization in oscillator networks. *Phys. Rev. E* 95, 6 (2017), 062215.
- [318] ZHAO, J., HILL, D. J., AND LIU, T. Synchronization of dynamical networks with nonidentical nodes: Criteria and control. *IEEE Trans. Circuits Syst. I, Reg. Papers* 58, 3 (2011), 584–594.
- [319] ZHOU, C., AND KURTHS, J. Noise-induced phase synchronization and synchronization transitions in chaotic oscillators. *Phys. Rev. Lett.* 88, 23 (2002), 230602.
- [320] ZHOU, C., AND KURTHS, J. Dynamical weights and enhanced synchronization in adaptive complex networks. *Phys. Rev. Lett.* 96, 16 (2006), 164102.
- [321] ZHOU, C., KURTHS, J., KISS, I. Z., AND HUDSON, J. L. Noise-enhanced phase synchronization of chaotic oscillators. *Phys. Rev. Lett.* 89, 1 (2002), 014101.
- [322] ZHOU, J. X., ALIYU, M., AURELL, E., AND HUANG, S. Quasi-potential landscape in complex multi-stable systems. *J. R. Soc. Interface* 9, 77 (2012), 3539–3553.
- [323] ZOU, W., SENTHILKUMAR, D., NAGAO, R., KISS, I. Z., TANG, Y., KOESKA, A., DUAN, J., AND KURTHS, J. Restoration of rhythmicity in diffusively coupled dynamical networks. *Nat. Commun.* 6 (2015), 7709.
- [324] ZOU, W., SENTHILKUMAR, D., ZHAN, M., AND KURTHS, J. Reviving oscillations in coupled nonlinear oscillators. *Phys. Rev. Lett.* 111, 1 (2013), 014101.

APPENDIX A

Supplemental Information on Topological Control of Synchronization Patterns

A.1. Stability analysis of nondiagonalizable clusters

When dealing with directed networks, one must be aware of the possibility of nondiagonalizable coupling matrices, which can be the case even for symmetric networks [92]. Here, we present details of how the analysis in the manuscript also applies to nondiagonalizable networks. To demonstrate that, our key observation is that the treatment of nondiagonalizable networks in Refs. [190, 189] can be generalized to the case of a cluster subnetwork in which each oscillator receives a common input from the rest of the network.

We start from the variational equation of the system in the form of Eq. (2.4) in the main text,

$$(A.1) \quad \delta \dot{\mathbf{X}} = \left[\mathbf{1}_m \otimes J\mathbf{f}(\mathbf{s}_I) - \sigma \hat{\mathbf{L}} \otimes J\mathbf{h}(\mathbf{s}_I) \right] \delta \mathbf{X},$$

but this time we lift the assumption that the matrix $\hat{\mathbf{L}}$ is diagonalizable. For such systems, in general we can not find m independent eigenvectors for $\hat{\mathbf{L}}$. Nevertheless, this matrix can always be transformed into a Jordan canonical form through a similarity transformation

defined by an invertible matrix \mathbf{P} , such that

$$(A.2) \quad \mathbf{B} = \mathbf{P}^{-1} \widehat{\mathbf{L}} \mathbf{P} = \begin{pmatrix} \tilde{\mu} & & & \\ & \mathbf{B}_1 & & \\ & & \ddots & \\ & & & \mathbf{B}_q \end{pmatrix}, \quad \mathbf{B}_j = \begin{pmatrix} \hat{v}_{j+1} & & & \\ & 1 & \hat{v}_{j+1} & \\ & & \ddots & \ddots \\ & & & 1 & \hat{v}_{j+1} \end{pmatrix},$$

where \hat{v}_{j+1} is the eigenvalue of $\widehat{\mathbf{L}}$ corresponding to the Jordan block \mathbf{B}_j , and the matrix entries not shown are zero. The eigenvalues are numbered from 2 to $q+1$ for consistency with the eigenvalue notation in the main text, and are thus ordered as in the rest of the chapter but now without relabeling the (identical) eigenvalues associated with the same Jordan block (which is why $q+1 < m$ in the nondiagonalizable case). The special case in which $\widehat{\mathbf{L}}$ is diagonalizable is also included in this transformation, and it merely corresponds to the case in which all Jordan blocks are 1×1 .

Equation (A.1) can now be decoupled into $q+1$ independent equations accounting for the Jordan blocks. The central difference between the case of an isolated network, as considered in Refs. [190, 189], and the cluster subnetworks considered here is the entry $B_{11} = \tilde{\mu}$, which is zero for isolated networks. However, this term corresponds to a perturbation mode parallel to the cluster synchronization manifold and hence has no influence on the stability of the synchronization state. (The input connections from the rest of the network to the cluster also impact the synchronization state \mathbf{s}_I and shift the eigenvalues \hat{v}_j , but those are not material differences since the same also occurs in the

diagonalizable case.) Thus, to analyze the transverse modes, we focus on the q block-decoupled equations associated with the Jordan blocks $\mathbf{B}_1, \dots, \mathbf{B}_q$:

$$(A.3) \quad \dot{\boldsymbol{\eta}}^{(j)} = [\mathbf{1}_k \otimes J\mathbf{f}(\mathbf{s}_I) - \sigma \mathbf{B}_j \otimes J\mathbf{h}(\mathbf{s}_I)] \boldsymbol{\eta}^{(j)}, \quad j = 1, \dots, q.$$

Assuming that \mathbf{B}_j is $k \times k$, the corresponding equation can be written explicitly for each mode as

$$(A.4) \quad \begin{aligned} \dot{\boldsymbol{\eta}}_1^{(j)} &= [J\mathbf{f}(\mathbf{s}_I) - \sigma \hat{v}_{j+1} J\mathbf{h}(\mathbf{s}_I)] \boldsymbol{\eta}_1^{(j)}, \\ \dot{\boldsymbol{\eta}}_2^{(j)} &= [J\mathbf{f}(\mathbf{s}_I) - \sigma \hat{v}_{j+1} J\mathbf{h}(\mathbf{s}_I)] \boldsymbol{\eta}_2^{(j)} - \sigma J\mathbf{h}(\mathbf{s}_I) \boldsymbol{\eta}_1^{(j)}, \\ &\dots \\ \dot{\boldsymbol{\eta}}_k^{(j)} &= [J\mathbf{f}(\mathbf{s}_I) - \sigma \hat{v}_{j+1} J\mathbf{h}(\mathbf{s}_I)] \boldsymbol{\eta}_k^{(j)} - \sigma J\mathbf{h}(\mathbf{s}_I) \boldsymbol{\eta}_{k-1}^{(j)}. \end{aligned}$$

Starting from the first equation in Eq. (A.4), we notice that $\boldsymbol{\eta}_1^{(j)}$ does not depend on any other $\boldsymbol{\eta}_i^{(j)}$ and its equation is exactly the master stability equation [Eq. (2.5) in the main text]. If Eq. (2.5) is stable for \hat{v}_{j+1} , then $\boldsymbol{\eta}_1^{(j)}$ converges to zero exponentially. Turning to the second equation in Eq. (A.4), we can see that the influence of $\boldsymbol{\eta}_1^{(j)}$ on $\boldsymbol{\eta}_2^{(j)}$ vanishes and $\boldsymbol{\eta}_2^{(j)}$ will also approach zero as $t \rightarrow \infty$ (under the reasonable assumption that $J\mathbf{h}(\mathbf{s}_I)$ is bounded). Applying the same argument iteratively, it follows that the stability of Eq. (A.4) is entirely determined by the stability of Eq. (2.5) for the eigenvalue \hat{v}_{j+1} (with $\boldsymbol{\eta}_i$ demoted by $\boldsymbol{\eta}_1^{(j)}$). The same applies for all j and leads to the conclusion that, even if $\hat{\mathbf{L}}$ is nondiagonalizable, the condition for the cluster synchronous state to be stable is that $\Lambda(\sigma \hat{v}_{j+1}) < 0$ for $j = 1, \dots, q$, where Λ is the largest Lyapunov exponent of Eq. (2.5) and $\hat{v}_2, \dots, \hat{v}_{q+1}$ represent the eigenvalues associated with the transverse modes. Therefore,

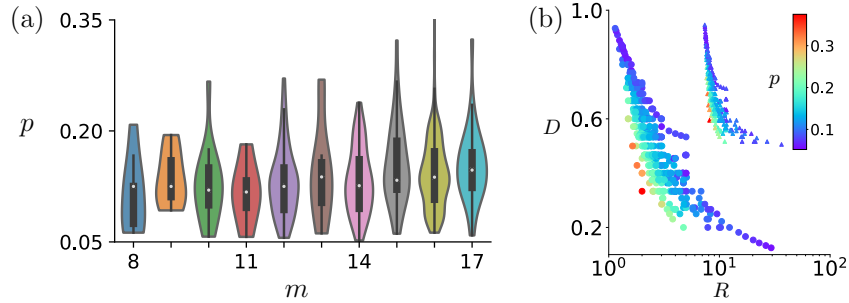


Figure A.1. Improvement of synchronizability by breaking the cluster symmetry through link rewiring. (a) Percentage of rewiring, p , needed to reduce the eigenratio gap $R - 1$ by half. The violin plots show the kernel density estimation of p over all connected undirected symmetry clusters for each cluster size m . Inside each violin plot, the white dot represents the median of the data, the thick line indicates the interquartile range, and the thin line encompasses the 95% confidence interval. (b) Color-coded p in the diagram of link density D versus eigenratio R for all symmetry clusters considered in panel (a), where each cluster corresponds to one data point.

our analysis of synchronizability presented in the main text (including the use of the eigenratio R) applies equally well to nondiagonalizable networks.

A.2. Improving synchronizability through minimal link rewiring

In this section, we consider the optimization of symmetry clusters by rewiring a small number of links. One rewiring consists of removing an existing link and adding a different link not yet present in the cluster. Specifically, we developed an algorithm to optimize synchronizability by rewiring intra-cluster connections (https://github.com/y-z-zhang/optimize_sym_cluster/), which preserves the nonintertwined nature of the clusters. This allows us to investigate how many directional links need to be rewired to reduce the eigenratio gap $R - 1$ by half.

Figure A.1 summarizes results for all connected symmetry clusters that are undirected of sizes between $m = 8$ and 17, where the rewiring percentage $p = h/\ell$ is the ratio between

the minimal number of link rewiring h that halves $R-1$ and the total number ℓ of internal directed links of the cluster. Figure A.1(a) shows that on average only about 14% of the links need to be rewired to significantly improve synchronizability of symmetry clusters, and it is largely size independent. Our algorithm also works for link addition and link removal. In the case of link addition, link density needs to increase by about 20% on average to reduce the eigenratio gap to half; for link removal, about 40% of the links need to be removed to achieve the same effect.

Figure A.1(b) shows the rewiring percentage p as function of the eigenratio R and link density $D = \frac{\ell}{m(m-1)}$, where each data point represents one symmetry cluster. It is clear that clusters that are small in both D and R require the highest percentage of links to be rewired in order to significantly reduce the eigenratio gap. This confirms the intuition that if a network achieves a small eigenratio with a relatively small number of links, then its organization is efficient and its synchronizability is relatively hard to improve. Conversely, a dense non-optimal network or a network with a relatively large eigenratio is easy to optimize with a small number of link modifications.

A.3. Application of the minimal-rewiring algorithm to global synchronization

In this section, we apply the algorithm from the last section to a case in which the full network is symmetric and we seek to optimize global synchronization. In Fig. A.2 we study a 16-node symmetric network and show explicitly through our experiments that it becomes more synchronizable with less symmetry. In the original network [Fig. A.2(a)], all nodes play exactly the same structural role. After seven directional link rewiring [marked in Fig. A.2(b)], the symmetry of the network is largely broken and almost all

nodes are now structurally different: the original 16-node symmetry cluster is reduced to 14 single-node clusters and only 2 nodes occupying symmetric positions. The eigenratio, however, reduces from $R = 4.62$ to $R = 2.80$ and thus improves significantly.

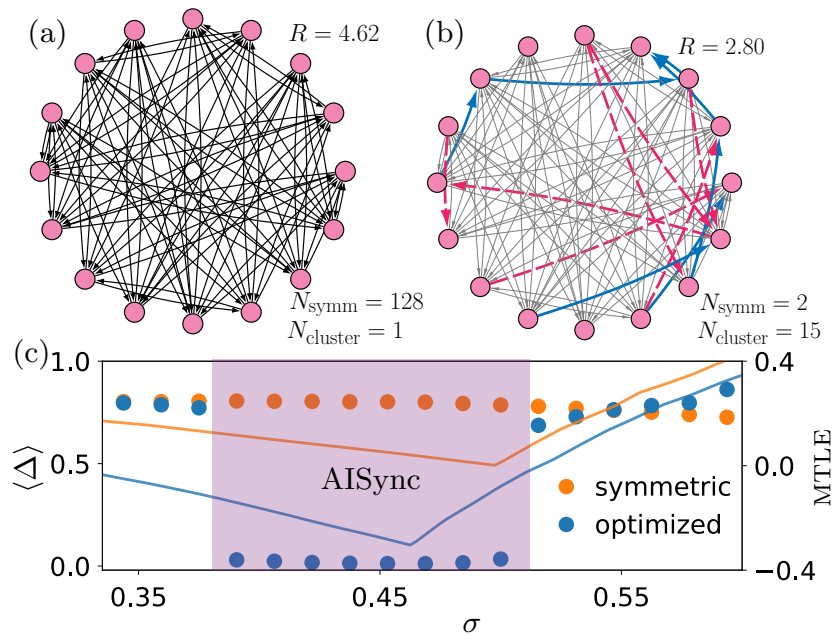


Figure A.2. Experimental demonstration of structural AISync in global synchronization. (a) Symmetric 16-node network of coupled optoelectronic oscillators used in the experiment, which has 128 symmetries, consists of a single (global) symmetry cluster, and has an eigenratio of $R = 4.62$. (b) Optimized network found through simulated annealing, where 7 links are removed (red) and 7 links are added (blue) to the network in (a), resulting in a network with only 2 symmetries and 15 symmetry clusters but an eigenratio of $R = 2.80$. (c) Experimentally measured average synchronization error $\langle \Delta \rangle$ for the symmetric and symmetry-broken network in (a) and (b), respectively, where only the latter can synchronize for a range of σ (purple region). The feedback strength was set to $\beta = 2.8$. This experimental result is consistent with the theoretically computed MTLE (color-coded curves), which is more negative for the symmetry-broken network.

The experimental results are presented in Fig. A.2(c), where we show the average synchronization error as a function of the coupling strength for both networks. The experimental data clearly demonstrates that synchronization is only achieved for the network with reduced symmetry. The experimental result is consistent with the MTLE determined from numerical calculations of the variational equation of the model in Eq. (2.6) [color-coded curves in Fig. A.2(c)]. Indeed, for values of σ close to the boundary of linear stability, synchronization is not observed in experiments due to noise in the ADC [108], but synchronization is consistently observed once the MTLE becomes sufficiently negative.

A.4. Experimental implementation of the coupled optoelectronic oscillators

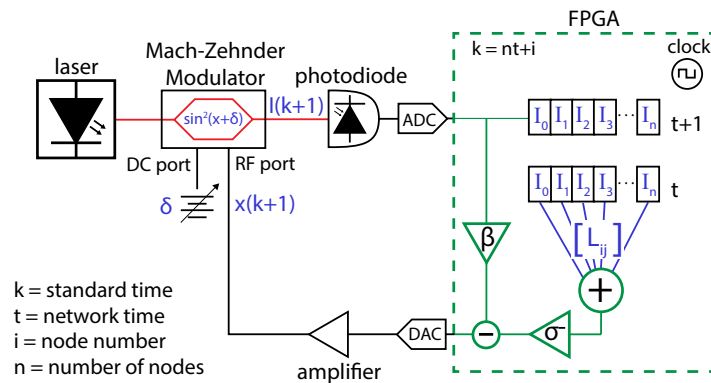


Figure A.3. Schematic illustration of the apparatus used in the optoelectronic experiments. The diagram shows the components of one optoelectronic oscillator (left) and associated coupling scheme (right), which is implemented using time multiplexing in the FPGA.

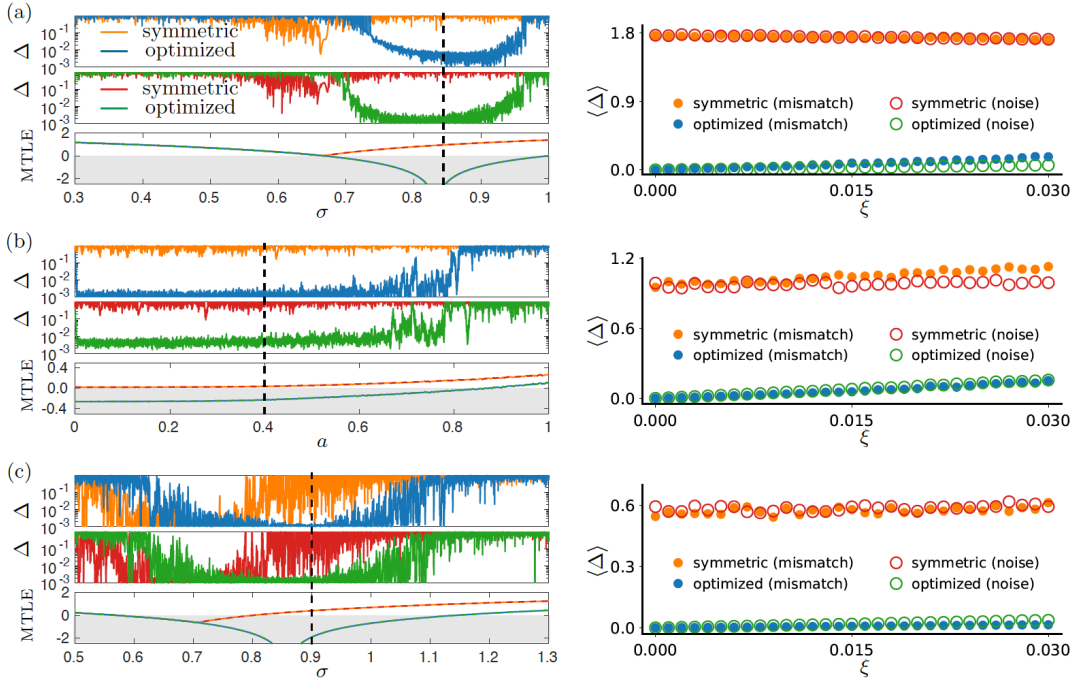


Figure A.4. Robustness of structural AISync against noise and oscillator heterogeneity, demonstrated for (a) the network of Bernoulli maps in Fig. A.5, (b) the network of Hénon maps in Fig. A.5, and (c) the network of optoelectronic oscillators in Fig. 2.1. Upper left panels: direct simulations with random parameter mismatch at magnitude $\xi = 10^{-3}$. Middle left panels: direct simulations with noise at intensity $\xi = 10^{-3}$. Lower left panels: MTLE of the synchronized state in the symmetry cluster and optimized cluster. Right panels: dependence of the average synchronization error $\langle \Delta \rangle$ on ξ , when the system parameters are fixed at the value indicated by the dashed lines on the left.

A.5. Robustness of structural AISync

In order to demonstrate the robustness of structural AISync, we perform direct simulations of three different systems in the presence of Gaussian noise or random oscillator heterogeneity; the results are summarized in Fig. A.4. The three systems include the Bernoulli maps and Hénon maps studied in Appendix A.7, as well as the optoelectronic oscillators from the main text.

In Fig. A.4(a), we fix the parameter of the Bernoulli map to be $r = 5$ and slowly increase the coupling strength σ from 0.3 to 1. For the trajectories in the upper left panel, a random mismatch of magnitude $\xi = 10^{-3}$ is introduced to the oscillator parameter r ; For the trajectories in the middle left panel, the oscillators are subject to Gaussian noise with zero mean and standard deviation equal to $\xi = 10^{-3}$ (approximately the noise intensity in the experimental system). Despite the noise and oscillator heterogeneity, the synchronization error Δ match well with the prediction based on the MTLE calculations shown in the lower left panel. We investigate the dependence of the time-averaged synchronization error $\langle \Delta \rangle$ on the magnitude ξ of noise/mismatch in the right panel, where σ is fixed at 0.85 (corresponding to the dashed line on the left).

The same analysis is performed for the Hénon maps in Fig. A.4(b) and for the optoelectronic oscillators in Fig. A.4(c). For the Hénon maps, mismatch is introduced in the parameter b , whose homogeneous value is set to $b = 0.3$, for coupling strength fixed at $\sigma = 0.5$. For the optoelectronic oscillators, mismatch is introduced in the parameter β , whose homogeneous value is set to $\beta = 6$. It can be seen that in all three cases structural AISync is robust against both noise and oscillator heterogeneity.

A.6. Optimizing intertwined clusters

In this section, we provide more details on the optimization of intertwined clusters. When two clusters are intertwined, desynchronization in one cluster will in general lead to the loss of synchrony in the other cluster (an example would be two equal-sized rings coupled in one-to-one fashion). This is because the symmetry group acting on the two

clusters does not admit a geometric decomposition; that is, symmetry permutations cannot be applied to each cluster independently. As a consequence, a desynchronized cluster sends incoherent signals to nodes in the other cluster, causing its intertwined counterpart to desynchronize as well. The irreducible representation transformation introduced in Ref. [219] is a powerful formalism that enables stability analysis on many cluster synchronization patterns. In that framework, the presence of intertwined clusters is reflected in nontrivial transverse blocks (i.e., blocks with dimension greater than 1) in the transformed coupling matrix, whereas nonintertwined clusters only give rise to 1×1 transverse blocks. Unfortunately, the high dimensionality of the transverse blocks makes the effect of topological perturbations on cluster synchronizability opaque, and thus the analysis of the transformed matrix offers little insight into how to optimize the clusters to support desired synchronization patterns.

We developed a new perspective that gives a simple necessary condition for the synchronization in intertwined clusters. This in turn points to an extension of the previous optimization scheme that is no longer limited to nonintertwined clusters.

Consider two intertwined clusters X and Y subject to transverse perturbations $\delta\mathbf{X}$ and $\delta\mathbf{Y}$, respectively. Their variational equation reads

$$(A.5) \quad \begin{cases} \delta\dot{\mathbf{X}} = (\mathbf{1}_m \otimes J\mathbf{f}(\mathbf{s}_{I_X}) - \sigma\hat{\mathbf{L}}_X \otimes J\mathbf{h}(\mathbf{s}_{I_X})) \delta\mathbf{X} + \sigma\mathbf{C} \otimes J\mathbf{h}(\mathbf{s}_{I_Y})\delta\mathbf{Y}, \\ \delta\dot{\mathbf{Y}} = (\mathbf{1}_{m'} \otimes J\mathbf{f}(\mathbf{s}_{I_Y}) - \sigma\hat{\mathbf{L}}_Y \otimes J\mathbf{h}(\mathbf{s}_{I_Y})) \delta\mathbf{Y} + \sigma\mathbf{D} \otimes J\mathbf{h}(\mathbf{s}_{I_X})\delta\mathbf{X}. \end{cases}$$

Here, $\mathbf{C}_{ij} = 1$ if the i -th oscillator in cluster X receives an input from the j -th oscillator in cluster Y and $\mathbf{C}_{ij} = 0$ otherwise. The intercluster coupling matrix \mathbf{D} is similarly defined with the role of two clusters exchanged ($\mathbf{D} = \mathbf{C}^\top$ if the intercluster coupling is

undirected). Without the cross-coupling term, Eq. (A.5) reduces to the nonintertwined case discussed in the main text

$$(A.6) \quad \begin{cases} \delta\dot{\mathbf{X}} = (\mathbf{1}_m \otimes J\mathbf{f}(\mathbf{s}_{I_X}) - \sigma\hat{\mathbf{L}}_X \otimes J\mathbf{h}(\mathbf{s}_{I_X})) \delta\mathbf{X}, \\ \delta\dot{\mathbf{Y}} = (\mathbf{1}_{m'} \otimes J\mathbf{f}(\mathbf{s}_{I_Y}) - \sigma\hat{\mathbf{L}}_Y \otimes J\mathbf{h}(\mathbf{s}_{I_Y})) \delta\mathbf{Y}. \end{cases}$$

Because of the intertwined nature of the two clusters, they must be considered concurrently when synchronization is desired in either of them. That is, $\hat{\mathbf{L}}_X$ and $\hat{\mathbf{L}}_Y$ should be optimized to ensure that $\delta\mathbf{X}$ and $\delta\mathbf{Y}$ both vanish in Eq. (A.5).

It is difficult to establish a synchronizability measure on two clusters based on Eq. (A.5), but we can see the following connection between Eqs. (A.5) and (A.6):

$$(A.7) \quad \|\delta\mathbf{X}\| \rightarrow 0 \text{ and } \|\delta\mathbf{Y}\| \rightarrow 0 \text{ in Eq. (A.5)}$$

↓

$$(A.8) \quad \|\delta\mathbf{X}\| \rightarrow 0 \text{ and } \|\delta\mathbf{Y}\| \rightarrow 0 \text{ in Eq. (A.6).}$$

That is, $\|\delta\mathbf{X}\|$ and $\|\delta\mathbf{Y}\|$ going to zero in Eq. (A.6) is a necessary condition for the synchronization in intertwined clusters. For example, if $\|\delta\mathbf{X}\|$ does not vanish in Eq. (A.6), then $\|\delta\mathbf{Y}\|$ must be away from zero in order for $\|\delta\mathbf{X}\| \rightarrow 0$ in Eq. (A.5). This connection between Eqs. (A.5) and (A.6) implies that we can promote synchronization in the intertwined clusters by optimizing each of the two clusters independently, using the same method originally developed for nonintertwined clusters. In particular, such optimization is guaranteed to expand the region in parameter space satisfying the necessary condition

in Eq. (A.8) (i.e., the condition in Eq. (2.7) in the main text). Inside this expanded region, one is likely to observe structural AISync, as experimentally demonstrated in the main text. It is worth mentioning that the same argument still holds when more than two clusters are intertwined.

A.7. Prevalence of structural AISync

To further demonstrate that the phenomenon we describe is common across different nodal dynamics and network structure, we present two additional examples. For both examples we consider a random network with five symmetry clusters, as shown in Fig. A.5(a). Within this network, we focus on the highlighted symmetry cluster (magenta nodes), which in isolation corresponds to the second symmetry cluster in Table 2.1, and we contrast its synchronizability with that of the non-symmetric cluster generated by removing a subset of its links (red links).

We first consider this system when the nodes are equipped with dynamics of a Bernoulli map,

$$(A.9) \quad x_i(t+1) = r x_i(t) - \sigma \sum_{j=1}^n L_{ij} x_j(t) \pmod{2\pi},$$

which, for being piecewise linear and one dimensional, is arguably one of the simplest possible nodal dynamics that one can consider in an oscillator network. Despite its simplicity, this system exhibits a rich stability diagram in the $r \times \sigma$ parameter space, including a wide region in which synchronization is stable for the non-symmetric cluster but unstable for the symmetric one, as shown in Fig. A.5(b). For $r \geq 5$, in particular, synchronization in the symmetric cluster is unstable for *any* coupling strength σ . Topological control is

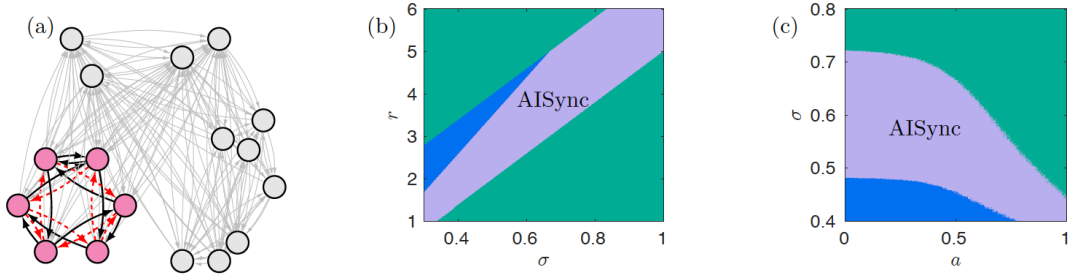


Figure A.5. Cluster synchronization stabilized by breaking the structural symmetry of the cluster. (a) Random network with five symmetry clusters (grouped nodes), in which the cluster considered in our examples is highlighted (magenta nodes). Upon removal of the marked links (red), this cluster becomes optimally synchronizable but non-symmetric. (b, c) Stability diagram in the $r \times \sigma$ space for Bernoulli map oscillators (b) and in the $\sigma \times a$ space for Hénon map oscillators (c). The different colors mark regions in which synchronization is stable in both clusters (blue), unstable for both clusters (green), and unstable for the symmetric cluster but stable for the asymmetric one (purple), as determined by our calculation of the MTLE.

particularly valuable in this case as it allows for stability that would be impossible by merely adjusting σ in the original cluster.

As an illustration of higher dimensional nonlinear nodal dynamics, we also consider the system in Fig. A.5(a) when equipped with the dynamics of a Hénon map,

$$(A.10) \quad \begin{cases} x_i(t+1) = 1 - a x_i^2(t) + y_i(t) - \sigma \sum_{j=1}^n L_{ij} y_j(t), \\ y_i(t+1) = b x_i(t), \end{cases}$$

where the variables x_i and y_i are defined on a torus and limited to $[-2, 2]$; the coupling between oscillators are through the y_i variables. As shown in Fig. A.5(c), fixing $b = 0.3$ and calculating the stability diagram in the $\sigma \times a$ parameter space, once again we identify a wide region in which the non-symmetric cluster exhibits stable synchronization whereas the symmetric one does not.

As illustrated by these and other systems we have studied in detail, in general a significant portion of the parameter space is occupied by a region in which synchronization is not stable for the symmetric cluster but it becomes stable when the structure of the cluster is optimized, which in turn goes in tandem with breaking its symmetry under the given constraints. These examples also further illustrate the excellent agreement between direct simulations and theoretical predictions observed throughout.

APPENDIX B

Supplemental Information on Asymmetry-Induced Synchronization in Multiscale Networks

B.1. Definition of Cayley graphs

Given a generating set S of a finite group G , the Cayley graph associated with S and G is defined as the network in which a node represents an element of G and a directed link from one node $g \in G$ to another $g' \in G$ represents the composition of some element $s \in S$ with g that gives g' (i.e., $gs = g'$). While such a network is generally directed, it will be undirected if the inverse of every element of S belongs to S . Choosing S to be a generating set guarantees that the resulting network is (strongly) connected. A generalization to multiple link types can be obtained if we assign different elements of S to different link types.

B.2. Details on multilayer models

Since Eq. (3.2) defines a subclass of systems governed by Eq. (3.1), it can always be written in the form of Eq. (3.1) for a given network structure specified by $A^{(\alpha)}$. This can be seen by stacking the m -dimensional vectors in Eq. (3.2) and defining appropriate

functions as follows:

$$(B.1) \quad \mathbf{X}_i := \begin{pmatrix} \mathbf{x}_1^{(i)} \\ \vdots \\ \mathbf{x}_L^{(i)} \end{pmatrix}, \quad \mathbf{F}_i := \begin{pmatrix} \mathbf{F}_1^{(i)} \\ \vdots \\ \mathbf{F}_L^{(i)} \end{pmatrix}, \quad \mathbf{H}^{(\alpha)} := \begin{pmatrix} \mathbf{H}_1^{(\alpha)} \\ \vdots \\ \mathbf{H}_L^{(\alpha)} \end{pmatrix},$$

$$(B.2) \quad \mathbf{F}_\ell^{(i)}(\mathbf{X}_i) := \mathbf{f}(\mathbf{x}_\ell^{(i)}) + \sum_{\ell'=1}^L \tilde{A}_{\ell\ell'}^{(ii)} [\mathbf{h}(\mathbf{x}_{\ell'}^{(i)}) - \mathbf{h}(\mathbf{x}_\ell^{(i)})],$$

$$(B.3) \quad \mathbf{H}_\ell^{(\alpha)}(\mathbf{X}_i, \mathbf{X}_{i'}) := \sum_{\ell'=1}^L B_{\ell\ell'}^{(\alpha)} [\mathbf{h}(\mathbf{x}_{\ell'}^{(i')}) - \mathbf{h}(\mathbf{x}_\ell^{(i)})],$$

where $B_{\ell\ell'}^{(\alpha)}$ is defined to be the value of $\tilde{A}_{\ell\ell'}^{(ii')}$ when node i' is connected to node i by a link of type α . Note that these node-to-node interactions are not necessarily diffusive, since we can have $\mathbf{H}^{(\alpha)}(\mathbf{X}_i, \mathbf{X}_{i'}) \neq \mathbf{0}$ even for $\mathbf{X}_i = \mathbf{X}_{i'}$, if $\mathbf{x}_\ell^{(i)} \neq \mathbf{x}_{\ell'}^{(i')}$ for some $\ell \neq \ell'$ [which in particular means that the coupling term cannot be written in the form $\mathbf{H}^{(\alpha)}(\mathbf{X}_i, \mathbf{X}_{i'}) = \tilde{\mathbf{H}}^{(\alpha)}(\mathbf{X}_{i'}) - \tilde{\mathbf{H}}^{(\alpha)}(\mathbf{X}_i)$]. For example, even when nodes 1 and 4 are synchronized in the network of Fig. 3.1, i.e., $\mathbf{X}_1 = \mathbf{X}_4 = (\mathbf{s}_1(t), \mathbf{s}_2(t))^T$, the coupling term corresponding to the link of type $\alpha = 3$ between them is in general not identically zero:

$$(B.4) \quad \mathbf{H}^{(3)}(\mathbf{X}_1, \mathbf{X}_4) = \begin{pmatrix} \mathbf{h}(\mathbf{s}_2) - \mathbf{h}(\mathbf{s}_1) \\ 0 \end{pmatrix} \neq \mathbf{0}.$$

However, since we assume identical dynamics for subnodes and diffusive coupling between subnodes, a synchronous state of Eq. (3.2) given by $\mathbf{x}_\ell^{(i)}(t) = \mathbf{s}(t)$, $\forall i, \ell$ with $\dot{\mathbf{s}} = \mathbf{f}(\mathbf{s})$ is guaranteed to exist even if $F^{(i)}$'s are heterogeneous. This corresponds to a global synchronous state of Eq. (3.1) defined by $\mathbf{X}_i = \mathbf{S} := (\mathbf{s}, \dots, \mathbf{s})^T$, $\forall i$, which can be verified by noting that $\mathbf{H}^{(\alpha)}(\mathbf{S}, \mathbf{S}) = \mathbf{0}$ and $\mathbf{F}_\ell^{(i)}(\mathbf{S}) := \mathbf{f}(\mathbf{s})$, $\forall i, \ell$.

B.3. Details on MSF analysis

Equation (3.2) can be rewritten as a monolayer network by defining a single index for all the $n := LN$ subnodes, in which node i has subnodes $j = k_{i1}, \dots, k_{iL}$ with $k_{i\ell} := (i-1)L + \ell$. This leads to the standard form for a (monolayer) diffusively coupled network of oscillators:

$$(B.5) \quad \dot{\mathbf{x}}_j = \mathbf{f}(\mathbf{x}_j) + \sum_{j'=1}^n \tilde{A}_{jj'} [\mathbf{h}(\mathbf{x}_{j'}) - \mathbf{h}(\mathbf{x}_j)],$$

where $\mathbf{x}_j = \mathbf{x}_\ell^{(i)}$ and $\tilde{A}_{jj'} := \tilde{A}_{\ell\ell'}^{(ii')}$ for $j = k_{i\ell}$ and $j' = k_{i'\ell'}$. In the monolayer adjacency matrix $\tilde{A} = (\tilde{A}_{jj'})$, the matrix $B^{(\alpha)} = (B_{\ell\ell'}^{(\alpha)})$ appears as multiple off-diagonal blocks of size L , and the arrangement of those blocks within \tilde{A} matches with the structure of the corresponding adjacency matrix $A^{(\alpha)}$, reflecting the topology of node-to-node interactions through links of type α [see Fig. 3.1(d) for an example]. This equation allows application of the MSF analysis [217] because subnodes and sublinks (and the associated coupling functions) are identical. The stability function $\psi(\lambda)$ is defined as the maximum Lyapunov exponent of the reduced variational equation,

$$(B.6) \quad \dot{\boldsymbol{\xi}} = [D\mathbf{f}(\mathbf{s}) - \lambda D\mathbf{h}(\mathbf{s})]\boldsymbol{\xi},$$

where $\boldsymbol{\xi}$ is an m -dimensional perturbation vector, $D\mathbf{f}(\mathbf{s})$ and $D\mathbf{h}(\mathbf{s})$ are the Jacobian of \mathbf{f} and \mathbf{h} , respectively, at the synchronous state, $\mathbf{x}_j = \mathbf{s}(t)$, $\forall j$, and λ is a complex-valued parameter.

B.4. Verifying the AISync conditions

Here we describe our scheme for verifying AISync conditions (C1) and (C2) given a symmetric network structure (adjacency matrices $A^{(\alpha)}$), external sublink configurations (matrices $B^{(\alpha)}$), a set \mathcal{F} of possible internal sublink configurations (from which matrices $F^{(i)}$ are chosen), isolated subnode dynamics \mathbf{f} , and sublink coupling function \mathbf{h} . We first obtain the stability function $\psi(\lambda)$:

- (1) Compute a trajectory $\mathbf{s}(t)$ of an isolated subnode by integrating $\dot{\mathbf{s}} = \mathbf{f}(\mathbf{s})$, which determines the synchronous state, $\mathbf{x}_\ell^{(i)}(t) = \mathbf{s}(t)$, $\forall i, \ell$.
- (2) Integrate Eq. (B.6) and calculate its maximum Lyapunov exponent (MLE), which defines $\psi(\lambda)$ for a range of λ in the complex plane.

Note that $\psi(\lambda)$ depends only on \mathbf{f} , \mathbf{h} , and $\mathbf{s}(t)$. For a given symmetric network structure and external sublink configurations, we can compute the stability Ψ of the synchronous state for any combination of $F^{(i)} \in \mathcal{F}$ by calculating and substituting the Laplacian eigenvalues λ_j into the formula $\Psi = \max_{2 \leq j \leq n} \psi(\lambda_j)$. To establish the AISync property, we verify the following conditions:

- (C1)': For each matrix $F \in \mathcal{F}$, set $F^{(1)} = \dots = F^{(N)} = F$ (leading to a homogeneous system) and verify $\Psi > 0$.
- (C2)': Identify a combination of (heterogeneous) $F^{(i)} \in \mathcal{F}$ for which $\Psi < 0$ (e.g., by checking exhaustively or by using a numerical optimization algorithm to minimize Ψ over $F^{(i)}$).

The verification of condition (C1)' provides strong support for (C1), since the only other possibility for a stable synchronization of all nodes is a state of the form $\mathbf{x}_\ell^{(i)} = \mathbf{s}_\ell(t)$, $\forall i, \ell$,

with at least one $\mathbf{s}_\ell(t)$ different from the others (which we find does not exist in many cases, such as the examples in Fig. 3.3). To provide additional support for (C1), we directly simulate Eq. (3.2) from a set of initial conditions and verify that the synchronization error e does not approach zero whenever $F^{(1)} = \dots = F^{(N)}$, where e is defined as the standard deviation of the node state vectors, or equivalently,

$$(B.7) \quad e^2 := \frac{1}{N} \sum_{i=1}^N \sum_{\ell=1}^L \|\mathbf{x}_\ell^{(i)} - \bar{\mathbf{x}}_\ell\|^2, \quad \bar{\mathbf{x}}_\ell := \frac{1}{N} \sum_{i=1}^N \mathbf{x}_\ell^{(i)}.$$

Here $\|\cdot\|$ denotes the 2-norm in the state space of the subnode dynamics, and $e = 0$ is achieved if and only if the system is in a synchronous state of the form $\mathbf{x}_\ell^{(i)} = \mathbf{s}_\ell(t)$. To complete our procedure, we verify condition (C2)', which rigorously establishes (C2).

B.5. Details on the example in Fig. 3.3

In the example system from Fig. 3.3, the coupling matrices for the two link types are $B^{(1)} = \begin{pmatrix} b & b \\ 0 & 0 \end{pmatrix}$ and $B^{(2)} = \begin{pmatrix} 0 & 0 \\ 0 & b \end{pmatrix}$, where the constant b represents the coupling strength common to all external sublinks. The coupling matrix $F^{(i)}$ for internal sublinks is chosen from the binary set $\mathcal{F} = \left\{ \begin{pmatrix} 0 & a \\ 0 & 0 \end{pmatrix}, \begin{pmatrix} 0 & 0 \\ a & 0 \end{pmatrix} \right\}$, corresponding to the two possible sublink directions [and thus to two types of nodes indicated by green and cyan color, respectively, in Fig. 3.3(a)], where the constant a represents the coupling strength common to all internal sublinks. The Lorenz dynamics of the subnodes and the coupling represented by sublinks are given by

$$(B.8) \quad \mathbf{f}(\mathbf{x}) = \begin{pmatrix} \gamma(x_2 - x_1) \\ x_1(\rho - x_3) - x_2 \\ x_1x_2 - \beta x_3 \end{pmatrix}, \quad \mathbf{h}(\mathbf{x}) = \begin{pmatrix} x_2 \\ 0 \\ 0 \end{pmatrix}, \quad \mathbf{x} = \begin{pmatrix} x_1 \\ x_2 \\ x_3 \end{pmatrix}$$

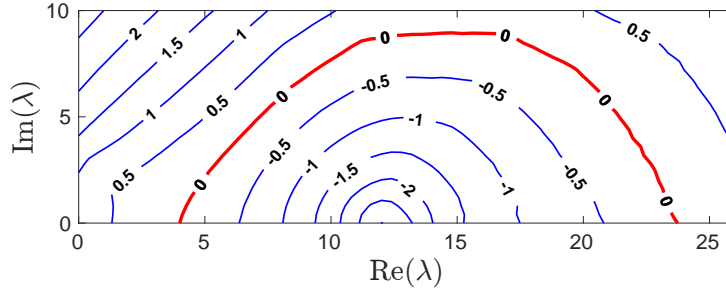


Figure B.1. Stability function $\psi(\lambda)$ for the AISync system in Fig. 3.3.

with the standard parameters, $\gamma = 10$, $\rho = 28$, and $\beta = 8/3$.

The stability function $\psi(\lambda)$ is determined by Eq. (B.6), which for this system reads

$$(B.9) \quad \begin{pmatrix} \dot{\xi}_1 \\ \dot{\xi}_2 \\ \dot{\xi}_3 \end{pmatrix} = \begin{pmatrix} -\gamma & \gamma - \lambda & 0 \\ \rho - s_3 & -1 & -s_1 \\ s_2 & s_1 & -\beta \end{pmatrix} \begin{pmatrix} \xi_1 \\ \xi_2 \\ \xi_3 \end{pmatrix},$$

where $\boldsymbol{\xi} := (\xi_1, \xi_2, \xi_3)^T$ is the variation of the state vector \boldsymbol{x} and the synchronous state $\boldsymbol{s} := (s_1, s_2, s_3)^T$ satisfies the equation for a single isolated Lorenz oscillator:

$$(B.10) \quad \begin{cases} \dot{s}_1 &= \gamma(s_2 - s_1), \\ \dot{s}_2 &= s_1(\rho - s_3) - s_2, \\ \dot{s}_3 &= s_1 s_2 - \beta s_3. \end{cases}$$

For a given λ in the complex plane, we compute $\psi(\lambda)$ by numerically integrating Eqs. (B.9) and (B.10) for 2×10^4 time units and estimating the MLE [303] associated with the variable $\boldsymbol{\xi}$. Figure B.1 shows the resulting estimate of $\psi(\lambda)$, which has a bounded stability region $\{\lambda \in \mathbb{C} \mid \psi(\lambda) < 0\}$.

For a given combination of a and b , we obtain $\Psi_{=}$ and Ψ_{\neq} , which are shown in Fig. 3.3(b). Note that for this example there are only two distinct homogeneous systems and two distinct heterogeneous systems. One of these heterogeneous systems is shown in Fig. 3.3(a). We also note that $\Psi_{=} > 0$ and $\Psi_{\neq} < 0$ are equivalent to the conditions (C1)' and (C2)' in Appendix B.4, respectively. For each combination of a and b satisfying both conditions [on a grid covering Fig. 3.3(b) with a resolution of 0.2], we additionally run 24 direct simulations of Eq. (3.2) for 200 time units. The initial condition $\mathbf{x}_\ell^{(i)}(0)$ for each subnode is chosen randomly and independently from the uniform distribution in the region $[0, 10] \times [0, 10] \times [0, 10]$ of its state space. The results confirm that the synchronization error e defined in Eq. (B.7) and averaged over the last 100 time units does not fall below 10^{-3} in all 24 runs for both homogeneous systems, providing solid evidence that the system satisfies the AISync condition (C1) for these combinations of a and b . Since $\Psi_{\neq} < 0$ implies (C2)' and thus (C2), this confirms AISync in the region shaded purple in Fig. 3.3(b).

The initial condition for the sample trajectory in Fig. 3.3(c) is chosen randomly within a distance of 10^{-3} from the synchronous state. The trajectory is then computed by integrating the system with all nodes green for $t \leq 25$, instantaneously switching the direction of the sublink between subnodes $2'$ and $2''$, and then continuing to integrate for $25 \leq t \leq 50$.

B.6. Sampling protocol used in Fig. 3.5

We randomly sample systems whose network structure $A^{(\alpha)}$ is a circulant graph (with directed links of possibly multiple types) of given size N and external sublink in-degree D

(i.e., the total number of sublinks received by the subnodes of a given node). Each of the D sublinks coming into node 1 is chosen randomly; it connects a random subnode chosen uniformly from the other $N - 1$ nodes to a random subnode chosen uniformly from node 1. The incoming sublinks into nodes 2 to N are then chosen to precisely match those coming into node 1, which ensures that the network structure is a circulant graph. This simultaneously specifies $A^{(\alpha)}$ and $B^{(\alpha)}$ defining the system. To determine σ_{\neq} , $\sigma_{=}$, and r for this system, we calculate the eigenspread σ of the monolayer network representation for all the possible internal sublink configurations $F^{(i)}$, chosen here from the binary set $\left\{\begin{pmatrix} 0 & 1 \\ 0 & 0 \end{pmatrix}, \begin{pmatrix} 0 & 0 \\ 1 & 0 \end{pmatrix}\right\}$. For each combination of N and D , we generate a sample of 4,000 such systems to compute the fraction of AISync-favoring networks.

B.7. Approximate symmetry in Fig. 3.5

The approximate symmetry with respect to the vertical line at density 0.5 observed in Fig. 3.5(a) can be explained using the notion of network complement. The complement of a given (unweighted) network with adjacency matrix $\tilde{A} = (\tilde{A}_{jj'})$ is defined as the network having the adjacency matrix $\tilde{A}^c = (\tilde{A}_{jj'}^c)$ given by

$$(B.11) \quad \tilde{A}_{jj'}^c := (1 - \tilde{A}_{jj'})(1 - \delta_{jj'}).$$

The external sublink density of a network and its complement add up to one, placing them symmetrically about the vertical line at density 0.5 in Fig. 3.5(a). When the nontrivial Laplacian eigenvalues of the network and its complement, which we denote $\lambda_2, \dots, \lambda_n$ and $\lambda_2^c, \dots, \lambda_n^c$, respectively, are both indexed in the order of increasing real part, they are related by $\lambda_j + \lambda_{n+2-j}^c = n$ [191]. This implies that, if σ is the eigenvalue spread for a

monolayer network with given internal sublink configurations $F^{(i)}$, then the spread for its complement is given by

$$(B.12) \quad \sigma^c = \frac{\tilde{m}\sigma}{n(n-1) - \tilde{m}},$$

where $\tilde{m} := \sum_j \sum_{j' \neq j} \tilde{A}_{jj'}$ is the number of directed links in the network \tilde{A} . Now consider two systems with n subnodes and adjacency matrices \tilde{A}_1 and \tilde{A}_2 , whose σ values are σ_1 and σ_2 , respectively. If we denote the σ values of the complement of these systems by σ_1^c and σ_2^c , respectively, we have

$$(B.13) \quad \frac{\sigma_1}{\sigma_2} = \frac{\sigma_1^c}{\sigma_2^c}$$

when \tilde{A}_1 and \tilde{A}_2 have the same number of directed links, i.e., $\tilde{m}_1 = \tilde{m}_2$. It follows from Eq. (B.12) that if \tilde{A}_1 is the best homogeneous system and \tilde{A}_2 the best heterogeneous system for a given external connection pattern with density x , then their complements are the best homogeneous and heterogeneous system for an external connection pattern with density $1 - x$. Thus, the value of AISync strength r is the same at density x and $1 - x$. The symmetry, however, is not perfect between sparse and dense parts of the plot, since we exclude the cases in which the network is not synchronizable (i.e., we require $\min_{j \geq 2} \text{Re}(\lambda_j) > 0$), the effect of which is not symmetric between sparse and dense cases.

APPENDIX C

Supplemental Information on Outperforming Design with Random Heterogeneity in Network Synchronization

C.1. Random heterogeneity in all parameters

In Fig. C.1, we show that disorder can also consistently induce synchronization when it is present in all three parameters. In this case, the parameters $\{\omega_j\}$, $\{\lambda_j\}$, and $r_0^2\{\gamma_j\}$ are all independently drawn from a Gaussian distribution with standard deviation σ .

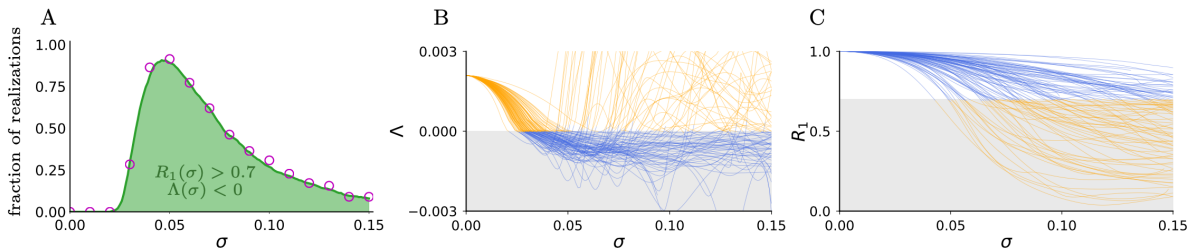


Figure C.1. Effect of random heterogeneity in all parameters. (A) Probability of inducing synchronization when disorder is present in $\{\omega_j; \gamma_j; \lambda_j\}$, estimated from 1000 realizations of the heterogeneity profile. (B) MTLE $\Lambda(\sigma)$ for 100 such realizations, where the portions highlighted in blue correspond to $\Lambda(\sigma) < 0$. (C) Order parameter $R_1(\sigma)$ of the (possibly unstable) phase-locked state for the same 100 realizations, where blue indicates $R_1(\sigma) > 0.7$. The network and parameters are the same as in Fig. 5.3.

C.2. Effect of network size

In Fig. C.2, we explore how the network size affects the probability of inducing synchronization with random oscillator heterogeneity. In all cases the effect is persistent

across a wide range of network sizes, for directed ring networks ranging from $N = 9$ to $N = 72$. It can be seen that the peak of the curve shifts leftward as N increases, but it always maintains its height above 0.9 for all sizes N investigated here.

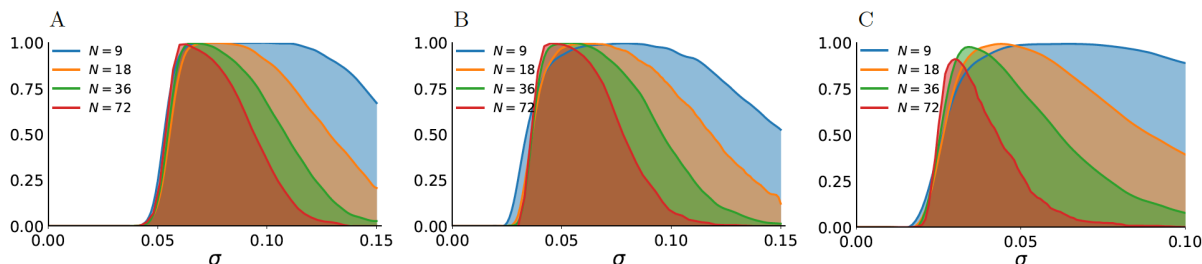


Figure C.2. Effect of random heterogeneity across network sizes. (A–C) Probability of inducing synchronization for heterogeneous $\{\omega_j\}$ (A), $\{\omega_j; \gamma_j\}$ (B), and $\{\omega_j; \gamma_j; \lambda_j\}$ (C) in directed ring networks of various sizes N . Each probability curve is estimated from 1000 realizations of the heterogeneity profile. The parameters are $\lambda = 0.1$, $\omega = 1.35$, $\gamma = 3.81$, $K = 0.3$, and $\tau = 1.8\pi$.

C.3. Random heterogeneity in random networks

In Fig. C.3, we show that random oscillator heterogeneity can also induce synchronization in networks beyond directed rings. Two representative examples of random networks with common indegrees are studied in detail. Direct simulations show that random heterogeneity in any or all of the three parameters can consistently promote synchrony in both networks.

C.4. Experimental protocols

The experiments are performed using a standard three-electrode cell with a platinum counter, a $\text{Hg}/\text{Hg}_2\text{SO}_4/\text{sat.K}_2\text{SO}_4$ reference, and a nickel array working electrode. The

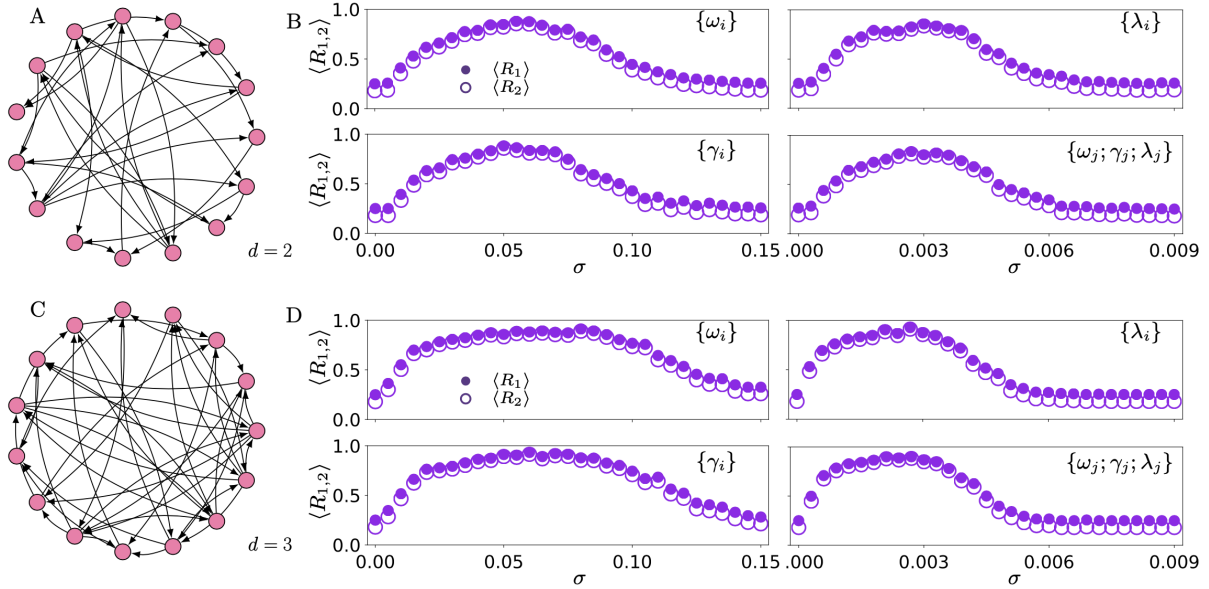


Figure C.3. Effect of random oscillator heterogeneity in random networks. (A) Random network with indegree $d = 2$. (B) Average order parameters for the network in A with heterogeneity introduced in $\{\omega_j\}$, $\{\lambda_j\}$, $\{\gamma_j\}$, and $\{\omega_j; \gamma_j; \lambda_j\}$, respectively. (C) Random network with indegree $d = 3$. (D) Counterpart of B for the network in C. The results in B and D are based on 300 realizations of the heterogeneity profile. The parameters for the homogeneous systems are chosen from the region where synchronization is unstable: $\lambda = 0.1$, $\omega = -2.7$, $\gamma = -30$, $K = 0.05$, and $\tau = 1.8\pi$ in B; $\lambda = 0.1$, $\omega = -3.9$, $\gamma = -42.8$, $K = 0.033$, and $\tau = 1.8\pi$ in D.

electrolyte was 3M H_2SO_4 at 10°C . The electrode array consisted of sixteen 1 mm diameter nickel wires with a spacing of 3 mm. The wires were embedded in epoxy, so that only the wire ends were exposed to the electrolyte. Before the experiments, the electrode array was polished with a series of sandpapers. A multichannel potentiostat (Gill-IK64, ACM Instruments), interfaced with a real-time LabVIEW controller, was used to measure the current $I_j(t)$ and set the potential $V_j(t)$ of the j th wire according to Eq. 5.9 at a rate of 200 Hz. Throughout the experiments we set the circuit potential $V_0 = 1.240$ V. Without heterogeneity, the individual resistors were set to 1.06 k ohm. Parametric heterogeneity

was introduced by setting the individual resistors to different values drawn from a normal distribution while keeping the mean resistance fixed to 1.06 k ohm. To avoid accidentally balancing out the intrinsic heterogeneity, only heterogeneity profiles that have a negligible correlation with the natural frequencies of the unperturbed oscillators were used (we require that the absolute value of the correlation coefficient be smaller than 0.2). The coupling delay τ was set to 75% of the mean natural period of the oscillations, which corresponds to τ in the range of 1.50 s to 1.75 s throughout the reported experiments. The coupling strength K was set to values about 10% larger than the desynchronization threshold (between -0.12 and -0.10 V/mA in the reported experiments).

APPENDIX D

Supplemental Information on Critical Switching in Globally Attractive Chimeras

D.1. Switching chimeras in systems with continuous-time dynamics

As an example of continuous-dynamics switching chimeras, we consider the multilayer network depicted in Fig. D.1(a), where each layer consists of six identical Lorenz oscillators interacting through the coupling function $\mathbf{H}_1 = (0, 0, z)^\top$. In addition, the two layers are all-to-all coupled through the coupling function $\mathbf{H}_2 = (0, 0, x)^\top$. The oscillators in the first layer are thus described by the equations

$$\begin{aligned}
 \dot{x}_i^{(1)} &= \alpha (y_i^{(1)} - x_i^{(1)}), \\
 \dot{y}_i^{(1)} &= x_i^{(1)} (\rho - z_i^{(1)}) - y_i^{(1)}, \\
 \dot{z}_i^{(1)} &= x_i^{(1)} y_i^{(1)} - \beta z_i^{(1)} + \sigma (z_{i-1}^{(1)} + z_{i+1}^{(1)} - 2z_i^{(1)}) + c\sigma \sum_j (x_j^{(2)} - x_i^{(1)}),
 \end{aligned}
 \tag{D.1}$$

where we set $\alpha = 10$, $\beta = 2$, and $c = 0.2$, leaving the parameters ρ and σ to be varied [Fig. D.1(b)]. The oscillators in the second layer are described by similar equations.

A representative trajectory of the system for $\rho = 60$ and $\sigma = 2$ is shown in Fig. D.1(c). The lower and upper panels show the dynamics of the x variables for oscillators in the respective layer, while the middle panel shows their synchronization error. A space-time

plot of the synchronization error in each layer is presented in Fig. D.1(d), where the intermittently alternating dynamics is more apparent.

D.2. Linear stability analysis of chimera states

In order to assess the linear stability of a chimera state, we calculate the synchronization stability in the coherent cluster while taking into account the influence of the incoherent cluster. This calculation can be done efficiently using a generalization of the master stability function formalism developed in Ref. [109], which is tailored to describe the synchronization stability of individual clusters.

Consider a network of $2n$ diffusively coupled identical oscillators:

$$(D.2) \quad x_i[t+1] = f(x_i[t]) - \sigma \sum_{j=1}^{2n} L_{ij} h(x_j[t]),$$

where x_i is the state of the i -th oscillator, f is the mapping function governing the uncoupled dynamics of each oscillator, $\mathbf{L} = \{L_{ij}\}$ is the Laplacian matrix describing the structure of an undirected network with two nonintertwined identical clusters, h is the interaction function, and $\sigma > 0$ is the coupling strength.

Let $\tilde{\mathbf{L}}$ be the $n \times n$ Laplacian matrix that encodes the intracluster connection inside the coherent cluster, μ be the total strength of intercluster connections each oscillator in the coherent cluster receives from the incoherent cluster, and $x_1 = x_2 = \dots = x_n = s$ be the synchronization manifold for the n oscillators in the coherent cluster. The variational equation describing the evolution of the deviation away from s can be written as

$$(D.3) \quad \delta \mathbf{X}[t+1] = \left(\mathbf{1}_n \otimes f'(s[t]) - \sigma \hat{\mathbf{L}} \otimes h'(s[t]) \right) \delta \mathbf{X}[t],$$

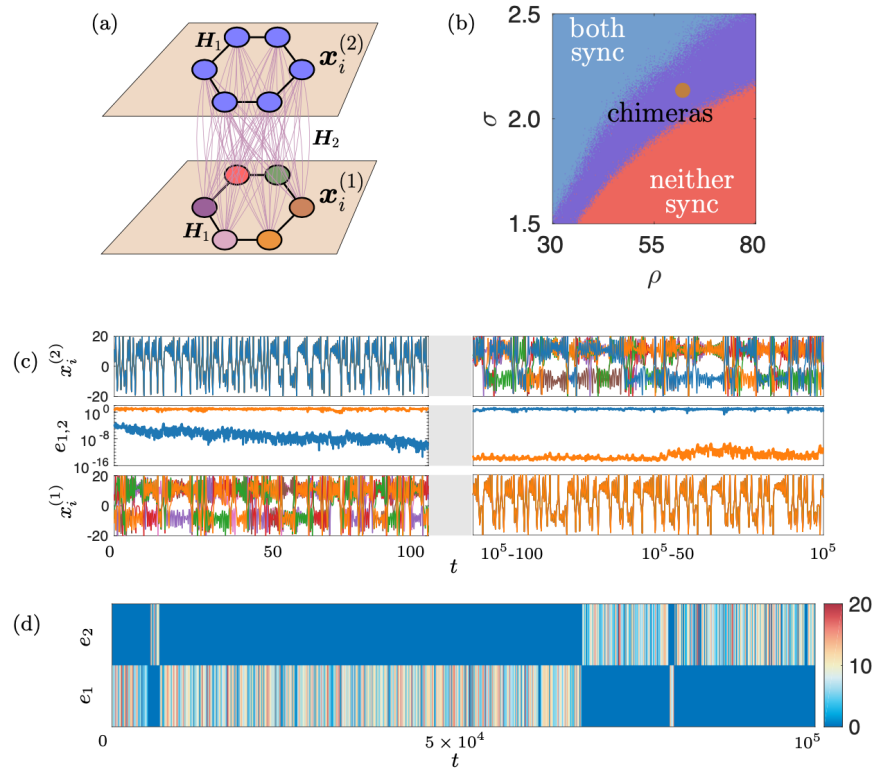


Figure D.1. Switching chimera in a multilayer network of Lorenz oscillators. (a) Two-layer network of Lorenz oscillators with different intralayer and interlayer interactions, given by $\mathbf{H}_1 = (0, 0, z)^\top$ and $\mathbf{H}_2 = (0, 0, x)^\top$, respectively. The color coded nodes represent a chimera state in which the first layer is incoherent and the second layer is synchronized. (b) Diagram in the ρ - σ plane characterizing the linear stability of synchronization in the two layers. The color codes are the same as those in Fig. 7.1(b). (c) Direct simulation of the system for $\sigma = 2.1$ and $\rho = 60$ [brown dot in (b)], where the different panels show the color-coded trajectories for the x component of the oscillators (bottom and top) and the synchronization error in each layer (middle). (d) Switching chimera dynamics visualized in a space-time representation of synchronization error. In (c) and (d), the switching is induced by round-off errors in the simulations performed using double precision.

where $\mathbb{1}_n$ is the identity matrix, $\hat{\mathbf{L}} = \tilde{\mathbf{L}} + \mu \mathbb{1}_n$, $\delta \mathbf{X} = (\delta x_1, \dots, \delta x_n)^\top = (x_1 - s, \dots, x_n - s)^\top$, and \otimes denotes the Kronecker product. Although the incoherent cluster does not enter the equation explicitly, it influences the matrix $\hat{\mathbf{L}}$ and the synchronization trajectory $s[t]$ through the intercluster coupling. We note that the input from the incoherent cluster faithfully accounts for the state of those oscillators and is time dependent in general.

Equation (D.3) can be decoupled into n independent equations by diagonalizing $\hat{\mathbf{L}}$:

$$(D.4) \quad \eta_i[t+1] = \left(f'(s[t]) - \sigma \hat{v}_i h'(s[t]) \right) \eta_i[t],$$

where $\boldsymbol{\eta} = (\eta_1, \dots, \eta_n)^\top$ is $\delta \mathbf{X}$ expressed in the new coordinates that diagonalize $\hat{\mathbf{L}}$ and $\hat{v}_i = \tilde{v}_i + \mu$ are the eigenvalues of $\hat{\mathbf{L}}$ in ascending order. Synchronization in the coherent cluster is stable if and only if $\Lambda(\sigma \hat{v}_i) < 0$ for $i = 2, \dots, n$, where

$$(D.5) \quad \Lambda(\sigma \hat{v}_i) = \lim_{T \rightarrow \infty} \frac{1}{T} \sum_{t=0}^{T-1} \ln \left| f'(s[t]) - \sigma \hat{v}_i h'(s[t]) \right|$$

is the Lyapunov exponent of Eq. (D.4) and $\hat{v}_2, \dots, \hat{v}_n$ represent the perturbation modes transverse to the synchronization manifold of the coherent cluster. The maximum transverse Lyapunov exponent (MTLE) determining the synchronization stability is $\max_{2 \leq i \leq n} \Lambda(\sigma \hat{v}_i)$. A chimera state is stable for $\xi = 0$ if the MTLE for synchronization in the coherent cluster is negative under the influence of the incoherent cluster.

D.3. Dominant switching route

Here, we provide more evidence that short-wavelength bifurcation is the dominant mechanism to initiate switching between the two symmetric subchimeras. Again, we simulate Eq. (7.1) to extract the average switching period \bar{T} for various levels of noise

intensity ξ , but this time the short-wavelength component Δ_{sw} is filtered out from the noise applied to each ring. If a short-wavelength bifurcation is indeed the dominant route for switching, then one would expect the average switching period to become independent of the noise intensity after filtration.

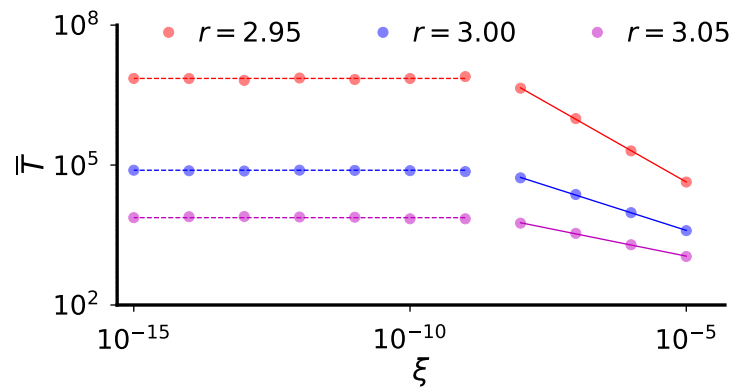


Figure D.2. Average switching period \bar{T} as a function of noise intensity ξ for various r . The system is the network of logistic maps in Fig. 7.1(a) for $\sigma = 1.7$, and the noise is Gaussian (but with the short-wavelength component filtered out). The flatness of the fitting lines below $\xi = 10^{-9}$ confirms that short-wavelength bifurcation is the dominant route for chimera switching.

This is exactly the case shown in Fig. D.2, where the slope becomes completely flat for each r when the noise intensity goes below 10^{-9} (compare with Fig. 7.2). Due to the presence of round-off errors in our simulations, whose short-wavelength component cannot be filtered, switching can still be observed in the flat region at a rate induced by the round-off errors (noise intensity around 10^{-16}). When the noise intensity goes above 10^{-9} , new switching pathways besides the short-wavelength bifurcation start to become available, as demonstrated by the resulting decrease of the average switching period.

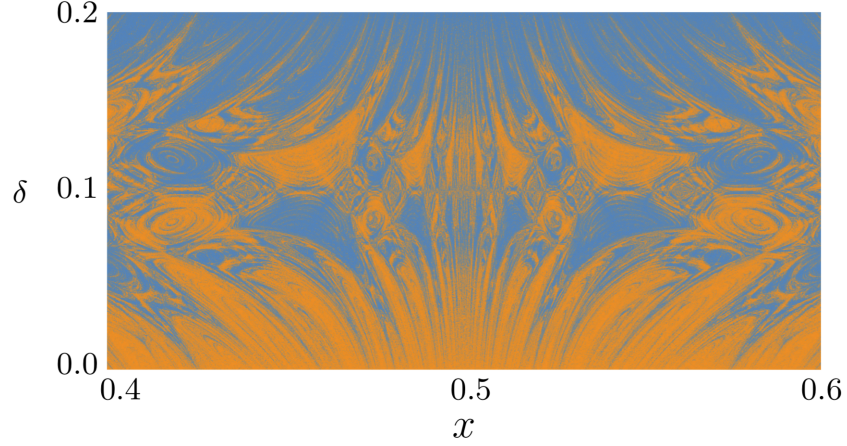


Figure D.3. Transversal section of the intermingled basins that directly connects the two symmetric subchimeras. This corresponds to a different state-space section of the system considered in Fig. 7.7.

D.4. Transversal section of intermingled basins

Figure D.3 shows the intermingled basins for a two-dimensional section of the state space for the logistic map system described by Eq. (7.1). This section is defined by

$$(D.6) \quad \mathbf{x}^{(1)} = x\mathbf{1}_6 + \mathbf{\Delta}_{sw}(\delta), \quad \mathbf{x}^{(2)} = x\mathbf{1}_6 + \mathbf{\Delta}_{sw}(\delta_{\max} - \delta),$$

where δ_{\max} is taken to be 0.2. For $\delta = 0$, the first ring is synchronized and the second ring is incoherent (orange subchimera), while for $\delta = \delta_{\max}$, the second ring is synchronized and the first ring is incoherent (blue subchimera). Thus, this section of the state space directly connects the two symmetric subchimeras. As one approaches the orange (blue) subchimera, the points become predominantly orange (blue), but no matter how close δ is to zero (δ_{\max}), speckles of blue (orange) dots can always be found.

D.5. Robustness against oscillator heterogeneity

In Fig. D.4, we quantify the effect of oscillator heterogeneity on the switching dynamics, explicitly demonstrating the robustness of the switching chimeras. We start from a system of identical oscillators (the system in Fig. 7.1 for $r = 3$ and $\sigma = 1.7$) and introduce independent random perturbations to the parameter r of each oscillator, drawn from a Gaussian distribution of zero mean and standard deviation Δ .

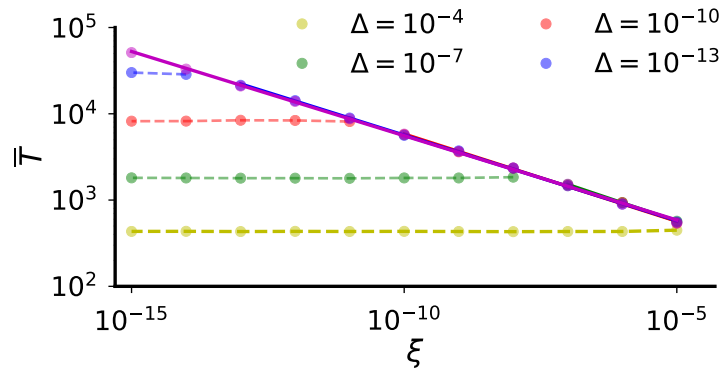


Figure D.4. Effect of oscillator heterogeneity on the switching behavior determined from direct simulations. The solid line indicates the power-law scaling for $\xi \geq \Delta$, which is precisely the scaling observed in the absence of oscillator heterogeneity. For each of the four levels of heterogeneity Δ considered, when $\xi < \Delta$ the effect of heterogeneity becomes dominant and the average switching period \bar{T} becomes independent of ξ .

For $\xi \geq \Delta$, the average switching periods in the homogeneous and heterogeneous systems become indistinguishable, with both following a well-defined power-law distribution on noise intensity. For $\xi < \Delta$, the effect of heterogeneity dominates the effect of noise; as a result, the average switching period (dashed lines) branches out of the original power-law relation (solid line) and approaches a constant determined by Δ . These results are largely independent of the particular realization of oscillator heterogeneity.

D.6. Animated dynamics of a switching chimera

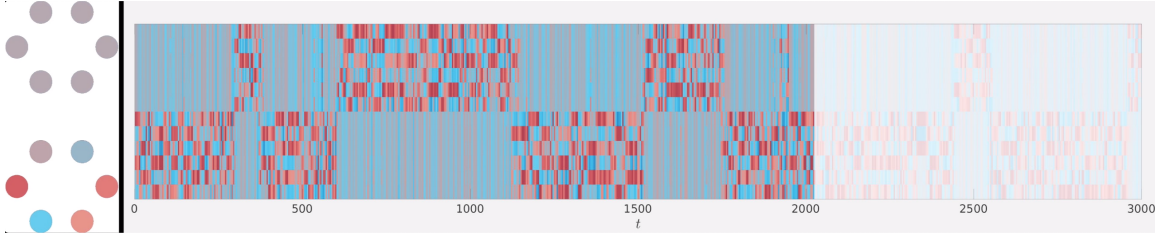


Figure D.5. Animation of a switching chimera from the optoelectronic experiment. Left: Nodes of the two-ring network of optoelectronic oscillators (links not shown), where each oscillator is color coded according to its state $x_i^{(1,2)}$. Right: Spatiotemporal representation of the data on the left, following the same color code. The defining features of a switching chimera are evident in both representations. The animation is available online at <https://youtu.be/PIVgurLIGN0>.

D.7. Predicted intermingled basins in experimental system

Figure D.6 shows intermingled basins for one of the optoelectronic systems studied in Fig. 7.8.

D.8. Effect of system size

We surveyed the $\sigma \times r$ plane for different cluster sizes n to determine the area where each of the five possible dynamical behaviors is observed. The results are presented in Fig. D.7(a) and indicate a decreasing propensity for the switching between subchimeras as n increases. For parameters in the switching region, we also calculated the average switching period as a function of ring size. As shown in Fig. D.7(b) for $\sigma = 2.1$, $r = 2.3$, and various values of noise intensity ξ , the average switching period \bar{T} increases exponentially with n .

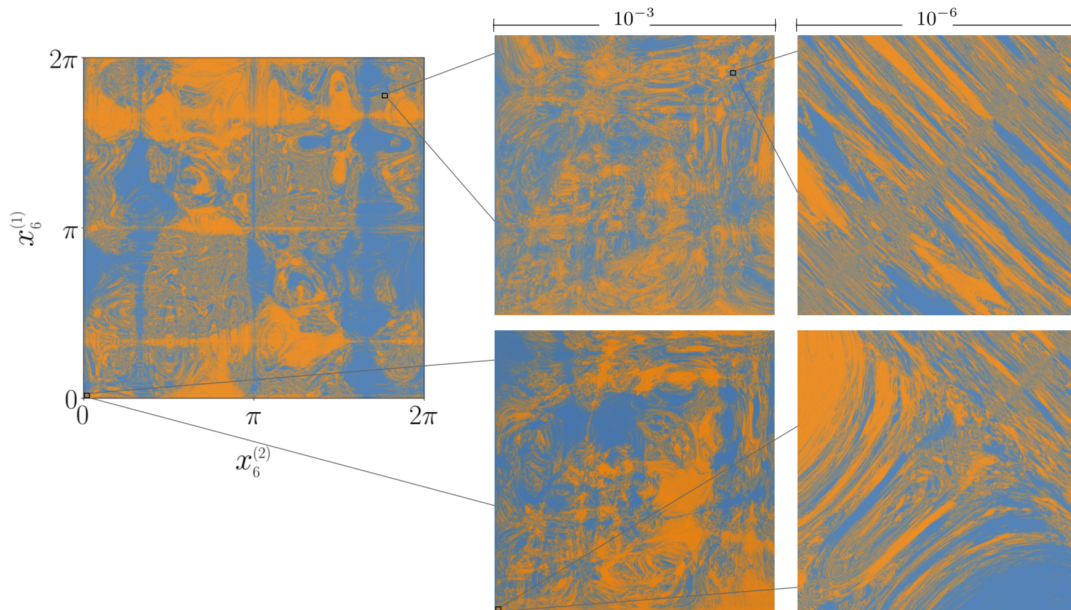


Figure D.6. Counterpart of Fig. 7.7 for the experimental system studied in Fig. 7.8. The parameters used are $\beta = 1.3$ and $\sigma = 1.05$.

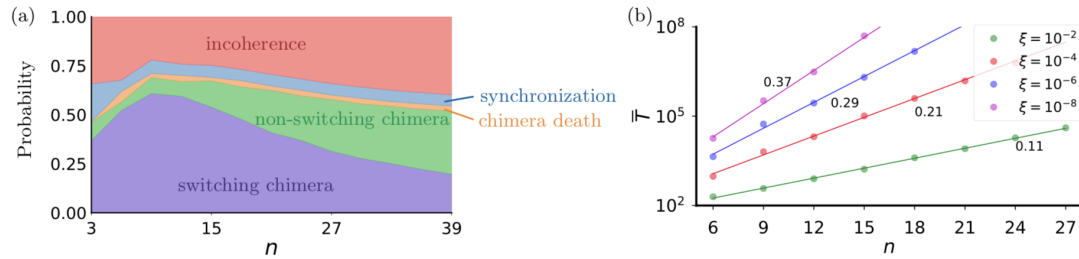


Figure D.7. Impact of system size on switching propensity. (a) Probabilities of observing the five distinct dynamical behaviors as functions of ring size n . The parameter region sampled is $[2.3, 3.1] \times [1.4, 2.8]$ in the $\sigma \times r$ plane, and is chosen so as to encompass most of the chimera regions. Comparing the purple and green shades, one can see that chimeras are less likely to be switching when n is large. (b) Average switching period \bar{T} as a function of ring size n for $\sigma = 2.1$, $r = 2.3$, and various values of noise intensity ξ . The smaller the noise intensity, the stronger the dependence of the switching period on system size.